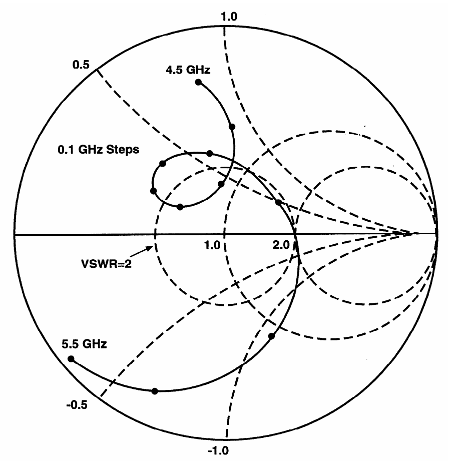

Applied Computational Electromagnetics Society Journal

Special Issue on Innovative Approaches to the Solution of Large and Multiscale Electromagnetic Radiation and Scattering Problems

Guest Editor
Raj Mittra

April 2009
Vol. 24 No. 2
ISSN 1054-4887

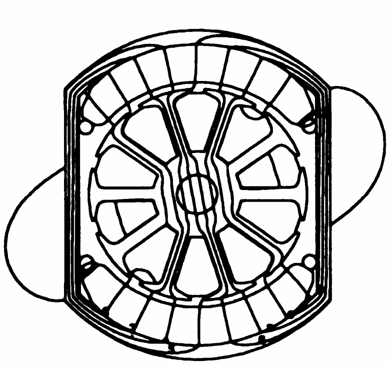

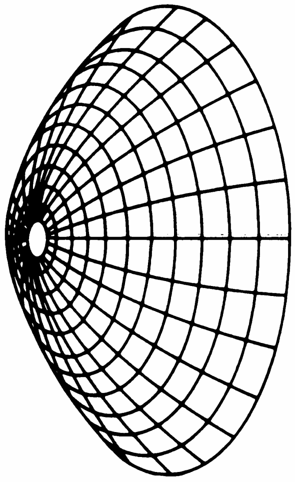

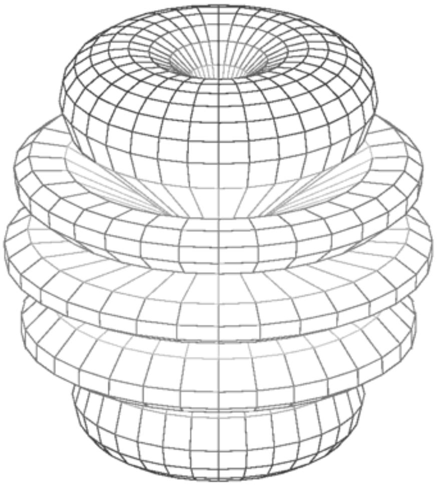

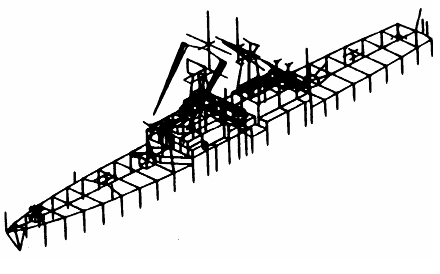

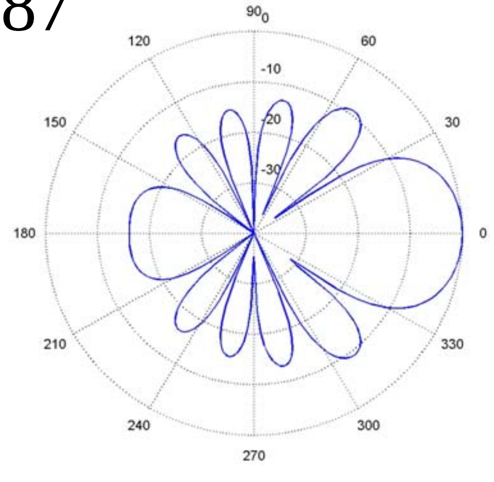

GENERAL PURPOSE AND SCOPE: The Applied Computational Electromagnetics Society ***(ACES)*** Journal hereinafter known as the ***ACES Journal*** is devoted to the exchange of information in computational electromagnetics, to the advancement of the state-of-the art, and the promotion of related technical activities. A primary objective of the information exchange is the elimination of the need to "re-invent the wheel" to solve a previously-solved computational problem in electrical engineering, physics, or related fields of study. The technical activities promoted by this publication include code validation, performance analysis, and input/output standardization; code or technique optimization and error minimization; innovations in solution technique or in data input/output; identification of new applications for electromagnetics modeling codes and techniques; integration of computational electromagnetics techniques with new computer architectures; and correlation of computational parameters with physical mechanisms.

SUBMISSIONS: The ***ACES Journal*** welcomes original, previously unpublished papers, relating to applied computational electromagnetics. Typical papers will represent the computational electromagnetics aspects of research in electrical engineering, physics, or related disciplines. However, papers which represent research in applied computational electromagnetics itself are equally acceptable.

Manuscripts are to be submitted through the upload system of ***ACES*** web site http://aces.ee.olemiss.edu See "Information for Authors" on inside of back cover and at ***ACES*** web site. For additional information contact the Editor-in-Chief:

Dr. Atef Elsherbeni
Department of Electrical Engineering
The University of Mississippi
University, MS 386377 USA
Phone: 662-915-5382 Fax: 662-915-7231
Email: atef@olemis.edu

SUBSCRIPTIONS: All members of the Applied Computational Electromagnetics Society who have paid their subscription fees are entitled to receive the ***ACES Journal*** with a minimum of three issues per calendar year and are entitled to download any published journal article available at http://aces.ee.olemiss.edu.

Back issues, when available, are $15 each. Subscriptions to ***ACES*** is through the web site. Orders for back issues of the ***ACES Journal*** and changes of addresses should be sent directly to ***ACES***:

Dr. Allen W. Glisson
302 Anderson Hall
Dept. of Electrical Engineering
Fax: 662-915-7231
Email: aglisson@olemiss.edu

Allow four week's advance notice for change of address. Claims for missing issues will not be honored because of insufficient notice or address change or loss in mail unless the Executive Officer is notified within 60 days for USA and Canadian subscribers or 90 days for subscribers in other countries, from the last day of the month of publication. For information regarding reprints of individual papers or other materials, see "Information for Authors".

LIABILITY. Neither ***ACES***, nor the ***ACES Journal*** editors, are responsible for any consequence of misinformation or claims, express or implied, in any published material in an ***ACES Journal*** issue. This also applies to advertising, for which only camera-ready copies are accepted. Authors are responsible for information contained in their papers. If any material submitted for publication includes material which has already been published elsewhere, it is the author's responsibility to obtain written permission to reproduce such material.

APPLIED COMPUTATIONAL ELECTROMAGNETICS SOCIETY JOURNAL

Special Issue on Innovative Approaches to the Solution of Large and Multiscale Electromagnetic Radiation and Scattering Problems

Guest Editor
Raj Mittra

April 2009
Vol. 24 No. 2
ISSN 1054-4887

The ACES Journal is abstracted in INSPEC, in Engineering Index, DTIC, Science Citation Index Expanded, the Research Alert, and to Current Contents/Engineering, Computing & Technology.

The first, fourth, and sixth illustrations on the front cover have been obtained from the Department of Electrical Engineering at the University of Mississippi.

The third and fifth illustrations on the front cover have been obtained from Lawrence Livermore National Laboratory.

The second illustration on the front cover has been obtained from FLUX2D software, CEDRAT S.S. France, MAGSOFT Corporation, New York.

THE APPLIED COMPUTATIONAL ELECTROMAGNETICS SOCIETY
http//:aces.ee.olemiss.edu

ACES JOURNAL EDITOR-IN-CHIEF

ACES JOURNAL ASSOCIATE EDITORS-IN-CHIEF

ACES JOURNAL EDITORIAL ASSISTANTS

ACES JOURNAL EMERITUS EDITORS-IN-CHIEF

ACES JOURNAL EMERITUS ASSOCIATE EDITORS-IN-CHIEF

APRIL 2009 REVIEWERS

THE APPLIED COMPUTATIONAL ELECTROMAGNETICS SOCIETY

JOURNAL

Vol. 24 No. 2 April 2009

TABLE OF CONTENTS

Preface

Recently, there has been great interest on part of the Computational Electromagnetics (CEM) community in developing innovative techniques for solving real-world antenna and scattering problems involving a large number of degrees of freedom, or DoFs, which can often run upwards of millions. The advent of high performance computers has made the task somewhat easier, in many cases, though not all, because not all algorithms scale well on parallel machines.

Historically, before the introduction of the Fast Multipole Method, there were no systematic approaches available for solving large EM problems, except perhaps by using asymptotic methods, such as the GTD (geometrical theory of diffraction) and PTD (Physical Theory of Diffraction). However, such asymptotic methods were not numerically rigorous, and they could only handle scatterers with canonical shapes and perfectly conducting nature.

The advent of the Fast Multipole Method changed the computing landscape dramatically and enabled us to solve very large problems without either storing the associated MoM (Method of Moments) matrix, or solving it directly. It was essentially the “only game in town,” for about a decade or so, since there was no other algorithm that could come even close to competing with it. The FMM technique is reviewed in this Special issue by Vikram and Shanker. An approach to accelerating the FMM is discussed in a contribution by Chen and his colleagues

Four other approaches to solving large problems, that have been developed more recently, are presented in the Special issue, all of which follow different strategies for solving large CEM problems than that employed by the FMM. The first of these is the IE-FFT approach by Seo et al., which takes advantage of the efficiency of the FFT algorithm to perform the matrix-vector products needed in the iterative solution, and which the FMM does by using multipole methods. An alternative method is employed by Gedney and his colleagues, who utilize a preconditioner developed by using a Sparse Direct solver. Next, methods based on the use of macro-basis functions, which enable one to reduce the size of the original MoM matrix significantly, are described by Matekovits and his co-workers, and also by Casaletti and his colleagues.

Next, three contributions by Maaskant et al., Delgado et al. and Mittra, all present techniques based on the Characteristic Basis Function Method (CBFM), which also may be viewed as being based on the use of macro-basis functions. The issue of solving large problems on parallel machines using the CBFM is addressed in the Mittra paper.

Additionally, an innovative approach that takes advantage of the identical nature of the array elements to solve a phased-array-type problem, and a hybrid method that combines FEM with the Mode matching method to also address the array problem, are contributed by Craye et al. and Pellegreni and her colleagues, respectively.

Finally, an interesting takeoff on the Physical Optics approach, which employs iteration, is discussed by the contribution from Burkholder et al.

We firmly believe that this Special issue would be secure its place in the literature as a major contribution in CEM, and we hope that the various techniques described in this issue, which cover a wide spectrum, would find a very receptive as well as appreciative audience, both among the researchers and practitioners of CEM.

An Incomplete Review of Fast Multipole Methods–from Static to Wideband–as Applied to Problems in Computational Electromagnetics

Melapudi Vikram, and Balasubramaniam Shanker
Department of Electrical and Computer Engineering
Michigan State University, East Lansing, MI 48824, USA
vikramr@egr.msu.edu , bshanker@egr.msu.edu

***Abstract*―** Fast multipole methods (FMM) and their immediate predecessors, tree codes, were developed in response to the need for solving N-body problems that occur in applications as varied as biophysics, computational chemistry, astrophysics and electromagnetics. In all these areas, it is necessary to compute long range potentials of the form $1/R$ between a dense distribution of point charges, where R is the distance between any two charges. Often, repeated evaluation of these potentials is necessary. It is apparent that the cost of direct evaluation, which scales as $O(N^2)$ for N degrees of freedom, forms a fundamental bottleneck. FMM and tree methods ameliorate the cost associated with these computation; CPU times of these method scale as $O(N)$. It stands to reason that FMM has had a seminal impact on a multitude of fields, so much so, that it was recognized as one of the top ten algorithms of the past century. A method to rapidly compute potentials of the form $e^{-j\kappa R}/R$ soon followed. As the reader is aware, these potentials are the crux of integral equation based analysis tools in electromagnetics and the advent of these methods have transformed the face of computational electromagnetics. Consequently, the state of art of integral equation solvers has grown by leaps and bounds over the past decade. This paper attempts to present a detailed review of the state of art of FMM based methods that are used in computational electromagnetics, from the static to the high frequency regime.

***Index Terms*―** Fast Multipole Method (FMM), FMM review, Multiscale, Wideband FMM, Multipole methods, Cartesian expansions, ACE.

I. INTRODUCTION

The numerical solution of Maxwell's equations has typically proceeded along two different paths. The first, and perhaps the more popular, is the direct discretization of Maxwell's equations [1, 2]. Finite difference and finite element methods belong to this class of solvers. Their popularity stems from two salient features; (i) they are typically simpler to program and (ii) their memory and CPU cost scales as $O(N)$, where N denotes the number of degrees of freedom. The second methodology for solving Maxwell's equations are based on developing integral equations (IE) derived by evoking the Green's identity/equivalence theorems. While the latter was introduced in electromagnetics more than four decades ago [3], they were not a popular option for electromagnetic analysis. The bottlenecks to their adoption was due to both the memory and CPU complexity, both of which scale as $O(N^2)$. This is despite some of the inherent advantages of integral equations for analyzing open region problems, viz., better condition numbers, possibility of using surface integral equations and incorporation of the radiation boundary condition in the Green's function.

The introduction of the fast multipole methods (and tree codes) significantly altered the landscape. Both these methods were developed in response to accelerating pairwise potential evaluations in N-body problems in fields ranging from biophysics to computational chemistry to astrophysics, etc. Here, it is necessary to compute long-range Coulombic potentials repeatedly between N randomly distributed particles. The tree methods [4, 5] and the fast multipole method (FMM) [6–9] reduced the computational complexity of computing these pairwise potentials from $O(N^2)$ to $O(N)$. FMM and tree codes are based on a hierarchical decomposition of the computational domain, and using multipole/local expansions to compute the influence between sub-domains that are sufficiently separated. The FMM,

1054-4887 © 2009 ACES

as introduced in [7], exploits the representation of the potential in terms of spherical harmonics. As we shall see, this is a consequence of using addition theorems to represent the potential as a series wherein each term is a product of two functions. These functions depend either on the coordinates of the source or the observer only. The separation between source and observer is crucial to creating a fast scheme. At about the same time, an algorithm that achieves the same reduction on complexity, *albeit* using Cartesian tensors was introduced [10]. This derivation relies on using Taylor expansion of the potential function to provide the necessary addition theorems [11]. Cartesian expansions have been used extensively in tree codes. More recently, FMM codes based on Cartesian expansions have used recurrence relations to avoid derivatives [12]. Typically, FMMs derived using the Cartesian expansion are more expensive as spherical harmonics are optimal in representing Coulombic potentials. However, it was recently shown that it is possible to develop a FMM using Maxwell-Cartesian harmonics that are as optimal as using spherical harmonics with one singular advantage; it avoids the need for special functions [13]. Both FMM and tree codes have revolutionized analysis in various application domains ranging from molecular dynamics [14], elastostatics [15, 16], elastic wave equations [17], flow problems [18], capacitance [19] and impedance [20] extraction in micro-electronic circuits, evaluation of splines [21] and spherical harmonics [22, 23]. The FMM framework has also been extended to the solution of potentials resulting from parabolic equations [24–26].

However, direct extension of FMM to the solution of potentials arising from hyperbolic equations is not as straightforward. The first solution to this problem was presented in two dimensions [27, 28], and soon extended to three dimensions [29, 30]. The crux to developing these algorithms was the derivation of a diagonalized form of the translation operator [30–32]. Since then, there has been a virtual explosion in research in application of these methods to various problems in electromagnetics; see [33–35] and references therein. The state of art is such that problems of the order of tens million spatial degrees of freedom have been solved [36– 41]. However, the development of FMM based method continues on many fronts [42–50]. This paper reviews progress in FMM technology since its inception and details current trends in FMM research.

With this introduction, the rest of the paper is organized as follows; in Section II, we will outline the overall problem, introduce notation that is common to the article. Next, static FMM is presented in Section III. Methods based on both Spherical harmonics and Accelerated Cartesian expansions (ACE) will be presented. In Section IV, we will detail the development of FMMs and their variants for the Helmholtz equation. Finally, in Section IV-B we will elaborate on the methods used for wideband analysis. In all cases, we will first present theorems to implement a single level algorithm followed by the steps necessary to implement a multilevel version. The CPU time of all steps will be elucidated as well as "some" algorithmic improvements to these methods since they were first introduced. Finally, Section VI will summarize the state of art of FMM. In what follows, a time dependence of $e^{j\omega t}$ is tacitly assumed. As an aside, while we have tried to be as complete as possible in our citations, it is almost certain that we have unknowingly missed some.

II. HIERARCHICAL COMPUTATION SCHEME

The purpose of this section is to outline the structure of fast multipole methods and introduce notation that will be used in the rest of the paper.

A. Preliminaries

Consider a source distribution $q(r)$ such that $supp\ \{q(r)\} = \Omega \subset \mathbb{R}^3$. Likewise, it is assumed that the observers are also distributed in Ω. With no loss of generality, it is assumed that $q(r) = \sum_{i=1}^{N} q_i \delta\left(r - r_i\right)$, where N is the number of degrees of freedom. The field due to this source constellation at any point $r \in \mathbb{R}^3$ is given by

$$\phi(r) = g\left(|r|\right) * q(r) = \sum_{i=1}^{k} g\left(|r - r_i|\right) q_i \ , \tag{1}$$

where $g\left(|r|\right)$ is the appropriate Green's function, and * denotes a spatial convolution. It is apparent from this expression that the field evaluation scales as $O(N^2)$ for N observation points. Ideas introduced by [4] to ameliorate this cost for static problems relies on exploiting the fact that the field at a point due to a cluster of sources is rank deficient, where the rank depends on the distance between the point and the center of the cluster. In other words, for a given accuracy, potential at an observation point sufficiently separated from a cluster of sources can be computed with few multipole expansions. Similarly, for given accuracy, few local expansions can be used to compute potential at a cluster of observation point due to a well-separated source. These ideas were cast in a more formal framework as tree-codes [5] and FMM [6]. At this point, we note that there is rampant confusion in terminology; both FMM and tree codes are used interchangeably. While the two methods are closely related, there are subtle but significant differences between the two [51]. Tree codes compute interactions between source pairs using one of three methods: (i) directly, (ii) evaluating fields at each observation point using multipole expansion due to a cluster of sources, or (iii) using local expansion at observation clusters to find fields. The decision on the operation used depends on which one is computationally efficient. On the other hand, the algorithmic structure of FMM enables the computation of potentials in an optimal manner [51]. Two additional operations that permit this are aggregation and disaggregation functions. These permit the computation of information at coarser (or finer) levels using information at finer (or coarser) levels. Thus, FMM relies on a hierarchical decomposition of the computational domain. This is achieved using the following strategy [8]; the computational domain Ω is embedded in a fictitious cube that is then divided into eight sub-cubes, and so on. This process continues recursively until the desired level of refinement is reached; an N_l-level scheme implies N_l -1 recursive divisions of the domain, see Fig. 1. At any level, the (sub) domain that is being partitioned is called the parent of all the eight children that it is being partitioned into. At the lowest level, all source/observers are mapped onto the smallest boxes. This hierarchical partitioning of the domain is referred to as a regular octtree data structure. Regular oct-tree representations are optimal only for geometries with uniform distribution [52]; non-uniform distributions can be represented using compressed oct-trees [39, 51]. In compressed oct-trees, sub-division of a domain is stopped when number of source/observer in that domain becomes less than a pre-fixed limit. While many algorithm exist for constructing a tree, the one that we have found to be efficient is the use of key data-structure to represent the nodes of a tree. In this approach the root box enclosing the entire geometry is represented with integer value 1; each of the eight (four) children of a parent is identified with a three (two) bit code which is appended to the parent box key to obtain their global unique key. Figure 2 shows an example compressed oct-tree where each box is represented using key-codes. This representation has several advantages: the nodes of tree at each level automatically follow Morton ordering and it plays an important role when partitioning the boxes among processors in parallel algorithm, all antecedents of a box and essential information like size of box, center position, level etc. can be readily recovered from its key-code using bit manipulations [38, 53, 54]. Mapping the computational domain onto a tree facilitates partition/classification of interactions as being either in the near or farfield. This is done using the following rule: at any level in the tree, all boxes/sub-domains are classified as being either in the near or far field of each other using the following dictum: two sub-domains are classified as being in the farfield of each other if the distance between the centers is at least twice the side length of the domain, and their parents are in the near field of each other; see Fig. 3 for an illustration of these classification. Once, the interaction list have been built for all levels, the computation proceeds as follows; at the lowest level, interaction between the elements of boxes that are in the near-field of each other is computed directly, i.e., using (1). All other interactions are computed using a three stage algorithm: (i) compute multipoles of sources that reside in each box; (ii) convert these to local expansion at all boxes that are in its far field; (iii) from the local expansion, compute the field at each observer. This simple three stage scheme is called a one-level scheme, and necessitates the development of theorems for (i) computation of multipoles at leaf (or smallest boxes), (ii) translate multipole expansion to local expansion and (iii) finally, aggregate the local expansions in a box to compute the field at all the observers. It is apparent that one can derive a more efficient computational scheme by embedding this scheme within itself as shown in Fig. 4. That is, if two sets of sub-domains that interact with each other are sufficiently far away, then these clusters may be combined to form large clusters that then interact with each other at a higher level and so on; this is referred to here as a multilevel scheme. This implies that it is necessary to develop additional theorems that enable (i) shifting the origins of multipole so that effects of small clusters can be grouped together to form larger clusters and (ii) move the origin of local expansion so that expansions at the origin of the parent may be disaggregated to those of its children. In concert, these theorems enable one to traverse up and down the tree, and are presented next. This said the various steps involved in the hierarchical computing are shown in Algorithm 1.

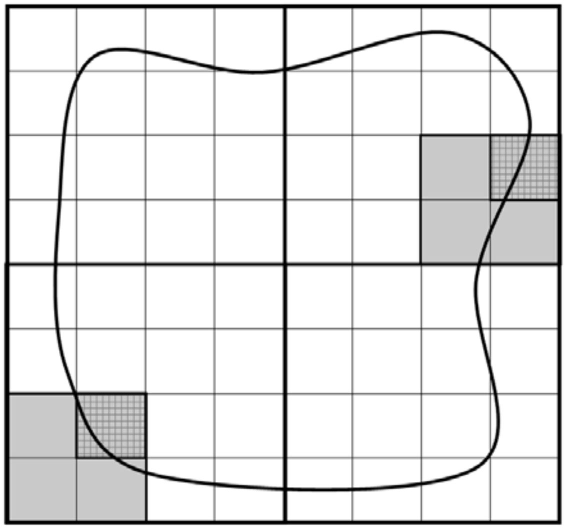

Fig. 1. Hierarchical decomposition of a 2D computational geometry.

Note that in single level algorithm the upward and downward tree traversal (steps 5 and 7) are absent. Next, we will detail these operations for different FMMs. Starting with well known static FMM to those for Helmholtz and finally to those for wideband FMM. Details are presented for the first two despite the fact that they are well known. The rationale for doing so is two fold (i) it is important to understand when FMM for Helmholtz fails and (ii) techniques developed for static FMM and some of the new FMM approaches find their way into the development of wideband FMM.

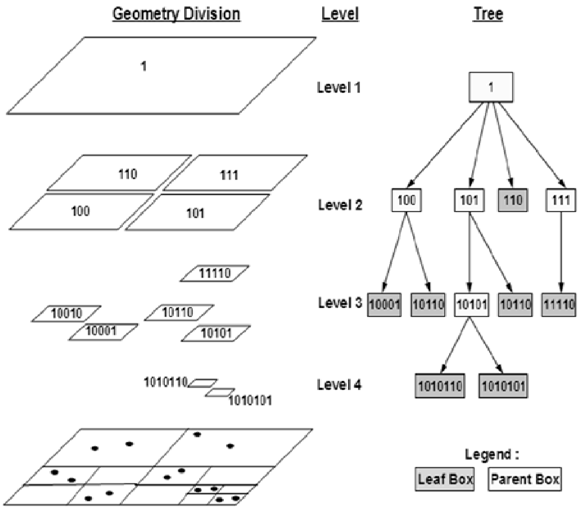

Fig. 2. Representation of 2D computational geometry using quad-trees. Boxes at different levels and corresponding nodes in tree are represented using binary keys.

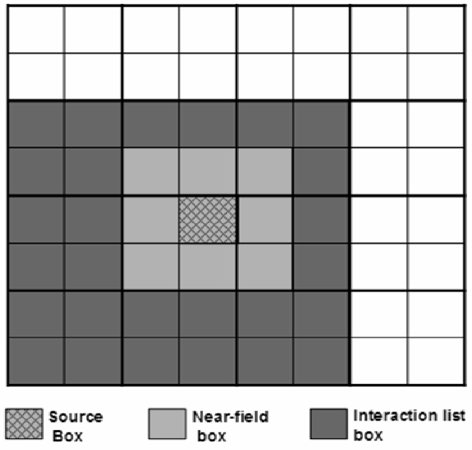

Fig. 3. Illustration of interaction list; dark boxes are contained in the interaction list of source box.

III. STATIC FAST MULTIPOLE METHOD

This section provides the appropriate theorems for fast evaluation of potential defined in terms of $g\left(|r|\right)=1/|r|$. Such potentials are commonly used in study of plasma dynamics, magnetostatic problems, eddy currents etc. While on first glance, one might be inclined to exclude methods developed for rapid evaluation of the Coulomb potential but these play an important role in developing fast methods for wideband problems.

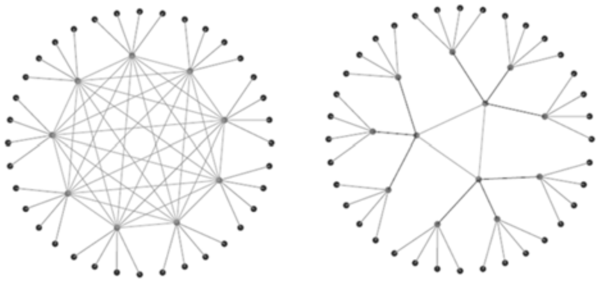

Fig. 4. Illustration of computational load in singleand multi-level FMMs. Dark nodes correspond to actual sources while light shaded nodes represent centers of multipole and local expansions.

Algorithm 1 Hierarchical computing

```
Construct the tree representation for the given geometry (distribution of discrete points).
Build interaction list using the above definition, for all boxes in the tree and the near-field list for leafless boxes.
NF: Use direct method for computation of nearfield potential at observation points in each leafless box from sources contained in its near-field boxes.
S2M: compute multipole expansions for each leafless boxes from sources contained within it.
M2M (upward traversal): for all parent boxes compute the multipole expansion by combining the multipole expansions at their children boxes.
M2L (translation): for all boxes in the tree convert the multipole expansions to local expansions about centers of boxes in their interaction list.
L2L (downward traversal): update the local expansion information at a child box using the local expansion of their parent box.
L2O: use the local expansions about each leafless box to compute the farfield potential at its observation points
```

A. Single Level Scheme

Consider two domains $\mathbf{\Omega}_s \subset \mathbb{R}^3$. and $\mathbf{\Omega}_o \subset \mathbb{R}^3$ that comprises of randomly located source and observer points, respectively. With no loss of generality, it is assumed that the number of sources and observers are *k*, these domains can be embedded in spheres of radius *a*. The centers of $\mathbf{\Omega}_s$ and $\mathbf{\Omega}_o$ are denoted by r_s and r_o, respectively. It is assumed that $\Omega_s \subset \bar{\Omega}_s$, and $\Omega_o \subset \bar{\Omega}_o$, and $\bar{\Omega}_s \cap \bar{\Omega}_o = \varnothing$, and the domains of $\mathbf{\Omega}_s$ and $\mathbf{\Omega}_o$ are sufficiently separated. In what follows, the domains $\bar{\Omega}_s$ and $\bar{\Omega}_o$ will be called parents of $\mathbf{\Omega}_s$ and $\mathbf{\Omega}_o$, respectively. The parent domains can be embedded in a sphere of radius 2*a*, and their center are denoted by r_s^p and r_o^p, respectively. Next, we will present a single level FMM constructed using two methods; (i) spherical harmonics and (ii) Cartesian tensors.

1) Spherical harmonics: The theorems for a single and multilevel FMMs using spherical coordinates were introduced in a series of papers [7, 8], and have found extensive application in various disciplines; a sampling of these can be found in [6, 8, 19, 20, 55–57]. The genesis of the method is the well known generating function for Legendre polynomials [58],

$$\frac{1}{R} = \frac{1}{r\sqrt{1-2\dfrac{r'}{r}\cos\gamma + \left(\dfrac{r'}{r}\right)^2}} = \sum_{n=0}^{\infty} \frac{r'^n}{r^{n+1}} P_n(\cos\gamma) \qquad (2)$$

with

$$\cos\gamma = \cos\theta\cos\theta' + \sin\theta\sin\theta'\cos(\phi-\phi'), \qquad (3)$$

where $P_n(u)$ represents Legendre polynomial of degree *n*, $r' = (r', \theta', \phi')$ and $r = (r, \theta, \phi)$. Legendre polynomials in (2) can be represented in terms of spherical harmonics $Y_{nm}(\theta, \phi)$ using the addition theorem [59],

$$P_n(\cos\gamma) = \sum_{m=-n}^{n} Y_{nm}^*(\theta,\phi) Y_{nm}(\theta',\phi'), \qquad (4)$$

where the superscript * represents complex conjugate. Using (4) in (2) results in complete separation of source and observation quantities,

$$\frac{1}{R}=\sum_{n=0}^{\infty}\sum_{m=-n}^{n} r'^{n} Y_{nm}^{*}\left(\theta',\phi'\right)\frac{Y_{nm}\left(\theta,\phi\right)}{r^{n+1}}. \qquad (5)$$

These expressions enable the derivation of the following theorems necessary for steps 4, 6 and 8 in Algorithm 1.

Theorem 3.1: *Multipole Expansion (S2M), spherical*: Let k charges of strengths $\{q_i, i=1,...,k\}$ be located at $r_i \in \Omega_s$ with $|r_i - r_s| < a$. Then for any $r \in \Omega_o$, the potential ϕ is given by,

$$\phi(r)=\sum_{n=0}^{\infty}\sum_{m=-n}^{n} M_n^m \frac{Y_{nm}\left(\theta,\phi\right)}{\left|r-r_i\right|^{n+1}}, \qquad (6)$$

where

$$M_n^m=\sum_{i=1}^{k} q_i \left|r_i-r_s\right|^n Y_{nm}^{*}\left(\theta',\phi'\right), \qquad (7)$$

where the parameters $\{\theta_i, \phi_i\}$ and $\{\theta, \phi\}$ are spherical coordinates of r_i and r w.r.t the origin at r_s. In Theorem 3.1, M_n^m is the multipole expansion at r_s constructed from the source quantities $q_i(r_i)$. Proofs for the error bounds in the above expressions can be obtained from [8, 9]. Next, these multipoles are translated from r_s to r_o.

Theorem 3.2: *Multipole to Local Translation operator* (*M2L*)*, spherical*: Given a multipole expansion O_n^m about r_s, it can be mapped to local expansion L_n^m at r_o using

$$L_i^k=\sum_{n=0}^{\infty}\sum_{m=-n}^{n} \times\frac{O_n^m\left(-j\right)^{|k-m|-|m|-|k|} A_n^m Y_{i+n}^{m-k}\left(\theta,\phi\right)}{\left(-1\right)^n A_{i+n}^{m-k}\left|r_s-r_o\right|^{i+n+1}}, \qquad (8)$$

where $\{\theta, \phi\}$ are the spherical coordinates of the r_s w.r.t r_o, and $A_n^m=\frac{\left(-1\right)^n}{\sqrt{\left(n-m\right)!\left(n+m\right)!}}$.

Finally, the local expansions at any leaf node may be mapped onto the observers using the theorem presented next.

Theorem 3.3: *Local Expansions to Observer* (*L2O*)*, spherical*: The potential at a point $r \in \Omega_o$ due to local expansion L_n^m about origin is given by,

$$\phi(r)=\sum_{n=0}^{\infty}\sum_{m=-n}^{n} L_n^m\left|r-r_o\right|^n Y_{nm}\left(\theta,\phi\right). \qquad (9)$$

As before, the parameters $\{\theta, \phi\}$ are the spherical coordinates of r with respect to the origin at r_o. The above theorems, in a one level setting, permit the rapid computation of potentials at all points in Ω_o due to sources in Ω_s. It is evident that this scheme can be embedded within itself to create a multilevel scheme. But prior to doing so, it is instructive to re-examine the fundamentals of FMM from a Cartesian perspective.

2) Cartesian Tensors: While FMMs that were based on spherical harmonics and Cartesian tensors were introduced approximately at the same time [10], the latter did not receive much recognition as it was perceived to be more expensive and cumbersome. But, these expansions were used extensively in developing tree-codes [60], as well as FMM type algorithms for magnetostatics [12] and potentials of the form $R^{-\nu}$ [61, 62]. Our rationale for including this approach here is that there is an intimate relationship between spherical harmonics and the Cartesian tensors, and these connections are well known and have been explored extensively (as early as Maxwell!); see [63–65] and references therein. The following statements hold true: (i) components of a traceless tensor of rank n serve as constant coefficients in a spherical harmonic of degree n, and (ii) there is a class of traceless tensors of rank n whose components are n-degree spherical harmonics functions of x, y, z. Indeed, recurrence relationship that were conjectured for translating multipole expansions [12] can be rigorously derived using traceless tensors. Therefore, it stands to reason that the two seemingly disparate methods should have identical cost structure. In what follows, we shall briefly present theorems that permit an FMM algorithm using Cartesian tensors. Proofs for theorems presented here, and the myriad advantages of this method are detailed in [13].

In what follows, we will denote an nth rank tensor using the notation $\mathrm{A}^{(n)}$, and as is well known, it comprises of 3^n components and may be expressed in component form as $A_{\alpha_1,...,\alpha_n}$. If the tensor is totally symmetric, i.e., its value is not altered with permutation of indices, then it contains only (n + 1)(n + 2)/2 independent components. A n-fold contraction between an (n + m)*th* rank tensor and (n)*th* results in an (m)*th* rank tensor and is denoted using $C^{(m)} = A^{(n)} \bullet n \bullet r^{(n)}$. Any homogeneous polynomial in r can be written in terms of tensors as $f(r) = A^{(n+m)} \bullet n \bullet B^{(n)}$, and if $A^{(n)}$ is totally traceless, then $f_n(r)$ is a solid spherical harmonic of degree n. Here, r^n is a polyadic. These concepts are illustrated using Taylor's expansion of the Green's function as

$$\begin{aligned}\frac{1}{R} &= \sum_{n=0}^{\infty} \frac{(-1)^n}{n!} r'^n \bullet n \bullet \nabla^n r^{-1} \\ &= \sum_{n=0}^{\infty} \frac{1}{n!} \frac{r'^n}{r^{n+1}} \hat{r}'^n \bullet n \bullet D_n \hat{r}^n , \qquad (10) \\ &= \sum_{n=0}^{\infty} \frac{r'^n}{r^{n+1}} P_n\left(\hat{r}' - \hat{r}\right)\end{aligned}$$

where D_n is called the detracer which extracts the traceless component of any tensor $A^{(n)}$. The equivalence between (2) and (10) is readily apparent as

$$P_n\left(\hat{r}' - \hat{r}\right) = \frac{1}{n!} \hat{r}'^n \bullet n \bullet D_n \hat{r}^n . \qquad (11)$$

It should be noted that a traceless tensor contains only (2n + 1) components. This mathematical apparatus is critical to theorems necessary to traverse the tree, and these are enumerated next.

Theorem 3.4: *Multipole Expansion* (*S2M*), *Cartesian:* The total potential at any point $r \in \Omega_o$ due to k sources q_i, i = 1,…, k located at points $r_i \in \Omega_s$ is given by

$$\begin{aligned}\phi(r) &= \sum_{n=0}^{\infty} M_t^{(n)} \bullet n \bullet \nabla^n \frac{1}{\left|r - r_s\right|} \\ &= \frac{1}{(2n-1)!!} D_n M^{(n)} \qquad (12) \\ &= \sum_{n=0}^{\infty} (-1)^n \frac{q_i}{n!} \left(r - r_s\right)^n ,\end{aligned}$$

where (2n - 1)!! denotes a double factorial. This theorem is derived using a Taylor expansion of the potential function. It follows that a similar expansion can be used again to map these multipoles that exist at r_s to local expansions at r_o.

Theorem 3.5: *Multipole to Local* (*M2L*), *Cartesian:* Assume that the domains $\bar{\Omega}_s$ and $\bar{\Omega}_o$ are sufficiently separated, and the distance between their centers, $r_{os} = \left|r_{os}\right| = \left|r_o - r_s\right|$, is greater than $diam\{\Omega_s\}$ and $diam\{\Omega_o\}$. If a traceless multipole expansion $M_t^{(n)}$ for all n is located at r_s, then another expansion $L_t^{(n)}$ that produces the same field $\forall r \in \Omega_o$ is given as

$$L_t^{(n)} = \sum_{m=n}^{\infty} \frac{1}{n!} \nabla^n \frac{1}{r_{os}} \bullet (m-n) \bullet M_t^{(m-n)} , \qquad (13)$$

where $\nabla^n r^{-1} = (-1)^n r^{-2n-1} D_n r^n$. This expression permits simple computation of derivatives and is a generalization of the formulae provided in [12]. Finally, as in the spherical case, the final step is mapping this local expansion onto the observers. This can be accomplished by exploiting Taylor expansion, and results in the following theorem.

Theorem 3.6: *Local to Observer* (*L2O*), *Cartesian*: Given a local expansion $L_t^{(n)}$ that exist in the domain Ω_o centered around r_o, it can be shifted to any point $r \in \Omega_o$ using

$$\phi(r) = \sum_{m=0}^{\infty} (r - r_0^c)_t^m \bullet m \bullet L_t^{(m)} . \qquad (14)$$

These theorems indicate that the classical FMM can be expressed as a cascaded series of Taylor's expansion. And when properly formulated/ structured, it has identical computational complexity as the original FMM [13]; a consequence of the fact that traceless rank n tensors in the above expressions contain only (2n + 1) independent components. It is also apparent that FMM-type algorithm can be developed without resorting to traceless tensors. The advantage of such representation is elaborated in [13] and will be detailed in the next section together with methods necessary for creating a multilevel algorithm. Finally, cost of the single level algorithm is computed in the following manner. Let s be the average number of source/observation points in each leafless box and P be the maximum order of harmonics used is above expansions. Then the cost of creating P^2 multipole coefficients from sources (in S2M) and computing potential from local expansions (in L2O) scales $O(P^2N)$; cost of translating multipole to local expansions (in M2L) scales as $O(N^2/s^2P^4)$

and $O(N_s)$ is the cost for direct evaluation for nearfield. It can be shown that for optimal s, the overall cost scales as $O(N^{4/3}P^{4/3})$.

B. Multilevel FMM algorithm

It is apparent that the $O(N^{4/3})$ cost of single level algorithm can be further reduced by embedding this scheme within itself, as is evident from Fig. 4. To implement such a scheme it is necessary to develop methods that enable one to construct multipole expansions at a parent level from those at their children. These are effected using the following theorems.

Theorem 3.7: *Multipole to Multipole (M2M), spherical*: A multipole expansion O_n^m about r_s can be mapped onto one that exists around r_s^p using

$$M_i^k = \sum_{n=0}^{i} \sum_{m=-n}^{n} (-j)^{|k|-|m|-|k-m|} O_{i-n}^{k-m} \times \frac{A_n^m A_{i-n}^{k-m} \left(r_s^{cp}\right)^n Y_{nm}^* (\theta, \phi)}{A_i^k}, \tag{15}$$

where $r_s^{cp} = \left| r_s^{cp} \right| = r_s - r_s^p$, and $\{\theta, \phi\}$ are the polar coordinates of r_s w.r.t. r_s^p.

Theorem 3.8: *Local to Local* (*L2L*), *spherical*: Given a local expansion O_n^m about r_o^p, it can be mapped to one around r_o using

$$L_i^k = \sum_{n=i}^{p} \sum_{m=-n}^{n} (-j)^{|m|-|k|-|m-k|} O_n^m \times \frac{A_{n-i}^{m-k} A_i^k \left(r_o^{cp}\right)^{n-i} Y_{n-i}^{m-k} (\theta, \phi)}{(-1)^{n+i} A_n^m}, \tag{16}$$

where $r_o^{cp} = \left| r_o^{cp} \right| = r_o - r_o^p$, and $\{\theta, \phi\}$ are the polar coordinates of r_o w.r.t. r_o^p. The equivalent theorems for Cartesian expansion likewise follow.

Theorem 3.9: *Multipole to Multipole (M2M), Cartesian:* A traceless multipole tensor $O_t^{(m)}$ at r_s is related to $M_t^{(m)}$ that is centered at r_s^p via

$$M_t^{(m)} = \sum_{n=0}^{m} \frac{(-1)^n}{n!} \frac{D_n \left(r_s^{pc}\right)^n}{(2n-1)!!} O_t^{(m-n)}, \tag{17}$$

where $r_s^{cp} = r_s^p - r_s$.

Theorem 3.10: *Local to Local* (*L2L*), *Cartesian*: Given a local expansion $O_t^{(n)}$ that exist in the domain $\bar{\Omega}_o$ centered around r_o^p, it can be shifted to the domain Ω_o centered around r_o using

$$L_t^{(m)} = \sum_{n=0}^{\infty} \binom{m+n}{m} O_t^{(m+n)} \bullet m \bullet (r_o^{cp})_t^n, \tag{18}$$

where $r_o^{cp} = r_o - r_c^p$.

These theorems, in concert, permit traversing up and down the oct-tree, see figure 5. While these theorems are the bare-bones presentation of the steps required, there have been several attempts to make these more efficient [7, 8, 14, 66]. As both methods are based on Taylor expansions the upperbounds in using these approaches can be readily derived. Such a derivation is presented in [8, 13]. Alternatively, another interesting algorithm was introduced in [13] that permits exact evaluation of the multipole expansion at the parent given the multipole expansion at the children–this has been shown both analytically and numerically for different potential functions. However, in order to get this exact expression, one has to abandon the use of traceless tensors. It follows that the cost of using exact multipole to multipole translations is higher. But in our experience, we have found that we need a smaller number of multipoles for the same precision, and this can significantly affect the total cost, especially for large data sets [13]. Abandoning the use of traceless operators has three salient benefits; (i) the algorithms can be used for any potential function whose Taylor's series converges rapidly, (ii) it does not depend on special functions and (iii) only the translation operator depends on the potential function which implies that multiple potentials may be easily combined [67].

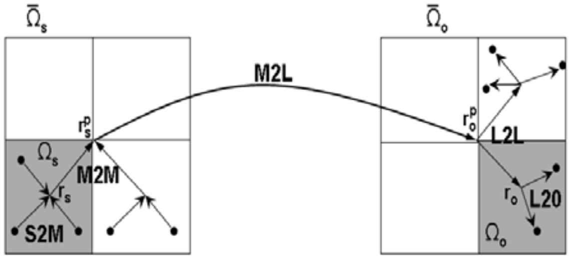

Fig. 5. Various operators involved in a multilevel FMM.

In all the above expressions, it was assumed that the number of multipoles used was infinite. The analytical estimates regarding truncation of this sum for both the spherical and Cartesian form can be found in [8, 13]. The cost analysis for multilevel approach is as follows: the total number of boxes in the tree is $O(N/s)$ and the cost for S2M and L2O operations remains the same; the cost of applying M2L translation operation across levels scales as $O(P^4N/s)$. In addition the cost of applying M2M and L2L operations for all boxes scales as $O(N/sP^4)$. Thus, the overall computational cost associated with both schemes scales as $O(P^4N)$. This cost is largely dominated by the time for multipole to local translation (M2L) and considerable research effort has been expended on reducing this cost. A closer examination of the M2L operation reveals that (i) the number of translations per box is 189 and (ii) the cost per translation scales as $O(P^4)$. The latter is due to the fact that this operation is not diagonal. Greengard et. al. [9] remedied this deficiency by introducing a novel algorithm that diagonalizes the translation operator. Additional modifications to the overall algorithm introduced there [42, 68] further reduces the number of translations, making the “revamped” FMM extremely efficient. Ideas behind this diagonalization can be exploited by either both varieties of FMM; spherical and Cartesian. It also plays a key role in FMMs for lowfrequency, and consequently, will be presented in some detail next. An FFT based implementation of above un-diagonalized form results in a overall cost that scale as $O(NP^2 \log P)$ [66], but will not be dwelt here.

C. Diagonalized Translation Operators

A diagonal translation operator may be derived using a spectral representation of the Green’s function [9], viz.,

$$\frac{1}{R} = \frac{1}{2\pi}\int_0^\infty d\lambda\, e^{-\lambda z}\int_0^{2\pi} d\alpha\, e^{-j\lambda\left(x\cos\alpha + y\sin\alpha\right)} \tag{19}$$

for $z > 0$. It is apparent that the inner integral is in fact a zeroth order Bessel function. The computation of potentials using the above expressions hinge on the existence of an integration rule that is efficient to a given precision and scale invariant if this formula is to be used at different levels in the FMM tree. Given the existence of such a rule [69], the potential at any point can be written as [9]

$$\begin{aligned}\phi\left(r\right) = &\sum_{k=1}^{s(\varepsilon)}\sum_{i=1}^{M(k)} W\left(k,i\right) e^{-\lambda_k z - j\lambda_k\left(x\cos\alpha_i + y\sin\alpha_i\right)} \\ &+ O\left(\varepsilon\right)\end{aligned}, \tag{20}$$

where the coefficients $W(k, i)$ are a combination of the charges q_i and integration weights ω_k, $s(\varepsilon)$ and $M(k)$ denotes the number of integration points for ε accuracy. Evidently, in above discrete representation, the number of integration points $M(k)$ for evaluating α integral depends on k to account for the varying bandwidth, λ_k, of its integrand. The advantages of above scheme are immediately apparent in that it readily permits translation of the origin; translation of the origin is quite simply a shift in the exponentials. The similarity between (20) and those in Theorems (3.1), and (3.4) are readily apparent. The mapping from spherical harmonic multipole coefficients M_n^m onto exponential expansions $W(k, j)$ is given as [9],

$$\begin{aligned}W\left(k,i\right) = \frac{\omega_k}{M\left(k\right)} &\sum_{m=-\infty}^{\infty}\sum_{n=|m|}^{\infty} \left(j\right)^{|m|} e^{-jm\alpha_i} \\ &\times \frac{M_n^m \lambda_k^n}{\sqrt{\left(n-m\right)!\left(n+m\right)!}}\end{aligned}, \tag{21}$$

and given $W(k, i)$ coefficients the spherical harmonic local expansion L_n^m can be computed with,

$$\begin{aligned}L_n^m = &\frac{\left(j\right)^{|m|}}{\sqrt{\left(n-m\right)!\left(n+m\right)!}} \\ &\sum_{k=1}^{s(\varepsilon)}\left(-\lambda_k\right)^n \sum_{i=1}^{M(k)} W\left(k,i\right) e^{-jm\alpha_i}\end{aligned}. \tag{22}$$

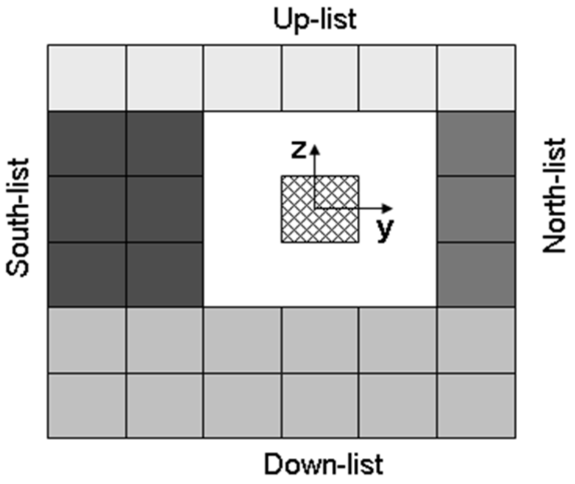

Fig. 6. Re-grouped boxes in original interaction list, in figure 3, for application of diagonal translation operator (20).

The multipole to local translation operation, with diagonalized translation forms, can be computed as a three stage process: multipole coefficients are mapped to $W(k, i)$, translate $W(k, i)$, and then map the translated coefficients back to local expansions, and then proceed as usual. It is evident that cost of all operators involving exponential expansions scale as $O(P^2)$. Various symmetry considerations in implementation reduces the number of total translation count from 189 to 40. Additionally, one can exploit symmetry in the expressions involved to further reduce the overall cost, if not the asymptotic complexity [56]. Thus, properly modifying and augmenting either spherical or Cartesian multipole based algorithms with plane wave translation operators can considerably ameliorate the cost. However, a couple of issues must be noted; (i) the plane wave expression is valid for $z > 0$, this implies that the interaction list must be modified [9]; (ii) additional operators must be introduced to rotate the multipole operators along the required axis; (iii) the operator developed should be scale invariant for the scheme to be efficient. In implementation the spherical harmonic multipole coefficient is converted into six plane wave expansions corresponding to each face of the cube and the interaction list definition is changed accordingly. For example, exponential expansions corresponding to $+z$ cube face is valid only for boxes present above x-y plane, as illustrated in Fig. 6. Boxes in original interaction list are divided into six new sets termed as up-list, down-list, north-list, south-list, east-list and west-list corresponding to $+z$, $-z$, $+y$, $-y$, $+x$ and $-x$ cube faces respectively [9]. Overall, the diagonalized version of the translation operator reduces both the total number of translation operation and per translation cost leading to a much faster algorithm. This approach is very similar to spectral approaches developed for alternative derivation of Helmholtz FMM [42, 70] and is the crux of many methods developed for wideband FMM.

IV. FMM FOR HELMHOLTZ EQUATIONS

Thus far, we have seen that cascaded Taylor expansions can be used to develop static FMM. While these ideas are readily extended to the solution of parabolic equations as well [24], they are not readily extendable to Helmholtz equation kernels, especially at high frequencies. Furthermore, as was evident from last section, the scheme developed should be diagonal. Consider a problem setting that is identical to what was described in Section II. We shall seek development of methods to accelerate the evaluation of the potential integral in (1) with $g\left(|r|\right) = \exp\left[-j\kappa|r|\right]/|r|$. One expression that readily suggests itself is the Gegenbauer addition theorem [31, 59, 71],

$$\frac{e^{-j\kappa|X+d|}}{|X+d|} = -j\kappa\sum_{l=0}^{\infty}\left(-1\right)^{l}\left(2l+1\right)jl\left(\kappa d\right)h_{l}^{(2)}\left(\kappa X\right)P_{l}\left(\hat{d}\cdot\hat{X}\right), \tag{23}$$

where X and d are position vectors such that $r = X+d$ and $|X| = |d|$, j_l and $h_l^{(2)}$ are l^{th} order spherical Bessel and Hankel function of second kind, $X = |\mathrm{X}|$ and $d = |\mathrm{d}|$. Augmenting this theorem with another addition theorem for Legendre polynomials in (4) completes the separation between the source and observer coordinates.

$$\begin{aligned}\frac{e^{-j\kappa|X+d|}}{|X+d|} &= -j\kappa\sum_{l=0}^{L}(-1)^l(2l+1)jl(\kappa d)h_l^{(2)}(\kappa X), \\ &\times\sum_{m=-l}^{l}Y_{lm}(\theta_X,\phi_X)Y^*_{lm}(\theta_d,\phi_d)\end{aligned} \tag{24}$$

where L is the number of terms used in the summation, $\{\theta_X, \phi_X\}$ and $\{\theta_d, \phi_d\}$ are the polar coordinates of $\hat{X}$ and $\hat{d}$ respectively. It is evident that one may use a sequence of addition theorems to create hierarchical computational methodology. However, the principal bottleneck to such a scheme is the fact that the operators involved are not diagonal. However, diagonal operators are easily developed by recognizing that

$$4\pi(-j)^l\, jl(\kappa d)P_l(\hat{d}\cdot\hat{X}) = \int d^2\hat{\kappa}e^{-j\kappa.d}P_l(\hat{\kappa}\cdot\hat{X}), \tag{25}$$

where $d^2\hat{\kappa} = \sin\theta d\theta d\phi$ and $\kappa = \kappa\hat{\kappa}$.. The relation (25) can be derived from well known orthogonality relation among spherical harmonics and expansion for plane waves given as.

$$\int d^2\hat{\kappa}Y_{lm}(\hat{\kappa})Y^*_{l'm'}(\hat{\kappa}) = \frac{4\pi}{2l+1}\delta_{mm'}\delta_{ll'}, \tag{26}$$

$$e^{-jz\cos\gamma} = \sum_{l=0}^{\infty}jl(z)P_l(\cos\gamma). \tag{27}$$

Substituting (25) in (23), interchanging the summation and the integral, and truncating the summation over l yields the final diagonalized form,

$$\begin{aligned}\frac{e^{-j\kappa|X+d|}}{|X+d|} &= \frac{-j\kappa}{4\pi}\int d^2\hat{\kappa}e^{-j\kappa.d} \\ &\times\sum_{l=0}^{L}(-1)^l(2l+1)h_l^{(2)}(\kappa X)P_l(\hat{\kappa}\cdot\hat{X}).\end{aligned} \tag{28}$$

Several derivation that result in above diagonalized form exist and are based on different set of starting formulas [30–32, 72, 73]. First scheme for diagonalizing (23) was presented in [30] with the use of forward and inverse far field transform defined as,

$$\tilde{f}(\theta,\phi) = \sum_{l=0}^{\infty}\sum_{m=-l}^{l}(-j)^l\, Y_{\mathrm{l}m}(\theta,\phi)\, f_{lm}, \tag{29}$$

$$f_{lm} = \int d^2\hat{\kappa}(-j)Y_{lm}(\hat{\kappa})\,\tilde{f}(\theta,\phi). \tag{30}$$

Above definition is a simple spherical harmonic transform from $\hat{\kappa}$ to $\{l, m\}$ basis with direct analogy to Fourier transform. A simpler version of derivation in [30] is presented in [35, 73]. In [31], the expansion in (23) is represented as matrix vector multiplication which reveals a convolution relation in indices $\{l, m\}$. Such convolutions in $\{l, m\}$ can be computed as one-to-one multiplication in $\hat{\kappa}$ domain using the far field transform [31]. A detailed discussion on deriving the above diagonalized forms from the convolution representation of original multipole expansion for both Laplace and Helmholtz equation is presented in [31]. An alternate derivation based on similarity transform and their relation to group theory is presented in [32] to yield the same expansion in (28).

1) Single Level FMM: As before, assume that Ω_s and Ω_o denote the source and observation domain, and it is necessary to find the fields $\forall r\in\Omega_o$. It is further assumed that the domains are cubes, in keeping with the data structure of oct-tree and that each domain can be embedded in a sphere of radius a. Furthermore, the clusters are assumed to be well separated. The separation distance is closely related to error bounds [30, 71], and will be dealt with in later part of the paper. Given these conditions, traversal up and down the tree is effected using the following set of theorems:

Theorem 4.1: *Farfield signature*: The far field signature due a set of source q_i for i = 1, … , k located at $r_i\in\Omega_s$ is given by

$$\begin{aligned}M(r_s,\kappa) &= \sum_{i=1}^{k}M(q_i,\kappa,r_s-r_i) \\ &= \sum_{i=1}^{k}q_i\exp\left[-j\kappa.(r_s-r_i)\right]\end{aligned} \tag{31}$$

Theorem 4.2: *Translation operator*: If a farfield signature exists at a point r_s such that it is valid for all points outside the domain Ω_s, then the translation operator that maps this farfield to the local expansion that is centered around r_o and valid in the domain Ω_o is given by

$$T\left(\kappa, r_{os}\right) = \sum_{l=0}^{\infty} \left(-1\right)^l \left(2l+1\right) h_l^{(2)}\left(\kappa\left|r_{os}\right|\right) P_l\left(\hat{\kappa}.\hat{r}_{os}\right), \tag{32}$$

where $r_{os} = r_o - r_s$. Finally, the potential at any point $r \in \Omega_o$ can be constructed using

$$\phi\left(r\right) = \frac{-jk}{4\pi} \int d^2\hat{\kappa} M\left(1, -\kappa, r_o - r\right) \times T\left(\kappa, r_{os}\right) M\left(r_s, \kappa\right), \tag{33}$$

While these equations are readily derived from (28). More insight into the derivation of these equations can be obtained by realizing that the farfield (and local expansions) can be represented in terms of spherical harmonics. In turn, this interpretation leads to expressions that reveal convergence rates of these and error bounds as a function radius a and the separation distance. More importantly, this insight leads to the type of quadrature rules that must be used to implement these schemes numerically. In other words, the continuous integral is evaluated using

$$\phi\left(r\right) = \frac{-jk}{4\pi} \sum_{p=1}^{L} \sum_{q=-p}^{p} \omega_{pq} M\left(1, -\kappa, r_o - r\right) \times T\left(\kappa_{pq}, r_{os}\right) M\left(r_s, \kappa_{pq}\right), \tag{34}$$

where L is the order of the Gauss Legendre rule, ω_{pq} are the integration weights, p and q are the integration points in θ and ϕ axis,

$$\phi_q = \frac{2\pi q}{2L+1}$$

θ_p is the $\left(p+1\right)^{th}$ zero of $P_{L+1}\left(\cos\theta\right)$

$$\omega_{pq} = \frac{4\pi\left(1-\cos^2\theta_p\right)}{\left(2L+1\right)\left[\left(L+1\right)P_L\left(\cos\theta_p\right)\right]^2}$$

$$\hat{\kappa}_{pq} = \hat{x}\sin\theta_p\cos\phi_q + \hat{y}\sin\theta_p\sin\phi_q + \hat{z}\cos\theta_p . \tag{35}$$

As is apparent form the above equations, uniform sampling is used to evaluate the integral along ϕ. Other applicable rules may be found in [74]. We have yet to elaborate the underlying factors that decide the order of Gauss-Legendre rule that is used along θ. A number of formulae exist for choosing the number of Gauss-Legendre quadrature point [30, 71, 75]. However, examination of (28) yields interesting insight. If only the exponential terms are considered in this integral, it is apparent that these expressions can be represented using L = $O(\kappa d)$ = $O(2\kappa a)$ harmonics. This, in turn, implies that the summation is also truncated using L terms. Though the reasoning here is based on economical means to discretize the integral a deeper reason, arriving at same conclusion, exists for choice of L based on original multipole expansion [71]. Choice of L should be large enough for the series (24) to converge, but not too large to cause numerical instability due to the asymptotic behavior of spherical Bessel and Hankel functions. Given that only a finite number of terms are being used, one can explicitly derive error bounds that, in turn, depend on the translation distance also [30]. Deriving rigorous error bounds has been a focus of considerable work [43, 75–78], and the behavior of error is well understood [79, 80] as are the means to overcome these. A simple choice for truncation limit L applicable to most practical problems is,

$$L = \kappa d + C\log\left(\kappa d + \pi\right), \tag{36}$$

where C is a number that depends on the desired accuracy ε; typically for $\varepsilon = \{10^{-3}, 10^{-6}, 10^{-14}\}$ the choice for $C = \{3, 5, 10\}$, respectively [71, 81]. This estimate is semi-empirical and assumes that the two boxes are well separated if they are one box apart. Other estimates [75, 79, 82] based on approximation of Bessel and Hankel function exists both in two- and three-dimensions and can account for multiple box separation between interacting boxes [78, 80]. Cost of this scheme can be computed in the same manner as in the static with $P = L$ and the diagonalized form of translation operator implies $O(P^2)$ cost per operation. However choice of L depends on size of box kd, which in turn dictates the number of unknowns per box s (assuming uniform discretization). It can be show that the optimal cost of the above scheme scales as $O(N^{3/2})$ for surface problems.

2) Multilevel FMM: While the above exposition details the necessary mathematics for implementing a single level scheme, nesting these in a hierarchical setting is the next logical extension. The first robust attempts to do so are [83–85]. Extension to multilevel is different from that encountered for the Laplace FMM; there, the number of multipoles at all level of the tree was constant. But as is evident from (36) and (34) as the size of the source/receiver boxes increases, the bandwidth increase increases by a factor of two, which implies that the number of directions increase by a factor of four. This then creates a need for developing robust methods for going up and down the tree for the stages of aggregation and disaggregation. These operators can be thought of as filters. But before we proceed into intricate details of the methods to implement these, the theorems that help achieve these are as follows:

Theorem 4.3: *Translation of farfield signatures*: If the farfield signature $M(r_s,\ \kappa)$ around the point $r_s \in \Omega_s$ is known, then the farfield signature $M\left(r_s^p,\kappa\right)$ around the point $r_s^p \in \Omega_s^p$ is given by

$$M\left(r_s^p,\kappa\right) = M\left(r_s,\kappa\right)e^{-j\kappa\cdot\left(r_s^p - r_s\right)}. \tag{37}$$

An identical theorem for can be derived for translating local expansion at the parent level to that of its child. Numerical implementation of these theorems is not as simple as it seems. To maintain uniform accuracy across levels, employing (36), the L for parent is approximately twice that of its child. This implies that the number of direction for parent box is approximately four times that of its child; thus the multipole expansions for the child and parent box are defined on different grids. This process of computing a higher bandwidth representation from lower bandwidth farfield signature is referred to as interpolation and anterpolation is its inverse analogue applied during downward tree traversal. Implementing the above theorems calls for efficient methods to interpolate (or anterpolate). Several methods that exist have been elaborated upon in [33] and summarized as well in [75]. An efficient and exact algorithm can be devised using the forward and inverse farfield transform for both interpolation and anterpolation [23, 35, 85, 86]. This algorithm relies on the fact that at any level the farfield signature can be represented in terms of spherical harmonics., viz.

$$M\left(.,\kappa\right) = \sum_{n=0}^{\infty}\sum_{m=-n}^{n} a_{nm}Y_{nm}\left(\theta,\phi\right). \tag{38}$$

As is well known, the farfield signature of a source constellation is bandlimited to $O(\kappa a)$ harmonics. This implies that the above expression can be truncated. Furthermore, since an Lth order rule is chosen to evaluate the spectral integral in (28), it follows that the upper limit in the summation over n can be chosen to be L. This said, direct computation of a_{nm} is expensive. Alternate methods both exact and approximate have been discussed in [23, 87]. Consider the computation of a_{nm} from child farfield signature $M(r_s,\ \kappa_{kp})$ represented using $(2L^2 + 1)$ coefficients, i.e. $p = 1, \ldots, L$ and $q = 1, \ldots, (2L + 1)$,

$$\begin{aligned} a_{nm} &= \int d^2\hat{\kappa}M\left(r_s,\kappa\right)Y_{nm}^*\left(\theta,\phi\right) \\ &= \sum_{p=1}^{L}\omega_p P_{nm}\left(\cos\theta_p\right)\left(\sum_{q=1}^{(2L+1)} M\left(r_s,\kappa_{pq}\right)e^{jn\phi_q}\right) \\ &= \sum_{p=1}^{L}\omega_p P_{nm}\left(\cos\theta_p\right)\alpha_m\left(\theta_p\right) \end{aligned} \tag{39}$$

where ω_p are numerical quadrature weights. Since, the integration along ϕ is performed using uniform sampling, fast Fourier transform (FFT) can be used for summation inside the brackets. These coefficients are then used to compute samples along new polar coordinates $\left(\tilde{\theta}_p,\tilde{\phi}_q\right)$ with $p = 1,\ldots,\tilde{L}$ and $q = 1,\ldots,\left(2\tilde{L}+1\right)$ as,

$$M\left(r_s,\tilde{\kappa}_{pq}\right) = \sum_{m=-\tilde{L}}^{\tilde{L}} e^{-jm\tilde{\phi}_q}\sum_{n=1}^{\tilde{L}} a_{nm}P_{nm}\left(\cos\tilde{\theta}_p\right). \tag{40}$$

Again, FFT can be used to evaluate the outer summation. In interpolation, $\tilde{L} > L$ to accommodate for the increase in bandwidth and $\tilde{\kappa}_{pq}$ represents the discrete directions of the farfield signature corresponding to the parent. The required multipole coefficients about parent origin r_s^p can be obtained using a simple shifting operation,

$$M\left(r_s^p,\tilde{\kappa}_{pq}\right) = M\left(r_s,\tilde{\kappa}_{pq}\right)e^{-j\tilde{\kappa}_{pq}\cdot\left(r_s^p - r_s\right)}. \tag{41}$$

An inverse procedure is performed when translating local expansions from parent to child where anterpolation is used in place of interpolation. First, the parent local expansion about r_o^p is shifted about child origin r_o; then in anterpolation, the forward and inverse farfield transform are performed to reduce the bandwidth in an exact manner as described above but with $\tilde{L} < L$, where L represents the number of harmonics in parent domain. Above procedure for interpolation/anterpolation can be further accelerated with the use of fast Legendre transform [23] where the coefficients a_{nm} are not computed explicitly. Though this approach scales favorably the break-even point is large and not suitable for most practical applications [35]. This can be overcome to some extent using the 1D FMM for fast Legendre transforms [87]. Cost of Interpolation/anterpolation using this approach scales as $O(Q\log Q)$, where Q denotes the number of directions in farfield signature. This said it can be shown that overall cost of the multilevel algorithm scales as $O(N \log^2 N)$ [35]. Other methods used for interpolation and anterpolation have been presented in detail in [33, 75, 84]. These include the use of polynomials and approximate prolate spheroidal wave functions. The singular advantage of these methods is their cost scales linearly with the number of samples, thus the overall cost scales as $O(N \log N)$. However, while interpolation is sufficiently accurate, one has to be more careful when anterpolating functions as it is necessary to remove higher order harmonics. While we have not digressed into implementation of these schemes for vector electromagnetic problems, we must caution that it is not a trivial extension. It is important to realize that the farfield component represented in terms of polar components in not bandlimited [88], whereas they are bandlimited when represented in terms of Cartesian components. This means that one either uses a fast scheme based on vector spherical harmonics [88] or converts these to Cartesian before interpolation/anterpolation. Another intriguing method for interpolation and anterpolation was introduced by Sarvas [48], wherein he introduced modifications that enabled the use of FFTs. In other words, bandlimited farfield signatures can be represented in terms of Fourier basis as

$$M(\kappa) \approx \sum_{p=-P}^{P} \sum_{q=-Q}^{Q-1} a(p,q) e^{i(p\theta+q\phi)} , \qquad (42)$$

where,

$$\begin{aligned} a(p,q) &= DFT\left\{M(\kappa)\right\} \\ &= \sum_{p=-P}^{P} \sum_{q=-Q}^{Q-1} e^{-j(m\theta+n\phi)} M(\kappa_{pq}) \\ \theta &= \frac{p2\pi}{2P+1}, \\ \phi &= \frac{\pi q}{Q}, \end{aligned} \qquad (43)$$

where DFT(.) represents forward discrete Fourier transform, $2M$ and $2N$ are number of samples or basis function in θ and ϕ axis respectively. Then the integral over the surface of sphere can be written as,

$$\begin{aligned} &\int_{-\pi}^{\pi} d\phi \int_{0}^{\pi} d\theta \sin\theta U(\theta,\phi) \\ &= \int_{-\pi}^{\pi} d\phi \int_{-\pi}^{\pi} d\theta \left|\sin\theta\right| U(\theta,\phi) \end{aligned} . \qquad (44)$$

Note that the above modification changes the limit on θ integral to [-π, π], thus it can also be evaluated in fast manner using FFT. In single level implementation, the integrand in (24) are first represented in terms of Fourier basis using (42) and then (44) is used for fast evaluation of integrals. In multilevel implementation the interpolation and anterpolation, for varying bandwidth of multipole and local expansion, can be achieved by zero padding and truncating the Fourier coefficients respectively. In anterpolation the Fourier coefficients of parent local expansions are symmetrically truncated before inverse Fourier transform, to obtain the local expansion about child domain with the desired bandwidth. Thus all operations, including the evaluation of integral, can be evaluated using FFT. Reader is referred to [48] for related theorems, proofs and numerical results. Finally, the numerical implementation of multilevel FMM has been scrutinized in terms of different errors and to ensure stability. This includes discussion on the relation between truncation and integration error in (34) [77], and interpolation/anterpolation error using Lagrange interpolation [79] and spherical transform [75]. In addition, errors due to round off and evaluation of special-function have been considered along with stability criterion [80]. Numerical experiments show that truncation error in (34) is lower bounded [43, 79]; thus for applications that routinely demand very high accuracies it is preferable to increase the distance between wellseparated boxes. Evidently this amounts to an increase in number of boxes in near-field interaction.

A. Other FMMs

The above exposition presented FMMs that are apt for analyzing very general problems. However, for certain problems it is possible to develop FMM schemes that take advantage of topological features of scatterer to reduce the asymptotic complexity. The first of such algorithm was the fast steepest descent path algorithm [89] that exploited spectral representation of the Green's function. The next incarnation of this was the steepest descent FMM. It was developed following realization that when analyzing scattering from objects whose height is considerably lesser that its lateral dimension, it is not particularly useful to expand the fields using the complete spectrum. In other words, SDFMM can be interpreted to be a windowed FMM, and results in a method whose complexity scales as *O*(*N*). In SDFMM, it is achieved naturally using the Sommerfeld integral representation of the Green's function and evaluating this integral using a combination of two-dimension FMM and steepest descent. More specifically,

$$\begin{aligned}\frac{e^{-jkR}}{R} &= \frac{-j}{2}\int_{-\infty}^{\infty} dk_z e^{-jk_z(z-z')} H_0^{(2)}\left(\kappa_\rho\left|\rho-\rho'\right|\right) \quad , \qquad (45)\\ &= \frac{-j}{2}\sum_{n=1}^{N_{sd}} \omega_n \kappa_\rho^{(n)} H_0^{(2)}\left(\kappa_\rho\left|\rho-\rho'\right|\right) e^{-jk_z(z-z')}\end{aligned}$$

where N_{sd} is quadrature rule along the integration path, ω_n is the integration weight, $\kappa_\rho^{(n)} = \kappa \sin\alpha_n$ and $k_z = \kappa\cos\alpha_n$, and α is defined along steepest descent path. It is immediately apparent that the summation over Hankel functions can be accelerated using a generalization of the two-dimensional FMM, and as before, this algorithm can be cast within a multilevel framework. Another algorithm along these lines was the fast inhomogeneous plane wave algorithm (FIPWA) [47, 68]. This algorithm follows directly from Weyl's identity

$$\frac{e^{-j\kappa R}}{R} = \frac{-j}{2}\int_0^{2\pi} d\phi \int_{SIP} d\theta \sin\theta e^{-j\kappa . R} . \qquad (46)$$

The path of integration yields contributions from both homogeneous and inhomogeneous plane waves. As written, the above integral is slowly converging, but the contour can be deformed along the steepest descent path. This integral is evaluated numerically. However, values of the radiation pattern for complex θ is obtained using interpolation/ extrapolation. Manipulation of the requisite equations results in a diagonal translation operator. This method has been extended for analysis of scattering from objects above a layered medium [45, 47]. Additionally, they have been modified for developing stable algorithms for broadband applications [90]. However, we shall describe these algorithms and others [42] for rapidly computing potentials for wideband applications in the next section.

Finally, other variants of FMM exist that exploit the fact that between well separated boxes, one may construct windowed translation operators to lower the cost. One such method is the ray propagation FMM (RPFMM) [72, 91]. Other windowed translation operators have been used in two-dimensions for the analysis of scattering from bianisotropic objects [92]. However, it follows from complexity analysis that these methods will be fruitful only when the objects are sufficiently far away from each other. This implies that the algorithm is most useful when used in a one-level setting and may not be effective with a multilevel implementation.

B. Wideband FMM

In above discussion, a significant highlight is the restrictive choice of L used to truncate the expansions. This choice, based on the asymptotic behavior of Bessel and Hankel function, reveals the behavior of above expansions when applied to low frequency problems where κ is very small. It is well known that Hankel function is singular at origin and as $\kappa \to 0$ the expansion in (28), though valid, becomes numerically unstable. This breakdown is referred to as low-frequency breakdown [42, 43]. Consequently for fixed κ the size of source domain, which also defines the translation distance, cannot be made arbitrarily small. This issue becomes significant when the geometry is densely discretized, much more than the conventional $\lambda/10$ criterion, mostly to represent intricate structural details.

1) Scaled expansions: At low frequencies the numerical instability can be averted by using a normalized form of the original expansion (28)

[44, 46]. This approach is motivated by the asymptotic behavior of spherical Bessel and Hankel function for small argument. Let t be a normalization constant such that $t = O(kd)$ then the multipole expansions in (24) can be written as,

$$
\begin{aligned}
&t h_0^{(2)}\left(-j\kappa\left|X+d\right|\right) \\
&= -j\kappa \sum_{l=0}^{L} \sum_{m=-l}^{l} (-1)^l (2l+1) \times \\
&\left[\frac{1}{t^l} jl(\kappa d) Y_{lm}^*(\theta_d, \phi_d)\right] t^{l+1} h_l^{(2)}(\kappa X) Y_{lm}(\theta_X, \phi_X)
\end{aligned} \tag{47}
$$

In above expression, terms inside the square brackets are the new normalized multipole coefficients. As $\kappa \to 0$, using small argument approximation for spherical functions and with $t = \kappa$, it is a straightforward exercise to show that the normalized expansions reduces to the expansions (2) used in static case. While the normalized form ensures numerical stability, the low-frequency nature of the problem implies that one can choose the number of multipoles to be same at every level. This in turn implies that the multilevel version of this approach scales as $O(N)$ [46]. A constant normalization factor is sufficient when the geometry is uniformly discretized. However to accommodate wide variation in domain sizes and maintain the stability of expansion different normalization factor should be chosen in different parts [33]. This approach has been successfully used in integral equation solution for scattering from sub-wavelength structures [46, 93].

2) Spectral representation based plane wave expansions: An alternate approach, inspired by the diagonalized form for static FMM, was introduced in [42] and later implemented in [49, 50, 90]. It is based on the following well-known spectral representation of solution to Helmholtz equation [94],

$$
\begin{aligned}
\frac{e^{-j\kappa R}}{R} &= \frac{1}{2\pi}\int_0^\infty d\lambda e^{-\sqrt{\lambda^2-\kappa^2}\,z} \frac{\lambda}{\sqrt{\lambda^2-\kappa^2}} \\
&\times \int_0^{2\pi} d\alpha\, e^{-j\lambda(x\cos\alpha + y\sin\alpha)}
\end{aligned}, \tag{48}
$$

this relation is valid for $z > 0$. Further it is straightforward to identify the purely propagating part of spectrum as $0 \le \lambda \le \kappa$ and the evanescent part as $\kappa \le \lambda \le \infty$; with simple change of variables, above expression can be written as [42],

$$
\frac{e^{-j\kappa R}}{R} = \left(\frac{e^{-j\kappa R}}{R}\right)_{evan.} + \left(\frac{e^{-j\kappa R}}{R}\right)_{prop.}, \tag{49}
$$

where,

$$
\begin{aligned}
\left(\frac{e^{-j\kappa R}}{R}\right)_{evan.} &= \frac{1}{2\pi}\int_0^\infty d\sigma\, e^{-\sigma z} \times \\
&\int_0^{2\pi} d\alpha\, e^{-j\sqrt{\sigma^2+\kappa^2}(x\cos\alpha + y\sin\alpha)}, \\
\left(\frac{e^{-j\kappa R}}{R}\right)_{prop.} &= \frac{j\kappa}{2\pi}\int_0^{\pi/2} d\alpha\, e^{-j\kappa\cos\theta} \times \\
&\int_0^{2\pi} d\theta\, e^{-j\kappa\sin\theta(x\cos\alpha + y\sin\alpha)}.
\end{aligned} \tag{50}
$$

Notice that with $\kappa \to 0$ the propagating part vanishes and the evanescent part reduces to the diagnolized form (19) used in static FMM. Now it remains to discretize the above integrals for numerical evaluation and generalized Gaussian quadratures can be employed for this. However, unlike in static case, the integrand cannot be rendered scale independent and this means quadrature points and weights should be pre-computed for all possible translation distances at all levels. It is worthwhile to recount that the multipole and local expansions are computed and stored as they appear in original spherical harmonics expansion (28); they are converted to exponential expansions back and forth during multipole to local translation only and these relations can be found in [50]. This approach avoids the floating point overflow as all the computed quantities and operations are regular and numerically stable. Other approaches based on above spectral representation have been presented [49, 90, 95, 96] and they differ significantly in their numerical implementation and structure. In all these methods the multipole and local expansion are represented directly in terms of exponential expansion coefficients; hence they require new interpolation/anterpolation operators for multilevel implementation. In [90], an extension of FIPWA as introduced for multi-layered structures, the integrand is sampled along the steepest descent path (SDP) and extrapolation techniques to estimate the evanescent portion of the spectrum from samples of the propagating portion. However, one has to treat “shallow” evanescent waves differently from “deep” evanescent waves. In [49], the evanescent integrand is sampled along the traditional Sommerfeld integral path (SIP) and singular value decomposition (SVD) of the integrand is used to obtain expressions for multipole coefficient and multilevel translation operators. An interpolation matrix approach is presented in [96] to relate exponential expansions at different levels. Using sample points in child and parent domain an overdetermined system of equation is formed and solved for the interpolation matrix entries in a least square sense. The advantage of latter approaches is that they avoid the spherical harmonic to exponential expansion and reverse mapping operations.

3) Cartesian harmonics: At sufficiently low frequencies Cartesian harmonics provides the following convergent series expansions,

$$\frac{e^{-j\kappa|r-r_s|}}{|r-r_s|}=\sum_{p=0}^{\infty}\left(r_s\right)^{(p)}\bullet p\bullet\nabla^{p}\frac{e^{-j\kappa|r|}}{|r|},\qquad(51)$$

where,

$$\nabla^{n}\frac{e^{-jkR}}{R}\left(n_1,n_2,n_3\right)=$$

$$\sum_{m_1=0}^{\left\lfloor\frac{n_1}{2}\right\rfloor}\sum_{m_2=0}^{\left\lfloor\frac{n_2}{2}\right\rfloor}\sum_{m_3=0}^{\left\lfloor\frac{n_3}{2}\right\rfloor}\left(-1\right)^{n+m}R^{2m-2n-1}g\left(n-m,R\right)\times\qquad(52)$$

$$\begin{bmatrix}n_1\\m_1\end{bmatrix}\begin{bmatrix}n_2\\m_2\end{bmatrix}\begin{bmatrix}n_3\\m_3\end{bmatrix}x^{n_1-2m_1}x^{n_1-2m_2}x^{n_3-2m3}$$

and

$$g\left(n,R\right)=\sqrt{2/\pi}\left(j\kappa r\right)^{(n+0.5)}K_{n+0.5}(jkR)$$

$$\begin{bmatrix}n\\m\end{bmatrix}=\frac{n!}{2^{m}m!(n-2m)!}\qquad(53)$$

In above expressions $K_n(.)$ represents the modified Hankel function of order n, $r=x\hat{x}+y\hat{y}+z\hat{z}$, $R=|r|$ and $\lfloor.\rfloor$ is the floor operation. Interestingly, it can be shown that above expansions reduces to the spherical harmonic expansions in (28) with low argument approximation for spherical Bessel and Hankel functions [97, 98]. This assures the accuracy and stability of above expansions for low frequency problems. Again the number of harmonics can remain constant for all levels and this results in an $O(N)$ algorithm. As mentioned earlier the multipole and local expansions are independent of the form of potential; thus definitions of all operators, except M2L, remains same as that for static.

4) Hybrid methods: In multiscale geometries the low-frequency breakdown occurs only in parts when the domain size is much smaller than the incident wavelength. This implies that both low and high-frequency FMM should be used simultaneously. Henceforth, the different versions of FMM are referred to as LF-FMM and HF-FMM. When using different forms of expansions a switchover between LF-FMM and HF-FMM quantities is necessary to handle both large and small domain sizes simultaneously. Such hybrid methods have been developed by combining HF-FMM with plane wave expansions [50] and with Cartesian harmonics [99]. A smooth transition between the two versions of FMM is a key necessity of these hybrid methods and operators are prescribed to map quantities from LF-FMM onto HF-FMM and vice versa. In plane wave based LF-FMM, the multipole and local coefficients are represented in terms of the original expansion; thus the conversion to farfield signature required in HF-FMM and the reverse mapping operation can be simply performed using the forward and inverse farfield transform using (30). Mapping the Cartesian harmonics, represented by tensors, onto farfield signatures is slightly involved. It follows from the observation that farfield signatures are essentially plane waves in different directions and following Taylor’s series expansion is possible,

$$\begin{aligned}e^{-i\kappa.\left(r_s^{p}-r_s\right)}&=\sum_{p=0}^{\infty}r_s^{(p)}\bullet p\bullet\nabla^{(p)}e^{-i\kappa.r_s^{p}}\\&=\sum_{p=0}^{\infty}r_s^{(p)}\bullet p\bullet T^{(p)}\left(\kappa,r\right)\end{aligned}\qquad(54)$$

where,

$$\begin{aligned}T^{(p)}\left(\kappa,r\right)\left(p_1,p_2,p_3\right)&=\partial_{p_1}\partial_{p_2}\partial_{p_3}e^{-i\kappa.r_s^{p}}\\&=\left(-j\right)^{p}\kappa_x^{p_1}\kappa_y^{p_2}\kappa_z^{p_3}e^{-i\kappa.r}\end{aligned}\qquad(55)$$

In above expressions $p = p_1 + p_2 + p_3$, $\kappa=\kappa_x\hat{x}+\kappa_y\hat{y}+\kappa_z\hat{z}$, r_s and r_s^{p} represents the center of child and parent domain respectively. Here $T^{(p)}$ is the mapping operator relating the Cartesian multipole coefficient about child box, r_s^p, to the farfield signature about parent box. Since the local expansions take the same form as multipole expansions in both Cartesian and spherical forms, the reverse mapping is same as $T^{(p)}$ and in addition should evaluate the spherical integral $\int d^2\kappa$. In implementation the infinite sum in (54) is truncated and it is fairly straight-forward to show that error due to this decreases rapidly as the translation distance ($\left|r_s^p - r_s\right|$) decreases or as the number of harmonics increases. This is shown numerically in Table 1, where the L2 norm error between multipole coefficients evaluated using farfield transform and by mapping from Cartesian multipoles are shown for different orders of Cartesian harmonics (P) and translation distance $a = \left|r_s^p - r_s\right| / \lambda$. As expected the error uniformly reduces to machine precision with increasing *P* and *a*.

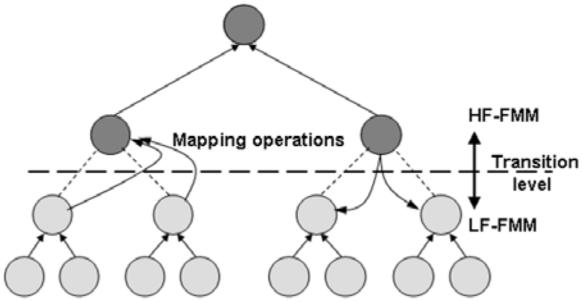

Fig. 7. Tree representation for hybrid methods.

Table 1: Error convergence of Cartesian to spherical harmonics mapping operator (55).

a	P=3	P=6	P=9	P=12
0.5	2.13	5.58E-3	9.62E-6	5.90E-9
0.25	2.58E-2	8.04E-6	1.51E-9	1.27E-13
0.125	3.49E-4	1.30E-8	1.55E-13	2.24E-15
0.0625	1.04E-5	5.34E-11	1.41E-15	1.41E-15

The overall execution of hybrid algorithm, in both cases, proceeds as follows: an adaptive (compressed) oct-tree is constructed to represent the geometry and a transition level is chosen such that LF-FMM and HF-FMM are stable for all boxes below and above this level respectively. Further, for simplicity, it is assumed that all leaf boxes are below this transition level, see Fig. 7 for an illustration. First the LF-FMM multipole coefficients are computed at all leaf boxes and upward tree traversal is executed until the transition level. At this point, for Cartesian harmonics based LF-FMM, the farfield signature of parent box above the transition level are computed from the Cartesian expansions in child boxes at the transition level using mapping operators (54); in plane wave based LF-FMM the farfield signature of box at the transition level is computed from the plane wave expansion coefficients of the same box. With this the upward tree traversal is performed for all boxes above the transition level. Next, the multipole coefficients in each box are translated into local coefficients of boxes in its interaction list which, by definition, are at the same level. In downward tree traversal, the local expansion coefficients of all boxes in HF-FMM region are updated with that of their parents. At transition level, for Cartesian harmonics based LF-FMM the child box Cartesian local expansions are computed by mapping the farfield signature about the parent box; for plane wave based LF-FMM the child box farfield signature is first computed and then converted as spherical harmonic local expansion using inverse farfield transform. Then the downward tree traversal continues for all boxes below the transition level. Finally the local expansion coefficients at leafless boxes are used to compute the farfield potential at their respective observation points. As in all algorithms the complete potential is computed by accounting for the near-field contribution by direct evaluation. The choice of transition level is influenced by different constraints in both the methods and in general it is determined through numerical experiments. In Cartesian-spherical harmonics hybrid method, the O(N) scaling of Cartesian expansion algorithm may favor a higher transition level, however, this implies more number of Cartesian harmonics to maintain the accuracy of both LF-FMM and the mapping operations. Similar considerations for plane wave expansion based LFFMM and HF-FMM hybrid algorithm are detailed in [50] along with numerical experiments. Tables 2 and 3 shows the convergence and efficiency of the hybrid method obtained by combining the Cartesian and spherical harmonics. Table 2 presents the error in potential evaluation for different orders of Cartesian and spherical harmonics. Here χ_{sph} is the oversampling factor in spherical harmonics FMM i.e. the truncation L = χ_{sph} κd and P_{Cart} denotes the maximum order of Cartesian harmonics used. All errors reported here are the L2 norm error in farfield values computed using hybrid algorithm and direct evaluation; also, in the numerical experiments reported here, 16,000 source and observer points were randomly distributed following a uniform distribution within a domain of size $4\times 2\times 2\lambda$. The separation between interacting boxes was kept as three boxes to ensure uniform error convergence till machine precision (10^{-12}) in both LF- and HF-FMM. Note that this is the worst case error as including the near-field contribution will only decrease the error further. Table 3 shows the time taken by the hybrid algorithm for evaluation of farfield potentials as the total number of unknowns is varied. N source/observer points were randomly distributed, following a uniform distribution, within a domain size $4\times 2\times 2\lambda$ and the boxes were subdivided hierarchically until the number of unknowns per box was 64 on average. The orders of expansion in Cartesian and spherical harmonics were chosen so as to obtain an accuracy of $O(10^{-4})$. For this accuracy the distance between interacting boxes is reduced to one box separation. The time scaling (complexity) of this hybrid algorithm depends on the number of levels in LF- and HF-FMM i.e. the complexity would scales as $O(N)$ if the number of LF-FMM levels are much more than that in HF-FMM part. In essence the complexity of this algorithm has an $O(N \log N)$ upper-bound.

Table 2: Error convergence of Cartesian-spherical harmonics hybrid algorithm for 16,000 random points in $4\times 2\times 2\lambda$ domain.

χ_{sph}	P_{Cart}	ε
1.5	3	2.14E-2
1.7	4	3.91E-3
2.0	6	3.91E-4
2.2	8	6.74E-6
2.5	12	4.84E-9
3.2	16	6.08E-12

Table 3: Time vs. N corresponding to an error of $O(1.0\mathrm{E}^{-4})$ in Cartesian-spherical harmonics hybrid algorithm

N	T_{fast}	T_{direct}
64000	9.38	468.81
128000	16.25	-
256000	34.40	-
512000	65.15	-
1024000	133.25	-
2000000	268.98	-

V. APPLICATIONS

This section provides an overview on applications of above discussed algorithms in different contexts. As mentioned in introduction, FMM and other fast methods, e.g. FFT and tree code based, were developed primarily to accelerate the evaluation of potential or field in N body problems. Integral equation solution, a common choice in simulation of many electromagnetic applications, sought through iterative solvers requires repeated evaluation of potential or field at source points itself. Thus fast algorithms play a significant role in solving real world problems within realistic time duration. The literature referenced here is only selective and not exhaustive as the use of these algorithms has become more common during recent years. Also, only topics related to electromagnetics are listed here; for applications in other research field refer to introduction.

First, electromagnetic application of static or Laplace FMM was evaluation of electrostatic potential in 2D [6, 100]. The extension to 3D has seen lot of applications, particularly, in plasma dynamics [8, 101]. FMM based FastCap and FastHenry are widely popular tools for extraction of equivalent capacitance and impedance among multiconnects in micro-electronic components [19, 20]. Static FMM is also used in integral equation solution of magnetostatic problems predominantly for analysis and design of electric machines [102].
Simulations with non-linear materials have benefited much as they demand multiple solution before attaining stability [56, 103, 104]. It has also been applied to quasi-static case especially in simulation of eddy-current phenomena [105, 106] and micromagnetics is another area of practical interest [107, 108].

The recently published book on fast methods in electromagnetics is a virtual treasure house of FMM methods and their applications to various problems in high frequency electromagnetics [33]. As is to be expected, Helmholtz FMM has been applied to accelerate iterative solution of surface and volume integral equations. The means to modify Helmholtz equation such that they are applicable to vector electromagnetics problems was first presented in [84]. More detailed description can be found [33, 81, 109]. Since their introduction, they have been applied extensively to scattering and radiation problems of different flavors; for instance, scattering from perfect electrically conducting surfaces [28, 71, 75, 84, 109–114], scattering from dielectric/ composite bodies [115–120], volume integral equations [76, 121–123], anisotropic objects [124, 125], scattering from rough surfaces [126–128], application to microstrips [129], EMC/EMI analysis [130–132], antennas [133–135]. Efficient implementation of FMM in solvers with higher order geometry and basis function representations have led to the development of fast and accurate solvers [116, 136, 137]. [138, 139].

Multipole accelerated algorithms have also been employed in various hybrid methods where solution is obtained with use of moment method combined with one or more of following techniques: to impose global radiation boundary conditions in finite element solvers [140–142], ray tracing and diffraction methods [143], multi-grid methods [144] and physical optics [145, 146]. These techniques are primarily used in applications with multi-scale scatterers like antenna interactions [147] and field predications for urban mobile communications [148]. Implementation of FMM was also modified to accommodate perfectly matched layer (PML) assisted integral equation methods used in simulation of monolithic microwave integrated circuit (MMIC) and photonic crystals [149–151]. Fast inhomogeneous plane wave (FIPWA) method and other forms of FMM have been used to accelerate solution of scattering simulations involving layered media structures with applications in design of microstrip antennas [138, 139, 152–157] and geophysical investigations for sub-surface scatterers [70, 158–166]. A combined FMM-FFT algorithm [167, 168] and SDFMM have been used in electromagnetic analysis of general quasi-planar structures with applications to rough surface scattering, grating structure design in quantum devices and radiation from microstrip patch antenna [127, 169–171]. Parallel versions of FMM [36, 38, 41, 54, 81, 172–176], especially on cluster computers with distributed memory, have been employed to solve problems with few millions of unknowns [37, 40], aided with developments in different preconditioning techniques [177–181]. Finally, we note that while FMMs reviewed here primarily accelerate the solution off frequency domain integral equations, equivalent models have been developed for time domain integral equations also [88, 182, 183].

VI. SUMMARY

Introduction of FMM changed the landscape of numerical simulation in many fields and the developments in past two decades have made it an ubiquitous tool for fullwave analysis. This paper reviews different FMMs and their applications to problems in electromagnetics. The development of FMM is traced from static to dynamic, and covers various methodologies that form the current state of art FMM. These include the spectral representation to obtain diagonalized operators in both static and dynamic FMM, farfield signatures for diagonalized forms in dynamic, Cartesian harmonics based expansions for static and low-frequency dynamic case and other application specific techniques to improve both accuracy and efficiency. This review also includes an overview of recent developments in combining different FMMs to obtain hybrid algorithms that are applicable to wideband analysis. But, all said and done, while we have tried to be as comprehensive as possible in this review, the papers cited herein provide only snapshot of the papers that exploit FMM for accelerating integral equation solvers.

ACKNOWLEDGEMENTS

We are grateful to NSF for support under CCF-0729157, DMS-0811197 and NIH under R21 CA121235.

REFERENCES

[1] M. N. O. Sadiku, *Numerical Techniques in Electromagnetics*. CRC press, 2000.

[2] J. Jin, *The Finite Element Method in Electromagnetics*. John wiley and sons, 2002.

[3] J. H. Richmond, "Digital computer solutions of the rigorous equations for scattering problems," *Proceeding of the IEEE*, vol. 53, pp. 796–804,1965.

[4] A. Appel, "An efficient program for many body simulations," *SIAM J. Sci. Comput*., vol. 6, pp. 85–103, 1985.

[5] J. Barnes and P. Hut, "A hierarchical O(n log n) force calculation algorithm," *Nature*, vol. 324, pp. 446–449, 1986.

[6] V. Rokhlin, "Rapid solution of the integral equations of classical potential theory," *J. of Comp. Phy.*, vol. 60, pp. 187– 207, 1985.

[7] L. Greengard and V. Rokhlin, "A fast algorithm for particle simulations," *J. of Comp. Phy.*, vol. 20, pp. 63–71, 1987.

[8] L. Greengard, *The Rapid Evaluation of Potential Fields in Particle Systems*. Cambridge, MA: MIT Press, 1988.

[9] L. Greengard and V. Rokhlin, "A new version of the fast multipole method for the Laplace equation in three dimensions," *Acta Numerica*, vol. 6, pp. 229–269, 1997.

[10] F. Zhao, "An O(n) algorithm for three dimensional n-body simulation," *Master's thesis*, Massachusetts Institute of Technology, 1987.

[11] E. J. Weniger, "Addition theorems as threedimensional Taylor expansions," *International J. of Quantum Chemistry*, vol. 76, pp. 280–295, 2000.

[12] P. B. Visscher and D. M. Apalkov, "Charge based recursive fast multipole micromagnetics," *Physica B: Physics of Condensed Matter*, vol. 343, pp. 184–188, 2004.

[13] B. Shanker and H. Huang, "Accelerated Cartesian expansions - a fast method for computing of potentials of the form $R^{-\nu}$ for all real ν," *J. of Comp. Phy.*, vol. 226, pp. 732–753, 2007.

[14] W. D. Elliott and J. A. Board, "Multipole algorithms for molecular dynamics simulation on high performance computers," Tech. Rep. TR95-003.html, Duke University, 1995.

[15] Y. Fu, K. J. Klimkowski, G. J. Rodin, E. Berger, J. C. Browne, J. K. Singer, R. A. van de Geijin, and K. S. Vemaganti, "A fast solution method for three-dimensional manyparticle problems of linear elastosticity," *J. Numer. Methods Eng.*, vol. 42, pp. 1215–1229, 1998.

[16] K. Yoshida, N. Nishimura, and S. Kobayashi, "Application of fast multipole Galerkin boundary integral equationmethod to elastostatic crack problems in 3D," *Int. J. Numer. Methods Eng.*, vol. 50, pp. 525–527, 2001.

[17] Y. H. Chen, W. C. Chew, and S. Zeroug, "Fast multipole method as an efficient solver for 2D elastic wavesurface integral equations," *Computational mechanics*, vol. 20, pp. 495– 506, 1997.

[18] Y. Fu and G. J. Rodin, "Fast solution method for three-dimensional Stokesian manyparticle problems," *Commun. Numer. Meth. Eng.*, vol. 16, pp. 145–149, 2000.

[19] K. Nabors and J. White, "Fastcap: A multipole accelerated 2-D capacitance extraction program," *IEEE Trans. Computer Aided Design*, vol. 10, pp. 1447–1459, 1991.

[20] M. Kamon, M. J. Tsuk, and J. K. White, "FASTHENRY: A multipole accelerated 3-D inductance extraction program," *IEEE Trans. Microwave Theory Tech.*, vol. 42, pp. 1750–1758, 1994.

[21] F. Chen and D. Suter, "Using a fast multipole method to accelerate spline evaluations," *IEEE Computational Science and Engineering*, vol. 5, pp. 24–31, 1998.

[22] J. R. Driscoll and J. D. M. Healy, "Asymptotically fast algorithms for spherical and related transforms," *in 30th annual symposium on foundations of computer science*, (Research Triangle Park, NC), pp. 344–349, IEEE Computer Society Press, 1989.

[23] R. J. Chien and B. K. Alpert, "A fast spherical filter with uniform resolution," *J. of Comp. Phy.*, vol. 136, pp. 580–584, 1997.

[24] L. Greengard and J. Strain, "A fast algorithm for the evaluation of heat potentials," *Comm. Pure Appl. Math.*, vol. 43, pp. 949–963, 1990.

[25] J. Tausch, "A fast method for solving the heat equation by layer potentials," *J. of Comp. Phy.*, vol. 224, no. 2, pp. 956–969, 2007.

[26] J. R. Li and L. Greengard, "On the numerical solution of the heat equation I: fast solvers infree space," *J. of Comp. Phy.*, vol. 226, pp. 1891–1901, 2007.

[27] V. Rokhlin, "Rapid solutions of integral equations of scattering theory in two dimensions," *J. of Comp. Phy.*, vol. 86, pp. 414–439, 1990.

[28] C. C. Lu and W. C. Chew, "Fast algorithm for solving hybrid integral equations," IEE *Proceedings H: Microwaves and Antennas*, vol. 140, pp. 455–460, 1992.

[29] N. Engheta, W. D. Murphy, V. Rokhlin, and M. S. Vassiliou, "The fast multipole method (FMM) for electromagnetic scattering problems," *IEEE Trans. Antennas Propagat.*, vol. 40, pp. 634–641, 1992.

[30] V. Rokhlin, "Diagonal forms of translation operators for the Helmholtz equation in three dimensions," *Applied and Computational Harmonic Analysis*, vol. 1, pp. 82–93, 1993.

[31] M. A. Epton and B. Dembart, "Multipole translation theory for three dimensional Laplace and Helmholtz equations," *SIAM J. Sci. Compt.*, vol. 16, pp. 865–897, 1995.

[32] W. C. Chew, S. Koc, J. M. Song, C. C. Lu, and E. Michielssen, "A succint way to diagonalized the translation matrix in three dimensions," *IEEE AP-S Int. Symp.*, pp. 2072–2075, 1997.

[33] W. C. Chew, J. M. Jin, E. Michielssen, and J. Song, eds., *Fast and Efficient Algorithms in Computational Electromagnetics*. Artech House Publishers, 2001.

[34] N. Nishimura, "Fast multipole accelerated boundary integral equation methods," *Appl. Mech. Rev.*, vol. 55, pp. 299–324, 2002.

[35] M. F. Gyure and M. A. Stalzer, "A prescription for the multilevel Helmhotz FMM," *IEEE Computational Science and Engineering*, vol. 5, no. 3, pp. 39–47, 1998.

[36] S. Velamparambil, J. M. Song, W. C. Chew, and G. K., "ScaleME: A portable scalable multipole engine for electromagnetic and acoustic integral equation solvers," *IEEE AP-S Int. Symp.*, vol. 3, pp. 1774–1777, 1998.

[37] S. Velamparambil, W. C. Chew, and J. Song, "10 million unknowns: is it that big*?,*" *IEEE Trans. Antennas and Propagat.*, vol. 45, pp. 43–58, 2003.

[38] B. Hariharan, S. Aluru, and B. Shanker, "A scalable parallel fast multipole method for analysis of scattering from perfect electrically conducting surfaces," in *Supercomputing, ACM/IEEE 2002 Conference*, pp. 42–42, 16-22 Nov. 2002.

[39] B. Hariharan and S. Aluru, "Efficient parallel algorithms and software for compressed octrees with applications to hierarchical methods," *Parallel Computing*, vol. 31, pp. 311– 331, 2005.

[40] L. Gurel and O. Ergul, "Fast and accurate solutions of extremely large integral-equation problems discretised with tens of millions of unknowns," *Electronics Lett.*, vol. 43, no. 9, pp. 499–500, April 26 2007.

[41] O. Ergul and L. Gurel, "Hierarchical parallelization strategy for multilevel fast multipole algorithm in computational electromagnetics," *Electronics Lett.*, vol. 44, no. 1, pp. 3–5, January 3 2008.

[42] L. Greengard, J. Huang, V. Rokhlin, and S. Wandzura, "Accelerating fast multipole methods for the Helmholtz equation at low frequencies," *IEEE Computational Science and Engineering*, vol. 5, pp. 32–38, 1998.

[43] B. Dembart and E. Yip, "The accuracy of fast multipole methods for Maxwell's equations," *IEEE Computational Science and Engineering*, vol. 5, pp. 48–56, 1998.

[44] J. S. Zhao and W. C. Chew, "MLFMA for solving boundary equations of 2D electromagnetic scattering from static to electrodynamic," *Microw. and Opt. Tech. Lett.*, vol. 20, pp. 306–311, 1999.

[45] T. J. Cui and W. C. Chew, "Fast algorithm for electromagnetic scattering by buried conducting plates of large size," *IEEE Trans. Antennas Propagat.*, vol. 47, no. 6, pp. 1116–1118, 1999.

[46] J. S. Zhao and W. C. Chew, "Threedimensional multilevel fast multipole algorithm from static to electrodynamic," *Microw. and Opt. Tech. Lett.*, vol. 26, pp. 43–48, 2000.

[47] B. Hu and W. C. Chew, "Fast inhomogenous plane wave algorithm for scattering from objects above the multilayered medium," *IEEE Trans. Geoscience and Remote Sensing*, vol. 39, pp. 1028–1038, 2001.

[48] J. Sarvas, “Performing interpolation and anterpolation entirely by fast Fourier transform in the 3-D multilevel fast multipole algorithm,” *SIAM Journal on Numerical Analysis*, vol. 41, pp. 2180–2196, 2003.

[49] E. Darve and P. Have, “Efficient fast multipole method for low-frequency scattering,” *J. of Comp. Phy.*, vol. 197, pp. 341– 363, January 2004.

[50] H. Cheng, W. Y. Crutchfield, Z. Gimbutas, L. F. Greengard, J. F. Ethridge, J. Huang, V. Rokhlin, and N. Y. andJ. Zhao, “A wideband fast multipole method for the Helmholtz equation in three dimensions,” *J. of Comp. Phy*, vol. 216, pp. 300–325, 2006.

[51] H. Cheng, L. Greengard, and V. Rokhlin, “A fast adaptive multipole algorithm in three dimensions,” *J. of Comp. Phy*, vol. 155, pp. 468–498, 1999.

[52] S. Aluru, “Greengard’s N-body algorithm is not order N,” *SIAM J. Sci. Comput.*, vol. 17, pp. 773–776, 1996.

[53] M. S. Warren and J. K. Salmon, “A parallel hashed oct-tree N-body algorithm,” in Supercomputing ’93: Proceedings of the 1993 *ACM/IEEE conference on Supercomputing*, (New York, NY, USA), pp. 12–21, ACM, 1993.

[54] F. Sevilgen, S. Aluru, and N. Futamura, “Parallel algorithms for tree accumulations,” *Journal of Parallel and Distributed Computing*, vol. 65, pp. 85–93, 2005.

[55] J. T. J. White, “A multiscale method for fast capacitance extraction,” in Proceedings of the *IEEE/ACM DAC*, 1998.

[56] S. Balasubramanian, L. N. Subramaniam, and B. Shanker, “Fast integral equation based analysis of magneto-static fields in bulk nonlinear media,” *IEEE Trans. Magnetics*, vol. 35, pp. 100–107, 2002.

[57] V. Rokhlin and S. M. Wandzura, “The fast multipole method for periodic structure,” in *IEEE AP-S Int. Symp.*, pp. 424–427, 1994.

[58] J. A. Stratton, *Electromagnetic theory*. McGraw-Hill, 1941.

[59] M. Abramowitz and I. A. Stegun, *Handbook of Mathematical Functions with Formulas, Graphs, and Mathematical Tables*. New York, NY: Dover Publications, Inc., 1972.

[60] Z. Duan and R. Krasny, “An adaptive treecode for computing nonbonded potential energy in classical molecular systems,” *J. Comp. Chem.*, vol. 22, pp. 184–195, 2001.

[61] I. Chowdhury and V. Jandhyala, “Single level multipole expansions and operators for potentials of the form $r^{-\nu}$,” *SIAM J. Sci. Comput.*, vol. 26, pp. 930–943, 2005.

[62] I. Chowdhury and V. Jandhyala, “Multilevel multipole and local operators for potentials of the form $r^{-\nu}$,” *Appl. Math. Lett.*, vol. 18, pp. 1184–1189, 2005.

[63] E. W. Hobson, *The Theory of Spherical and Ellipsoidal Harmonics.* Cambridge University Press, 1931.

[64] T. M. MacRobert, *Spherical Harmonics*. Dover, 1947.

[65] J. Applequist, “Traceless cartesian tensor forms for spherical harmonic functions: new theorems and applications to electrostatics of dielectric media,” *J. Phys. A: Math. Gen.*, vol. 22, pp. 4303–4330, 1989.

[66] W. D. Elliott and J. A. Board, “Fast Fourier transform accelerated fast multipole algorithm,” *SIAM J. Sci. Comput.*, vol. 17, pp. 398– 415, 1996.

[67] M. Vikram and B. Shanker, “Fast evaluation of time domain fields in sub-wavelength source/observer distributions using accelerated Cartesian expansions (ace),” *J. of Comp. Phy*, vol. 227, pp. 1007–1023, 2007.

[68] B. Hu, W. C. Chew, E. Michielssen, and J. Zhao, “An improved fast steepest descent algorithm for the fast analysis of twodimensional scattering problems,” *Radio Sci.*, vol. 34, pp. 759–772, 1999.

[69] N. Yarvin and V. Rokhlin, “Generalized Gaussian quadratures and singular value decompositions of integral operators,” *tech. rep.*, *Department of Computer Science*, Yale University 1996.

[70] B. Hu, W. C. Chew, E. Michielssen, and J. Zhano, “Fast inhomogeneous plane wave algorithm for fast analysis of two-dimensional scattering problems,” *Radio Sci.*, vol. 34, pp. 759–772, 1999.

[71] R. Coifman, V. Rokhlin, and S. Wandzura, “The fast multipole method for the wave equation: A pedestrian prescription,” *IEEE Antennas Propagat. Mag.*, vol. 35, pp. 7–12, June 1993.

[72] V. Rokhlin, “Sparse diagonal forms for translation operators for the Helmholtz equation in two dimensions,” *Tech. Rep. YALEU/DCS/RR-1095,* Yale University, 1995.

[73] J. Rahola, “Diagonal forms of the translation operators in the fast multipole algorithm for scattering problems,” *BIT Numerical Mathematics*, vol. 36, pp. 333–358, 1996.

[74] A. D. McLaren, “Optimal numerical integration on a sphere,” *Mathematics of Computation*, vol. 17, pp. 361–383, 1963.

[75] E. Darve, “The fast multipole method: Numerical implementation,” *J. of Comp. Phy* vol. 160, pp. 195–240, 2000.

[76] J. Song and W. C. Chew, “Error analysis for the truncation of multipole expansion of vector Green’s functions,” *IEEE Microwave and Wireless Components lett.*, vol. 11, pp. 311–313, 2001.

[77] J. Y. Li, L. W. Li, B. L. Ooi, P. S. Kooi, and M. S. Leong, “On the accuracy of the addition theorem for a scalar green’s function used in the FMM,” *Micro. Opt. Techn. Lett.*, vol. 31, pp. 439–442, 2001.

[78] M. L. Hastriter, S. Ohnuki, and W. C. Chew, “Error control of the translation operator in 3D MLFMA,” *Micro. Opt. Techn. Lett.*, vol. 37, pp. 184–188, 2003.

[79] S. Koc, J. Song, and W. C. Chew, “Error analysis for the numerical evaluation of the diagonal forms of the scalar spherical addition theorem,” *SIAM J. Numer. Anal.*, vol. 36, no. 3, pp. 906–921, 1999.

[80] M. Nilsson, “Stability of the high frequency fast multipole method for helmholtz equation in three dimensions,” *BIT Numerical Mathematics*, vol. 44, pp. 773–791, 2004.

[81] J. M. Song, C. C. Lu, W. C. Chew, and S. W. Lee, “Fast illinois solver code (FISC),” *IEEE Antennas Propagat. Mag.*, vol. 40, pp. 27–34, 1998.

[82] E. Darve, “The fast multipole method i: Error analysis and asymptotic complexity,” *SIAM J. Numer. Anal.*, vol. 38, pp. 98–128, 2000.

[83] C. C. Lu and W. C. Chew, “A multilevel algorithm for solving boundary integral wave scattering,” *Micro. Opt. Techn. Lett.*, vol. 7, pp. 466–470, 1994.

[84] J. M. Song and W. C. Chew, “Multilevel fastmultipole algorithm for solving combined field integral equations of electromagnetic scattering,” *Micro. Opt. Techn. Lett.*, vol. 10, no. 1, pp. 14–19, 1995.

[85] B. Dembart and E. Yip, “A 3D fast multipole method for electromagnetics with multiple levels,” in Proceedings of the 11th Annual Conference on *Applied Computational Electromagnetics*, vol. 1, (Monterey, CA), pp. 621– 628, 1995.

[86] T. Hrycak and V. Rokhlin, “An improved fast multipole algorithm for potential fields,” *SIAM Journal on Scientific Computing*, vol. 19, pp. 1804–1826, 1998.

[87] N. Yarvin and V. Rokhlin, “A generalized 1D fast-multipole method, with applications to filtering of spherical harmonics,” *tech. rep., Yale University*, 1998.

[88] B. Shanker, A. Ergin, M. Lu, and E. Michielssen, “Fast analysis of transient electromagnetic scattering phenomena using the multilevel plane wave time domain algorithm,” *IEEE Trans. Antennas Propagat.*, vol. 51, no. 3, pp. 628–641, March 2003.

[89] E. Michielssen and W. C. Chew, “Fast steepest descent path algorithm for analyzing scattering from two-dimensional objects,” *Radio Sci.*, vol. 31, pp. 1215–1224, 1996.

[90] L. J. Jiang and W. C. Chew, “Low-frequency fast inhomogeneous plane-wave algorithm (LFFIPWA),” *Micro. Opt. Techn. Lett.*, vol. 20, pp. 117–122, 2004.

[91] R. L. Wagner and W. C. Chew, “A raypropagation fast multipole algorithm,” *Micro. Opt. Techn. Lett.*, vol. 7, pp. 435–438, 1994.

[92] B. Shanker, S.-K. Han, and E. Michielssen, “A fast multipole approach to computing scattering from an inhomogeneous bianisotropic cylindrical object using Beltrami fields,” *Radio Sci.*, vol. 33, pp. 17–31, 1998.

[93] T. J. Cui and W. C. Chew, “Accurate analysis of wire structures from very-low frequency to microwave frequency,” *IEEE Trans. Antennas Propagat.*, vol. 50, pp. 301–307, 2002.

[94] W. C. Chew, *Waves and Fields in Inhomogeneous Media*. IEEE Press New York, 1995.

[95] L. Xuan, A. Zhu, A. R. J., and S. D. Gedney, "A broadband multilevel fast multipole algorithm," *IEEE AP-S Int. Symp. And USNC/URSI National Radio Science Meeting*, vol. 2, pp. 1195–1198, 2004.

[96] H. Wallen and J. Sarvas, "Translation procedures for broadband MLFMA," *Progress in Electromagnetics Research*, vol. 55, pp. 47–78 2005.

[97] H. Huang and B. Shanker, "A o(n) procedure for evaluating the Yukawa potential and the Ewald summation for peroidic systems," Submited to *Journal of Computational Physics* (Tech. Report Available at https://www.egr.msu.edu/ece/Technicalpapers/), 2007.

[98] H. Huang and B. Shanker, "Accelerated Cartesian expansion based method for rapidly computing the shielded Coulomb potential," in *URSI Int. Symp*., 2007.

[99] M. Vikram, H. Huang, and B. Shanker, "Fast evaluation of fields from sub-wavelength structures in frequencydomain," in *URSI Int. Symp*., 2007.

[100] J. Carrier, L. Greengard, and V. Rokhlin, "A fast adaptive multipole algorithm for particle simulations," *SIAM J. Sci. Stat. Comput*., vol. 9, pp. 669–686, 1988.

[101] K. Nabors and J. White "Multipoleaccelerated capacitance extraction for 3-D structures with multilayer dielectrics," *IEEE Tran. Circ. Syst*., vol. 39, pp. 946–954, 1992.

[102] A. Adedoyin and P. Andrei, "3-D magnetostatic using the fast multiple method," *IEEE Trans. Magnetics*, vol. 43, no. 6, pp. 2914–2916, June 2007.

[103] I. Mayergoyz, P. Andrei, and M. Dimian, "Nonlinear magnetostatic calculations based on fast multipole method," *IEEE Trans. Magnetics*, vol. 39, no. 3, pp. 1103–1106, May 2003.

[104] W. Hafla, A. Buchau, F. Groh, and W. Rucker, "Efficient integral equation method for the solution of 3-D magnetostatic problems," *IEEE Trans. Magnetics*, vol. 41, no. 5, pp. 1408– 1411, May 2005.

[105] Y. Takahashi, Y. Fujishima, and S. Wakao, "Large-scale analysis of surface charge in eddy-current problems by the fast multipole method," *IEEE Trans. Magnetics*, vol. 41, no. 5, pp. 1700–1703, May 2005.

[106] G. Rubinacci, A. Tamburrino, S. Ventre, and F. Villone, "A fast 3-D multipole method for eddy-current computation," *IEEE Trans. Magnetics*, vol. 40, no. 2, pp. 1290–1293, March 2004.

[107] C. Seberino and H. Bertram, "Concise, efficient three-dimensional fast multipole method for micromagnetics," *IEEE Trans. Magnetics*, vol. 37, no. 3, pp. 1078–1086, May 2001.

[108] D. Apalkov and P. Visscher, "Fast multipole method for micromagnetic simulation of periodic systems," *IEEE Trans. Magnetics*, vol. 39, no. 6, pp. 3478–3480, Nov. 2003.

[109] J. M. Song, C. C. Lu, and W. C. Chew, "MLFMA for electromagnetic scattering by large complex objects," *IEEE Trans. Antennas Propagat*, vol. 45, pp. 1488–1493, 1997.

[110] T. Eibert, "Some scattering results computed by surface-integral-equation and by the multilevel fast multipole method," *IEEE Antennas Propagat. Mag.*, vol. 49, no. 2, pp. 61–69, April 2007.

[111] L. Hamilton, P. Macdonald, M. Stalzer, R. Turley, J. Visher, and S. Wandzura, "3D method of moments scattering computations using the fast multipole method," *Antennas and Propagation Society International Symposium*, 1994. AP-S. Digest, vol. 1, pp. 435–438, 20-24 Jun 1994.

[112] T. J. Cui, W. C. Chew, G. Chen, and J. Song, "Efficient MLFMA, RPFMA, and FAFFA algorithms for EM scattering by very large structures," *IEEE Trans. Antennas Propagat*., vol. 52, no. 3, pp. 759–770, March 2004.

[113] K. Sertel and J. L. Volakis, "Effects of the fast multipole method (FMM) parameters on radar cross section computations," *IEEE AP-S Int. Symp.*, pp. 624–627, 1999.

[114] Z. Q. Zhang, Q. H. Liu, and X. M. Xu, "RCS computation of large inhomogeneous objects using fast integral equation solver," *IEEE Trans. Antennas Propagat.*, vol. 51, pp. 613 618, March 2003.

[115] J. M. Song and W. C. Chew, "Fast multipole method solution using parametric geometry,"

Micro. Opt. Tech. Lett., vol. 7, pp. 760–795, 1994.

[116] K. Donepudi, J. M. Jin, and W. C. Chew, "A higher order multilevel fast multipole algorithm for scattering from mixed conducting/dielectric bodies," *IEEE Trans. Antennas Propagat.*, vol. 51, pp. 2814–2821, 2003.

[117] K. Donepudi, J. Song, J. M. Jin, G. Kang, and W. Chew, "A novel implementation of multilevel fast multipole algorithm for higher order Galerkin's method," *IEEE Trans. Antennas Propagat.*, vol. 48, no. 8, pp. 1192–1197, Aug 2000.

[118] J. Liu and J. M. Jin, "A novel hybridization of higher order finite element and boundary integral methods for electromagnetic scattering and radiation problems," *IEEE Trans. Antennas Propogat.*, vol. 49, no. 12, pp. 1794–1806, Dec 2001.

[119] H. Wallen, S. Jarvenpaa, P. Yla-Oijala, and J. Sarvas, "Broadband Muller-MLFMA for electromagnetic scattering by dielectric objects," *IEEE Trans. Antennas Propagat.*, vol. 55, no. 5, pp. 1423–1430, May 2007.

[120] V. Jandhyala, B. Shanker, E. Michielssen, and W. Chew, "Fast algorithm for the analysis of scattering by dielectric rough surfaces," *J. of Opt. Society of America*, vol. 15, pp. 1877–1885, 1998.

[121] X. Q. Sheng, J. J. M., J. M. Song, C. W. C., and C. C. Lu, "Solution of combined-field integral equation using multilevel fast multipole algorithm for scattering from homogeneous bodies," *IEEE Antennas Propagat. Mag.*, vol. 46, pp. 1718–1726, 1998.

[122] C. C. Lu, "A fast algorithm based on volume integral equation for analysis of arbitrarily shaped dielectric radomes," *IEEE Trans. Antennas Propogat.*, vol. 51, no. 3, pp. 606–612, March 2003.

[123] J. Y. Li and L. W. Li, "Characterizing scattering by 3d arbitrarily shaped homogeneous dielectric objects using fast multipole method," *IEEE Antennas Wireless Propagati. Lett.*, vol. 3, pp. 1–4, 2004.

[124] G. Kobidze, K. Aygun, and B. Shanker, "Efficient integral equation based analysis of scattering from PEC-anisotropic bodies," in *Antennas and Propagation Society International Symposium*, 2004. IEEE, vol. 4, pp. 3887– 3890Vol.4, 20-25 June 2004.

[125] G. Kobidze and B. Shanker, "Integral equation based analysis of scattering from 3-d inhomogeneous anisotropic bodies," *IEEE Trans. Antennas Propagat.*, vol. 52, pp. 2650–2658, Oct. 2004.

[126] R. Wagner, J. Song, and W. Chew, "Monte carlo simulation of electromagnetic scattering from two-dimensional random rough surfaces," *IEEE Trans. Antennas Propagat.*, vol. 45, no. 2, pp. 235–245, 1997.

[127] M. El-Shenawee, C. Rappaport, E. Miller, and M. Silevitch, "Three-dimensional subsurface analysis of electromagnetic scattering from penetrable/PEC objects buried under rough surfaces: use of the steepest descent fast multipole method," *IEEE Trans. Geoscience and Remote Sensing*, vol. 39, no. 6, pp. 1174–1182, Jun 2001.

[128] V. Jandhyala, B. Shanker, E. Michielssen, and W. Chew, "A combined steepest descent-fast multipole algorithm for the analysis of threedimensional scattering by rough surfaces," in *Antennas and Propagation Society International Symposium*, 1997. IEEE., 1997 Digest, vol. 4, pp. 2308–2311vol.4, 13-18 July 1997.

[129] V. Jandhyala, E. Michielssen, B. Shanker, and W. Chew, "SDFMM-based fast analysis of radiation and scattering from finite microstrip structures," in *Antennas and Propagation Society International Symposium*, 1998. IEEE, vol. 3, pp. 1530–1533 vol.3, 21-26 June 1998.

[130] G. Hoyler and R. Unbehauen, "The fast multipole method for EMC problem," *Electrical Engineering*, vol. 80, pp. 403–411, 1997.

[131] H. Y. Chao, W. C. Chew, E. Michielssen, and J. M. Song, "The multilevel fast multipole algorithm for electromagnetic compatibility analysis," *IEEE-EMC Int. Symp.*, vol. 2, pp. 844– 847, 1999.

[132] T. J. Cui, W. C. Chew, J. S. Zhao, and H. Y. Chao, "Full-wave analysis of complicated transmission-line circuits using wire models," *IEEE Trans. Antennas Propagat.*, vol. 50, no. 10, pp. 1350–1360, 2002.

[133] Z. Z. Oo, L. Le-Wei, J. Y. Li, and E. P. Li, "Analysis and design of reflector and horn antennas using multilevel fast multipole algorithms (MLFMA)," *IEEE AP-S Int. Symp.*, vol. 2, pp. 758–761, 22-27 June 2003.

[134] J. Lord, S. Benham, and R. Mittra, "Multilevel fast multipole for antenna modelling," *Antennas and Propagation, 2003*. (ICAP 2003). Twelfth International Conference on (Conf. Publ. No. 491), vol. 1, pp. 308–311, 31 March- 3 April 2003.

[135] H. Y. Chao, J. S. Zhao, and W. C. Chew, "Application of curvilinear basis functions and MLFMA for radiation and scattering problems involving curved PEC structures," *IEEE Trans. Antennas Propagat.*, vol. 51, no. 2, pp. 331–336, Feb 2003.

[136] K. Donepudi, J. M. Jin, S. Velamparambil, J. M. Song, and W. C. Chew, "A higher-order parallelized fast multipole algorithm for 3D scattering," *IEEE Trans. Antennas Propagat.*, vol. 49, pp. 1069–1078, 2001.

[137] K. Donepudi, J. M. Song, J. M. Jin, G. Kang, and W. C. Chew, "Point-based MLFMA for Galerkin's method," *IEEE Trans. Antennas Propagat.*, vol. 48, pp. 1192–1197, 2000.

[138] L. Gurel and M. Aksun, "Fast multipole method in layered media: 2-D electromagnetic scattering problems," in *IEEE AP-S Int. Symp.*, pp. 1734–1737, 1996.

[139] L. Gurel and M. Aksun, "Electromagnetic scattering solution of conducting strips in layered media using the fast multipole method," *IEEE Microwave and Guided Wave Letters*, vol. 6, pp. 277, 1996.

[140] J. M. Jin, *The Finite Element Method in Electromagnetics*. New York: Wiley, 2002.

[141] S. Bindiganavale and J. Volakis, "A hybrid FEFMM technique for electromagnetic scattering," *IEEE Trans. Antennas Propagat.*, vol. 45, no. 1, pp. 180–181, Jan 1997.

[142] N. Lu and J.-M. Jin, "Application of fast multipole method to finite-element boundaryintegral solution of scattering problems," *IEEE Trans. Antennas Propogat.*, vol. 44, no. 6, pp. 781–786, Jun 1996.

[143] Z. Zhao, L. Li, J. Smith, and L. Carin, "Analysis of scattering from very large threedimensional rough surfaces using MLFMM and ray-based analyses," *IEEE Antennas Propagat. Mag.*, vol. 47, no. 3, pp. 20– 30, June 2005.

[144] P. L. Rui, R. S. Chen, D. X. Wang, and E. Kai-Ning Yung, "A spectral multigrid method combined with MLFMM for solving electromagnetic wave scattering problems," *IEEE Trans. Antennas Propagat*, vol. 55, no. 9, pp. 2571–2577, Sept. 2007.

[145] T. Eibert, "Modeling and design of offset parabolic reflector antennas using physical optics and multilevel fast multipole method accelerated method of moments," *Multitopic Conference, 2006*. INMIC '06. IEEE, pp. 377–382, 23-24 Dec. 2006.

[146] L. Gurel, A. Manyas, and O. Ergul, "POMLFMA hybrid technique for the solution of electromagnetic scattering problems involving complex targets," *Antennas and Propagation, EuCAP* 2007. The Second European Conference on, pp. 1–5, 11-16 Nov. 2007.

[147] A. Tzoulis and T. Eibert, "Antenna modeling with the hybrid finite element – boundary integral - multilevel fast multipole – uniform geometrical theory of diffraction method," *2nd International ITG Conference on Antennas, INICA '07*, pp. 91–95, 28-30 March 2007.

[148] X. Yin, X. Zai, W. Hong, and X. Zhu, "A fast algorithm based on MEI and FMM for field prediction in urban mobile communications," *IEEE AP-S Int. Symp.*, vol. 2, pp. 1384–1387, Aug 1999.

[149] D. Pissoort, E. Michielssen, D. Ginste, and F. Olyslager, "Fast-multipole analysis of electromagnetic scattering by photonic crystal slabs," *Journal of Lightwave Technology*, vol. 25, no. 9, pp. 2847–2863, Sept. 2007.

[150] D. Ginste, E. Michielssen, F. Olyslager, and D. De Zutter, "An efficient perfectly matched layer based multilevel fast multipole algorithm for large planar microwave structures," *IEEE Trans. Antennas Propagat.*, vol. 54, no. 5, pp. 1538–1548, May 2006.

[151] D. Pissoort, D. Ginste, and F. Olyslager, "Including PML-based absorbing boundary conditions in the MLFMA," *IEEE Antennas*

and Wireless Propagat. Lett., vol. 4, pp. 312–315, 2005.

[152] V. Jandhyala, E. Michielssen, and R. Mittra, “Multipole-accelerated capacitance computation for 3-d structures in a stratified dielectric medium using a closed form green’s function,” *Int. J. Microwave. Millimeter Wave Comput. Aided Eng.*, vol. 5, pp. 68–78, 1995.

[153] L. Gurel and M. I. Aksun, “Electromagnetic scttering solution of conducting strips in layered media using the fast multipole method,” *IEEE Microwave Guided Wave Letters*, vol. 6, pp. 277–279, 1996.

[154] P. A. MacDonald and T. Itoh, “Fast simulation of microstrip structures using the fast multipole method,” *Int. J. Numerical Modelling: Electron. Networks, Devices and Fields*, vol. 9, pp. 345–357, 1996.

[155] J. Zhao, W. C. Chew, C. C. Lu, E. Michielssen, and J. M. Song, “Thin-stratified medium fastmultipole algorithm for solving microstrip structures,” *IEEE Trans. Microwave Theory Tech.*, vol. 46, pp. 395–403, 1998.

[156] V. Jandhyala, E. Michielssen, B. Shanker, and W. C. Chew, “A fast algorithm for the analysis of radiation and scattering from arrays on finite substrates,” *Micro. Opt. Tech. Lett.*, vol. 23, pp. 306–310, 1999.

[157] F. Ling, J. M. Song, and J. M. Jin, “Multilevel fast multipole algorithm for analysis of large scale microstripstructures,” *IEEE Microwave and Guided Wave Letts.*, vol. 9, pp. 508–510, 1999.

[158] B. Hu and W. C. Chew, “Fast inhomogeneous plane wave algorithm for electromagnetic solutions in layered medium structures-2D case,” *Radio Sci.*, vol. 35, 2000.

[159] B. Hu and W. C. Chew, “Fast inhomogeneous plane wave algorithm for multilayered medium problems,” *IEEE Trans. Geoscience. Remote Sensing*, vol. 39, pp. 1028–1038, 2001.

[160] N. Geng, A. Sullivan, and L. Carin, “Multilevel fast-multipole algorithm for scattering from conducting targets above or embedded in a lossy half space,” *IEEE Trans. Geoscience Remote Sensing*, vol. 38, pp. 1567–1579, 2000.

[161] N. Geng, A. Sullivan, and L. Carin, “Fast multipole method analysis of scattering from a three-dimensional target in a half-space environment,” *IEEE Trans. Antennas Propagat.*, vol. 49, pp. 740–748, 2001.

[162] Z. Liu, J. He, Y. Xie, A. Sullivan, and C. L., “Multi-level fast multipole algorithm for general targets on a half-space interface,” *IEEE Trans. Antennas Propagat.*, vol. 50, pp. 1838–1849, 2002.

[163] Z. Liu, R. J. Adams, and C. L., “New MLFMA formulation for closed pec targets in the vicinity of a half space,” *IEEE Trans. Antennas Propagat.*, vol. 51, pp. 2822–2829, 2003.

[164] X. Dong, Z. Liu, and L. Carin, “Volume and surface MLFMA formulations for dielectric targets in the presence of a half space,” *Radio Sci.*, vol. 39, 2004.

[165] L. Li and L. Carin, “Multi-level fast multipole method calibration of ray models with application to wireless propagation,” *IEEE Trans. Antennas Propagat.*, vol. 52, pp. 2794–2799, 2004.

[166] M. A. Seville, Multilevel Multipole Free Fast Algorithm for Elecgromagnetic Scattering Problems in Layered Media. *PhD thesis*, University of Illinois at Urbana, 2006.

[167] R. L. Wagner, Efficient computational techniques for electromagnetic propagation and scattering. *PhD thesis*, University of Illinois at Urbana-Champaign, 1996.

[168] R. L. Wagner, J. Song, and C. W. C., “Monte Carlo simulation of electromagnetic scattering from two-dimensional random rough surfaces,” *IEEE Trans. Antennas Propogat.*, vol. 45, pp. 235–245, 1997.

[169] V. Jandhyala, B. Shanker, E. Michielssen, and W. C. Chew, “A combined steepest descent fast multipole algorithm for the fast analysis of three-dimensional scattering by rough surfaces,” *IEEE Trans. Geoscience Remote Sensing*, vol. 36, pp. 738–748, 1998.

[170] V. Jandhyala, D. Sengupta, B. Shanker, E. Michielssen, M. Feng, and G. Stillman, “Two-dimensional rough surface couplers for broadband quantum-well infrared photodetectors,” *Appl. Phys. Lett.*, vol. 73, pp. 3495–3497, 1998.

[171] V. Jandhyala, D. Sengupta, B. Shanker, E. Michielssen, M. Feng, and G. Stillman,

"Efficient electromagnetic analysis of twodimensional finite quasi-random gratings of quantum well infrared photodetectors," *J. Appl. Phys.*, vol. 83, pp. 3360–3363, 1998.

[172] Z. Wang, Y. Yuan, and Q. Wu, "A parallel multipole accelerated 3-D capacitance simulator based on an improved model," *IEEE Trans. Computer-Aided Design*, vol. 15, pp. 1441–1450, 1996.

[173] J. Dull, K. Gallivan, J. M. Song, and W. C. Chew, "Parallel fast multipole capacitance solver," *IEEE AP-S Int. Symp*., vol. 3, pp. 1766–1769, 1998.

[174] S. Velamparambil, J. E. Schutt-Aine, J. G. Nickel, J. M. Song, and W. C. Chew, "Solving large sclae electromagnetic problems using a linux cluster and parallel MLFMA," *IEEE APS Int. Symp*., vol. 1, pp. 636–639, 1999.

[175] F. Wu, Y. Zhang, Z. Z. Oo, and E. Li, "Parallel multilevel fast multipole method for solving large-scale problems," *IEEE Antennas Propagat. Mag.*, vol. 47, no. 4, pp. 110– 118, Aug. 2005.

[176] C. Waltz, K. Sertel, M. Carr, B. Usner, and J. Volakis, "Massively parallel fast multipole method solutions of large electromagnetic scattering problems," *IEEE Trans. Antennas Propagat.*, vol. 55, no. 6, pp. 1810–1816, June 2007.

[177] J. Lee, J. Zhang, and C.-C. Lu, "Sparse inverse preconditioning of multilevel fast multipole algorithm for hybrid integral equations in electromagnetics," *IEEE Trans. Antennas Propagat.*, vol. 52, no. 9, pp. 2277–2287, Sept. 2004.

[178] P. Wang, Y. Xie, and R. Yang, "Analysis of electrical large radiation problem with precorrected multilevel fast multipole algorithm," *IEEE Antennas and Wireless Propagat. Lett.*, vol. 6, pp. 340–343, 2007.

[179] P. L. Rui, R. S. Chen, D. X. Wang, and E. N. Yung, "Spectral two-step preconditioning of multilevel fast multipole algorithm for the fast monostatic RCS calculation," *IEEE Trans. Antennas Propogat.*, vol. 55, no. 8, pp. 2268– 2275, Aug. 2007.

[180] T. Malas and L. Gurel, "Incomplete LU preconditioning strategies for MLFMA," *IEEE AP-S Int. Symp*., pp. 3921–3924, 2006.

[181] O. Ergul, T. Malas, C. Yavuz, A. Unal, and L. Gurel, "Computational analysis of complicated metamaterial structures using MLFMA and nested preconditioners," *Antennas and Propagation, EuCAP 2007*. The Second European Conference on, pp. 1–6, 11-16 Nov. 2007.

[182] A. Ergin, B. Shanker, and E. Michielssen, "The plane-wave time-domain algorithm for the fast analysis of transient wave phenomena," *IEEE Antennas Propagat. Mag.*, , vol. 41, pp. 39–52, Aug. 1999.

[183] B. Shanker, A. Ergin, K. Aygun, and E. Michielssen, "Analysis of transient electromagnetic scattering phenomena using a twolevel plane wave time-domain algorithm," *IEEE Trans. Antennas Propagat.*, vol. 48, no. 4, pp. 510–523, 2000.

Vikram Melapudi received his B'Tech from the Indian Institute of Technology, Madras, India in 2003. From 2003, he has been working towards his Ph.D. degree in Electrical Engineering at Michigan State University. His primary research interest is in the broad area of computational science and its applications; especially, in the development of fast and parallel algorithms for electromagnetics and multiphysics simulations. Among his other research interests are signal and image processing, applied analysis and non destructive evaluation. He was the recipient of the third prize award in the student paper competition of 2008 IEEE AP-S International Symposium and USNC/URSI National Radio Science Meeting, San Diego, CA, 2008.

Balasubramaniam Shanker received his B'Tech from the Indian Institute of Technology, Madras, India in 1989, M.S. and Ph.D in 1992 and 1993 respectively from the Pennsylvania State University. From 1993 to 1996 he was a research associate in the Department of Biochemistry and Biophysics at Iowa State University where he worked on the Molecular Theory of Optical Activity. From 1996 to 1999 he was with the Center for Computational Electromagnetics at the University of Illinois at Urbana-Champaign as a Visiting Assistant Professor, and from 1999-2002 with the Department of Electrical and Computer Engineering at Iowa State University as an Assistant Professor. Currently, he is a Professor in the Department of Electrical and Computer Engineering at Michigan State University. He has authored/co-authored over 250 journal and conferences papers and presented a number of invited talks. His research interest include all aspects of computational electromagnetics (frequency and time domain integral equation based methods, multi-scale fast multipole methods, fast transient methods, higher order finite element and integral equation methods), propagation in complex media, mesoscale electromagnetics, and particle and molecular dynamics as applied to multiphysics and multiscale problems. He was an Associate Editor for IEEE Antennas and Wireless Propagation Letters (AWPL), is a senior member of the IEEE and a full member of the USNC-URSI Commission B. He has also been awarded the Withrow Distinguished Junior scholar (in 2003) and the Withrow teaching award (in 2007).

Fast Multipole Method Accelerated by Lifting Wavelet Transform Scheme

Ming-Sheng Chen[1], Xian-Liang Wu[1, 2], Wei Sha[3], and Zhi-Xiang Huang [2]
[1] Department of Physics and Electronic Engineering, Hefei Teachers College, 1688 LianHua Road, Economic and Technological Development Zone, Hefei, Anhui 230601, China
cmsh@ahu.edu.cn , xlwu@ahu.edu.cn

[2] Key Laboratory of Intelligent Computing & Signal Processing, Anhui University, Hefei, Anhui 230039, China
zxhuang@ahu.edu.cn

[3] Department of Electrical and Electronic Engineering, the University of Hong Kong, Pokfulam Road, Hong Kong, China
wsha@eee.hku.hk

***Abstract*―** The lifting wavelet like transform (LWLT) is applied to the fast multipole method (FMM) to complete the scattering analysis of three-dimensional (3D) objects. The aggregation matrix and disaggregation matrix are sparsified by the LWLT scheme in time. Numerical results for different shaped three-dimensional objects are considered. It is shown that the proposed method can speed up FMM with lower memory required.

***Index Terms*―** Lifting wavelet like transform (LWLT), Method of moments (MOM), Fast multipole method (FMM), Electromagnetic scattering.

I. INTRODUCTION

As an efficient numerical algorithm for the analysis and computation of electromagnetic scattering by arbitrarily shaped three-dimensional objects, the method of moments (MOM) is widely used in computational electromagnetics (CEM). However, traditional MOM technique is inherently limited because its direct solution has $O(N^3)$ complexity for a problem with N unknowns, and even though the iterative methods are adopted, the matrix-vector multiplication (MVM) can be $O(N^2)$. Over the past few decades, a number of techniques have been proposed to speed up the process of MVM. The fast multipole method (FMM) [1-3] and the multilevel fast multiple algorithm (MLFMA) [4] are well known among them, which can reduce $O(N^2)$ for MVM to $O(N^{1.5})$ and $O(N \log N)$, respectively, and some techniques are proposed to further improve the efficiency. In [5] the Cartesian components of the radiation patterns are represented in a spherical harmonics basis to optimize the memory requirements. Another interesting method is the wavelet matrix method [6-10], which can sparsify the dense moment matrix due to its multiresolution and vanishing moment properties, leading to a reduced solution time for the resulting sparse matrix. The applications of wavelet matrix transform have been widely used but are mainly confined to the analysis of two-dimensional (2-D) problems, or to special structures such as wire in which the current direction is one-dimensional. When 3-D scattering problems are considered, the impedance elements distribution will be more oscillatory than that in 2-D or 1-D cases, and the sparsity obtained by ordinary wavelet can be unsatisfying, which makes the application of wavelet transform to such problems greatly restricted.

II. THEORY

For perfectly electrically conducting (PEC) objects illuminated by an incident field $\mathbf{E}^i(\mathbf{r})$, the electric field integral equation (EFIE) is given by

$$\hat{\mathbf{n}} \times \iint_S \bar{\mathbf{G}}(\mathbf{r},\mathbf{r}') \bullet \mathbf{J}(\mathbf{r}') dS' = \frac{1}{jk\eta} \hat{\mathbf{n}} \times \mathbf{E}^i(\mathbf{r}) , \qquad (1)$$

where $\mathbf{J}(\mathbf{r}')$ is the unknown current distribution, $\hat{\mathbf{n}}$ is the unit outwardly directed norm vector of surface S, $\bar{\mathbf{G}}(\mathbf{r},\mathbf{r}')$ is the well-known free-space dyadic Green's function given by

$$\bar{\mathbf{G}}(\mathbf{r},\mathbf{r}') = \left(\bar{\mathbf{I}} + \frac{\nabla\nabla}{k^2} \right) g(\mathbf{r},\mathbf{r}') ; \; g(\mathbf{r},\mathbf{r}') = \frac{e^{-jk|\mathbf{r}-\mathbf{r}'|}}{4\pi|\mathbf{r}-\mathbf{r}'|} , \qquad (2)$$

with $\bar{\mathbf{I}}$ being the unit dyad.

When $\mathbf{J}(\mathbf{r})$ is represented by the Rao-Wilton-Glisson (RWG) basis functions and FMM is applied, equation (1) will be reduced to a matrix equation. For the far groups, the matrix-vector multiplication can be rewritten as

$$\mathbf{Z}^{far}\mathbf{x} = \mathbf{DTAx} \; , \qquad (3)$$

where $\mathbf{x}$ is the unknown current coefficients, and $\mathbf{D}$, $\mathbf{A}$, $\mathbf{T}$ are the disaggregation matrix, aggregation matrix, and translation matrix respectively, which are defined as

$$\mathbf{D}_{mp} = \int_S (\bar{\mathbf{I}} - \hat{\mathbf{k}}_p \hat{\mathbf{k}}_p) \bullet \mathbf{f}_m^S(\mathbf{r}) e^{-j\mathbf{k}_p \bullet (\mathbf{r}-\mathbf{r}_o)} dS , \qquad (4)$$

$$\mathbf{A}_{pn} = \int_{S'} (\bar{\mathbf{I}} - \hat{\mathbf{k}}_p \hat{\mathbf{k}}_p) \bullet \mathbf{f}_n^S(\mathbf{r}') e^{j\mathbf{k}_p \bullet (\mathbf{r}'-\mathbf{r}'_o)} dS' , \qquad (5)$$

$$\mathbf{T}_p = \frac{k^2\eta}{16\pi^2} \omega_p \sum_{l=0}^{L} (-j)^l (2l+1) h_l^{(2)}(kX) P_l(\hat{\mathbf{k}}_p \bullet \hat{\mathbf{X}}) \qquad p = 1, 2, \cdots, 2L^2 , \qquad (6)$$

in which $\mathbf{f}_m^S(\mathbf{r})$ and $\mathbf{f}_n^S(\mathbf{r}')$ are the RWG functions, k is the wavenumber in free space, $\mathbf{r}_o$ and $\mathbf{r}'_o$ are field group center and source group center respectively, $\mathbf{k}_p = k\hat{\mathbf{k}}_p$, $\hat{\mathbf{k}}_p = (\sin\theta_p \cos\phi_p, \sin\theta_p \sin\phi_p, \cos\theta_p)$, (θ_p, ϕ_p) are the sampled points over the unit sphere, X is the center distance between field group and source group, $h_l^{(2)}(x)$ is a spherical Hankel function of the second kind, and $P_l(x)$ refers to a Legendre polynomial.

The translation matrix $\mathbf{T}$ is highly sparse and can be further sparsified through the use of a windowed translation operator [12]. In this paper, discussions are focused on the sparsify operations of $\mathbf{D}$ and $\mathbf{A}$. As we know that for the interaction between two far groups, $\mathbf{D}$ is an $M_i \times K$ matrix and $\mathbf{A}$ is a $K \times N_i$ matrix with $K = 2L^2$.

As can be seen from (4) and (5), for a given $\mathbf{f}_m^S(\mathbf{r})$ or $\mathbf{f}_n^S(\mathbf{r}')$, the elements in the corresponding row or column vary with the sampled points on the surface of an unit sphere according to the Gauss-Legendre method. Compared with the elements distribution in traditional impedance matrix for 3-D problem, the elements distribution in $\mathbf{D}$ (row) or $\mathbf{A}$ (column) is relatively regular. That is the reason that the wavelet transform is introduced for the row in $\mathbf{D}$ and the column in $\mathbf{A}$.

The wavelet matrix transformation is applied and the interaction between the two groups can be represented by

$$[\mathbf{D}]_{M_i \times K} [\mathbf{T}]_{K \times K} [\mathbf{A}]_{K \times N_j} \mathbf{x}$$
$$= [\mathbf{D}]_{M_i \times K} [\mathbf{W}]_{K \times K} [\tilde{\mathbf{W}}]_{K \times K} [\mathbf{T}]_{K \times K} [\mathbf{W}]_{K \times K} [\tilde{\mathbf{W}}]_{K \times K} [\mathbf{A}]_{K \times N_j} \mathbf{x} , \qquad (7)$$

where $\tilde{\mathbf{W}}$ and $\mathbf{W}$ are forward and inverse wavelet transform matrices respectively and have the identity $\tilde{\mathbf{W}}\mathbf{W} = \mathbf{I}$, and for orthogonal wavelet $\tilde{\mathbf{W}} = \mathbf{W}^T$.

Equation (7) can be rewritten as

$$\mathbf{DTAx} = \tilde{\mathbf{D}}\tilde{\mathbf{W}}\mathbf{T}\mathbf{W}\tilde{\mathbf{A}}\mathbf{x} \; , \qquad (8)$$

with $\tilde{\mathbf{D}} = \mathbf{DW}$ and $\tilde{\mathbf{A}} = \tilde{\mathbf{W}}\mathbf{A}$.

Then the MVM will be completed by the following steps:

- Firstly, $\mathbf{D}$, $\mathbf{A}$ and $\mathbf{T}$ are generated and wavelet matrix transform is applied simultaneity by $\tilde{\mathbf{D}} = \mathbf{DW}$ and $\tilde{\mathbf{A}} = \tilde{\mathbf{W}}\mathbf{A}$, then $\tilde{\mathbf{D}}$ and $\tilde{\mathbf{A}}$ is a sparse matrix by the threshold σ_m .
- Secondly, complete aggregation by $\mathbf{x}_1 = \tilde{\mathbf{A}}\mathbf{x}$, and the inverse wavelet transform for $\mathbf{x}_1$ is implement by $\mathbf{x}_2 = \mathbf{W}\mathbf{x}_1$.
- Thirdly, complete translation by $\mathbf{x}_3 = \mathbf{T}\mathbf{x}_2$.
- Finally, the forward wavelet transform for $\mathbf{x}_3$ is applied by $\mathbf{x}_4 = \tilde{\mathbf{W}}\mathbf{x}_3$, and the disaggregation is completed by $\mathbf{x}_5 = \tilde{\mathbf{D}}\mathbf{x}_4$.

To save CPU time and memory consumed for transform matrix, the lifting wavelet like transform is introduced to complete the forward transform and inverse transform. In the LWLT scheme, the wavelet transform is directly operated to the object matrix according to the polyphase matrices

$$\tilde{\mathbf{P}}(z) = \prod_{i=1}^{m} \begin{pmatrix} 1 & 0 \\ -s_i(z^{-1}) & 1 \end{pmatrix} \begin{pmatrix} 1 & -t_i(z^{-1}) \\ 0 & 1 \end{pmatrix} \begin{pmatrix} F & 0 \\ 0 & 1/F \end{pmatrix} , \qquad (9)$$

$$\mathbf{P}(z)=\prod_{i=1}^{m}\begin{pmatrix}1 & s_i(z)\\ 0 & 1\end{pmatrix}\begin{pmatrix}1 & 0\\ t_i(z) & 1\end{pmatrix}\begin{pmatrix}F & 0\\ 0 & 1/F\end{pmatrix}, \qquad (10)$$

in which $s_i(z)$ and $t_i(z)$ are Laurent polynomials, and F is a nonzero constant.

The forward transform is implemented according to $\tilde{\mathbf{P}}(z^{-1})^t$ and the inverse transform is operated by $\mathbf{P}(z)$, and specific examples can be found in [11].

For a field group with M_i RWG functions and a source group with N_j RWG functions, there are $2L^2$ elements in each row of $\mathbf{D}$ or in each column of $\mathbf{A}$, and in the presented scheme, the LWLT is actually applied to $\mathbf{D}$ row by row, and applied to $\mathbf{A}$ column by column. Take the matrix $\mathbf{D}$ for example, once a certain row is generated and the transform for it is implemented, then the clipping operation [13] is used with the threshold and only the left elements in the row are stored. The threshold for the m row is defined by

$$\sigma_m=\tau\cdot\frac{1}{K}\sum_{p=1}^{K}\left(\left|\tilde{\mathbf{D}}_{\theta}(m,p)\right|^2+\left|\tilde{\mathbf{D}}_{\varphi}(m,p)\right|^2\right)^{\frac{1}{2}}, \qquad (11)$$

and numerical simulations show that $\tau\in[0.8,1.2]$, and the accuracy is controlled by τ.

As we can see from the above operations, two wavelet implementations are added to each iterative step. The number of multiplication operations within the LWLT is set to be p which can be counted from the polyphase matrices. If the length of the signal is K, the total computational complexity for implementation LWLT for it can be computed by

$$p\times\frac{K}{2}\times\left(1+\frac{1}{2}+\frac{1}{4}+\ldots\right)=pK, \qquad (12)$$

and for Daubechies wavelets of 4 vanishing moments (db4) with the maximum level transform $p=12$, which is so smaller than M_i that can be neglected when electrically large problem is considered, since $M_i\approx\sqrt{N}$.

III. NUMERICAL RESULTS

Firstly the disaggregation matrix $\mathbf{D}$ for a PEC cube is considered with $L=10$. After the lifting wavelet like transform by db4, a row of $\tilde{\mathbf{D}}$ is presented in Figure 1.

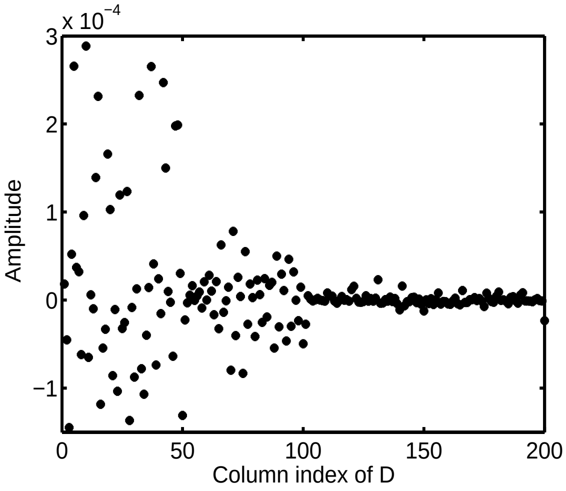

Fig. 1. The elements distribution in disaggregation matrix after the application of LWLT.

As can be seen from Fig. 1, most of the elements are far smaller than the others. The results after the clipping operation is shown in Fig. 2 and only about 30% of the total elements are left, then the inverse LWLT is implemented and the new row after transform is given in Fig. 3 which agrees well with the original row transform in $\mathbf{D}$, the relative error is 2.57%, which will ensure the accuracy of MVM computation for far field.

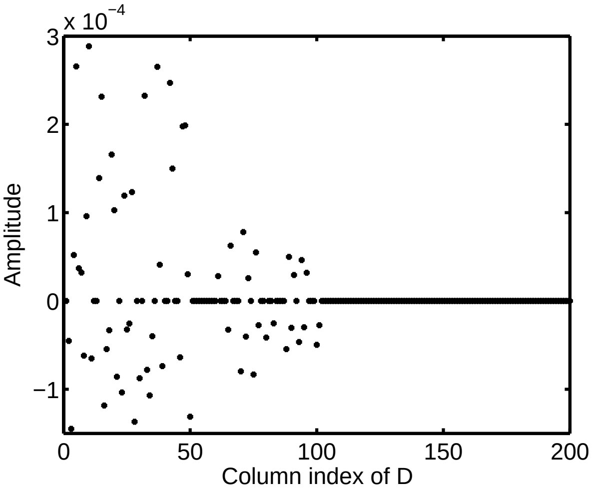

Fig. 2. The elements distribution in disaggregation matrix after the application of clipping technique.

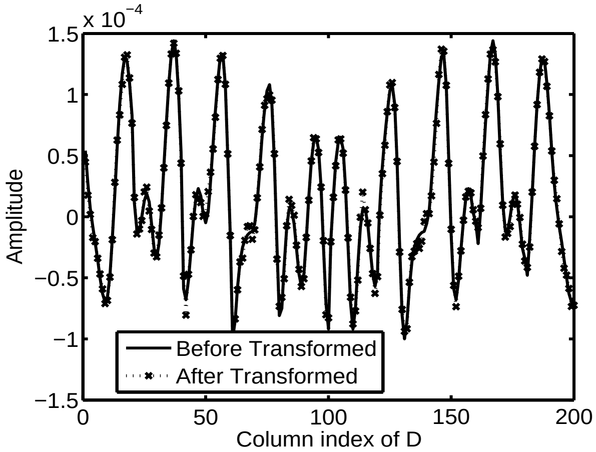

Fig. 3. The elements distribution in disaggregation matrix obtained by inverse lifting wavelet transform from the row presented in Fig. 2, which is compared with the row in $\mathbf{D}$.

As the first example, a PEC sphere with a diameter of 5λ is considered. The total number of unknowns is 15870 and the unknowns are divided into 98 groups with group size $d = 1\lambda$. When the sparsity (defined as the percentage content of nonzero elements) of disaggregation matrix and aggregation matrix is 32.44% ($\tau = 0.9$), the radar cross section (RCS) of the sphere computed by the LWLT-FMM scheme is compared with that of the analytical solution and shown in Fig. 4.

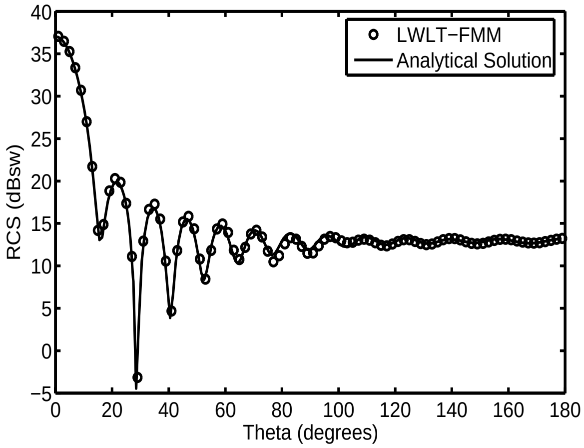

Fig. 4. The E-plane RCS of a PEC sphere with a diameter of 5λ.

A PEC cube with a side length of 4λ is considered as the second example. The surface of it is discretized into 12288 triangular elements, and 98 nonempty boxes are formed with group size $d = 0.8\lambda$. The sparsity of disaggregation matrix and aggregation matrix obtained is 33.13% ($\tau = 1.1$), the LWLT-FMM method obtained the accurate result more quickly as compared with the traditional FMM, which is shown in Fig. 5.

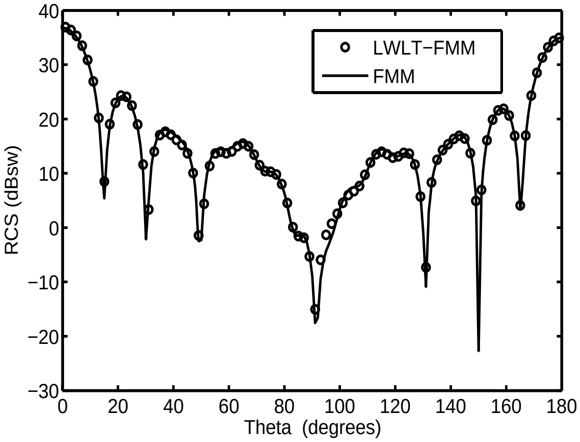

Fig. 5. The E-plane RCS of a PEC cube with a side length of 4λ.

The total CPU time and memory consumed for the MVM in far-field computation is shown in Table I. We can conclude that the proposed method can speed up the FMM by a factor of two with half memory consumed.

Table I The CPU time and memory required for the MVM operations of far-field interactions

Example	CPU time for far field computation		Memory required for Far-field computation	
	FMM	LWLT-FMM	FMM	LWLT-FMM
PEC Sphere $L = 12$	192 seconds	107 seconds	213MB	96MB
PEC Cube $L = 10$	177 seconds	98 seconds	170MB	74MB

IV. DISCUSSION

To validate the effectiveness of the formula presented in equation (11) for the threshold, we define the relative root mean square (RMS) error as

$$Err_{RMS} = \left\{ \frac{1}{M} \sum_{m=1}^{M} \left| 10 \log_{10} \left[\hat{\sigma}(\theta_m) / \sigma(\theta_m) \right] \right|^2 \right\}^{\frac{1}{2}}, \qquad (13)$$

where the θ_m represent M selected scattering directions. $\hat{\sigma}$ and σ are the radar cross section obtained by direct FMM solution and LWLT-FMM method, respectively.

For the given two examples mentioned above, the relationship between relative RMS RCS error and the value of parameter τ are shown in Fig.6 and Fig. 7, while the sparsity of disaggregation matrix and aggregation matrix is given in Fig.8, from which we can conclude that the relative RMS RCS error can be controlled under 0.5 dB with the sparsity about 30% when the value of parameter τ is chosen from 0.8 to 1.2.

Finally, when we set $\tau = 0.9$ and $\tau = 1.1$ for the PEC sphere and PEC cube described in the previous section, the nonzero element distribution in disaggregation matrix for the first nonempty box are shown in Fig. 9 and Fig. 10, respectively.

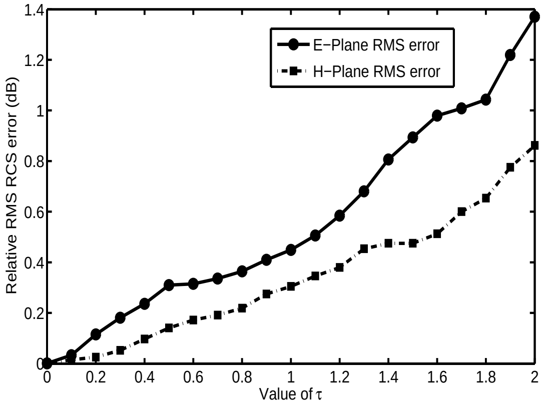

Fig. 6. Relative RMS RCS error of PEC sphere varies with value of τ.

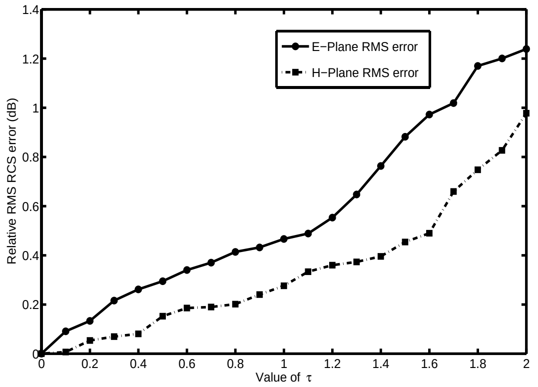

Fig. 7. Relative RMS RCS error of PEC cube varies with value of τ.

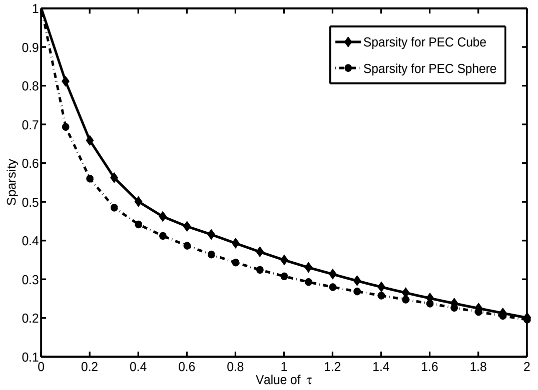

Fig. 8. Sparsity of disaggregation matrix and aggregation matrix varies with value of τ.

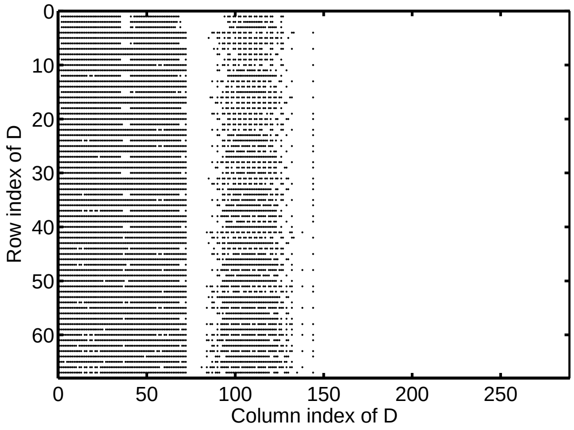

Fig. 9. Nonzero elements distribution for disaggregation matrix of a PEC sphere.

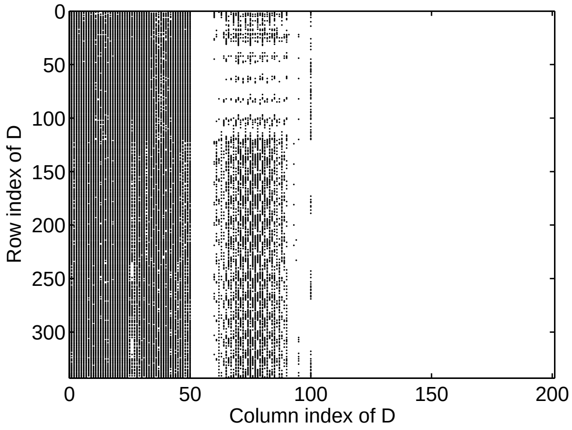

Fig. 10. Nonzero elements distribution for disaggregation matrix of a PEC cube.

V. CONCLUSION

The fast multipole method in conjugation with the LWLT scheme is proposed to the scattering analysis of different shaped three-dimensional PEC objects, the CPU time and memory consumed by FMM are reduced by sparsify the disaggregation matrix and aggregation matrix in time.

ACKNOWLEDGEMENT

The author wishes to acknowledge the anonymous reviewers for their useful comments and constructive suggestions. This work is supported by the Natural Science Foundation of the Anhui Higher Education Institution of China under Grant No KJ2008A036 and partially by the National Natural Science Foundation of China under Grant No 60671051.

REFERENCES

[1] V. Rokhlin, “Rapid solution of integral equations of scattering theory in two dimensions,” *J. of Comput. Phys.*, vol. 86, no. 2, pp. 414-439, 1990.

[2] N. Engheta, W. D. Murphy, V. Rokhlin, and M. S. Vassiliou, “The fast multipole method (FMM) for electromagnetic scattering problems,” *IEEE Trans. Antennas Propagat.*, vol. 40, no. 6, pp. 634-641, 1992.

[3] R.Coifman and V.Rokhlin, “The fast multipole method for the wave equation:a pedestrian prescription,” *IEEE Antennas Propagat. Mag.*, vol. 35, no. 3, pp. 7-12, 1993.

[4] J. M. Song and W. C. Chew, “Multilevel fast-multipole algorithm for solving combined field integral equations of electromagnetic scattering,” *Micro. Opt. Tech. Lett.*, vol. 10, no. 1, pp. 14-19, 1995.

[5] T. F. Eibert, “A diagonalized multilevel fast multipole method with spherical harmonics expansion of the k-space integrals,” *IEEE Trans. Antennas Propag.*, vol. 53, no. 2, pp. 814-817, 2005.

[6] R. L. Wagner and W. C. Chew, “A Study of Wavelets for the Solution of Electromagnetic Integral-Equations,” IEEE Transactions on Antennas and Propagation, vol. 43, no. 8, pp. 802-810, 1995.

[7] Z. G. Xiang and Y. L. Lu, “A study of the fast wavelet transform method in computational electromagnetics”, *IEEE Trans. Magnetics*, vol. 34, no. 5, pp. 3323-3326, 1998.

[8] H. Deng and H. Ling, “Preconditioning of electromagnetic integral equations using pre-defined wavelet packet basis,” *Elect. Lett.*, vol. 35, no. 14, pp. 1144-1145, 1999.

[9] J. Yu and A. A. Kishk, “Use of wavelet transform to the method-of-moments matrix arising from electromagnetic scattering problems of 2D objects due to oblique plane-wave incidence,” *Micro. Opt. Tech. Lett.*, vol. 34, no. 2, pp. 130-134, 2002.

[10] D. Huybrechs and S. Vandewalle, “A two-dimensional wavelet-packet transform for matrix compression of integral equations with highly oscillatory kernel,” *J. Comput. App. Math.*, vol. 197, no. 1, pp. 218-232, 2006.

[11] I. Daubechies and W. Sweldens, “Factoring wavelet transforms into lifting steps,” *J. of Fourier Analysis and App.*, vol. 4, no. 3, pp. 247-269, 1998.

[12] R. L. Wagner, and W. C. Chew, “A ray-propagation fast multipole algorithm,” *Micro. Opt. Tech. Lett.*, vol. 7, no. 10, pp. 435-438, 1994.

[13] F. P. Andriulli, G. Vecchi, F. Vipiana, P. Pirinoli, and A. Tabacco, “Optimal A priori clipping estimation for wavelet-based method of moments matrices,” *IEEE Trans. Antennas Prop.*, vol. 53, no. 11, pp. 3726-3734, 2005.

Ming-Sheng Chen was born in Nanling, Anhui Province, China, in 1981. He received the B.S. degree in applied mathematics from Anhui University, Hefei, China, in 2003, and received the Ph.D. degree in electromagnetic scattering, inverse scattering, and target identification at the same university. He is currently working at Department of Physics and Electronic Engineering, Hefei Teachers College. He has authored or coauthored more than 30 papers. His current research interests include frequency-domain numerical methods and wavelet theory.

Xian-Liang Wu was born in Bozhou, Anhui Province, China, in 1955. He received the B.S. degree in electronic engineering from Anhui University, Hefei, China, in 1982. He is a full professor of department of electronic engineering and the director of laboratory of electromagnetic field and microwave technology at Anhui University. He is currently the principal of Hefei Teachers College. He has authored or coauthored more than 70 papers and 2 books. His current research interests include electromagnetic field theory, electromagnetic scattering and inverse scattering, wireless communication, etc.

Prof. Wu is a senior member of Chinese Institute of Electronics, and an associate director of Chinese Institute of Microwave Measurement. He received the “Ministry of Education Award for Science & Technology Progress” and “Science & Technology Award of Anhui Province”.

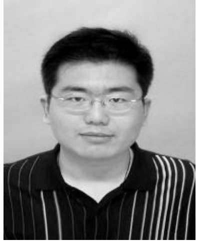

Wei Sha was born in Suzhou, Anhui Province, China, in 1982. He received the B.S. degree in electronic engineering from Anhui University, Hefei, China, in 2003 and received the Ph.D. degree in electromagnetic scattering, inverse scattering, and target identification at the same university. He is currently a postdoctoral research fellow at department of electrical and electronic engineering, the University of Hong Kong. His current research interests include time-domain numerical methods and signal processing.

Zhi-Xiang Huang was born in Guangde, Anhui Province, China, in 1979. He received the B.S. degree in mathematical statistics and the Ph.D. degree in electromagnetic scattering, inverse scattering, and target identification from Anhui University, Hefei, China, in 2002 and 2007, respectively. His current research interests include numerical methods for scattering.

Analyzing PEC Scattering Structure Using an IE-FFT Algorithm

Seung Mo Seo[1], Chao-Fu Wang [2], and Jin-Fa Lee [1]
[1] Department of Electrical Engineering
The Ohio State University, Columbus, OH 43212, USA
lee.1863@osu.edu

[2] Temasek Laboratories,
National University of Singapore,
5 Sports Drive 2, Singapore 117508, Singapore.
cfwang@nus.edg.sg

***Abstract*—** In this paper a fast integral equation method, termed IE-FFT, is developed, analyzed and applied to the electromagnetic (EM) solution of scattering problems. The methodology is developed for the Method of Moments (MoM) solution of the Electric Field Integral Equation (EFIE) on electrically large Perfect Electric Conducting (PEC) structures. Similar to other Fast Fourier Transform (FFT) based algorithms, IE-FFT uses a Cartesian grid to drastically decrease memory storage and speed up the matrix-vector multiplication. The IE-FFT algorithm employs two discretizations, one for the unknown current on an unstructured triangular mesh and the other on a uniform Cartesian grid for interpolating the Green's function. The uniform interpolation of the Green's function allows the fast computation of well-separated MoM interaction terms with the aid of a global FFT. Nevertheless, the coupling between near-interaction terms should be adequately corrected. The major contribution of this paper lies on the Lagrangian interpolation of the Green's function. This not only allows simple and efficient algorithmic implementation, but also naturally suggests a rigorous error analysis of the algorithm. The efficiency of the method is based on the Toeplitz structure of the interpolated Green's function. Therefore, it is applicable on both asymptotically-smooth and oscillatory kernels arisen in static and wave propagation problems, respectively. Through numerical simulations of electromagnetic wave scattering from a PEC sphere, the complexity of the IE-FFT algorithm is found to scale as $O(N^{1.5})$ and $O(N^{1.5}logN)$ for memory and CPU time, respectively. Various numerical results verify the high accuracy and efficiency of the method.

***Index Terms*—** Methods of Moment, Numerical method, Fast Fourier Transform, Electromagnetic Scattering, and Integral Equation.

I. INTRODUCTION

The Method of Moments (MoM) solution of surface Integral Equations (IE) has been proven very successfully in analyzing electromagnetic radiation and scattering from arbitrarily shaped conducting objects. A conventional MoM process produces high-accuracy results for both near- and far-field quantities, but requires prohibitive $O(n^2)$ memory and fill-in CPU time. This paper introduces yet another approach on reducing the computational burden of MoM while maintaining an explicit error control of the method.

During the last decades a large number of methods have been proposed to reduce the computational complexity and memory requirement of IE based methods. Perhaps the most successful and popular is the Fast Multipole Method (FMM) and its multilevel implementation MLFMM [1] – [4]. Careful implementations of MLFMM achieve $O(N)$ and $O(NlogN)$ complexities for memory and matrix-vector-multiplication time [2]. Unfortunately, the strong reliance of multipole-based methods on kernel-specific mathematical apparatus makes the methods inadequate for general purpose kernel-independent solvers.

Unlike FMM, a number of recent developments have focused on less kernel-dependent fast integral methods. Such methods are the IES3 [6], IE-QR [7], [8] and Adaptive Cross-Approximation (ACA) [9], [10] algorithms. These are "algebraic" methods, in the sense that they consider the IE matrix from a linear algebra point of view. The computational reduction is achieved by compressing, in a multilevel fashion, the rank-deficient sub-matrices of geometrically well-separated interactions.

Another class of fast IE methods, which directly relates to the proposed method, is the grid-based or FFT-based category. The well-known precorrected-FFT (p-FFT) [11], [12] and the Adaptive Integral Method (AIM) [13], [14] are among the most popular and well documented. Both p-FFT and AIM approaches are of $O\left(N^{1.5}\right)$ for storage and $O(N^{1.5}\log N)$ for matrix-vector multiplication. Both approaches are based on an "equivalent" source approximation. Namely, the unstructured grid sources are mapped onto a uniformly distributed set of equivalent multipole moment sources. To establish "equivalence", the fields of the two sets of sources need to be matched at selected locations. Recently, a fast, high-order algorithm, based on "two-face" equivalent source approximation, was proposed in [15]. The fast, high-order algorithm achieves $O\left(N^{6/5}\log N\right)$ to $O\left(N^{4/3}\log N\right)$ by placing equivalent sources only on the faces of cubic cells. Nevertheless, the method is strongly dependent of the integral kernel due to the use of the addition theorem. The Sparse-Matrix/Canonical-Grid (SM/CG) method of [16] is yet another grid-based fast IE method. Unlike previous mentioned methods, The SM/CG method does not utilize equivalent sources, but employs the Taylor expansion of the Green's functions on a uniformly spaced canonical grid. Subsequently, the impedance matrix is solved by an FFT-based iterative procedure based on the number of Taylor expansion terms. The SM/CG method does require the detail knowledge of the integral kernel. Due to the Toeplitz symmetry, the memory complexity of SM/CG is $O\left(N^{1.5}\right)$. Gedney in [17] proposed the Quadrature Sampled Pre-Corrected Fast-Fourier Transform (QS-PCFFT) algorithm to project the unknown currents to a uniform grid. The QS-PCFFT algorithm evaluates the discrete Fourier transform of the current directly using discontinuous FFT, which is based on quadrature sampling of the currents. The algorithm provides controllable accuracy and exponential convergence. Finally, the Green's function interpolation together with the FFT (GIFFT) [18] algorithm has developed for arrays with arbitrary shape. The GIFFT algorithm uses an array mask function to identify the array boundaries and specify the domain on which the Green's function is interpolated. The FFT is used to accelerate the matrix-vector products in an iterative solver. Consequently, the GIFFT algorithm reduces storage and solution time. For volume IE methods and planar structures, all grid or FFT-based algorithms end up with $O\left(N\right)$ complexity for the memory.

The IE-FFT algorithm described in this paper is in essence the same as the GIFFT algorithm, although developed completely independent. Its basic attributes can be summarized in its simplicity, error control and generality due to the Lagrangian interpolation of the kernel, and efficiency due to the FFT. Before start summarizing the approach, it should be emphasized that the choice of Lagrange interpolation of the Green's function was based on the simplicity. Only minor modifications are needed to extend to other standard interpolation schemes such as Hierarchical Lagrangian, Newton, trigonometric, etc. The proposed approach is more versatile than the FMM and is also simpler than other grid-based methods. The less-kernel dependent algorithm is easily applied to various applications with little modification. For fast evaluation of integral operators, simple polynomial interpolation of the integral kernel is constructed on a regular grid. The IE-FFT algorithm employs algebraically simple Lagrange polynomials on each 3-D Cartesian cell. Regardless of the order of the polynomials and the electrical size of the scatterer, the sampling segments per wavelength should be kept constant. In accordance to the Nyquist sampling theorem, the proposed algorithm for 3-D surface IE leads to $O\left(N^{1.5}\right)$ complexity for the memory requirement. Unlike p-FFT and AIM methods, uniform grid does not represent "equivalent" source, but correspond to interpolation tools for the Green's functions. The error analysis of IE-FFT algorithm is considerably easier than other grid-based methods due to Lagrangian interpolations. Upper bounds of the Green's function interpolation error versus the sampling segments are derived and verified for arbitrary polynomial orders. High order polynomials or more sampling segments for the interpolation could be chosen to get improved accuracy. The trade-off could be straightforwardly controlled over the accuracy and efficiency of the IE-FFT algorithm. Finally, the IE-FFT algorithm demonstrates $O\left(N^{1.5}\right)$ complexity and achieves good accuracy for solving 3-D arbitrarily shaped PEC scattering structures. Since the proposed method shares many common features with other FFT based methods, it is expected to achieve almost linear complexity when used to accelerate planar (2.5D) multilayer IE solvers or volume integral equations (VIEs).

The outline of the paper is as follows. For completeness a short summary of the EFIE formulation for 3-D PEC scattering problems is described in Section II. The algorithmic development and details of the IE-FFT algorithm are presented in Section III. Section IV is devoted to the error analysis of the algorithm, and to demonstrate the error control of interpolating the Green's function. To validate the theory and analytical developments, scattering from a PEC sphere is first considered in Section V. Through numerous numerical experiments, the accuracy and performance of the current approach are demonstrated. Finally, the proposed method is tested, and compared with other methods, in an example involving the scattering from a generic battleship. Concluding remarks are discussed in Section VI.

II. FORMULATION

Let's start with the discrete Galerkin statement for the electric field integral equation (EFIE), find $\vec{J}_h\left(\vec{r}\right) \in \mathbf{X}_h \subset \mathbf{H}_{\|}^{-1/2}\left(\mathbf{div}_\Gamma;\Gamma\right)$ such that

$$
\begin{aligned}
k_0^2 \int_{\Gamma_h} \vec{\lambda}_h\left(\vec{r}\right) \cdot \int_{\Gamma_h} g\left(\vec{r};\vec{r}'\right) \vec{J}_h\left(\vec{r}'\right) dx'^2 dx^2 \\
- \int_{\Gamma_h} \mathbf{div}_\Gamma \vec{\lambda}_h\left(\vec{r}\right) \int_{\Gamma_h} g\left(\vec{r};\vec{r}'\right) \mathbf{div}'_\Gamma \vec{J}_h\left(\vec{r}'\right) dx'^2 dx^2 \\
= -\frac{jk_0}{\eta_0} \int_{\Gamma_h} \vec{\lambda}_h\left(\vec{r}\right) \cdot \vec{E}^{inc}\left(\vec{r}\right) dx^2 \quad , \forall \vec{\lambda}_h \in \mathbf{X}_h ,
\end{aligned}
\tag{1}
$$

where Γ_h denotes the facetized surface of the PEC object. $\mathbf{X}_h$ is the finite dimensional trial and testing spaces, and $\mathbf{H}_{\|}^{-1/2}\left(\mathbf{div}_\Gamma;\Gamma\right) = \left\{ \vec{v} \middle| \vec{v} \in \left(L^2\left(\Gamma\right)\right)^2 , \quad \mathbf{div}_\Gamma \vec{v} \in L^2\left(\Gamma\right) \right\}$ is the correct spaces where the unknown currents reside [20]. The unknown electric current density is denoted by $\vec{J}_h\left(\vec{r}\right)$ and the testing function is $\vec{\lambda}\left(\vec{r}\right)$. $\vec{r}$ and $\vec{r}'$ are observation and source points, respectively, and $\vec{E}^{inc}\left(\vec{r}\right)$ is the incident electric field. In the present application, the free-space Green's function $g\left(\vec{r};\vec{r}'\right)$ is considered. The free space wave number and characteristic impedance are respectively denoted by k_0 and η_0. Throughout the paper the $e^{j\omega t}$ time convention is assumed, and j denotes the imaginary unit, except when stated otherwise. From the discrete Galerkin statement a system of equations is obtained by expanding trial and testing functions into a set of basis functions

$$
\vec{J}_h\left(\vec{r}'\right) = \sum_{i=0}^{N-1} J_i \vec{\alpha}_i\left(\vec{r}'\right), \tag{2}
$$

where $\vec{\alpha}\left(\vec{r}\right)' s$ are surface div-conforming vector Rao-Wilton-Glisson (RWG) basis functions [19]. Finally, the resulting matrix equation can be written as

$$
\mathbf{Z} \bullet \mathbf{J} = \mathbf{V} . \tag{3}
$$

The entries of the impedance matrix $\mathbf{Z}$ and those of the right-hand vector $\mathbf{V}$ are given by

$$
Z_{ij} = k_0^2 A_{ij} - D_{ij}, \quad 0 \le i, j \le N-1 , \tag{4}
$$

where

$$
\begin{aligned}
A_{ij} &= \int_{\mathrm{supp}\left(\vec{\alpha}_i\right)} \vec{\alpha}_i\left(\vec{r}\right) \cdot \int_{\mathrm{supp}\left(\vec{\alpha}_j\right)} g\left(\vec{r};\vec{r}'\right) \vec{\alpha}_j\left(\vec{r}'\right) dx'^2 dx^2 \\
D_{ij} &= \int_{\mathrm{supp}\left(\vec{\alpha}_i\right)} \mathbf{div}_\Gamma \vec{\alpha}_i\left(\vec{r}\right) \int_{\mathrm{supp}\left(\vec{\alpha}_j\right)} g\left(\vec{r};\vec{r}'\right) \mathbf{div}'_\Gamma \vec{\alpha}_j\left(\vec{r}'\right) dx'^2 dx^2
\end{aligned}
\tag{5}
$$

and

$$
V_i = -\frac{jk_0}{\eta_0} \int_{\mathrm{supp}\left(\vec{\alpha}_j\right)} \vec{\alpha}_i\left(\vec{r}\right) \cdot \vec{E}^{inc}\left(\vec{r}\right) dx^2 , \tag{6}
$$

where N is the number of unknowns, notice that *supp()* indicates the finite support of every non-boundary edge related basis function.

III. IE-FFT ALGORITHM

As stated in the introduction, the heart of the IE-FFT algorithm is the uniform Cartesian interpolation of the Green's function. The IE-FFT algorithm starts by constructing a rectangular bounding box that encloses the entire computational domain. This box is the domain for interpolating the Green's functions. The key outcome of the Green's functions interpolation is the decoupling of the sources and the receivers. This is the same idea as the FMM, but instead of approximation the Green's function through the spherical multipole expansion, the Green's function is expanded into a Cartesian Lagrange polynomial. Therefore the Green's function can be expressed as

$$g\left(\vec{r};\vec{r}'\right)=\frac{e^{-jk_0\left|\vec{r}-\vec{r}'\right|}}{\left|\vec{r}-\vec{r}'\right|}\simeq\sum_{n=0}^{N_g-1}\sum_{n'=0}^{N_g-1}\beta_n^p\left(\vec{r}\right)g_{n,n'}\beta_{n'}^p\left(\vec{r}'\right), \quad (7)$$

where p is the order of Lagrange polynomial interpolation, N_g is the number of grid points, β_n^p and $\beta_{n'}^p$ are the p^{th} order Lagrange interpolation basis functions for grids $\vec{r}$ and $\vec{r}'$, $g_{n,n'}$ are the Lagrange coefficients of the Green's function, and n and n' are dimensional indexes of grids $\vec{r}$ and $\vec{r}'$, respectively The explicit forms of β_n^p can be found in a number of elementary interpolation books such as [21]. In equation (7), the source and observation terms for the Lagrange interpolation basis functions are completely decoupled. Having obtained the product form of $g\left(\vec{r};\vec{r}'\right)$ the coupling integrals of (5) are now written as

$$A_{ij}\simeq \int_{\mathrm{supp}(\vec{\alpha}_i)}\vec{\alpha}_i\left(\vec{r}\right)\cdot\int_{\mathrm{supp}(\vec{\alpha}_j)}\left[\sum_{n=0}^{N_g-1}\sum_{n'=0}^{N_g-1}\beta_n^p\left(\vec{r}\right)g_{n,n'}\beta_{n'}^p\left(\vec{r}'\right)\right]\vec{\alpha}_j\left(\vec{r}'\right)dx'^2dx^2, \quad (8)$$

and

$$D_{ij}\simeq\int_{\mathrm{supp}(\vec{\alpha}_i)}\mathbf{div}_\Gamma\vec{\alpha}_i\left(\vec{r}\right)\cdot\left(\int_{\mathrm{supp}(\vec{\alpha}_j)}\left[\sum_{(n)=0}^{N_g-1}\sum_{(n')=0}^{N_g-1}\beta_n^p\left(\vec{r}\right)g_{n,n'}\beta_{n'}^p\left(\vec{r}'\right)\right]\mathbf{div}'_\Gamma\vec{\alpha}_j\left(\vec{r}'\right)dx'^2\right)dx^2, \quad (9)$$

respectively. Interchanging summation and integration orders, and grouping primed and unprimed variables, leads to

$$A_{ij}\simeq\sum_{n=0}^{N_g-1}\sum_{n'=0}^{N_g-1}\int_{\mathrm{supp}(\vec{\alpha}_i)}\left\{\left(\vec{\alpha}_i\left(\vec{r}\right)\beta_n^p\left(\vec{r}\right)\right)g_{n,n'}\cdot\int_{\mathrm{supp}(\vec{\alpha}_j)}\left(\beta_{n'}^p\left(\vec{r}'\right)\vec{\alpha}_j\left(\vec{r}'\right)\right)dx'^2\right\}dx^2, \quad (10)$$

and

$$D_{ij}\simeq\sum_{n=0}^{N_g-1}\sum_{n'=0}^{N_g-1}\int_{\mathrm{supp}(\vec{\alpha}_i)}\left\{\left(\mathbf{div}_\Gamma\vec{\alpha}_i\left(\vec{r}\right)\beta_n^p\left(\vec{r}\right)\right)g_{n,n'}\cdot\int_{\mathrm{supp}(\vec{\alpha}_j)}\left(\beta_{n'}^p\left(\vec{r}'\right)\mathbf{div}'_\Gamma\vec{\alpha}_j\left(\vec{r}'\right)\right)dx'^2\right\}dx^2. \quad (11)$$

The product forms of impedance matrix terms in (10)(11) are valid for all interactions, except the ones that reside on the same Green's function cell. At these location the Green's function coefficient matrix $g_{n,n'}$ is singular, thus need to be appropriately corrected. In summary the IE-FFT algorithm proceeds in four steps:

1) Represent free-space Green's function as simple Lagrange polynomials.
2) Construct four projection matrices $\mathbf{\Pi}$ using the EFIE formulation.
3) Correct entries from near-interaction elements.
4) Accelerate the matrix-vector products using the global FFT.

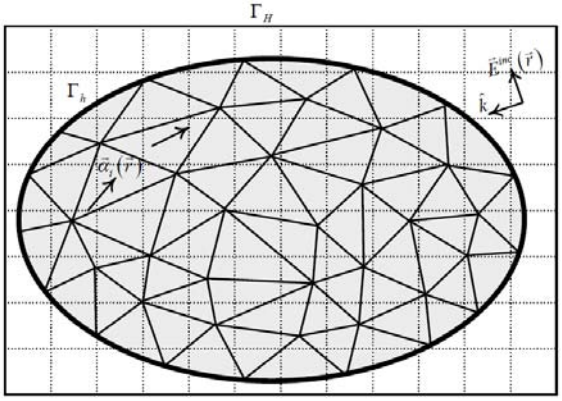

Fig. 1. Two discretizations for a problem domain. One is the regular triangular mesh (inside the boundary Γ_h on the scatterer) for the unknown surface current induced by the incident field. The other is a uniform Cartesian grid of the rectangular box (Γ_H) enclosing the problem domain.

The detail of the IE-FFT algorithm could be shown below.

A. Representation of Green's function using simple Lagrange polynomials

To interpolate the 3-D free-space Green's function, a rectangular box with dimension $L_x\times L_y\times L_z$ in the Cartesian coordinate is constructed first. The rectangular bounding box that encloses the problem domain, as shown in Fig. 1, will be considered as the domain of the Green's function. The bounding box is uniformly interpolated with simple Lagrange polynomials. In the current implementation, the sampling segment between two grid points is typically set to be $d = \lambda / 7$. The number of sampling points affects the accuracy of the approximation, and need to exceed Nyquist sampling rate for good accuracy. In equation (7), the number of grid points is $N_g = N_x \times N_y \times N_z$ where $N_x = L_x / d$, $N_y = L_y / d$, and $N_z = L_z / d$. Also, the dimensional indexes could be expressed as $n = (i, j, k)$ and $n' = (i', j', k')$ where $0 \le i, i' < N_x$, $0 \le j, j' < N_y$, and $0 \le k, k' < N_z$. The p^{th} order interpolation basis functions β_n^p are the 3-D tensor products form of one-dimensional piecewise Lagrange polynomials on a Cartesian grid

$$\beta_n^p(\vec{r}) = \beta_i^p(x) \cdot \beta_i^p(y) \cdot \beta_k^p(z) . \qquad (12)$$

Combined with equation (7) and(12), the Green function is written in the matrix form

$$g(\vec{r};\vec{r}') \simeq \left(\boldsymbol{\beta}(\vec{r})\right)^T \bullet \mathbf{G} \bullet \boldsymbol{\beta}(\vec{r}') , \qquad (13)$$

where

$$\boldsymbol{\beta}(\vec{r}) = \left[\beta_0^p(\vec{r}) \quad \beta_1^p(\vec{r}) \quad \cdots \quad \beta_{N_g-1}^p(\vec{r}) \right]$$
$$= \begin{bmatrix} \beta_0^p(x)\beta_0^p(y)\beta_0^p(z) \\ \beta_1^p(x)\beta_0^p(y)\beta_0^p(z) \\ \vdots \\ \beta_{N_x-1}^p(x)\beta_{N_y-1}^p(y)\beta_{N_z-1}^p(z) \end{bmatrix}^T \qquad ,(14)$$

$$\mathbf{G} = \begin{bmatrix} g_{0,0} & g_{0,1} & \cdots & g_{0,N_g} \\ g_{1,0} & g_{1,1} & \cdots & g_{1,N_g} \\ \vdots & \vdots & \ddots & \vdots \\ g_{N_g,0} & g_{N_g,1} & \cdots & g_{N_g,N_g} \end{bmatrix} . \qquad (15)$$

For general Green's function, one needs to store the entire $\mathbf{G}$, resulting in a $O\left(N_g^2\right)$ storage. Fortunately, most of the Green's functions appearing in static or electromagnetic field computations are of a difference-form. Namely, $g(\vec{r};\vec{r}') = g(\vec{r} - \vec{r}')$. Naturally, such integral kernels would lead to a 3-D block-Toeplitz structure for equation . For a 3-D block-Toeplitz matrix, we only need to store $2N_g$ entries of the $\mathbf{G}$. As it was mentioned above, the numerical values of $g_{n-n'}$ for $n = n'$ are infinite. For simplicity, they are set to zero, and the near field contributions will be appropriately corrected during the correction step.

B. Representation of Π matrices

There are two projection matrices needed in the IE-FFT algorithm, as evidenced from equation (10) and (11). They are:

$$\vec{\mathbf{\Pi}}_A = \int_\Gamma \begin{bmatrix} \vec{\alpha}_0(\vec{r}) \\ \vec{\alpha}_1(\vec{r}) \\ \vdots \\ \vec{\alpha}_{N-1}(\vec{r}) \end{bmatrix} \left[\beta_0^p(\vec{r}) \quad \beta_1^p(\vec{r}) \quad \cdots \quad \beta_{N_g-1}^p(\vec{r}) \right] dx^2 , \qquad (16)$$

and

$$\mathbf{\Pi}_D = \int_\Gamma \begin{bmatrix} \mathbf{div}_\Gamma \vec{\alpha}_0(\vec{r}) \\ \mathbf{div}_\Gamma \vec{\alpha}_1(\vec{r}) \\ \vdots \\ \mathbf{div}_\Gamma \vec{\alpha}_{N-1}(\vec{r}) \end{bmatrix} \left[\beta_0^p(\vec{r}) \quad \beta_1^p(\vec{r}) \quad \cdots \quad \beta_{N_g-1}^p(\vec{r}) \right] dx^2 \qquad (17)$$

respectively. Notice that $\vec{\mathbf{\Pi}}_A$ is a vector-valued matrix. Both matrices (16) and (17) are non-symmetric and more importantly sparse, since both RWG and the Lagrange interpolation basis functions have finite support. In other words, each RWG basis function is just projected onto only a few Lagrangian cells. Therefore, the memory requirement and CPU time of computing these matrices are $O(N)$.

C. Correction of matrix entries for touching or overlapping cells

From equation (5), the accuracy of approximating Z_{ij} by the IE-FFT algorithm depends on the distance between i^{th} basis and j^{th} testing functions. These functions are separated at least by $\alpha\lambda$ (we chose $\alpha = 0.2$) to assure accuracy in Fig. 2. In other words, the coupling between near-interaction terms should be adequately corrected. These entries should be substituted by accurate ones, which are computed by the conventional MoM technique. These entries should be corrected for fast computation before the matrix-vector products are performed. Finally, the correction entries from the interaction between i^{th} and j^{th} RWG basis functions are written as

$$Z_{ij}^{corr} = Z_{ij}^{MoM} - k_0^2 \left(\vec{\Pi}_A\right)_{iI} G_{IJ} \left(\vec{\Pi}_A\right)_{Jj}^T + \left(\Pi_D\right)_{iI} G_{IJ} \left(\Pi_D\right)_{Jj}^T , \qquad (18)$$

where $0 \le i < N$, $j \in C_{neig}$, and C_{neig} is the set of the near-interaction elements. The coupling between basis function i and j will be corrected by (18) if they are separated less than 0.2λ (our choice). The correction matrix $\mathbf{Z}^{corr}$ is unquestionably sparse. In the current implementation, the memory of correction matrix does not depends on the sampling segment of Cartesian grid and the order of Lagrange interpolation basis functions, used to interpolate the Green's function.

D. Fast matrix vector multiplication

Let Z_{ij} represent one entry of the impedance matrix and the matrix-vector product is written as

$$y_i = \sum_{j=0}^{N-1} Z_{ij} x_j \, , \quad 0 \le i < N-1 \, . \tag{19}$$

Combined with IE-FFT algorithm, the matrix-vector products could be rewritten as

$$\begin{aligned} y &= Z^{corr} \cdot x \\ &+ k_0^2 \vec{\Pi}_A \cdot IFFT\left\{ FFT\left(G\right) \cdot FFT\left(\left(\vec{\Pi}_A \right)^T \cdot x \right) \right\} \cdot \\ &- \Pi_D \cdot IFFT\left\{ FFT\left(G\right) \cdot FFT\left(\left(\Pi_D \right)^T \cdot x \right) \right\} \end{aligned} \tag{20}$$

From the above expression, the significant saving of memory due to the $O\left(N\right)$ complexity of $\mathbf{Z}^{corr}$ and $\mathbf{\Pi}$ matrices is clearly shown. Note that the FFT of the $\mathbf{G}$ matrix is computed only once. The memory requirement of the coefficient is $O\left(N^{1.5}\right)$ complexity. However, the FFT can be applied to speed up matrix vector multiplications significantly. It leads to $O\left(N^{1.5} \log N\right)$ complexity.

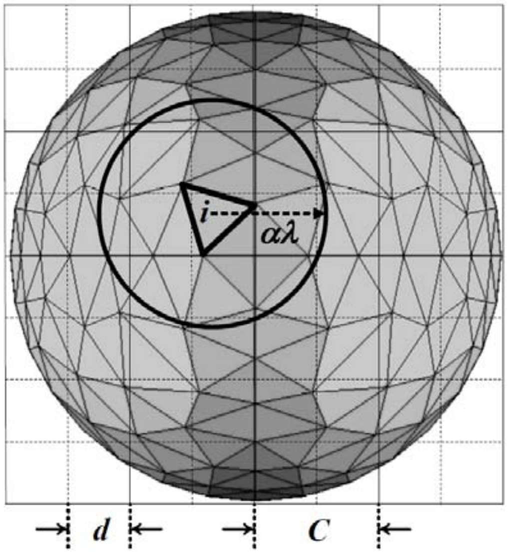

Fig. 2 A PEC sphere with two discretizations, a triangular mesh and a uniform Cartesian grid. Note that in the figure, *d* is the sampling resolution, *C* is the size of the Cartesian element, α is a constant used to define the local correction region, and λ is the wavelength.

IV. ERROR CONTROL

The only additional approximation of IE-FFT algorithm compared to the conventional MoM comes from the interpolation of the Green's function. Consequently, in order to assess the accuracy of the IE-FFT algorithm alone, the error analysis of the Green's function interpolation need to be considered. This section provides an error bound, which will guide the practical implementation of the IE-FFT algorithm for 3-D PEC scattering problems.

A. p^{th} order interpolation

Consider an analytical function $f\left(x\right), \; a \le x \le b$. A unique p^{th} order interpolation $f^{[p]}\left(x\right), \; a \le x \le b$ can be determined with

$$f^{[p]}\left(x_i\right) = f\left(x_i\right), a \le x_i \le b \quad x = 0, \cdots, p \tag{21}$$

Moreover, by Cauchy reminder theorem [21] for polynomial interpolation, we have

$$\begin{aligned} &\forall x \in \left[a,b\right], \exists \xi \in \left[a,b\right], s.t. \\ &f\left(x\right) - f^{[p]}\left(x\right) \\ &\quad = \frac{\left(x-x_0\right)\left(x-x_1\right)\cdots\left(x-x_p\right)}{\left(p+1\right)!} f^{(p+1)}\left(\xi\right), \end{aligned} \tag{22}$$

where $f^{(p+1)}\left(x\right)$ denotes the $\left(p+1\right)$ derivative of $f\left(x\right)$ at x. Subsequently, the following error bound is valid

$$\begin{aligned} &\frac{\left| f\left(x\right) - f^{[p]}\left(x\right) \right|}{\left| f\left(x\right) \right|} \le \\ &\qquad \frac{\max\limits_{a \le x \le b} \prod\limits_{i=0}^{p} \left| x - x_i \right|}{\left| f\left(x\right) \right|} \cdot \frac{\max\limits_{a \le \xi \le b} \left| f^{(p+1)}\left(\xi\right) \right|}{\left(p+1\right)!} \, . \end{aligned} \tag{23}$$

B. Free space Green's function and its derivatives

For free space scattering applications, $f\left(x\right) = \dfrac{\left(e^{-jk_0 x}\right)}{x}$ is considered. Note here that in order to fulfill the assumption that $f\left(x\right)$ is to be analytic, separation by $\alpha\lambda$ to be called well-separated should be persevered. The derivatives of $f\left(x\right)$ are summarized below

$$
\begin{aligned}
f(x) &= \frac{e^{-jk_0x}}{x} \\
f^{(1)}(x) &= -\left(jk_0+\frac{1}{x}\right)\frac{e^{-jk_0x}}{x} \\
f^{(2)}(x) &= \left(jk_0+\frac{1}{x}\right)^2\frac{e^{-jk_0x}}{x}+\frac{1}{x^2}\frac{e^{-jk_0x}}{x} \\
f^{(3)}(x) &= -\left(jk_0+\frac{1}{x}\right)^3\frac{e^{-jk_0x}}{x}-\left(jk_0+\frac{1}{x}\right)\frac{3}{x^2}\frac{e^{-jk_0x}}{x} \\
&\quad -\frac{2}{x^3}\frac{e^{-jk_0x}}{x} \qquad (24) \\
f^{(4)}(x) &= \left(jk_0+\frac{1}{x}\right)^4\frac{e^{-jk_0x}}{x}+\left(jk_0+\frac{1}{x}\right)^2\frac{3}{x^2}\frac{e^{-jk_0x}}{x} \\
&\quad +\left(jk_0+\frac{1}{x}\right)\left(jk_0+\frac{3}{x}\right)\frac{3}{x^2}\frac{e^{-jk_0x}}{x} \\
&\quad +\left(jk_0+\frac{4}{x}\right)\frac{2}{x^3}\frac{e^{-jk_0x}}{x}+\frac{3}{x^4}\frac{e^{-jk_0x}}{x} \\
&\quad \vdots
\end{aligned}
$$

C. Upper error bound in the IE-FFT algorithm

For p^{th} order interpolation polynomial in the IE-FFT algorithm, $b = a + pd$ and $d = \lambda / n$ are given (where n is the number of segments per wavelength). Also, as mentioned earlier, to assure the analyticity of the integral kernel, $a \geq \alpha\lambda$ should be kept. Furthermore, in the current IE-FFT implementation, uniform sampling is simply adopted, namely $\left|x_{i+1}-x_i\right| = d$. Subsequently, the following equation holds

$$
\frac{\max\limits_{a\leq x\leq b}\prod\limits_{i=0}^{p}\left|x-x_i\right|}{\left|f(x)\right|} \leq \begin{cases} \dfrac{2}{3\sqrt{3}}\left[\alpha+\dfrac{0.42}{n}\right]d^3, & p=2 \\ \left[\alpha+\dfrac{0.38}{n}\right]d^4, & p=3 \\ \vdots & \vdots \end{cases} \qquad (25)
$$

Additionally, we have the following inequalities

$$
\max_{a\leq\xi\leq b}\frac{\left|f^{(p+1)}(p)\right|}{(p+1)!} \leq \begin{cases} \dfrac{1}{a}\left[\sigma_1^3+\dfrac{3\sigma_1}{a^2}+\dfrac{2}{a^3}\right]\dfrac{1}{3!} & , p=2 \\ \dfrac{1}{a}\left[\sigma_1^4+\dfrac{3\sigma_1^2}{a^2}+\dfrac{3\sigma_1\sigma_3}{a^2}+\dfrac{2\sigma_4}{a^3}+\dfrac{3}{a^4}\right]\dfrac{1}{4!} & , p=3 \\ \vdots & \vdots \end{cases} \qquad (26)
$$

In equation (26), the parameters σ_i are given by

$$
\begin{aligned}
\sigma_1 &= \sqrt{k_0^2+\left(\frac{1}{a}\right)^2} \leq k_0\sqrt{1+\left(\frac{1}{2\pi\alpha}\right)} \\
\sigma_3 &= \sqrt{k_0^2+\left(\frac{3}{a}\right)^2} \leq k_0\sqrt{1+\left(\frac{3}{2\pi\alpha}\right)} \qquad (27) \\
\sigma_4 &= \sqrt{k_0^2+\left(\frac{4}{a}\right)^2} \leq k_0\sqrt{1+\left(\frac{2}{\pi\alpha}\right)}
\end{aligned}
$$

Substituting equation (24), (25) and (26) into (23) results in the final upper bound for the IE-FFT algorithm in (28) below.

In summary, the upper error bounds for the relative interpolation error versus the sampling segments, n , is plotted in Fig. 3 with $\alpha = 0.2$. The resulting equation is given by (29).

$$
\frac{\left|f(x)-f^{[p]}(x)\right|}{\left|f(x)\right|} \leq \begin{cases} \dfrac{88}{n^3}\left[1+\dfrac{2.1}{n}\right] & , p=2 \\ \dfrac{172}{n^4}\left[1+\dfrac{1.9}{n}\right] & , p=3 \\ \vdots & \vdots \end{cases} \qquad (29)
$$

The second-order and third-order interpolation polynomials in the IE-FFT are plotted with squares and circles. Fig. 4 shows the upper error bound for the relative interpolation error versus the minimum distance, α with $n = 7$. We should point out that in Fig. 4, the error approaching a constant as $\alpha \to \infty$. This is the unique feature of the wave propagation problems. Namely, any high-order derivatives

---

$$
\frac{\left|f(x)-f^{[p]}(x)\right|}{\left|f(x)\right|} \leq \begin{cases} 16\left[\left(\dfrac{\sigma_1}{k_0}\right)^3+\left(\dfrac{\sigma_1}{k_0}\right)\dfrac{3}{(2\pi\alpha)^2}+\dfrac{2}{(2\pi\alpha)^3}\right]\left[1+\dfrac{0.42}{\alpha n}\right]\dfrac{1}{n^3} & , p=2 \\ 10\left[\left(\dfrac{\sigma_1}{k_0}\right)^4+\left(\dfrac{\sigma_1}{k_0}\right)^2\dfrac{3}{(2\pi\alpha)^2}+\left(\dfrac{\sigma_1\sigma_3}{k_0^2}\right)\dfrac{3}{(2\pi\alpha)^2}+\left(\dfrac{\sigma_4}{k_0}\right)\dfrac{2}{(2\pi\alpha)^3}+\dfrac{3}{(2\pi\alpha)^4}\right]\left[1+\dfrac{0.38}{\alpha n}\right]\dfrac{1}{n^4} & , p=3 \\ \vdots & \vdots \end{cases} \qquad (28)
$$

of the Green's function will always exhibit $O(1/x)$ behavior asymptotically. If this is for static applications, the error will approach zero as $\alpha \to \infty$.

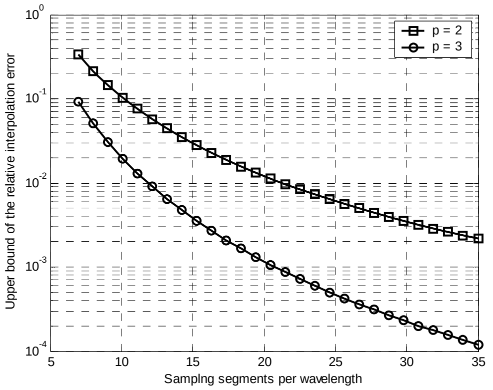

Fig. 3 Error bounds of the interpolated Green's function, plotted as a function of sampling rate and with *p*=2 and *p*=3.

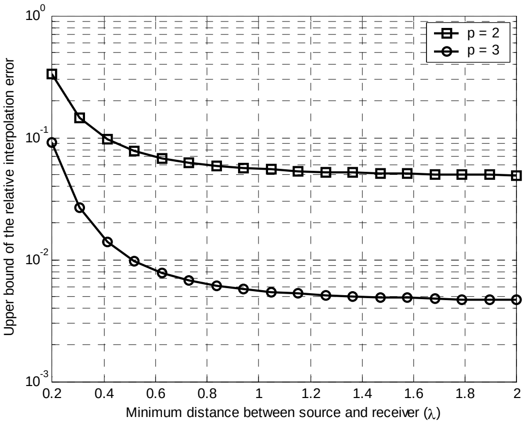

Fig. 4 Plots of upper error bounds for the Green's function interpolation of the IE-FFT algorithm as a function of minimum distance between source and receiver.

V. NUMERICAL RESULTS

In this section, studies on two numerical examples are conducted in order to demonstrate the complexity and accuracy of the IE-FFT algorithm. The EM scattering from a PEC sphere of various electrical sizes is first computed to validate the accuracy and efficiency of the IE-FFT algorithm. To demonstrate the IE-FFT algorithm, second-order and third-order Lagrange polynomials for interpolating the Green's function are used. For a very large-scale realistic problem, the scattering of a generic battleship, is considered. All numerical experiments are carried out on a 16 GB RAM, AMD® Opteron™ 246 64-bit workstation. All computations in this section have been performed in single precision arithmetic.

A. A PEC sphere

Scattering from a PEC sphere of radius 1 meter is first considered to demonstrate the complexity of the IE-FFT algorithm. In this example, the mesh density is kept constant, e.g. $h = \lambda / 7$, while the operating frequency increases. Table 1 and Table 2 summarize the performance, in terms of memory, of the IE-FFT algorithm for second-order and third order Lagrange polynomials, respectively. The total memory is split into the last three columns of each table, representing each individual matrix involved in (18).

Table 1: Memory requirement of the IE-FFT algorithm ($p = 2$) for scattering from a perfect conducting sphere

Frequency (MHz)	Unknowns	$\mathbf{Z}^{corr}$ (MB)	$\vec{\Pi}_A + \Pi_D$ (MB)	**G** (MB)
600	12,288	7.0	7.6	3.1
1,200	49,152	28.1	30.7	24.4
2,400	196,608	112.7	124.8	194.6
4,800	786,432	450.8	502.4	1547.7

Table 2: Memory requirement of the IE-FFT algorithm ($p = 3$) for scattering from a perfect conducting sphere

Frequency (MHz)	Unknowns	$\mathbf{Z}^{corr}$ (MB)	$\vec{\Pi}_A + \Pi_D$ (MB)	**G** (MB)
600	12,288	7.0	17.1	3.1
1,200	49,152	28.1	67.7	24.4
2,400	196,608	112.7	274.0	194.6
4,800	786,432	450.8	1088.7	1547.7

Having addressed the complexity of the algorithm, we shall now address the accuracy. For that reason, the bistatic echo area or scattering cross section (SCS) results of the IE-FFT algorithm for $p = 2$ are compared with those of the conventional MoM and Mie series solution in Fig. 5(a). To further quantify the error, the RMS error of the SCS is reported in each figure. The RMS error of SCS calculation is defined as

$$\eta = \sqrt{\frac{\int_0^{2\pi}\int_0^{\pi}\left|SCS_{IE-FFT}\left(\theta,\phi\right) - SCS_{Mie}\left(\theta,\phi\right)\right|^2 \sin\theta d\theta d\phi}{\int_0^{2\pi}\int_0^{\pi}\left|SCS_{Mie}\left(\theta,\phi\right)\right|^2 \sin\theta d\theta d\phi}} \quad (30)$$

where θ and ϕ are angles of the observation points, $SCS_{Mie}(\theta,\phi)$ is the SCS calculation by the Mie series, and $SCS_{IE-FFT}(\theta,\phi)$ is that of the IE-FFT algorithm. For MoM, the RMS error of SCS calculation relative to Mie series is computed as 6.2727e-04. The bistatic SCS solutions of MoM are very well matched to those of Mie series. For IE-FFT algorithm, the RMS error relative to MoM solutions is also computed and corresponds to 0.0443. The bistatic SCS is in very good agreement with that of MoM. The accuracy can be improved by increasing the order of the Lagrange polynomials or the sampling segments per wavelength, in the interpolation of the Green's function. Fig. 5(b) shows the improvement of the bistatic SCS calculations. By increasing the order of the Lagrange polynomials or the sampling segments, each RMS error has improved to 0.0165 and 0.0074, respectively. For the second-order and third-order Lagrange polynomials, 11 and 7 sampling segments per wavelength are used, respectively. To summarize these experiments, the RMS errors versus the size of sampling segments per wavelength are plotted in Fig. 6 for second-order and third order interpolation. Figure 7 compares the bistatic SCS from the IE-FFT algorithm ($p = 2,3$) with the result from Mie series at 2.4 GHz. It corresponds to 196,608 unknowns. The electrical size of the PEC sphere is 16λ . The memory of MoM and $\mathbf{\Pi}$ matrices, and the coefficients of Green's function are about 432 MB for second-order interpolation, and 661 MB for third-order interpolation. Both results agree very well with the solution of Mie series. As expected, the result from the third-order polynomials is more accurate. The RMS error of SCS is computed to be 0.0494 and 0.0160, respectively. In Fig.8, the bistatic SCS of the sphere with diameter 32λ is plotted. The number of IE-FFT unknowns is 786,432. The result of IE-FFT algorithm agrees well with those of Mie series. However, $p = 2$ answer oscillates around the exact values. The solution is improved by increasing the order of the polynomials, not by increasing the sampling segments. Due to $O\left(N^{1.5}\right)$ complexity, increasing the order of the polynomials is preferred in electrically large problems. The total memory required is about 2.5 and 3.1 GB for second and third order polynomials, respectively.

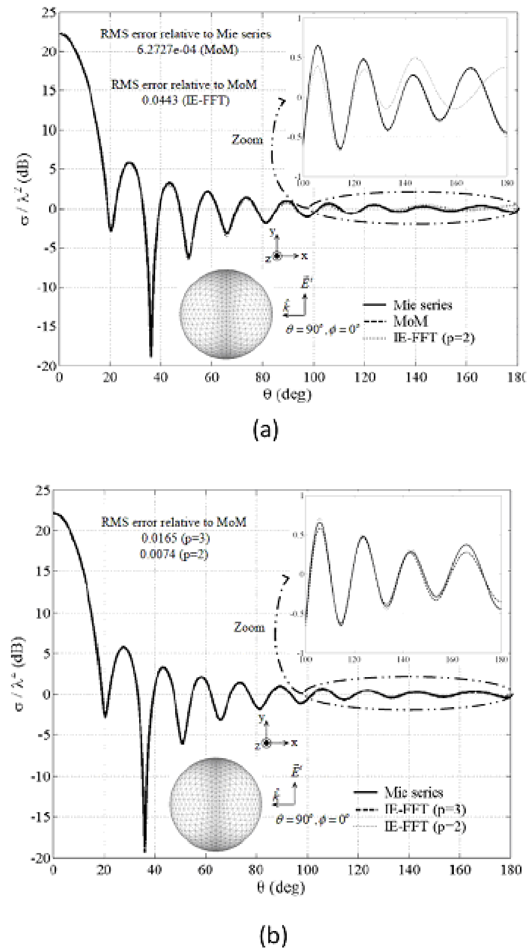

(a)

(b)

Fig. 5 Bistatic SCS for a PEC 4λ sphere. (a) IEFFT results, using p = 2 (d=λ/7); (b) using p = 2 (d=λ/7) and p = 3 (d=λ/7) with comparisons to conventional MoM and Mie series.

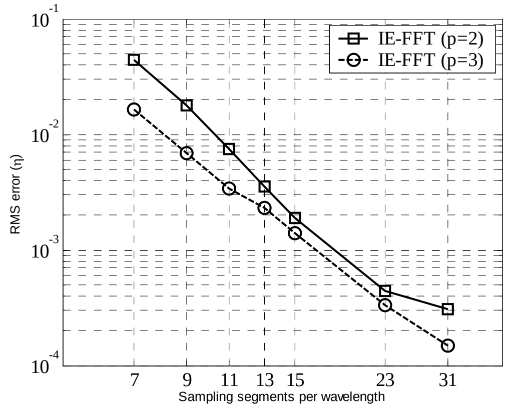

Fig. 6 The RMS error of bistatic SCS calculation versus sampling segments per wavelength. A 4λ PEC sphere is tested and the RMS error is relative to that of MoM solution. The second-order and third-order Lagrange polynomials are used.

B. Generic battleship

A realistic example considered here is a generic battleship. When the plane wave is incident from the nose direction, the bistatic SCS of $\theta\theta$ -polarization is computed by the IE-FFT algorithm and conventional MoM. Fig.9 shows the comparison between the bistatic SCS from the IE-FFT algorithm and the result of the conventional MoM at 30MHz. Both results agree very well.

In the next experiment, the frequency of operation is increased to 60MHz. The results of the IE-FFT algorithm are compared with those of ACA algorithm [9], as shown in Fig.10. The result of IE-FFT algorithm agrees well with that of ACA algorithms. Finally, the bistatic scattering of the battleship at the frequency of 240 MHz is considered in Fig. 11. In the IE-FFT computations N = 739,416 unknowns (corresponds to an average discretization size of $h = \lambda / 5$) are involved along with a third-order Green's function interpolation. The memory of MoM and Π matrices, and the coefficients of Green's function are about 4.3 GB. Two polar plots are also shown in Fig. 11. The left and right figures are plots in the azimuth and elevation planes, respectively. The bistatic SCS of $\phi\phi$-polarization is plotted in Fig. 12.

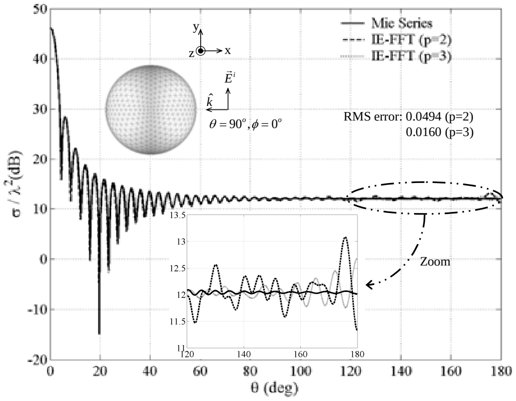

Fig. 7 Bistatic SCS for a PEC 16λ sphere. The results of the IE-FFT algorithm are compared with those of Mie series. It corresponds to 196,608 RWG unknowns.

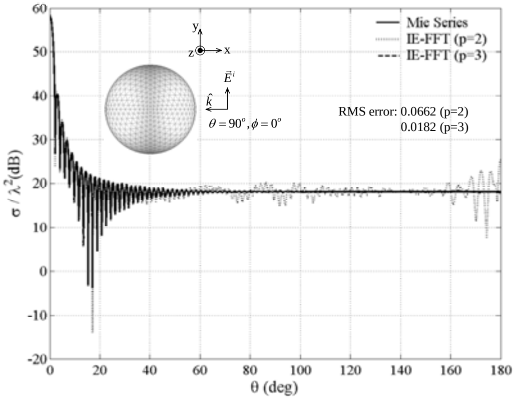

Fig. 8 Bistatic SCS for a PEC 32λ sphere. The results of the IE-FFT algorithm are compared with those of Mie series. It corresponds to 786,432 RWG unknowns.

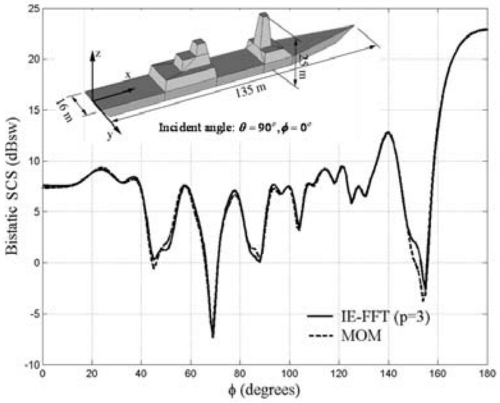

Fig. 9 Comparisons of the bistatic SCS for the battleship at 30 MHz ($\theta\theta$-polarization) using the IE-FFT and the conventional MoM.

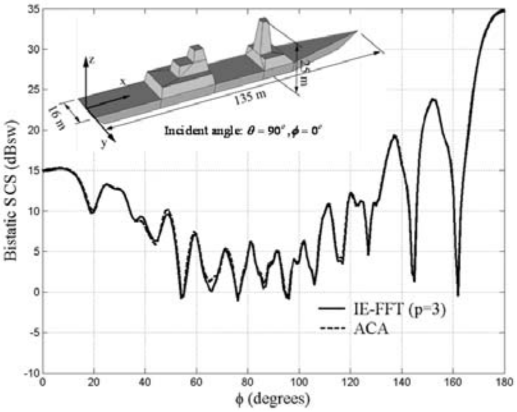

Fig. 10 Comparisons of the bistatic SCS for the battleship at 60 MHz ($\theta\theta$ -polarization) using the IE-FFT and the ACA algorithm [9].

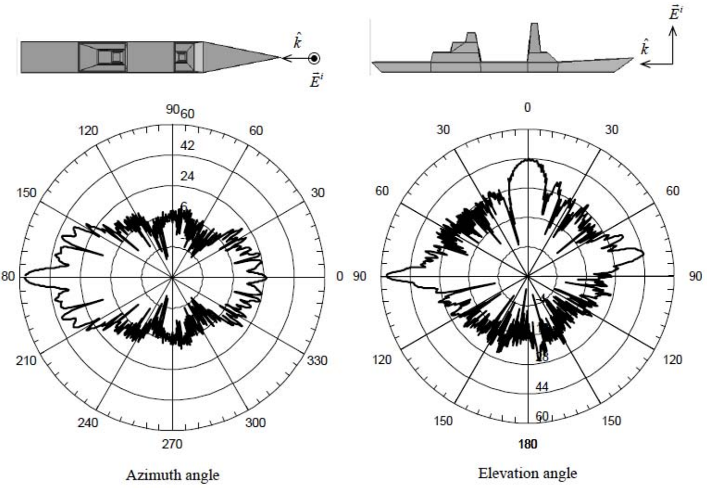

Fig. 11 The computed bistatic SCS of the battle ship at 240 MHz ($\theta\theta$ -polarization) using the IEFFT.

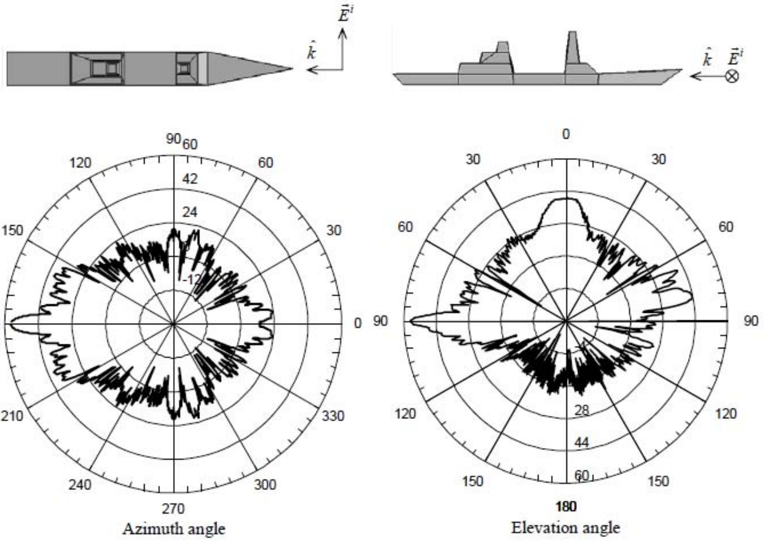

Fig. 12 The computed bistatic SCS of the battle ship at 240 MHz ($\phi\phi$ –polarization) using the IEFFT.

REFERENCES

[1] V. Rokhlin, "Rapid Solution of Integral Equations of Classical Potential Theory," *J. Comput. Phy.*, vol. 60, pp. 187-207, 1985.

[2] J. M. Song and W. C. Chew, "Multilevel Fast Multipole Algorithm for Solving Combined Field Integral Equation of Electromagnetic Scattering," *Mico. Opt. Tech. Lett.*, vol. 10, no. 1, pp. 14-19, Sep. 1995.

[3] R. Coifman, V. Rokhlin, and S. Wandzura, "The Fast Multipole Method for the Wave Equation: A Pedestrian Prescription," *IEEE Antennas Propagat. Mag.*, vol. 35, no. 3, pp. 7-12, Jun 1993.

[4] B. Dembart and E. Yip, "The Accuracy of Fast Multipole Methods for Maxwell's Equations," *IEEE Comput. Sci. Eng.*, vol. 5, no.3, 48-56, 1998.

[5] J. S. Zhao and W. C. Chew, "Three-dimensional Multilevel Fast Multipole Algorithm from Static to Electrodynamic," *Micro. Opt. Tech. Lett.*, vol. 26, no. 1, pp. 43-48, July 2000.

[6] S. Kapur and D. E. Long, "IES3: A Fast Integral Equation Solver for Efficient 3-Dimensional Extraction," *In 37th International Conference on Computer Aided Design*, Nov. 1997.

[7] S. M. Seo and J. F. Lee, "A Single-Level Low Rank IE-QR Algorithm for PEC Scattering Problems Using EFIE Formulation," *IEEE Trans. Antenna Propagat.*, vol. 52, no. 8, pp. 2141-2146, Aug. 2004.

[8] K. Zhao and J. F. Lee, "A Single-Level Dual Rank IE-QR Algorithm to Model Large Microstrip Antenna Arrays," *IEEE Trans. Antennas Propagat.*, vol. 52, no.10, pp. 2580-2585, Oct 2004.

[9] K. Zhao, M. N. Vouvakis, and J. F Lee, "Application of the Multilevel Adaptive Cross-Approximation on Ground Plane Designs," *IEEE EMC Symposium*, Santa Clara, CA, Aug. 9-13, 2004.

[10] S. Kurz, O. Rain, and S. Rjasanow, "The Adaptive Cross-Approximation Technique for the 3-D Boundary Element Method," *IEEE Tans. Magn.*, vol. 38, pp. 421-424, Mar. 2002.

[11] J. R. Phillips and J. K. White, "A Precorrected-FFT Method for Electrostatic Analysis of Complicated 3-D Structures," *IEEE Trans. Computed-Aided Design of Integrated Circuits and Systems*, vol. 16, pp. 1059-1072, 1997.

[12] J. R. Phillips, "Error and Complexity Analysis for A Collocation-Grid-Projection Plus Precorrected-FFT Algorithm for Solving Potential Integral Equations with Laplace or Helmholtz Kernels," in *Proc. 1995 Copper Mountain Conf. Multigrid Methods*, Apr. 1995.

[13] E. Bleszynski, M. Bleszynski, and T. Jaroszewicz, "AIM: Adaptive Integral Method for Solving Large-scale Electromagnetic Scattering and Radiation Problems," *Radio Science*, vol. 31, no. 5, pp. 1225-1251, 1996.

[14] C. F. Wang, F. Ling, J. M. Jin, "Adaptive Integral Solution of Combined Field Integral Equation," *Microwave Opt. Tech. Lett.*, vol. 19, no 5, pp. 321-328, Dec. 1998.

[15] O. P. Bruno and L. A. Kunyansky, "A Fast, High-Order Algorithm for the Solution of Surface Scattering Problems: Basic Implementation, Tests, and Applications," *J. Comput. Phy.*, 169, 80-110, 2001.

[16] S. Q. Li, Y. Yu, C. H. Chan, K. F. Chan, and L. Tsang, "A Sparse-Matrix/Canonical Grid Method for Analyzing Densely Packed Interconnects," *IEEE Trans. Micro. Theory Tech.*, vol. 49, no. 7, pp. 1221-1228, July 2001.

[17] S. Gedney, A. Zhu, W. H. Tang, G. Liu, and P. Petre, "A Fast, High-order Quadrature Sampled Pre-corrected Fast-Fourier Transform for Electromagnetic Scattering," *Microwave Opt. Tech. Lett.*, vol. 36, no. 5, Mar. 5 2003.

[18] B. J. Fasenfest, F. Capolino, D. R. Wilton, D. R. Jackson, and N. J. Champagne, "A Fast MoM Solution for Large Arrays: Green’s Function Interpolation with FFT," *IEEE Antennas Wireless Propagat. Lett.*, vol. 3, pp. 161-164, 2004.

[19] S. M. Rao, D. R. Wilton, and A. W. Glisson, "Electromagnetic Scattering by Surfaces of Arbitrary Shape," *IEEE Trans. Antennas Propagat.*, vol. AP-30, pp. 409-418, May 1982.

[20] M. N. Vouvakis, S.-C. Lee, K. Zhao, and J.-F. Lee, “A Symmetric FEM-IE Formulation with a Single-Level IE-QR Algorithm for Solving Electromagnetic Radiation and Scattering Problems,” *IEEE Trans. Antennas Propagat.*, vol. AP-52, pp. 409-418, Nov. 2004.

[21] P. J. Davis, *Interpolation & Approximation*, pp. 56, Dover publication, New York.

[22] W. C. Chew, “Computational Electromagnetics: The Physics of Smooth Versus Oscillatory Fields,” *Phil. Trans. R. Soc. Lond. A*, vol. 362, pp. 579-602, 2004.

Chao-Fu Wang received the B.Sc. degree in mathematics from the Henan Normal University, China, in 1985, the M.Sc. degree in applied mathematics from the Hunan University, China, in 1989, and the Ph.D. degree in electrical engineering from the University of Electronic Science and Technology of China in 1995. From 1987 to 1996, he was a Lecturer, and then an Associate Professor at the

Nanjing University of Science and Technology, China. From 1996 to 1999, he was a Postdoctoral Research Fellow in the Center for Computational Electromagnetics, University of Illinois at Urbana-Champaign. From 1999 to 2001, he was a Research Fellow in the Department of Electrical and Computer Engineering, National University of Singapore (NUS), Singapore. He was transferred to Temasek Laboratories at NUS as a Research Scientist in 2001, where he currently is a Senior Research Scientist and Head of Propagation & Scattering Group. His research interests include fast algorithms for computational electromagnetics, scattering and antenna analysis, ferrite components and their analysis, MMIC design and fast EM simulation.

Jin-Fa Lee received the B.S. degree from National Taiwan University, in 1982 and the M.S. and Ph.D. degrees from Carnegie-Mellon University in 1986 and 1989, respectively, all in electrical engineering. From 1988 to 1990, he was with ANSOFT Corp., where he developed several CAD/CAE finite element programs for modeling three-dimensional microwave and millimeter-wave circuits. From 1990 to 1991, he was a post-doctoral fellow at the University of Illinois at Urbana-Champaign. From 1991 to 2000, he was with Department of Electrical and Computer Engineering, Worcester Polytechnic Institute. Currently, he is a Professor at ElectroScience Lab., Dept. of Electrical Engineering, Ohio State University. Prof. Lee becomes an IEEE Fellow on year 2005. His students won the 4th place in student paper contest in IEEE APS/URSI 2004, 3rd place in IEEE APS/URSI 2005, and 1st place in EMC Zurich 2006, and were the two finalists in the APS/URSI 2006 student paper contest. Professor Lee’s research interests mainly focus on numerical methods and their applications to computational electromagnetics. Current research projects include: analyses of numerical methods, fast finite element methods, fast integral equation methods, three-dimensional mesh generation, domain decomposition methods, hybrid numerical methods and high frequency techniques based on domain decompositions approach, and RFID tag antenna designs, and large antenna arrays and Rotman lens.

The Discontinuous Galerkin Finite-Element Time-Domain Method Solution of Maxwell's Equations

Stephen D. Gedney [1], Chong Luo [1], J. Alan Roden [2], Robert D. Crawford [2], Bryan Guernsey [2], Jeffrey A. Miller [2], Tyler Kramer [2], and Eric W. Lucas [3]
[1] Department of Electrical and Computer Engineering
Univ. of Kentucky, Lexington, KY, 40506-0046 USA
gedney@engr.uky.edu, cluo01@engr.uky.edu

[2] The Aerospace Corporation,Chantilly, VA
JAlan.Roden@aero.org, Robert.D.Crawford@aero.org, Bryan.J.Guernsey@aero.org,
Jeffrey.A.Miller@aero.org, Tyler.C.Kramer@aero.org

[3] Alpha Omega Electromagnetics, LLC, Ellicott City, MD
alphaomega@maranatha.net

***Abstract*—** A Discontinuous Finite-Element Time-Domain method is presented that is based on a high-order finite element discretization of Maxwell's curl equations. The problem domain is decomposed into non-overlapping subdomains that couple through boundary integral terms. Within each subdomain, the tangential electric and magnetic fields are discretized via high-order curl conforming basis functions, leading to a high-order representation of the volume fields. For unbounded problems, a perfectly matched layer absorbing medium is used. The discrete equations are presented in a symmetric form. The method leads to an explicit time-dependent solution of Maxwell's equations that is high-order convergent.

***Index Terms*—** Discontinuous Galerkin Method, Finite-Element Time-Domain.

I. INTRODUCTION

Discontinuous Galerkin Time-Domain methods are a class of finite element methods that employ piecewise continuous basis and testing functions. The methods are characterized as being high-order accurate, able to model complex geometries, efficient, stable, and highly parallel [1]. Discontinuous Galerkin Time-Domain (DGTD) methods have more recently been employed for the solution of Maxwell's equations [2-8]. DGTD methods are typically based on a point-based discretization by sampling at Gauss-Lobatto Quadrature points. The fields are interpolated by a polynomial expansion over each cell, which are then projected onto the quadrature points [1, 4]. One can thus draw an analog between DGTD methods and point-based Nyström discretizations used for integral equation solutions [9, 10]. DGTD methods have proven to be highly accurate, providing exponential convergence and have provided an excellent solution method for large scale electromagnetic simulations. [2-8].

It is noted that the vector fields of DGTD methods are projected onto a polynomial complete function space. A concern arises that near discontinuities or geometric singularities spurious charges can corrupt the solution. Thus, penalty methods have been recommended to weakly enforce the divergence preserving properties of the fields [11]. Furthermore, for late-time stability, upwind flux methods have also been recommended [4, 5].

In this paper, a Discontinuous Galerkin method based on a finite-element discretization is presented. This method, which is referred to as the Discontinuous Galerkin Finite-Element Time-Domain (DGFETD) method, is based on a finite-element discretization of Maxwell's curl equations [12]. Rather than a point-based sampling, both the electric and magnetic fields are expanded via hierarchical Nedelec curl-conforming mixed-order basis functions [13, 14]. Similar to the DGTD method, tangential field continuity is weakly constrained across shared boundaries. Due to the properties of curl-conforming vector basis functions, only basis functions associated with

1054-4887 © 2009 ACES

topologies on a domain boundary (i.e., edges and faces) have a non-zero tangential projection. Thus, only local basis functions are shared across domain boundaries. This is similar to DGTD methods. The use of curl-conforming basis functions that satisfy Nedelec's criterion also avoids the concern of spurious solutions [15]. Hence, the formulation avoids the need for penalty methods [16]. Furthermore, the method does not require upwind flux terms for stability. The use of hierarchal curl-conforming basis functions allows for local *hp*-refinement of the discretization. Another advantage of the DGFETD formulation is that sub-domains are not restricted to single cells. Rather, an arbitrary partitioning of the domain can be employed.

Other finite-element time-domain discretizations of Maxwell's curl equations have been proposed [17-20]. The majority of these methods provide a reciprocal discretization based on a curl-conforming basis function representation for the electric field intensity, and a divergence conforming basis function representation of the magnetic flux density (or the dual H-D formulation). Time domain integration is typically performed using Symplectic time-integration methods. In contrast, the proposed DGFETD scheme expands both the electric and magnetic field intensities using high-order curl-conforming basis functions. Also, high-order Runge-Kutta time-integration methods are employed. The proposed DGFETD method thus provides an explicit solution scheme that is high-order in both space and time leading to exponential convergence

A salient feature of the proposed DGFETD formulation is that a PML termination is naturally represented. The perfectly matched quality of a PML medium is based on a dual behavior of the electric and magnetic properties of the material media. This is ideally represented by the proposed formulation, which has dual function space representations for the field intensities, and the flux densities. The time-integration scheme also assumes that the electric and magnetic fields are co-located in time. As a consequence, it is found that the PML implementation within the DGFETD scheme provides upwards to 5 digits of accuracy with only a 2 cell thick PML that has a constant material profile. In this paper, the DGFETD formulation and discretization are presented in Sections II – IV. The implementation of a perfectly matched layer absorbing medium for simulating unbounded domains is presented in Section V. A number of numerical simulations based on the DGFETD scheme are presented in Section VI. Through these examples, the exponential convergence of the DGFETD method is demonstrated, and the performance of the PML is validated.

II. THEORY

Consider the electromagnetic fields that are radiated by electric or magnetic current densities in a domain Ω bound by $\partial\Omega$. The fields must satisfy Maxwell's curl equations:

$$\nabla \times \vec{E} = -\frac{\partial}{\partial t}\bar{\bar{\mu}}\cdot\vec{H} - \bar{\bar{\sigma}}^{*}\cdot\vec{H} - \vec{M} \ , \qquad (1)$$

$$\nabla \times \vec{H} = \frac{\partial}{\partial t}\bar{\bar{\varepsilon}}\cdot\vec{E} + \bar{\bar{\sigma}}\cdot\vec{E} + \vec{J} \ , \qquad (2)$$

where, $\bar{\bar{\mu}}$, $\bar{\bar{\varepsilon}}$, $\bar{\bar{\sigma}}^{*}$, and $\bar{\bar{\sigma}}$ are permeability, permittivity, and conductivity tensors, and $\vec{J}$ and $\vec{M}$ are impressed current densities.

The domain Ω is subdivided into non-overlapping and contiguous subdomains. The i^{th} subdomain is defined by the volume V_i and bound by ∂V_i. Each subdomain is then discretized with fitted polyhedra, or finite elements. The field intensities are expanded within each finite element using suitable vector basis functions weighted by time-dependent coefficients. A set of testing functions that span the same function space as the basis functions is also introduced. The inner product of the coupled curl equations with a set of test functions is performed:

$$\int_{V_i}\vec{T}^{h}\cdot\left[\frac{\partial}{\partial t}\bar{\bar{\mu}}\cdot\vec{H} + \bar{\bar{\sigma}}^{*}\cdot\vec{H} + \vec{M} + \nabla\times\vec{E}\right]dv = 0 \ , \qquad (3)$$

$$\int_{V_i}\vec{T}^{e}\cdot\left[\frac{\partial}{\partial t}\bar{\bar{\varepsilon}}\cdot\vec{E} + \bar{\bar{\sigma}}\cdot\vec{E} + \vec{J} - \nabla\times\vec{H}\right]dv = 0 \ , \qquad (4)$$

where $\vec{T}^{h}$ and $\vec{T}^{e}$ are testing functions that span the $\vec{H}$ and $\vec{E}$-field function spaces, respectively. After applying a vector identity, the curl term in (3) can be written as:

$$\int_{V_i}\vec{T}^{h}\cdot\nabla\times\vec{E}dv = \int_{V_i}\vec{E}\cdot\nabla\times\vec{T}^{h}dv + \oint_{\partial V_i}\vec{T}^{h}\cdot\left(\hat{n}\times\vec{E}\right)ds \ , \qquad (5)$$

where $\hat{n}$ is the outward normal of ∂V_i. It is assumed that the tangential field $\hat{n}\times\vec{E}$ on ∂V_i is the field just interior to V. Let $\hat{n}\times\vec{E}^{+}$ represent the tangential field on ∂V_i just exterior to V_i. The exterior field is typically the field of a neighboring subdomain. For generality, assume there is an impressed magnetic surface current density on ∂V_i. Consequently, the tangential electric fields must satisfy the relationship:

$$\hat{n}\times\left(\vec{E}-\vec{E}^{+}\right)\Big|_{\partial V_i} = -\vec{M}_s \ , \qquad (6)$$

where, $\hat{n}$ is to be the outward normal to V_i. This boundary condition can be rewritten as:

$$2\hat{n}\times\vec{E}\Big|_{\partial V_i} = \left(\hat{n}\times\vec{E}^{+} + \hat{n}\times\vec{E}\right)\Big|_{\partial V_i} - \vec{M}_s\,, \qquad (7)$$

or, $$\hat{n}\times\vec{E}\Big|_{\partial V_i} = \frac{1}{2}\left(\hat{n}\times\vec{E} + \hat{n}\times\vec{E}^{+}\right)\Big|_{\partial V_i} - \frac{1}{2}\vec{M}_s\,, \qquad (8)$$

which is equivalent to averaging the tangential fields. Substituting this into (5) leads to:

$$\begin{aligned}&\int_{V_i}\vec{T}^h\cdot\nabla\times\vec{E}dv = \int_{V_i}\vec{E}\cdot\nabla\times\vec{T}^h dv + \\ &\frac{1}{2}\oint_{\partial V_i}\vec{T}^h\cdot\left(\hat{n}\times\vec{E}+\hat{n}\times\vec{E}^{+}\right)ds - \frac{1}{2}\oint_{\partial V_i}\vec{T}^h\cdot\vec{M}_s ds\end{aligned}\,. \qquad (9)$$

Next, from (5)

$$\begin{aligned}\frac{1}{2}\oint_{\partial V_i}\vec{T}^h\cdot\hat{n}\times\vec{E}ds = \frac{1}{2}\int_{V_i}\vec{T}^h\cdot\nabla\times\vec{E}dv \\ -\frac{1}{2}\int_{V_i}\vec{E}\cdot\nabla\times\vec{T}^h dv\end{aligned}\,. \qquad (10)$$

This is combined with (9), leading to:

$$\begin{aligned}\int_{V_i}\vec{T}^h\cdot\nabla\times\vec{E}dv = \frac{1}{2}\int_{V_i}\vec{T}^h\cdot\nabla\times\vec{E}dv + \frac{1}{2}\int_{V_i}\vec{E}\cdot\nabla\times\vec{T}^h dv \\ +\frac{1}{2}\oint_{\partial V_i}\vec{T}\cdot\hat{n}\times\vec{E}^{+}ds - \frac{1}{2}\oint_{\partial V_i}\vec{T}^h\cdot\vec{M}_s ds\end{aligned}\,. \qquad (11)$$

Finally, applying (11) within (3) leads to the operator:

$$\begin{aligned}&\int_{V_i}\left[\begin{array}{l}\frac{\partial}{\partial t}\vec{T}^h\cdot\bar{\bar{\mu}}\cdot\vec{H} + \vec{T}^h\cdot\bar{\bar{\sigma}}^{*}\cdot\vec{H} + \vec{T}^h\cdot\vec{M}_V \\ +\frac{1}{2}\vec{T}^h\cdot\nabla\times\vec{E} + \frac{1}{2}\vec{E}\cdot\nabla\times\vec{T}^h\end{array}\right]dv \\ &= -\frac{1}{2}\oint_{\partial V_i}\vec{T}^h\cdot\hat{n}\times\vec{E}^{+}ds + \frac{1}{2}\oint_{\partial V_i}\vec{T}^h\cdot\vec{M}_s ds\end{aligned}\,. \qquad (12)$$

By duality, (4) can also be written as:

$$\begin{aligned}&\int_{V_i}\left[\begin{array}{l}\frac{\partial}{\partial t}\vec{T}^e\cdot\bar{\bar{\varepsilon}}\cdot\vec{E} + \vec{T}^e\cdot\bar{\bar{\sigma}}\cdot\vec{E} + \vec{T}^e\cdot\vec{J}_V \\ -\frac{1}{2}\vec{T}^e\cdot\nabla\times\vec{H} - \frac{1}{2}\vec{H}\cdot\nabla\times\vec{T}^e\end{array}\right]dv \\ &= \frac{1}{2}\oint_{\partial V_i}\vec{T}^e\cdot\hat{n}\times\vec{H}^{+}ds + \frac{1}{2}\oint_{\partial V_i}\vec{T}^e\cdot\vec{J}_s ds\end{aligned}\,, \qquad (13)$$

where, $\vec{J}_s$ is an impressed surface current density, and $\vec{H}^{+}$ is the magnetic field exterior to V_i on ∂V_i.

Equations (12) and (13) represent the weak form of Maxwell's curl equations that will be applied within each sub-domain. The fields $\vec{E}$ and $\vec{H}$ are associated uniquely with subdomain V_i. Each subdomain is coupled with neighboring sub-domains, or an exterior region, through the boundary integral terms. It is noted that the surface current densities are zero unless an impressed current density is placed on the boundary. Hence, the boundary integral terms weakly constrain the continuity of the tangential fields across source-free sub-domain boundaries.

III. DISCRETIZATION

Each subdomain is discretized with a fitted polyhedral mesh, which can be hexahedron, tetrahedron, or prisms. Within each sub-domain, the field intensities $\vec{E}$ and $\vec{H}$ are expanded into a set of hierarchical H_p-curl conforming basis functions, such as those proposed in [13, 14]:

$$\vec{E} \approx \sum_{i=1}^{N_p} e_i(t)\,\vec{f}_i(\vec{r}), \quad \vec{H} \approx \sum_{i=1}^{N_p} h_i(t)\,\vec{f}_i(\vec{r}), \qquad (14)$$

where, $e_i(t)$ and $h_i(t)$ are unknown time-dependent coefficients weighting each basis functions. The test functions span an identical function space as the basis functions, leading to a Galerkin formulation. This leads to a set of coupled difference equations derived from (12) and (13) expressed as:

$$\mathbf{M}_{\mu}^{\mathbf{h,h}}\frac{\partial}{\partial t}\mathbf{h} + \mathbf{M}_{\sigma^*}^{\mathbf{h,h}}\mathbf{h} + \mathbf{S}^{\mathbf{h,e}}\,\mathbf{e} = -\mathbf{T}_M^{\mathbf{h}} - \mathbf{F}_E^{\mathbf{h,e}^{+}}\mathbf{e}^{+}\,, \qquad (15)$$

$$\mathbf{M}_{\varepsilon}^{\mathbf{e,e}}\frac{\partial}{\partial t}\mathbf{e} + \mathbf{M}_{\sigma}^{\mathbf{e,e}}\mathbf{e} - \mathbf{S}^{\mathbf{e,h}}\,\mathbf{h} = -\mathbf{T}_J^{\mathbf{e}} + \mathbf{F}_H^{\mathbf{e,h}^{+}}\mathbf{h}^{+}\,, \qquad (16)$$

where, the superscript **x,y** implies the **x**-field test function and **y**-field basis function, and **h** and **e** are the vectors of time-dependent coefficients $h_i(t)$ and $e_i(t)$. The vectors $\mathbf{h}^{+}$ and $\mathbf{e}^{+}$ are the coefficient vectors associated with exterior tangential fields from a coupled region. The matrix entries are computed as:

$$\left[\mathbf{M}_{\nu}\right]_{j,i} = \int_{V_i}\vec{f}_j\cdot\bar{\bar{\nu}}\cdot\vec{f}_i dv, \qquad (17)$$

$$\left[\mathbf{S}\right]_{j,i} = \frac{1}{2}\int_{V_i}\left(\vec{f}_j\cdot\nabla\times\vec{f}_i + \vec{f}_i\cdot\nabla\times\vec{f}_j\right)dv, \qquad (18)$$

$$\left[\mathbf{F}_{E/H}^{+}\right]_{j,k} = \frac{1}{2}\oint_{\partial V_i}\vec{f}_j\cdot\hat{n}_i\times\vec{f}_k^{+}ds, \qquad (19)$$

$$\left[\mathbf{T}_J\right]_j = \int_{V_i}\vec{f}_j\cdot\vec{J}_V dv, \text{ or } \left[\mathbf{T}_J\right]_j = -\frac{1}{2}\oint_{\partial V_i}\vec{f}_j\cdot\vec{J}_s ds\,, \qquad (20)$$

where, $\vec{f}_i$ and $\vec{f}_j$ are the basis and testing functions, respectively, for the appropriate e-field or h-field, and $\bar{\bar{\nu}} = \bar{\bar{\mu}}, \bar{\bar{\varepsilon}}$, or $\bar{\bar{\sigma}}$. The **S** matrices have the property $\mathbf{S}^{\mathbf{h,e}} = \mathbf{S}^{\mathbf{e,h}^{T}}$. The matrices **M** are symmetric for isotropic media, and for rotationally symmetric anisotropic media.

The "face" matrices $\mathbf{F}_E^{\mathbf{h,e}^{+}}$ or $\mathbf{F}_H^{\mathbf{e,h}^{+}}$ represent the coupling to the neighboring sub-domains. The operator involves only the tangential projections of the interior and exterior fields. Thus, when using curl-conforming basis functions, only the basis functions associated with the boundary topology (e.g., function spaces associated with faces and edges on ∂V_i) with overlapping support, contribute to these matrices. Consequently, the matrices are highly sparse. If the topology of the mesh on either side of ∂V_i are aligned (that is the faces and edges between the two sub-domains are shared), then $\mathbf{F}_E^{\mathbf{h},\mathbf{e}^+} = -\mathbf{F}_H^{\mathbf{e},\mathbf{h}^{+T}}$. In general, the meshes need not align, and only the overlapping support of the vector basis functions on ∂V_i contribute to the face matrices.

The coupled equations in (15) and (16) are combined into a single difference equation as:

$$\dot{\mathbf{x}} = \mathbf{A}\mathbf{x} + \mathbf{B}\mathbf{x}^+ + \mathbf{t}\,, \tag{21}$$

where

$$\mathbf{x} = \begin{pmatrix} \mathbf{h} \\ \mathbf{e} \end{pmatrix}, \quad \mathbf{x}^+ = \begin{pmatrix} \mathbf{h}^+ \\ \mathbf{e}^+ \end{pmatrix}, \tag{22}$$

$$\mathbf{A} = \begin{pmatrix} -\mathbf{M}_\mu^{\mathbf{h},\mathbf{h}^{-1}} \mathbf{M}_{\sigma^*}^{\mathbf{h},\mathbf{h}} & -\mathbf{M}_\mu^{\mathbf{h},\mathbf{h}^{-1}} \mathbf{S}^{\mathbf{h},\mathbf{e}} \\ \mathbf{M}_\varepsilon^{\mathbf{e},\mathbf{e}^{-1}} \mathbf{S}^{\mathbf{e},\mathbf{h}} & -\mathbf{M}_\varepsilon^{\mathbf{e},\mathbf{e}^{-1}} \mathbf{M}_\sigma^{\mathbf{e},\mathbf{e}} \end{pmatrix}, \tag{23}$$

$$\mathbf{B} = \begin{pmatrix} 0 & -\mathbf{M}_\mu^{\mathbf{h},\mathbf{h}^{-1}} \mathbf{F}_E^{\mathbf{h},\mathbf{e}^+} \\ \mathbf{M}_\varepsilon^{\mathbf{e},\mathbf{e}^{-1}} \mathbf{F}_H^{\mathbf{e},\mathbf{h}^+} & 0 \end{pmatrix}, \tag{24}$$

$$\mathbf{t} = \begin{pmatrix} -\mathbf{M}_\mu^{\mathbf{h},\mathbf{h}^{-1}} \mathbf{T}_M^{\mathbf{h}} \\ -\mathbf{M}_\varepsilon^{\mathbf{e},\mathbf{e}^{-1}} \mathbf{T}_J^{\mathbf{e}} \end{pmatrix}. \tag{25}$$

The local difference equation (21), represents the first-order coupled differential equation for the fields in each sub-domain. The difference operators in all sub-domains are then solved simultaneously using a high-order Runge-Kutta (RK) scheme [2], [21]. It is noted that the local difference operator is implicit. That is, it involves the inversion of the matrix **M.** However, this local linear system is generally quite small, and this can be efficiently performed using an LU-factorization. The global linear system of equations, which consists of the combination of all the local linear systems, is thus an explicit formulation. The global system is conditionally stable. To date, an analytical study of the stability criterion has not been completed. However, via a heuristic analysis, a general stability criterion has been determined, which is expressed as:

$$c_o \Delta t \le \min \begin{cases} \left(\dfrac{h}{2} \sqrt{\varepsilon_r \mu_r} \, \dfrac{1}{(p+1)^2} \right), \text{hexahedron} \\ \left(\dfrac{h}{4} \sqrt{\varepsilon_r \mu_r} \, \dfrac{1}{(p+1)^2} \right), \text{tetrahedron} \end{cases} \tag{26}$$

where, h is the edge length, and p is the order of the H_p curl conforming basis (e.g, H_0 basis are the classic Whitney curl-conforming vector basis functions). Consequently, the stability criterion is based on the minimum edge length in the mesh. It is noted that through experimentation, this stability limit has been dependable, even for elements with very poor aspect ratios, and very small Jacobians.

IV. BOUNDARY CONDITIONS

On perfectly electrical conducting boundaries (PEC), the tangential electric field is presumed to be zero. Consequently, the curl-conforming basis associated with all edges and faces on a PEC surface are constrained to be zero. Similarly, $\vec{E}^+$ and $\vec{M}_s$ = 0 on the PEC boundary. Since $\vec{T}^e$ spans the same space as the electric field, the test functions on the PEC surface are also constrained to be zero. Thus, the right-hand-side of (13) also has null contribution on a PEC surface. Note that if the conductor is infinitesimally thin, distinct meshes on either side of the conductor must be assumed, so that the magnetic field on either side of the conductor is distinct. If the sub-domains boundaries are defined on the thin PEC surface, this is implicitly constrained by the DGFETD formulation.

A dual formulation is used to constrain the function space on the surface of a perfectly magnetic conductor (PMC) boundary. An impressed surface current density can also be placed on an exterior or an interior boundary. Surface currents couple directly into the sub-domains through the boundary terms in (12) and (13). The current density can be on the exterior boundary $\partial\Omega$, such as demanded by a hybrid modal/FEM or Boundary Element/FEM formulation. In this case, the exterior tangential fields $\hat{n} \times \vec{E}^+$ and $\hat{n} \times \vec{H}^+$ are assumed to be zero, since they are effectively represented by the current densities.

The surface current density can also lie within Ω on a sub-domain boundary ∂V_i. In this case, $\hat{n} \times \vec{E}^+$ and $\hat{n} \times \vec{H}^+$ would represent the exterior fields of the neighboring subdomain, and $\vec{M}_s$ and $\vec{J}_s$ the impressed current densities. It is noted that the step discontinuity in the fields are naturally represented by the DGFETD formulation.

An alternative source is a discrete lumped source model, such as a voltage source, current source, or discrete circuit mode (with internal impedance). To describe the implementation of such sources, we will begin with the simplest case, which is a discrete voltage source, as illustrated in Fig. 1. The source is applied across a gap in a conductor path as represented by the shaded region on the left figure in Fig. 1. The gap has a length g along the unit axial vector of the gap, $\hat{g}$. If the gap is small relative to a wavelength, then the electric field in the gap can assumed to be constant, and is expressed as:

$$\vec{E}_g^{tot}(t) = \hat{g}\frac{V_s(t)}{g}\delta(g), \tag{27}$$

where, $V_s(t)$ is the time-dependent voltage. This can be incorporated into the finite element method by assuming that source gap field located on an edge of the mesh perpendicular to the gap axis. Then, from (12)

$$\begin{aligned} &\int_{V_i}\left[\frac{\partial}{\partial t}\vec{T}^h\cdot\bar{\bar{\mu}}\cdot\vec{H}+\vec{T}^h\cdot\vec{M}_V\right]dv + \\ &\int_{V_i}\left[\frac{1}{2}\vec{T}^h\cdot\nabla\times\vec{E}+\frac{1}{2}\vec{E}\cdot\nabla\times\vec{T}^h\right]dv, \\ &= -\frac{1}{2}\oint_{\partial V_i}\vec{T}^h\cdot\hat{n}\times\vec{E}_g^{tot}ds \end{aligned} \tag{28}$$

where, $\hat{n}$ is the unit normal directed out of V_i. (Note, the conductivity is assumed to be zero for simplicity). The surface integral is thus non-zero when tested with the edge basis $\vec{T}^h$ associated with the gap edge. It is further noted, that on the conductor, $\hat{n}\times\vec{E}$ and $\hat{n}\times\vec{T}^e = 0$.

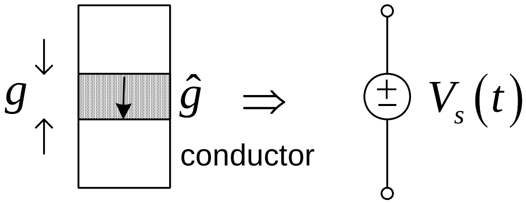

Fig. 1. Discrete voltage source model.

V. PML ABSORBING MEDIA

When simulating unbounded media, the FETD domain must be truncated and an exterior radiation boundary condition must be introduced on the truncation boundary. A number of approximate local absorbing boundary conditions could be employed [22]. However, such boundary conditions have limited accuracy, and require that the truncation boundary be placed a non-trivial distance from the device under test. Absorbing material layers have also been proposed to truncate the problem domain. The most accurate is the perfectly matched layer (PML) [23]. A number of PML formulations have been proposed for the DGTD method, including the anisotropic PML formulation[6, 8, 24], and a non-linear PML formulation [25]. In this paper, a PML formulation based on the stretched-coordinate formulation is presented [26, 27].

It is assumed that the extremity of the mesh is terminated by a PML media with Cartesian boundaries. Within the PML media, Maxwell's equations are expressed in a stretched coordinate form [26, 27]. The x-projections of Maxwell's equations in the frequency domain are then expressed as (note, a lossless anisotropic media is assumed for simplicity):

$$-j\omega\mu H_x = \frac{1}{s_y}\frac{\partial}{\partial y}E_z - \frac{1}{s_z}\frac{\partial}{\partial z}E_y, \tag{29}$$

$$j\omega\varepsilon\vec{E} = \frac{1}{s_y}\frac{\partial}{\partial y}H_z - \frac{1}{s_z}\frac{\partial}{\partial z}H_y, \tag{30}$$

where s_k ($k = x, y, z$) are the stretched coordinate metric coefficients [26]. The classical choice for the stretched coordinate coefficients is [28]:

$$s_k = \kappa_k + \frac{\sigma_k}{j\omega\varepsilon_o}, \quad k = x, y, z, \tag{31}$$

where κ_k and σ_k are assumed to be positive real, and can be one-dimensional functions along the k-direction. Starting with (29), both sides of the equation are multiplied by $s_y s_z$, leading to:

$$-j\omega\mu s_y s_z H_x = s_z\frac{\partial}{\partial y}E_z - s_y\frac{\partial}{\partial z}E_y. \tag{32}$$

Since, s_z and s_y are functions of z and y only, respectively, this can be re-written as:

$$-j\omega s_y s_z \mu H_x = \frac{\partial}{\partial y}s_z E_z - \frac{\partial}{\partial z}s_y E_y. \tag{33}$$

Defining the metric coefficients as in (31) leads to:

$$\begin{aligned} &-j\omega\left(\kappa_y+\frac{\sigma_y}{j\omega\varepsilon_o}\right)\left(\kappa_z+\frac{\sigma_z}{j\omega\varepsilon_o}\right)\mu H_x = \\ &\frac{\partial}{\partial y}\left(\kappa_z+\frac{\sigma_z}{j\omega\varepsilon_o}\right)E_z - \frac{\partial}{\partial z}\left(\kappa_y+\frac{\sigma_y}{j\omega\varepsilon_o}\right)E_y \end{aligned}. \tag{34}$$

Next, the variable substitutions are made:

$$P_k^h = \frac{H_k}{j\omega}, \quad P_k^e = \frac{E_k}{j\omega}, \quad (k = x, y, z). \tag{35}$$

This substitution is applied to (34), leading to:

$$\begin{aligned} &-\left(j\omega\kappa_y\kappa_z + \frac{(\sigma_y\kappa_z+\sigma_z\kappa_y)}{\varepsilon_o}\right)\mu H_x - \frac{\sigma_y\sigma_z}{\varepsilon_o^2}\mu P_x^h \\ &= \frac{\partial}{\partial y}\left(\kappa_z E_z + \frac{\sigma_z}{\varepsilon_o}P_z^e\right) - \frac{\partial}{\partial z}\left(\kappa_y E_y + \frac{\sigma_y}{\varepsilon_o}P_y^e\right) \end{aligned}. \tag{36}$$

A second variable substitution is made:

$$\begin{aligned}\tilde{H}_k &= \kappa_k H_k + \frac{\sigma_k}{\varepsilon_o} P_k^h, \\ \tilde{E}_k &= \kappa_k E_k + \frac{\sigma_k}{\varepsilon_o} P_k^e,\ \left(k = x, y, z\right)\end{aligned}. \quad (37)$$

This is substituted into (36), leading to:

$$-\mu \frac{1}{\kappa_x}\left(\begin{array}{l} j\omega\kappa_y\kappa_z\tilde{H}_x + \dfrac{\left(\sigma_y\kappa_z + \sigma_z\kappa_y\right)}{\varepsilon_o}\tilde{H}_x \\ -j\omega\kappa_y\kappa_z\dfrac{\sigma_x}{\varepsilon_o}P_x - \dfrac{\left(\sigma_y\kappa_z + \sigma_z\kappa_y\right)}{\varepsilon_o}\dfrac{\sigma_x}{\varepsilon_o}P_x \end{array}\right). \quad (38)$$
$$-\frac{\sigma_y\sigma_z}{\varepsilon_o^2}\mu P_x^h = \frac{\partial}{\partial y}\tilde{E}_z - \frac{\partial}{\partial z}\tilde{E}_y$$

From (35) and (37), it is further seen that:

$$j\omega P_x^h = H_x = \frac{1}{\kappa_x}\tilde{H}_x - \frac{1}{\kappa_x}\frac{\sigma_x}{\varepsilon_o}P_x . \quad (39)$$

Applying this to (38), leads to:

$$\begin{aligned}&-\left(j\omega\frac{\kappa_y\kappa_z}{\kappa_x} + \frac{\left(\sigma_y\kappa_z + \sigma_z\kappa_y\right)}{\kappa_x\varepsilon_o} - \frac{\kappa_y\kappa_z}{\kappa_x^2}\frac{\sigma_x}{\varepsilon_o}\right)\mu\tilde{H}_x \\ &-\left(\frac{\kappa_y\kappa_z}{\kappa_x^2}\frac{\sigma_x^2}{\varepsilon_o^2} + \frac{\sigma_y\sigma_z}{\varepsilon_o^2} - \frac{\sigma_x\left(\sigma_y\kappa_z + \sigma_z\kappa_y\right)}{\kappa_x\varepsilon_o^2}\right)\mu P_x \quad .(40) \\ &= \frac{\partial}{\partial y}\tilde{E}_z - \frac{\partial}{\partial z}\tilde{E}_y .\end{aligned}$$

The expression in (40) can be written in the time-domain, and then generalized to all projections of Faraday's law as:

$$-\frac{\partial}{\partial t}\overline{\overline{a}}\cdot\mu\vec{\tilde{H}} - \overline{\overline{b}}\cdot\mu\vec{\tilde{H}} - \overline{\overline{c}}\cdot\mu\vec{P}^h = \nabla\times\vec{\tilde{E}} , \quad (41)$$

where, from (39)

$$\frac{\partial}{\partial t}\vec{P}^h = \overline{\overline{\kappa}}^{-1}\cdot\vec{\tilde{H}} - \overline{\overline{d}}\cdot\vec{P}^h . \quad (42)$$

The tensors $\overline{\overline{a}}, \overline{\overline{b}}, \overline{\overline{c}}, \overline{\overline{d}}$, and $\overline{\overline{\kappa}}$ are all diagonal tensors, defined by:

$$\begin{aligned} a_{xx} &= \frac{\kappa_y\kappa_z}{\kappa_x}, \\ b_{xx} &= \frac{1}{\kappa_x\varepsilon_o}\left(\sigma_y\kappa_z + \sigma_z\kappa_y - a_{xx}\sigma_x\right), \\ c_{xx} &= \frac{\sigma_y\sigma_z}{\varepsilon_o^2} - b_{xx}\frac{\sigma_x}{\varepsilon_o}, \\ d_{xx} &= \frac{\sigma_x}{\kappa_x\varepsilon_o}, \quad \kappa_{xx} = \kappa_x . \end{aligned} \quad (43)$$

The remaining diagonal terms of the tensors are derived via a permutation of the subscripts ($x \to y, y \to z, z \to x$).

A similar analogy is followed for Ampere's law, leading to the dual form:

$$+\frac{\partial}{\partial t}\varepsilon\overline{\overline{a}}\cdot\vec{\tilde{E}} + \varepsilon\overline{\overline{b}}\cdot\vec{\tilde{E}} + \varepsilon\overline{\overline{c}}\cdot\vec{P}^e = \nabla\times\vec{\tilde{H}} , \quad (44)$$

where, from (39)

$$\frac{\partial}{\partial t}\vec{P}^e = \overline{\overline{\kappa}}^{-1}\cdot\vec{\tilde{E}} - \overline{\overline{d}}\cdot\vec{P}^e . \quad (45)$$

In summary, the pertinent PML equations governing the fields in the PM region are given by (41), (42), (44), and (45). The unknowns in this region are thus $\vec{\tilde{E}}$, $\vec{\tilde{H}}$, $\vec{P}^e$, and $\vec{P}^h$.

It is observed that outside the PML region, $\overline{\overline{\kappa}} = \overline{\overline{a}} = \overline{\overline{I}}$, the unit dyad, and $\overline{\overline{b}} = \overline{\overline{c}} = \overline{\overline{d}} = 0$. Thus, outside the PML region $\vec{\tilde{H}} = \vec{H}$ and $\vec{\tilde{E}} = \vec{E}$, (41) and (44) reduce to the classical Maxwell curl equations, and (42) and (45) are not needed. Thus, $\vec{P}^e$, and $\vec{P}^h$ are only used in the PML region.

The PML region is also sub-divided into non-overlapping contiguous subdomains that are discretized with finite-elements. Within the discrete space, the field intensities and the auxiliary fields are expanded using H$_p$-curl conforming basis. Test functions that span an identical function space as the basis functions, are introduced. Following the procedure in (3) – (20), a Galerkin formulation is thus derived. This leads to the discrete linear operator:

$$\frac{\partial}{\partial t}\mathbf{M}_a^{\mathbf{h},\mathbf{h}}\mathbf{h} + \mathbf{M}_b^{\mathbf{h},\mathbf{h}}\mathbf{h} + \mathbf{M}_c^{\mathbf{h},\mathbf{h}}\mathbf{p}^{\mathbf{h}} + \mathbf{S}^{\mathbf{h},\mathbf{e}}\mathbf{e} + \mathbf{F}^{\mathbf{h},\mathbf{e}}\mathbf{e}^+ = 0 , (46)$$

$$\frac{\partial}{\partial t}\mathbf{M}_a^{\mathbf{e},\mathbf{e}}\mathbf{e} + \mathbf{M}_b^{\mathbf{e},\mathbf{e}}\mathbf{e} + \mathbf{M}_c^{\mathbf{e},\mathbf{e}}\mathbf{p}^{\mathbf{e}} - \mathbf{S}^{\mathbf{e},\mathbf{h}}\mathbf{h} - \mathbf{F}^{\mathbf{e},\mathbf{h}}\mathbf{h}^+ = 0 , (47)$$

$$\frac{\partial}{\partial t}\mathbf{M}^{\mathbf{h},\mathbf{h}}\mathbf{p}^{\mathbf{h}} - \mathbf{M}_{\kappa^{-1}}^{\mathbf{h},\mathbf{h}}\mathbf{h} + \mathbf{M}_d^{\mathbf{h},\mathbf{h}}\mathbf{p}^{\mathbf{h}} = 0 , \quad (48)$$

$$\frac{\partial}{\partial t}\mathbf{M}^{\mathbf{e},\mathbf{e}}\mathbf{p}^{\mathbf{e}} - \mathbf{M}_{\kappa^{-1}}^{\mathbf{e},\mathbf{e}}\mathbf{e} + \mathbf{M}_d^{\mathbf{e},\mathbf{e}}\mathbf{p}^{\mathbf{e}} = 0 , \quad (49)$$

where the matrices are defined in (17) – (19). Equations (46) – (49) can be expressed as a first order difference operator:

$$\dot{\tilde{\mathbf{x}}} = \mathbf{A}\tilde{\mathbf{x}} + \mathbf{B}\tilde{\mathbf{x}}^+ , \quad (50)$$

where,

$$\tilde{\mathbf{x}} = \begin{bmatrix}\tilde{\mathbf{h}} \\ \tilde{\mathbf{e}} \\ \mathbf{p}^h \\ \mathbf{p}^e\end{bmatrix}, \quad \tilde{\mathbf{x}}^+ = \begin{bmatrix}\tilde{\mathbf{h}}^+ \\ \tilde{\mathbf{e}}^+\end{bmatrix}, \quad (51)$$

$$\mathbf{A} = \begin{bmatrix} -\mathbf{M}_a^{\mathbf{h},\mathbf{h}^{-1}}\mathbf{M}_b^{\mathbf{h},\mathbf{h}} & -\mathbf{M}_a^{\mathbf{h},\mathbf{h}^{-1}}\mathbf{S}^{\mathbf{h},\mathbf{e}} & -\mathbf{M}_a^{\mathbf{h},\mathbf{h}^{-1}}\mathbf{M}_c^{\mathbf{h},\mathbf{h}} & 0 \\ \mathbf{M}_a^{\mathbf{e},\mathbf{e}^{-1}}\mathbf{S}^{\mathbf{e},\mathbf{h}} & -\mathbf{M}_a^{\mathbf{e},\mathbf{e}^{-1}}\mathbf{M}_b^{\mathbf{e},\mathbf{e}} & 0 & -\mathbf{M}_a^{\mathbf{e},\mathbf{e}^{-1}}\mathbf{M}_c^{\mathbf{e},\mathbf{e}} \\ \mathbf{M}^{\mathbf{h},\mathbf{h}^{-1}}\mathbf{M}_\kappa^{\mathbf{h},\mathbf{h}} & 0 & -\mathbf{M}^{\mathbf{h},\mathbf{h}^{-1}}\mathbf{M}_d^{\mathbf{h},\mathbf{h}} & 0 \\ 0 & \mathbf{M}^{\mathbf{e},\mathbf{e}^{-1}}\mathbf{M}_\kappa^{\mathbf{e},\mathbf{e}} & 0 & -\mathbf{M}^{\mathbf{e},\mathbf{e}^{-1}}\mathbf{M}_d^{\mathbf{e},\mathbf{e}} \end{bmatrix}$$

(52)

$$\mathbf{B}=\begin{bmatrix} 0 & -\mathbf{M}_a^{\mathbf{h},\mathbf{h}^{-1}}\mathbf{F}^{\mathbf{h},\mathbf{e}} \\ \mathbf{M}_a^{\mathbf{e},\mathbf{e}^{-1}}\mathbf{F}^{\mathbf{e},\mathbf{h}} & 0 \end{bmatrix}. \tag{53}$$

It is observed that with this form of the PML, arbitrary unstructured meshing can be employed within the PML region. The restriction is that the global PML *boundaries* be planar and orthogonal. It is further noticed that $\mathbf{p}^{\mathbf{h}}$ and $\mathbf{p}^{\mathbf{e}}$ are local to each subdomain and are not shared. Consequently, only the exterior fields $\tilde{\mathbf{h}}^+$ and $\tilde{\mathbf{e}}^+$ couple the sub-domains. It is further noted that when ∂V_i lies on the PML interface, $\tilde{\mathbf{h}}^+=\mathbf{h}^+$, and $\tilde{\mathbf{e}}^+=\mathbf{e}^+$. This is proven by observing in (37), that κ_k and σ_k are functions of *k*-only, and hence only impact the normal-projections of the fields on the PML boundaries. As a consequence, the mapped fields $\tilde{H}_k$ and $\tilde{E}_k$ maintain tangential continuity with the physical fields H_k and E_k.

VI. NUMERICAL STUDIES

The focus of this section is the validation of the DGFETD method presented in the previous sections. In the simulations presented, either three-dimensional hexahedral or tetrahedral meshes are used to discretize the volume. In all cases presented, the sub-domains V_i consist of a single finite element. The subdomain boundary ∂V_i is thus the faces of the polyhedron. In all cases, the sub-domain boundary faces are contiguous. Over each finite element, a variant of Webb's curl-conforming mixed-order hierarchal vector basis [14] were employed for tetrahedral elements. Hierarchal curl-conforming mixed-order basis functions for hexahedral elements have also been derived, and were used for hexahedral elements. RK-4 time-integration was used for all simulations for the time-integration of (21) and (50).

Initially, we consider the cavity resonator problem that is a PEC cube. The cube had a dimension of 1 m edge lengths. The fields within the cavity were excited by a volume current source randomly placed in the cavity. The time-dependent source had a differentiated Gaussian time-signature. The electric and magnetic fields were also probed during the time-simulation at a random location. The resonant frequencies of the cavity were extracted from the time-dependent fields using the FFT. The cavity was discretized with fitted hexahedral elements. The mesh densities ranged from 2 elements along an edge to 16 elements along an edge. The resonant frequencies were extracted for various order elements.

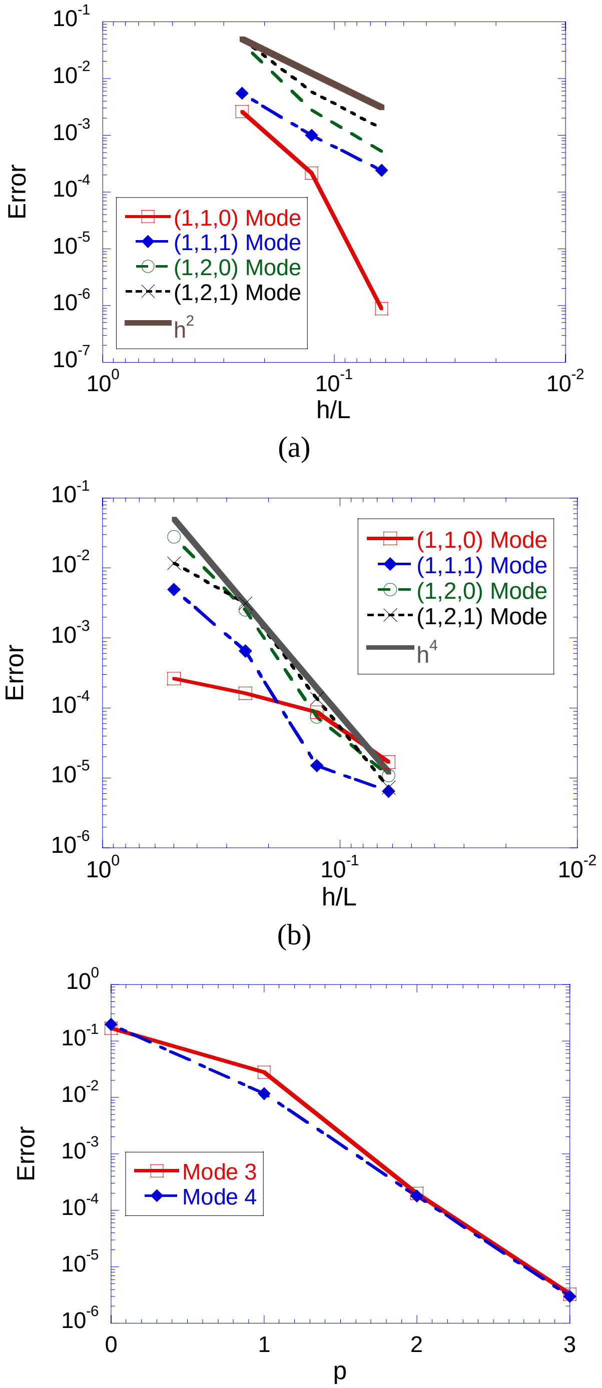

(a)

(b)

(c)

Fig. 2. Relative error for the first four modes of a 1 m PEC cube resonator. (a) H_0 basis, (b) H_1 basis, (c) varying basis order (h = 0.5 m).

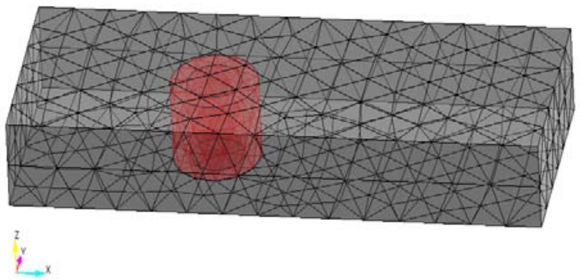

Fig. 3. Cavity ring resonator loaded with a dielectric ring tessellated with a quadratic tetrahedral mesh.

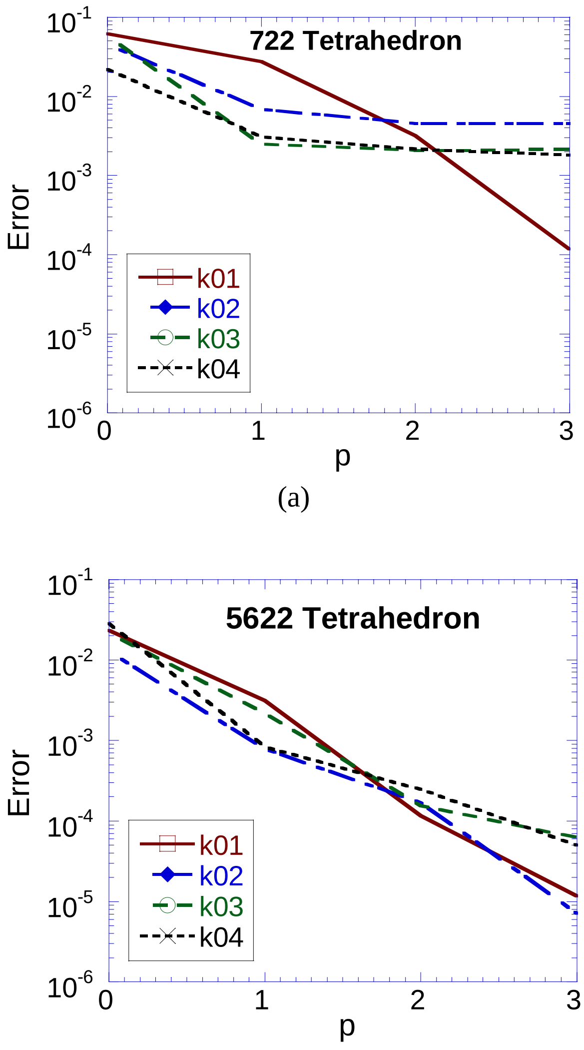

(a)

(b)

Fig. 4 Cavity ring resonator loaded with a dielec-tric ring tessellated with a quadratic tetrahedral mesh. (a) 722 quadratic tetrahedral mesh. (b) 5622 quadratic tetrahedral mesh.

Figures 2(a) and (b) illustrate the error of the first four modes in the cavity (the (1,1,0), (1,1,1), (1,2,0), and (1,2,1) modes, and their degenerate partners), as the mesh is refined for H_0 and H_1 basis functions. The error is expected to converge as $O(h^{2p})$ for the Galerkin procedure. Thus, a reference line is included. It is interesting to note that the (1,1,0) mode appears to super-converge. It is not clear why this is the case. Figure 2(c) illustrates the error in the predicted resonant frequency of the (1,2,0) and (1,2,1) modes for the coarsest mesh (2 elements on an edge) as the basis order is increased from p = 0 to 3. In each case, the error is observed to be converging as $O(h^{2p})$, as anticipated for the DGFETD method.

The next example studied is a cavity resonator loaded with a dielectric ring, as illustrated in Fig. 3 [29]. The rectangular PEC cavity has a dimension of 324 mm x 121 mm x 43 mm. The dielectric ring has an inner radius of 16.65 mm, and outer radious of 26.75 mm. The ring is sitting on the bottom of the cavity, but only has a height of 39 mm. The dielectric constant of the ring is 9.8. Again, the DGFETD method was used to extract the resonant frequencies of the loaded cavity. The cavity was excited in a similar manner as in the previous study.

The cavity was discretized with curvilinear second-order tetrahedron (10 nodes per tetrahedron). Here, two different meshes are presented. The first consisted of 722 quadratic tetrahedra. The second mesh consisted of 5,622 quadratic tetrahedra. (Note that curvilinear quadratic tetrahedra were used to more accurately resolve the ring geometry.) The basis function order was increased from p = 0 to 3 in each case. The error of the first 4 modes is presented in Figures (a) and (b) for the two meshes. A reference result was simulated using a denser mesh and high-order basis.

It is distinctly observed that for the coarse mesh, the error of the higher-order modes stagnate beyond p = 1. The reason for this is that the error is dominated by the boundary error of the surface of the dielectric ring. It appears that the lowest order mode is less dependent on the ring surface. The accuracy of the simulation could be improved by using higher-order tetrahedral elements. Unfortunately, such a meshing scheme was not available. Observing Fig. 4(b), the finer mesh leads to improved convergence to better than four digits of accuracy. If the basis order were increased further, the error will again stagnate due to the boundary error.

Table 1: Resonant frequencies of the PEC cavity loaded with the Dielectric ring as computed via the DSI, NFDTD, FETD, and DGFETD methods († reference [29])

Mode	DSI†	NFDTD†	FETD†	DGFETD
k01	0.952	0.952	0.9518	0.9518
k02	1.415	1.415	1.420	1.4151
k03	1.608	1.612	1.615	1.6109
k04	2.025	2.025	2.026	2.0257

Table 1 lists the resonant frequencies of the four modes to 5 digits calculated by the DGFETD method. As a reference, the resonant frequencies computed via the Discrete Surface Integral (DSI), the Non-Orthogonal FDTD (NFDTD), and a finite-element time-domain (FETD) method based on the vector wave equation are also provided. This data was obtained from [29].

The next set of problems involves unbounded domains that are terminated by the perfectly matched layer absorbing boundary condition. The first example is a parallel plate waveguide. The waveguide had PEC planes bounding the top and bottom boundaries. The side walls of the guide were PMC planes. The waveguide was discretized via rectangular hexahedron, which had 1 cm edge lengths. The waveguide was also meshed with tetrahedron with ~1 cm edge lengths.

The ends of the waveguide were terminated with PML layers. The TEM mode was excited in the guide via a surface current density. The time-dependent current had a Gaussian pulse time-signature with a 15 GHz bandwidth. The fields computed along the waveguide were Fourier transformed. The error of the phase and magnitude of the computed field relative to the exact field was computed. It is noted that the PML was tuned so that the PML reflection error was less than the computational error. Figure 5 (a) illustrates the maximum phase and magnitude error in the fields recorded over the frequency range of 0 to 15 GHz as a function of the order of the mixed-order curl-conforming basis functions. Typically, the maximum errors occurred at the highest frequencies. Exponential convergence of the solution is observed. It is noted that 6 digits of accuracy are realized for 4th order basis functions at this level of discretization. Figure 5 (b) illustrates the relative phase error for the tetrahedral mesh. This error is commensurate with that observed via the hexahedral mesh.

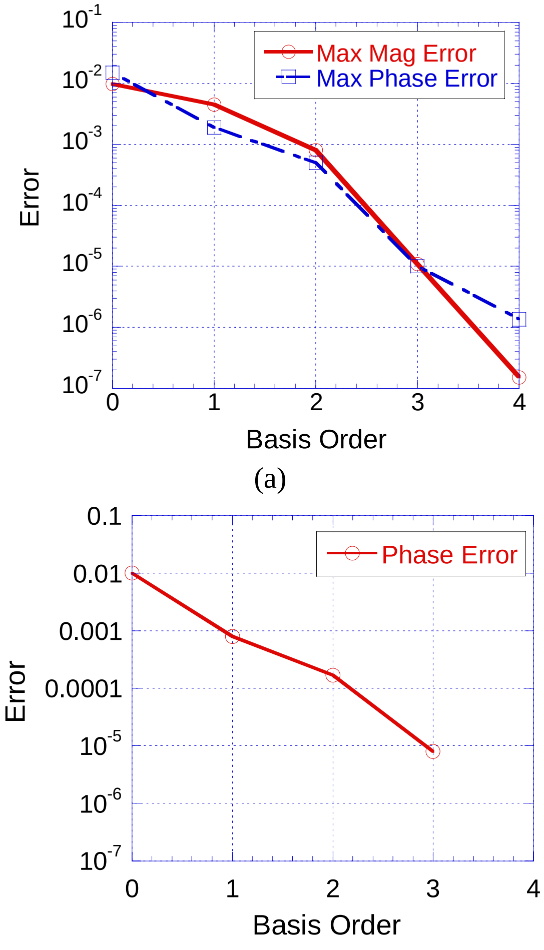

(a)

(b)

Fig. 5 Error in the electric field excited in a parallel plate waveguide discretized with (a) hexahedral, and (b) tetrahedral cells with 1 cm edge lengths. The maximum error over the 0 – 15 GHz frequency range is recorded as a function of the basis order.

Next, a more systematic study of the reflection error of the PML is presented. The parallel plate waveguide geometry is used again for this purpose. To extract the reflection error for the PML, a reference parallel plate waveguide was used that was sufficiently long so that the simulation would cease before reflections from the terminating boundary wall would return.

When applying the PML to FDTD applications, the PML is not actually perfectly matched since the discrete electric and magnetic fields are staggered in both space and time. As a consequence, the PML constitutive parameters must be spatially scaled to avoid large reflection errors. In the DGFETD formulation, the discrete electric and magnetic fields are co-located in both space and time. Thus, the PML is matched in the discrete space. Discretization errors will still lead to reflection error. However, spatial scaling is not as imperative, and thinner PML layers can be used.

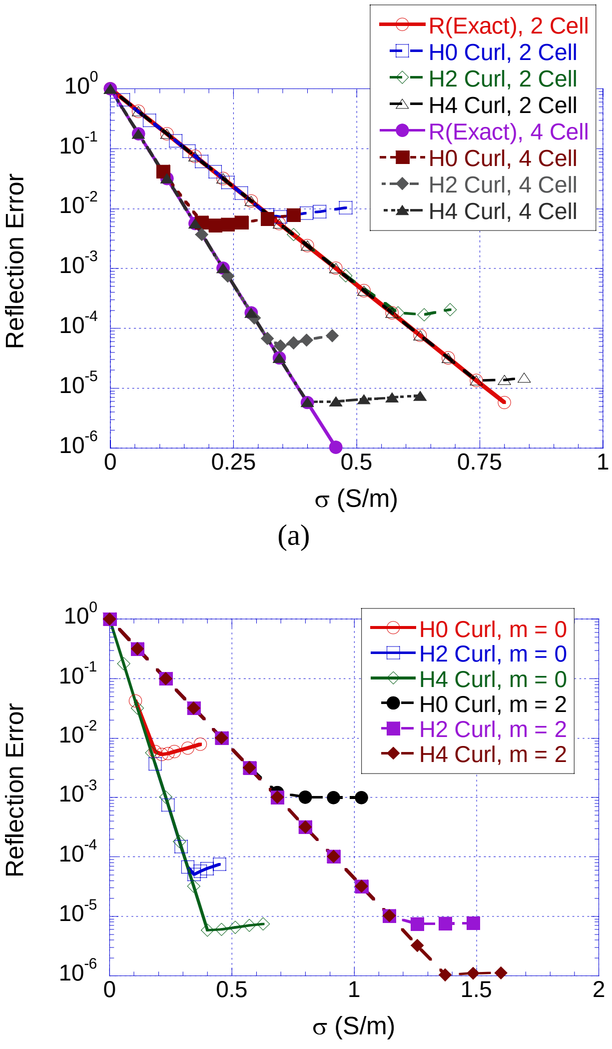

(a)

(b)

Fig. 6. Reflection error due to the PML termination of the parallel plate waveguide versus the PML conductivity ($\kappa = 1$) (a) for 2 and 4 cell thick PML layers with constant PML profile (m = 0), and (b) for a 4 cell thick PML with a polynomial scaled PML profile (m = 0, and m = 2).

The reflection error due to the PML as a function of the PML conductivity is presented in Fig. 6. The simulations used for Fig. 6 (a) assume PML parameters with a constant profile. Cases are presented where the PML was 2 and 4 hexahedral cells thick. H_0, H_2, and H_4 curl-conforming basis functions were employed. The exact reflection error is also illustrated in the plot, where

$$R(\text{Exact}) = e^{-2d\sigma\eta/(m+1)}, \tag{54}$$

where, d is the thickness of the PML slab (in meters), σ is the normal PML conductivity, η is the free-space wave impedance, and m is the polynomial scaling factor of σ. The PML reflection error is dominated by the reflection error at the back PEC wall (namely, due to a round trip of the wave through the PML) for sufficiently small values of sigma. As sigma becomes sufficiently large, the reflection error levels off due to discretization error of the fields.

It is observed that increasing the basis order dramatically improves the reflection error. Though, it is also striking that increasing the thickness of the PML bears only a few dB improvement in the minimum reflection error. This implies that the bulk of the reflection error occurs at the PML interface boundary. In an attempt to improve this, σ is scaled using polynomial scaling [28]. Quadratic scaling is compared to a constant profile. It is found that this improves the reflection error by approximately 10 dB.

The final example is the extraction of the scattering parameters of a printed microstrip patch antenna printed on a dielectric substrate. The dimensions of the patch antenna are given in [30]. The antenna was simulated using both the FDTD method and the DGFETD method. The FDTD lattice was terminated with a tuned CFS-PML absorbing media [27, 28] that were 10 cells thick. The DGFETD mesh was terminated using the proposed PML scheme that were 2 cells thick. The FDTD simulations were performed with (65x60x17) lattice grid cells (FDTD(A)), and a refined mesh of (191x111x31) lattice grid cells. The DGFETD simulations were performed with 780 hexahedron and H_3 basis (DGFETD(A)), and with a finer discretization consisting of 3,120 hexahedron and H_2 basis (DGFETD(B)). A cross section of the mesh with 780 hexahedron is illustrated in Fig. 7. The microstrip line was excited by a soft current source placed under the microstrip. The line was matched via the PML boundary.

The magnitude of the reflection loss (S_{11}) is presented in Fig. 8 as computed by the FDTD and DGFETD methods each with two successive refinements. FDTD (A) has the most significant error. DGFETD(A) is also not yet converged.

There is good agreement with the finer FDTD and DGFETD discretizations.

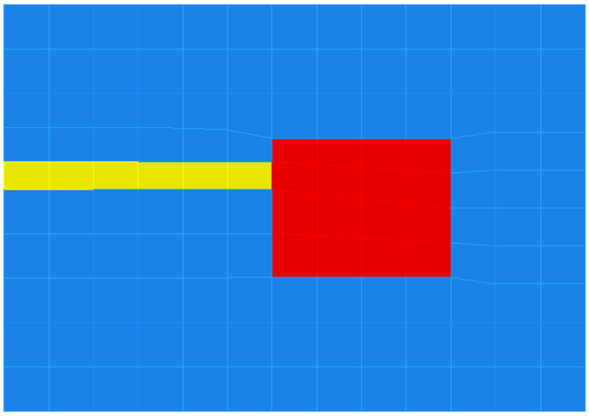

Fig. 7. Cross sectional view of the microstrip patch antenna fed by a microstrip line, discretized with the 780 cell hexahedral mesh.

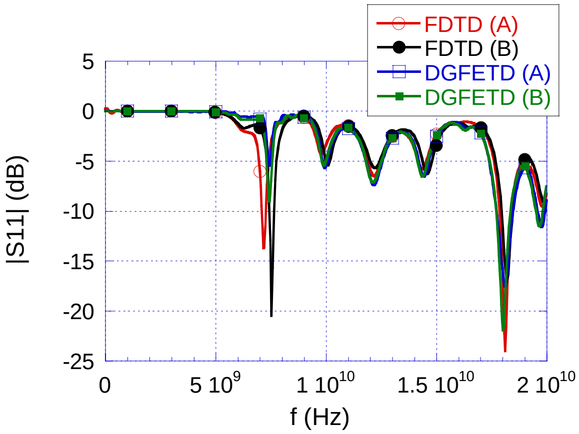

Fig. 8. Magnitude of scattering parameter S_{11} of the microstrip patch antenna computed via the FDTD method with lattice grids of dimension (A) (65x60x17) and (B) (191x111x31) lattice grid cells, and the DGFETD method with: (A) 780 hexahedron and H_3 basis and (B) 3,120 hexahedron and H_2 basis.

VII. CONCLUSIONS

A novel Discontinuous Galerkin Finite-Element Time-Domain (DGFETD) method has been presented in this paper. The DGFETD method is based on a spatial decomposition of the problem domain into non-overlapping sub-domains. A Galerkin formulation based on Maxwell's curl equations is imposed over each sub-domain. Each sub-domain is discretized independently using high-order hierarchal curl-conforming basis functions to discretize both the electric and the magnetic field intensities. The continuity of the fields across sub-domain boundaries is weakly enforced via boundary integral terms. By using curl-conforming basis, only basis functions associated with topologies that lie on the sub-domain boundary (i.e., face and edge basis functions) couple. The use of mixed-order curl-conforming basis avoids spurious solutions and the need for penalty methods.

The DGFETD method is a locally implicit/globally explicit method. That is, local to each sub-domain, a matrix inversion must be performed. However, since the sub-domains are generally quite small, this can be efficiently done via a LU-factorization. The global system of equations, which is superposition of all the sub-domains, is then solved via an explicit time-stepping algorithm. High-order Runge-Kutta (RK) schemes were used for this purpose.

For open region problems a perfectly matched layer (PML) absorbing boundary based on a stretched coordinate formulation was presented. PML absorbing layers have controllable accuracy, and are well suited for a high-order method. Since the electric and magnetic fields are co-located in both space and time, the scaling of the constitutive parameters is not necessary. In fact, reflection errors on the order of 0.001 % are possible with PML layers that are only 2 cells thick. However, it was shown that scaling the parameters can moderately reduce the reflection error.

Through numerical validation, it was demonstrated that the proposed DGFETD method does provide exponential convergence. It was also shown that the dispersion error can be dramatically reduced. This has great advantage when solving large scale problems, where phase errors are accumulated over long propagation distances. Unlike symplectic integration schemes, RK methods are also dissipative. However, it was also shown that the magnitude error is commensurate with the phase error, and the precision can be controlled via the high-order scheme.

Finally, since the DGFETD method is based on a spatial decomposition of the domain, and local solutions within these sub-domains, it is a naturally parallel algorithm. The most efficient parallel implementation of the algorithm is based on a distribution of sub-domains to processors based on contiguous non-overlapping domains of sub-domains. This will be the topic of a future publication.

REFERENCES

[1] B. Cockburn, G. E. Karniadakis, and C. W. Shu, *Discontinuous Galerkin Methods: Theory, Computation and Applications*, vol. 11. Berlin: Springer-Verlag Telos, 2000.

[2] M. H. Chen, B. Cockburn, and F. Reitich, "High-order RKDG methods for computational electromagnetics," *J. of Scientific Computing*, vol. 22 and 23, pp. 205-226, June 2005.

[3] J. S. Hesthaven, "High-order accurate methods in time-domain computational electromag-netics: A review," *Advances In Imaging And Electron Physics*, vol. 127, pp. 59-123, 2003.

[4] J. S. Hesthaven and T. Warburton, "Nodal high-order methods on unstructured grids - I. Time-domain solution of Maxwell's equations," *J. of Computational Physics*, vol. 181, pp. 186-211, 2002.

[5] J. S. Hesthaven and T. Warburton, "High-order nodal discontinuous Galerkin methods for the Maxwell eigenvalue problem," *Philosophical Trans. of The Royal Society of London Series A-Mathematical Physical And Engineering Sciences*, vol. 362, no. 1816, pp. 493-524, Mar 2004.

[6] T. Lu, P. W. Zhang, and W. Cai, "Discontinuous Galerkin methods for dispersive and lossy Maxwell's equations and PML boundary conditions," *J. of Computational Physics*, vol. 200, no. 2, pp. 549-580, Nov 2004.

[7] P. Monk and G. Richter, "A discontinuous Galerkin method for linear symmetric hyperbolic systems in inhomogeneous media," *J. of Scientific Computing*, vol. 22-23, no.1, 2005.

[8] T. Xiao and Q. H. Liu, "Three-dimensional unstructured-grid discontinuous Galerkin method for Maxwell's equations with well-posed perfectly matched layer," *Microwave Opt. Tech. Lett.*, vol. 46, no. 5, pp. 459-463, September 2005.

[9] L. F. Canino, J. J. Ottusch, M. A. Stalzer, J. L. Visher, and S. M. Wandzura, "Numerical solution of the Helmholtz equation in 2D and 3D using a high-order Nyström discretization," *J. of Computational Physics*, vol. 146, no. 2, pp. 627-663, 1998.

[10] S. D. Gedney, "On deriving a locally corrected Nyström scheme from a quadrature sampled moment method," *IEEE Trans. Antennas Propagat.*, vol. 51, no. 9, pp. 2402-2412, Sept. 2003.

[11] B. Cockburn, F. Y. Li, and C. W. Shu, "Locally divergence-free discontinuous Galerkin methods for the Maxwell equations," *J. Of Computational Physics*, vol. 194, no. 2, pp. 588-610, Mar 2004.

[12] S. Gedney, C. Luo, B. Guernsey, J. A. Roden, R. Crawford, and J. A. Miller, "The Discontinuous Galerkin Finite-Element Time-Domain Method (DGFETD): A High Order, Globally-Explicit Method for Parallel Computation," presented at *IEEE International Symposium on Electromagnetic Compatibility*, Honolulu, HI, 2007.

[13] D. K. Sun, J. F. Lee, and Z. Cendes, "Construction of nearly orthogonal Nedelec bases for rapid convergence with multilevel preconditioned solvers," *SIAM J. on Scientific Computing*, vol. 23, no. 4, pp. 1053-1076, 2001.

[14] J. P. Webb, "Hierarchical vector basis functions of arbitrary order for triangular and tetrahedral finite elements," *IEEE Trans. Antennas Propagat.*, vol. 47, no. 8, pp. 1244-1253, 1999.

[15] P. Fernandes and M. Raffetto, "Characterization of spurious-free finite element methods in electromagnetics," *Compel-The International Journal For Computation And Mathematics In Electrical And Electronic Engineering*, vol. 21, no. 1, pp. 147-164, 2002.

[16] J. S. Hesthaven and T. Warburton, "High-order accurate methods for time-domain electromagnetics," *CMES-Computer Modeling In Engineering & Sciences*, vol. 5, no. 5, pp. 395-407, May 2004.

[17] B. Donderici and F. L. Teixeira, "Mixed finite-element time-domain method for transient Maxwell equations in doubly dispersive media," *IEEE Trans. Micro. Theory Tech.*, vol. 56, no. 1, pp. 113-120, Jan 2008.

[18] R. N. Rieben, G. H. Rodrigue, and D. A. White, "A high order mixed vector finite element method for solving the time

dependent Maxwell equations on unstructured grids," *J. of Computational Physics*, vol. 204, no. 2, pp. 490-519, Apr 10 2005.

[19] R. Rieben, D. White, and G. Rodrigue, "High-order symplectic integration methods for finite element solutions to time dependent Maxwell equations," *IEEE Trans. Antennas Propagat.*, vol. 52, no. 8, pp. 2190-2195, Aug 2004.

[20] G. Rodrigue and D. White, "A vector finite element time-domain method for solving Maxwell's equations on unstructured hexahedral grids," *SIAM Journal On Scientific Computing*, vol. 23, no. 3, pp. 683-706, Oct 1 2001.

[21] S. Gottlieb, C. W. Shu, and E. Tadmor, "Strong stability-preserving high-order time discretization methods," *SIAM Review*, vol. 43, no. 1, pp. 89-112, 2001.

[22] J. Jin, *The Finite Element Method in Electromagnetics*. New York: John Wiley & Sons, Inc., 1993.

[23] J. P. Berenger, "A perfectly matched layer for the absorption of electromagnetic waves," *J. of Computational Physics*, vol. 114, no. 2, pp. 195-200, 1994.

[24] J. H. Lee and Q. F. Liu, "A 3-D spectral-element time-domain method for electromagnetic simulation," *IEEE Trans. Micro. Theory Tech.*, vol. 55, no. 5, pp. 983-991, May 2007.

[25] S. Abarbanel, D. Gottlieb, and J. S. Hesthaven, "Non-linear PML equations for time dependent electromagnetics in three dimensions," *J. Of Scientific Computing*, vol. 28, no. 2-3, pp. 125-137, Sep 2006.

[26] W. C. Chew and W. H. Weedon, "A 3D Perfectly Matched Medium from Modified Maxwells Equations with Stretched Coordinates," *Micro. Opt. Tech. Lett.*, vol. 7, no. 13, pp. 599-604, 1994.

[27] J. A. Roden and S. D. Gedney, "Convolutional PML (CPML): An Efficient FDTD Implementation of the CFS-PML for Arbitrary Media," *Micro. Opt. Tech. Lett.*, vol. 27, no.5, pp. 334-339, December 2000.

[28] S. D. Gedney, "Perfectly Matched Layer Absorbing Boundary Conditions," in *Computational Electrodynamics: The Finite-Difference Time-Domain Method*, A. Taflove and S. B. Hagness, Eds., 3rd ed. Boston: Artech House, 2005.

[29] S. D. Gedney and J. A. Roden, "Numerical stability of non-orthogonal FDTD methods," *IEEE Trans. Antennas Propagat.*, vol. 48, no. 2, pp. 231-239, 2000.

[30] D. M. Sheen, S. M. Ali, M. D. Abouzahra, and J. A. Kong, "Application of the three-dimensional finite-difference time-domain method to the analysis of planar microstrip circuits," *IEEE Trans. Micro. Theory Tech.*, vol. 38, no. 7, pp. 849-857, July 1990.

Stephen D. Gedney received the B.Eng.-Honors degree from McGill University, Montreal, P.Q., in 1985, and the M.S. and Ph.D. degrees in Electrical Engineering from the University of Illinois, Urbana-Champaign, IL, in 1987 and 1991, respectively. He is currently a Professor with the Department of Electrical and Computer Engineering at the University of Kentucky, where he has been since 1991. From 1985 to 1987, he worked for the U.S. Army Corps of Engineers, Champaign, IL. In the summers of 1992 and 1993 was a NASA/ASEE Faculty Fellow at the Jet Propulsion Laboratory, Pasadena, CA. In 1996 he was a visiting Professor at the Hughes Research Labs (now HRL laboratories) in Malibu, CA. He received the Tau Beta Pi Outstanding Teacher Award in 1995. In 2002, S. Gedney was named as the Reese Terry Professor of Electrical and Computer Engineering at the University of Kentucky. He is also a Fellow of the IEEE. Prof. Gedney's research is in the area of computational electromagnetics with focus in high-order solution techniques, fast solver technology, advanced time-domain methods, and parallel algorithms. His research has focused on applications in the areas of electromagnetic scattering and microwave circuit modeling and design.

Chong Luo was born in Sichuan, China, in 1972. He received B.S. degree, in Electrical Engineering from Beijing University of Aeronautics and Astronautics, Beijing, China, in 1994, the M.S. and Ph.D. degrees in Electrical Engineering from University of Kentucky, Lexington, in May 2002 and December 2005. He is currently Alpha Omega Electromagnetics. His primary research interest is in computational electromagnetics. Dr. Luo is a member of IEEE.

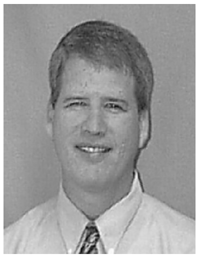

Alan Roden is a Senior Project Leader with The Aerospace Corporation where his responsibilities include electromagnetic analysis and design for satellite systems. Previously, Dr. Roden worked with The Georgia Tech Research Institute in Atlanta Georgia, and the IBM Corporation in Research Triangle Park, NC. He received his Ph.D. in Electrical Engineering from the University of Kentucky, Lexington, KY in 1997, his master's degree in electrical engineering from North Carolina State University in 1989, and his B.S. from the University of Tennessee at Chattanooga in 1984. Dr. Roden is a senior member of the IEEE and has published over 30 journal and conference papers.

Robert D. Crawford received a B.S. in Computer Science from the University of Illinois Urbana-Champaign in 1986 and an M.S. in Mathematics from Illinois State University in 1988. Mr. Crawford has been developing and managing the development of EM Simulation Software (both asymptotic and full-wave) for the past 8 years.

Bryan Guernsey graduated from Virginia Tech in 2005 with a BS in Electrical Engineering, 2007 from The University of Kentucky with a MSEE focusing in Computational Electromagnetics. He is currently working as a member of the technical staff for The Aerospace Corporation in Chantilly Va.

Jeffrey A. Miller received the BS, MS and PhD degrees in electrical engineering from Texas A&M University, College Station, in 1987, 1989, and 2001, respectively. Has has been employed by Texas Instruments, McKinney, TX, where he designed and analyzed broad-band antennas. He has also worked at Northrop Grumman, Pico Reivera, CA, in the area of low observable Technology. He is currently a Senior Engineering Specialist with the Aerospace Corporation, Chantilly, VA, where he specializes in antennas and electromagnetic analysis

Tyler C. Kramer (M'02) was born in Reading, PA. He obtained his BSEE and MSEE degrees from Virginia Tech in 2004 and 2007, respectively. From 2004 to 2005 he was employed as a Research Scientist at Nanosonic, Inc, Blacksburg VA. He is currently employed as a Member of the Technical Staff at The Aerospace Corporation, specializing in computational and applied electromagnetics.

Eric W. Lucas received the B.S. and M.S.E.E degrees from George Mason University, Fairfax, Va. In 1984 and 1989 respectively. In 1993, he received the Ph.D. degree from the University of Maryland, College Park under Professor Isaac Mayergoyz. In 1985 he joined the Microwave Branch of Harry Diamond Lab (Army Research Lab). In 1986 Dr. Lucas joined the Westinghouse (now Northrop Grumman) Antenna Aperture and Integrated Sensor Department, Baltimore MD. Dr. Lucas was a Fellow Engineer there, responsible for the development of wideband, wide-scanning low-observable phased array aperture technologies. In 1998 Dr. Lucas founded Alpha Omega Electromagnetics, LLC., a MD-based antenna and electromagnetic simulation software technology development firm. His research interests include diverse antenna technologies as well as state-of-the-art, industrial grade electromagnetic simulation software and algorithm development.

Physics-Based Aggregate-Functions Approaches to Large Mom Problems

Ladislau Matekovits[1], **Giuseppe Vecchi**[1], **Felipe Vico**[2]
[1]Department of Electronics, Antennas and EMC Laboratory
(Laboratorio Antenne e Compatibilita Elettromagnetica - LACE),
Politecnico di Torino, Corso Duca degli Abruzzi 24, I-10129 Torino, Italy
ladislau.matekovits@polito.it , giuseppe.vecchi@polito.it

[2] iTEAM - Universidad Politcnica de Valencia, 46022 Valencia, SPAIN
fevibon@teleco.upv.es

***Abstract*—** Aggregate functions approaches construct efficient MoM basis functions by suitably grouping standard (e.g. Rao-Wilton-Glisson) functions. The application domains, objectives and related means of achieving them can be significantly different. In this paper we review some recent advances in aggregate-functions methods, putting them in a unifying perspective. We address matrix compression, multi-resolution sets, low- and high-frequency constructs. They can reduce the degrees of freedom of the problem so as to allow a direct, iteration-free solution, or can accelerate the convergence rate of iterative methods. We analyze compressive methods in more detail, providing general discussion and specific implementation examples.

***Index Terms*—** Integral equation techniques, Method of Moments, Large structures, Aggregate functions.

I. INTRODUCTION

The Integral Equation (IE) approach is widely used to solve antenna and scattering problems, and known for its effectiveness and robustness. The standard implementation of its Method of Moment (MoM) discretization has obvious limitations on the matrix size in terms of memory and CPU time for large scattering bodies and large and complex antennas and arrays. Less obvious, but very relevant are also issues related to the matrix conditioning, especially for very large problems or for problems with fine meshes, or mesh cells of very different sizes. In order to reduce the problem numerical complexity, two different families of approaches can be adopted: the first one consists in the so called fast methods that are based on the use of iterative solvers, and essentially act on the cost and memory occupation needed at each step of the iterative algorithm. Another class of methods is based on the grouping of basis functions into “aggregate functions” that are constructed in such a way to inject information about nature of the solution directly into the representation of the unknown currents.

Function aggregation, in turn, may take two different routes and perspectives. In one of its embodiment, aggregation may be used to reduce the number of degrees of freedom (DOF) of a problem; such a reduction may be so drastic as to make the direct solution of the MoM linear system is attainable even for very large and/or complex problems; when not possible, it will in any case make the use of iterative solvers more expedite. The other type of aggregate function approaches instead aim at improving the stability of the system, or to allow a sparsification of the resulting MoM matrix.

In this paper, we will address the aggregate function methods from a general perspective at first, showing that in all cases they add considerable flexibility to the MoM; this flexibility in turn allows to exploit the physical and mathematical properties of the underlying problem to the advantage of the computational complexity or stability of the solution. We will then focus our attention on methods that lead to a ”compression” of the MoM matrix; two methods already proposed by these authors will be discussed in more detail for the sake of making clearer points. The two examined methods address different types of problems, and allow a broader perspective. The characteristics of the aforementioned algorithms

1054-4887 © 2009 ACES

have been presented, or will be presented, in more detail in other works; the main scope of this paper is not indeed a detailed discussion of these particular methods but a more general review.

While this paper will be devoted to aggregate function methods, it is important to underline that fast methods and aggregate function methods are complementary. It is indeed possible to arrive at hybrid techniques that sum up the advantages of both approaches. A brief discussion on the prospects of these issues will be addressed where appropriate in the following sections.

II. THE AGGREGATE BASIS FUNCTION PARADIGM

Electromagnetic analysis of radiators or scatterers with arbitrary geometries requires the dicretization of the descriptive equations (EFIE, MPIE, CFIE, or GCFIE) by basis functions defined on subdomains.

The unknowns will in general comprise both electric and magnetic currents; for the sake of simplicity here we will however refer to the electric current only, denoted by $\underline{J}(\underline{r})$. The unknown is initially approximated by a set of basis functions defined on the meshed structure; most often these will be RWG on triangular patches, and/or piecewise-linear functions on wire segments; we will denote these standard basis functions $\left\{\underline{f}_n(\underline{r}), n=1,...,N\right\}$ as ”elemental” basis functions, and $\underline{J}^e$ is the approximation obtained with such a basis:

$$\underline{J}^e(\underline{r}) = \sum_{n=1}^{N} I_n \underline{f}_n(\underline{r}). \tag{1}$$

The key of function aggregation is to look for a different basis, of dimension M,

$$\underline{J}^a(\underline{r}) = \sum_{k=1}^{M} i_k \underline{\psi}_k(\underline{r}) \tag{2}$$

constructed with the elemental functions,

$$\underline{\psi}_k(\underline{r}) = \sum_{n=1}^{N_k} U_{nk} \underline{f}_n(\underline{r}). \tag{3}$$

The new basis functions $\left\{\underline{\psi}_n(\underline{r}), n=1,...,M\right\}$ are called “aggregate” basis functions, and are combinations with fixed weights U_{nk} of the elemental basis functions $\underline{f}_n(\underline{r})$.

The new basis must of course present desirable numerical properties; this is discussed below. Also, one wants that the two bases yield the same accuracy, i.e. $\underline{j}^a = \underline{j}^e$ within the accuracy of both with respect to the actual solution.

Equation (3) describes the basis change from the initial elemental basis to the aggregate basis. We consider the initial MoM system for the elemental basis in (1)

$$\underline{J}^e(\underline{r}) = \sum_{n=1}^{N} I_n \underline{f}_n(\underline{r}) \quad \rightarrow [Z][I] = [B], \tag{4}$$

and the MoM for the aggregate basis (3)

$$\underline{J}^a(\underline{r}) = \sum_{k=1}^{M} i_k \underline{\psi}_k(\underline{r}) \quad \rightarrow [z][i] = [b]. \tag{5}$$

The basis change can likewise be written in terms of matrix operations via (3),

$$\underline{\psi}_k(\underline{r}) = \sum_{n=1}^{N_k} U_{nk} \underline{f}_n(\underline{r}) \quad \rightarrow [X] = \left[[U_1],...,[U_M]\right]. \tag{6}$$

With this notation, application of the Galerkin testing with ψ_k to the initial Integral Equation leads to the relationship between the MoM matrices for the two bases:

$$[I] = [X][i], \quad [z] = [X]^H [Z][X], \quad [b] = [X]^H [B], \tag{7}$$

that clearly defines a basis change operation. In the above, we have considered the general case of complex-valued coefficients in the aggregation; the hermitean (^{H}) adjoint (conjugate transpose) reduces to transpose operation (^{T}) for real coefficients.

The general description of the method presented above includes all kinds of aggregation (and specifies none). As a general remark, note that all aggregate function schemes allow the re-use of MoM codes, and they are kernel-independent; this is a strong advantage of this class of approaches.

On the basis of the values of *N* and *M*, we differentiate between two fundamental cases as follows.

II.1 M = N: One-to-one basis change

In this case the dimension of the system remains unchanged, but the matrix in the aggregate function basis exhibits ”better” properties: sparse matrix, faster convergence, etc.. To be practical, the (square) basis-change matrix [*X*] must obviously be very sparse.

The two bases { $\underline{f}_n(\underline{r})$, $n = 1, \ldots, N$} and { $\underline{\psi}_n(\underline{r})$, $n = 1, \ldots, N$} now span the same space, and with infinite-precision arithmetic the two solutions should be identical, $\underline{j}^a = \underline{j}^e$. However, when the aggregate basis is used to solve problems of the standard elemental basis, it might not be so, and $\underline{j}^a$ may be closer to the actual solution or more stable.

A classical example is the Helmholtz (Hodge) decomposition employed to avoid the low-frequency ill-conditioning of RWG (and wire) bases. This leads to the loop-star or loop-tree decompositions (e.g. [1, and references therein]); the MoM matrix in the aggregate basis has a far better conditioning.

Another important instance of this class of aggregate functions is the Multi-Resolution approach, where wavelet-like properties are introduced into the set of basis functions. Earlier applications of wavelet constructs were limited to simple geometries and mostly 2D scattering problems; in those cases wavelet functions similar to those employed in signal processing were used. More recently, realistic geometries have been addressed, either in planar or 3D cases; this has forced the wavelet functions to be significantly simpler, and the most successful approaches have managed to construct multiresolution functions as linear combinations of standard elemental basis functions: this ensures applicability to all those cases that can be analyzed by the employed elemental basis functions (e.g. RWG).

The first attempts addressed planar structures that can be discretized by rectangular cells [8] [9], [10], [11]; more recent approaches have addressed triangular cells [13], [12], [14], [15], [16].

In the early days, the motivation for MR approaches was the hope to ”sparsify” the MoM matrix, i.e. of achieving a high dynamic range of matrix entries that allows clipping smaller elements within a given accuracy bound. More recent works [10], [12], [16] have focused on the spectral properties of the resulting MR-MoM matrix, and the intrinsic pre-conditioning potential of the MR basis; the reasons of this pre conditioning effects are addressed in [17]. In all the above examples, aggregate functions are real.

II.2 M << N: compression

In this case the dimension of the system described by the aggregate functions is reduced, which corresponds to having the reduced degrees of freedom (DOF) of the solution. As will be discussed later on in Sec. III., this does not imply per se the necessity to reduce the accuracy. It is however important to assess the overhead introduced by the compression scheme into the overall solution, for a given degree of accuracy. For a given accuracy, the degree of compression and the overall efficiency depend on how the aggregate functions are generated; it is intuitive that it is important to incorporate information on the physical nature of the problem under analysis to affect this choice efficiently.

Since in this case the dimension of the system can be drastically reduced, even of orders of magnitude, the primary computational gain is achieved during the factorization of the system matrix in the reduced basis. Low memory occupation, the possibility to employ a direct solver, and with the ability to treat multiple right hand side (RHS) at marginal costs are the immediate advantages. The reduced number of DOF also preludes to a faster convergence of iterative solvers, if a direct solution is not viable. While memory occupation can be significantly reduced, the matrix fill time is not addressed directly. The aggregate nature of the basis functions, however, lends itself to various schemes to exploit fast matrix-vector multiplications to this aim, as discussed later on.

The overhead comes from two parts of the procedure: a) generation of the aggregate function basis; b) basis change in (7). Using standard matrix-vector products, it is $O(MN(M + N)) \approx O(MN^2)$, i.e. much less than the N^3 of the LU factorization. With fast matrix-vector products, this is reduced accordingly.

Works that belongs to this class where first developed for planar structures, and then extended to 3D problems [2], [3], [4], [5], [6], [7]; a com prehensive survey can be found in [7]. Aggregate functions have been termed with different names along the ”history” of this approach: diakoptic [2], ”macro” basis functions (MBF) [4], synthetic basis functions [6], [7], and characteristic basis functions (CBF) [5]. All of these methods are in essence domain-decomposition methods, i.e. they are based on the solution of the initial problem on parts of the overall structure, and employ this information in constructing the aggregate functions; the aggregate functions, in turn, are defined on sub-domains larger that the individual mesh cells and smaller than the entire structure. The more recent Wave-front Basis Function (WBF) method [24, and references therein] is slightly different. It addresses very large scattering problems, and employs phase information on the asymptotic (high-frequency) solution to construct the aggregate functions. While the associated aggregate functions are still defined on subdomains, the associated geometric partitioning has different (much less stringent) needs as in the case of the previous groups of methods. In what follows, we will discuss compression-type aggregate function schemes only.

III. COMPRESSION SCHEMES

III.1 General features

We begin by observing that the use of compressive aggregate-function bases is equivalent to the use of the space spanned by the elemental basis functions to approximate the unknown, but leaving only certain subspaces accessible to the solution algorithm. This can be seen from equations (4-7), and noting that the basis-change matrix [X] is $N \times N$. The specificity of the aggregate function algorithms is indeed in choosing and constructing these subspaces in which the solution is sought.

In particular, we assume that the initial discretization is accurate enough and can be considered ”exact” (i.e. we do not count on the improvement on condition number and stability that the compression scheme might allow). If we denote the concerned spaces by

$$\begin{aligned} &\underline{J}^e \in H_N^f, \quad H_N^f = \operatorname{span}\left\{ \underline{f}_n, n = 1,...,N \right\} \\ &\underline{J}^a \in H_M^\psi, \quad H_M^\psi = \operatorname{span}\left\{ \underline{\psi}_n, n = 1,...,M < N \right\}, \end{aligned} \tag{8}$$

because of (3), $[X] : H_N^f \to H_M^\psi$; since $M < N$ it is apparent that $H_M^\psi \subset H_N^f$. Per se, this does not prevent the equality $\underline{j}^a = \underline{j}^e$, but that depends on whether the ”exact” solution $\underline{j}^e$ lies in the subspace $H_M^\psi \subset H_N^f$.

It is the experience of the authors, that it is often counter-intuitive that a reduction of the DOF may be done without sacrificing solution accuracy. This issue is best addressed after two specific examples of compressive aggregate-functions methods are discussed, and will be addressed in Sec. III.4.

As mentioned previously, most methods of present interest can be considered domain-decomposition (DD) methods, i.e. methods in which the solution for the entire structure employs partial solutions for isolated parts of the entire structure to reduce the overall size of the problem. Domain-decomposition (DD) methods are well known and employed in finite-element solutions of differential problems (FEM) (a review of the related literature is outside the scopes of this work). There, DD is directly feasible (albeit far from trivial) thanks to the local nature of the interactions between basis functions that constitute the (exactly sparse) system matrix. In integral equation formulations no interaction is local, and this makes the DD effort more complex.

The first step of a DD method is the subdivision of the overall structure into portions, here called ”blocks”. Next, the electromagnetic (EM) problem is solved on these blocks, taken in isolation. Finally, these solutions are used to compute, at a reduced cost, the solution for the entire structure. Having to ”patch up” the solutions on individual blocks, three issues are crucial for an effective method.

1. Specify the forcing terms when solving for the isolated blocks;
2. Ensure continuity of the solution across boundaries of neighboring, contacting blocks (when present);
3. Avoid the artifacts arising from the solution for isolated blocks when these originate from ”tearing” an otherwise continuous surface. When treated as isolated, a block will have edges at which a correct solution of the EM problem exhibits a singular behavior; this latter constitutes an obvious artifact when patching up the structure, in which the inter-block boundary is not an edge.

The above steps and issues are common to all methods of the explicit DD type (SFX, CBF, MBF, diakoptics); the way these steps are performed, and how the above issues are tackled is precisely at the root of the differences for the various approaches.

In the following we present two instances of implementations of the compressive aggregate function scheme: the Synthetic Function eXpansion (SFX) approach and the Wavefront Basis Method (WBF).

As alluded in the Introduction, the details of the methods being presented do not belong to this paper; their main steps will be however be reported here for the sake of clarity, with the objective of putting them in perspective.

It can be observed that compressive aggregate function methods reduce memory storage requirements to the size of the largest block in the DD, and will drastically reduce solution times. However, function aggregation does not reduce per se the MoM filling time. However, as mentioned in the Introduction, aggregate function methods are conveniently coupled to fast methods to this end. While not claiming any literature completeness, one can report that macro-basis functions have been coupled to the Fast-Multiple Method (FMM) [18]; SFX has been coupled to AIM [19] and a multi-grid strategy [20]; CBF has been coupled to FMM [21] and to the Adaptive Cross Approximation (ACA) [22].

On the other hand, the Wavefront Basis Method (WBF) is naturally posed to be used in conjunction with a fast method.

III.2 The Synthetic Function Expansion (SFX) Approach

We now describe how the above general DD predicaments are implemented in practice, using the SFX method as example. The method is described in [6], and in [7] in a detailed manner: here we will only briefly summarize the key aspects. For the sake of readability, we will refrain from referring to the above-cited papers in describing the method here.

In the SFX approach, the DD step is followed by the identification of surface blocks (s-blocks) and line-blocks (l-blocks). The s-blocks are formed by all mesh cells (triangles) that geometrically constitute a block; the l-blocks are the mesh edges (segments) that are in common between two adjacent blocks; they are absent when the block subdivision does not generates ”cuts” in the metal (e.g. for isolated radiators in an array). This is the first step taken to address the current continuity across blocks. An example of this division is shown in Figs. 1 and 2.

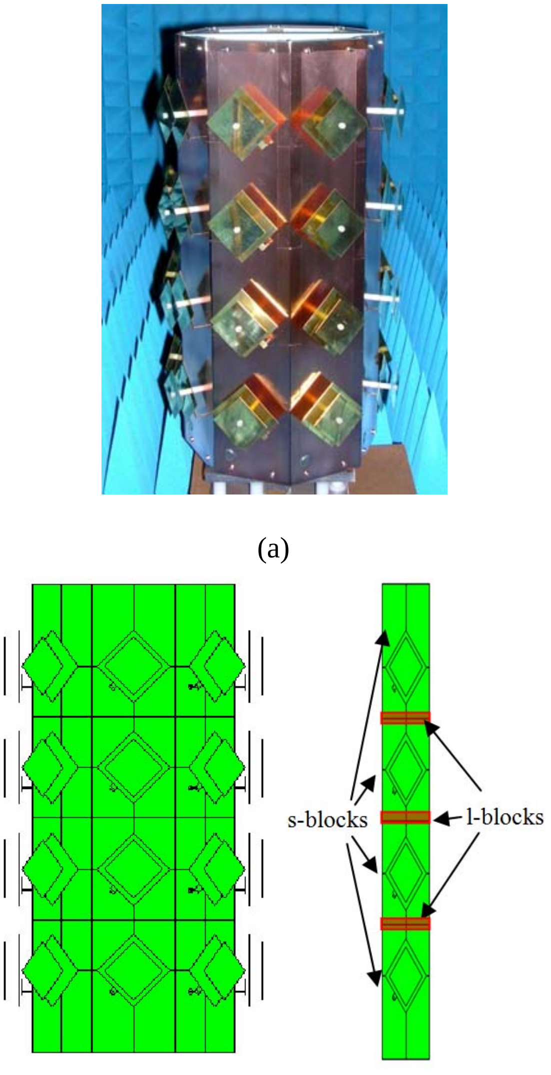
(a)
(b)
(c)

Fig. 1. Conformal base station antenna. (a) Photograph, (b) CAD model, (c) CAD model of the single column, with example indications of s-blocks and l-blocks.

It is important to stress that while unknowns are surface currents, the blocks have to be thought in terms of volumes that include the surfaces where the unknown currents reside; this allows to employ the (surface) Equivalence Theorem on the bounding box of the block. With this setting, the DD problem can be set in terms of coupled equations that involve the sources on the bounding box; in SFX, these are not treated as unknowns, but employed as forcing terms for the EM problem of the block in isolation (see Fig. 2 for an example).

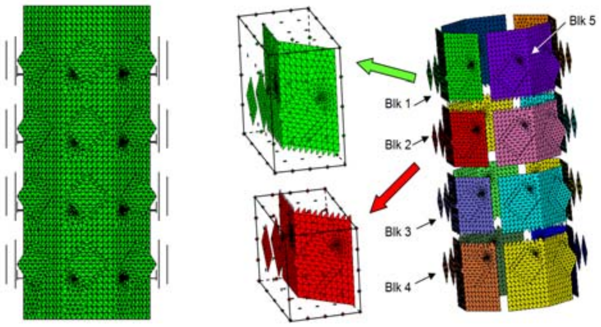

Fig. 2. CAD model of the conformal base station antenna: (a) Meshed geometry, (b) block separation used when analyzing it with SFX technique with the auxiliary sources around the Blocks 1 and 2 respectively.

Thanks to the Equivalent Theorem setting, if enough sources are considered, a linear combination of all the responses to the forcing terms on the bounding box will be able to correctly represent any currents inside the block, including the exact solution of the complete problem. Hence, if these responses are used to construct the aggregate basis functions the subspace $H_M^{\psi} \subset H_N^{f}$ will contain the desired solution. In order to make the procedure robust and efficient, an SVD is employed to retain those terms that are linearly independent (to a specified degree). The aggregate functions defined on the blocks of the structure are called ”Synthetic Functions” (SF).

With respect to the notation set in the previous section, the SF generation procedure can be summarized as follows. The conductor surface *S* is divided into N_{SB} portions S_s, $s = 1, \ldots, N_{SB}$ ($S = U_{s=1}^{N_{SB}} S_s$), the above-mentioned s-blocks (surface blocks); on each block, there will be $K_s << N$ unknowns. Some s-blocks may be contacting, i.e. a portion of their boundary may be shared with another s-block; these N_{LB} line segments are the l-blocks (line blocks).

The SF are defined on the s-blocks; this leaves out the individual elemental functions defined on the edges belonging to l-blocks. So far, these functions are left unconstrained as unknowns (i.e. not organized in aggregations). This allows a considerable flexibility in enforcing current continuity across blocks, which is naturally achieved – provided the above alluded spurious edge effects are not present.

In order to avoid artifacts due to edge-singularities in the single-block solution, the (edge) boundary condition has been modified on l-blocks; on these segments, half-RWG functions are inserted during the solution for the single-block problem, and deleted henceforth. This approach locally approximates a short-circuit (electric wall) condition, that effectively deletes the edge-singularity, and preludes to a successful current continuity. On the s^{th} *s*-block we will indicate by L_s the total number of these half-RWG. When solving for a block in isolation, there will therefore be $K_{Ts} = K_s + L_s$ unknowns.

In order to compute the responses that will lead to the SF, sources have first of all to be placed at the block feeding ports (if any is present); they will be called ”natural”, and their number (for the s^{th} block) denoted by N_{nat}^{s}; in case the problem entails an incident-wave forcing term, this will substitute for the port feeding as a natural source. Coupling with the rest of the structure is accomplished by considering two other types of sources.

- Sources placed on the block boundary, that are called ”coupling” sources; their number (for the s^{th} block) is denoted by N_{coup}^{s}. They are conveniently implemented as RWG, which allows re-use of the modules of any MoM code to compute the RHS of the single-block problem.

- If *l*-blocks are present (i.e. the block periphery cuts a solid metal of finite extent), sources have to be placed along that periphery, called ”connection” sources. They can be simply half-RWG, which simplifies the implementation. According to the previous discussion, on the s^{th} block there will N_{con}^{s} such sources.

The total number of sources on each block is therefore $N_S^s = N_{nat}^s + N_{con}^s + N_{coup}^s$. Each of these sources will constitute a RHS $[B_s^{(k)}]$, $k = 1, \ldots, N_S^s$ for the problem (1, 4), but limited to the number $K_{Ts} = K_s + L_s$ of the unknowns on the block. Denoting by $[Z_{B,s}]$ the pertinent MoM matrix of the problem, [$r_s^{(k)}$] the response to k^{th} source and omitting the block index for simplicity, the responses are defined by

$$[Z_B][r^{(k)}] = [B^{(k)}]$$

The responses are next assembled into a matrix

$$\left[R\right] = \left[\left[r^{(1)}\right],....,\left[r^{(N_s)}\right]\right]$$

and an SVD is performed on it, resulting in

$$[R] = [U][\rho][V\,]^{H} \tag{9}$$

Each column of $[U]$ identifies the coefficients of one aggregate function   in (6); the most relevant (largest) $N_{s,SF}$ terms are kept (note re-introduction of the block index s), and constitute the basis for the SF eXpansion (SFX) of the solution. In [7] an extensive study of the threshold used for the determination of the number of SFs has been presented. It is necessary at this stage to introduce the notion of SF (singular vectors) “associated” to a given type of source. While the SVD orthogonalization does not allow to identify an exact, direct correspondence between the sources and the SF, this relationship often exists approximately. In quantitative terms, a SF described by column $[U_j]$ is related to source k when the projection $[U_k]^H[r^{(j)}]$ is significantly larger than for all other responses. The correspondence is still stronger when one collectively considers homogeneous groups of sources and SF, e.g. natural, coupling, and connections. This justifies the ensuing terminology of “natural SF”, “coupling SF”, and ”connection SF”.

The scheme always calls for the inclusion of all N_{nat} natural SF; the number of the remaining SF to be kept is conveniently related to a thresholding of the SV sequence ρ_1, ρ_2, ..., ρ_{NS} . Upon fixing a threshold t, we will keep all SF associated to SV that satisfy

$$\rho_n \,/\, \rho_{N_{nat}} \leq t\,. \tag{10}$$

Examples of convergence studies and thresholding are given in Sec. IV.; convergence with respect to the employed number of coupling sources was studied in [7].

As to the SV thresholding issue, some general comments can be made:

- The threshold is problem dependent; very often the SV sequence has visible features that can guide a “manual” or automatic selection, like a clear jump or a clear change of slope. For example, if the block bounding box is the far region of [23], there is a jump in correspondence with the number of degrees of freedom of the radiated field; the latter is seldom observed in most practical problems, especially when the DD effects a “tearing” of the metal structure; nonetheless, the above example shows that the SV sequence depends on the physical structures, not on the source selection.

- The SV sequence and the effect of thresholding are expected to be different in antenna and scattering problems. Aside from the block-toblock interactions due to the cuts (discussed above), in antenna problems there will be often interaction between non-contacting but near features belonging to different blocks. The level of accuracy required in scattering problems is lower than required in antenna problems: these impacts on the threshold value selection. In this sense, it is very important that the convergence with respect to t be uniform, so that one can choose to be conservative in the absence of better knowledge. While no mathematical proof of uniform convergence can be presently offered for any of the existing compressive methods, the case studies in [7] and in Sec. IV.1 have always exhibited this convergence for SFX.

- When the DD calls for tearing of metal portions, it is to be expected that connection sources have almost the same importance as natural ones; therefore, to be on the safe side one can always include

  $$Q = N_{nat} + N_{con}$$

  SF$_{s}$, and start counting the SV threshold from that point; this corresponds to the modified threshold parameter

  $$\rho_n \,/\, \rho_Q \leq T \tag{11}$$

- Finally, we remark that the ratio between total number of SV and actual number of kept term is not necessarily an indication of numerical efficiency. As a matter of fact, the ideal situation knows exactly how many sources are necessary, which makes the abovementioned ratio one. This should be kept in mind, e.g., when interpreting the thresholding study in

Sec. IV.1. On the opposite end, the maximum dynamic range in the SV of the kept terms depends on the ”noise floor”, i.e. machine precision and accuracy of the implemented SVD algorithm.

III.3 Wavefront Basis Method (WBF)

This technique is a new approach to solve very large scattering electromagnetic problems based on the MoM. The method can be seen as an extension of the Asymptotic Phase front Extraction (APE) approach to MoM [25] - [29]. In what follows we will report on the key points of the method, and present preliminary results for 2D scattering problems. The presentation of WBF here is functional to exemplifying how the aggregate function paradigm can conveniently comprehend approaches of very different nature, and to discuss the issue of the DOF and the related sub-space choice. A more comprehensive description of the method will be presented in a forthcoming paper.

The Asymptotic Phasefront Extraction (APE) method is based on the observation that most of the degrees of freedom in the MoM are used just to follow the fast variation of the phase of the solution, while its amplitude varies on a much slower scale,

$$\underline{J}\left(\underline{r}\right)=\underline{J}_{slow}\left(\underline{r}\right)\exp\left(jk\Phi\left(\underline{r}\right)\right), \qquad (12)$$

so that it can be correctly described by much fewer basis functions having a multi-wavelength support. The APE produces a huge reduction in the matrix size, but matrix filling time is drastically more expensive due to the highly oscillatory behavior introduced by the inserted phase terms; overcoming this difficulty is the subject of several papers that we refrain to review here. The extraction of the ”asymptotic” phase function is a key issue. For smooth convex scatters the PO phase appears to be sufficient, while the issue for convex scatterers remains essentially open.

In the present approach [24], we employ the aggregation paradigm to construct the multiwavelength basis functions of APE starting from standard basis functions. In line with the aggregate functions approach discussed above, we consider our approach as an add-on to a fast MoM, of which it affects a compression. A key component of the method is the (novel) method for extracting the phase front of the induced currents, which leads to ”Wavefront Basis Functions” (WBF) aggregate functions. It is essentially a kind of numerical Beam Tracing performed with algebraic operations on the standard MoM matrix. This process permits reusing standard Fast-MoM codes as FMM or AIM. The method will be presented with specific reference to 2D scattering problems (TE incidence), and results will be presented for this case; because of the scalar nature of the problem, with respect to the previous sections we will drop the vector sign in all relevant notation. It can be extended to 3D problems; due to the algebraic nature of the procedure, most of the extension steps are straightforward, and we will briefly discuss those issues that are not obvious.

The problem is initially discretized with standard (sub-wavelength) basis functions as in (1); in the 2D problem explicitly considered, these are piece-wise triangular (PWT) functions. It is convenient to indicate them as $f_n\left(\underline{r};l\right)$ where the second argument is their (sub-wavelength) length l; as for the other aggregate-function methods, these will be termed ”elemental” basis functions. Next, one approximates the slow variation of the solution with the same type of functions used for the initial discretization (RWG or PWT), but of much larger, multi-wavelength extent; this is conveniently expressed as

$$J_{slow}\left(t\right)=\sum_{m=1}^{M}I_m^{slow}f_m\left(\underline{r};L_m\right), \qquad (13)$$

where $f_n\left(\underline{r};l\right)$ is the (phaseless) amplitude behavior of the (large) functions, that have the same expression of the elemental functions but different (multi-wavelength) support L. The definition of the aggregate functions follows from insertion of (12) and (13) into (1); the terms $f_m\left(\underline{r};L_m\right)\exp\left(jk\Phi\left(\underline{r}\right)\right)$ are conveniently approximated using the elemental basis functions, apt to represent the fast variations of the solution J; that is, one can write

$$f_m\left(\underline{r};L_m\right)\exp\left(jk\Phi\left(\underline{r}\right)\right)=\sum_{p=1}^{Km}\exp\left(jk\Phi\left(\underline{r}_p\right)\right)f_p\left(\underline{r};L_p\right)$$

where $\underline{r}_p$ is the center of the p^{th} elemental basis function; comparison with (2) and (6) yields

$$\begin{aligned}
&\psi_m\left(\underline{r}\right)=F_m^{AP}\left(\underline{r}\right)=\sum_{p=1}^{Km}U_{p,m}\,f_p\left(\underline{r};L_p\right) \\
&U_{p,m}=\exp\Big(j\,k\,\Phi\big(\underline{r}_p\big)\Big)\,f_m\left(\underline{r};L_m\right)
\end{aligned} \quad . \qquad (14)$$

The aggregate functions $\psi_m\left(\underline{r}\right)=F_m^{AP}\left(\underline{r}\right)$ have multi-wavelength support, and this results in a drastic compression of the standard MoM matrix. These functions are the ”Wavefront Basis Functions” (WBF) to be discussed here; a pictorial description of the WBF can be found in Fig. 3. The geometric aggregation underlying theWBF is trivial in the 2D case; in 3D it requires geometric aggregations like those employed in the oct-tree partitioning employed for fast multi-level methods; two different examples of how to do it can be found in [15] and [16](the aggregation is carried out with a different aim in these works).

We observe that the aggregate (multiwavelength) functions are overlapped; this makes enforcement of current continuity on sub-domains a non-issue.

With reference to the setting in Sec. III.1, one can observe that the method above is equivalent to look for a solution in the subspace $H_M^{\psi}\subset H_N^{f}$ with the pre-calculated asymptotic phase. Therefore, the accuracy of the method hinges about this Ansatz, and the ability to correctly estimate this phase.

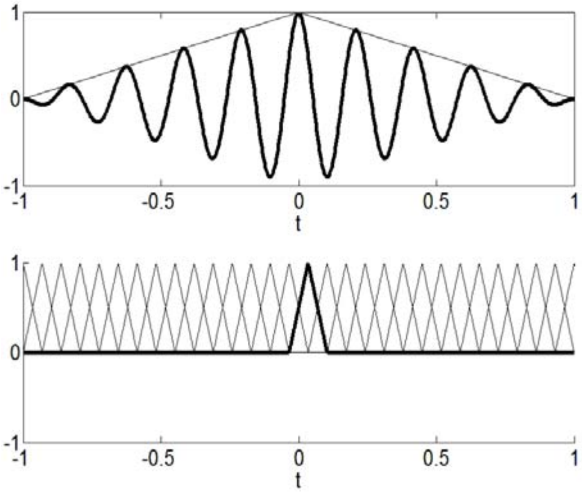

Fig. 3. WBF Aggregate basis function (top; real part) as linear combination of standard (sub-wavelength) basis functions (bottom).

Next, we use a Galerkin scheme with respect to the M aggregate functions. Assembling the basis change in algebraic form as in Sec. Sec. II., we have

$$\left[z\right]=\left[Z_{HF}\right]=\left[X_{HF}\right]^{H}.\left[Z\right].\left[X_{HF}\right]$$

$$X_{HF}=\begin{bmatrix}
U_{1,1} & & & \\
. & U_{1,2} & & \\
U_{k1,1} & . & & \\
 & U_{k2,2} & . & U_{1,M} \\
 & & . & . \\
 & & & U_{kM,M}
\end{bmatrix}, \qquad (15)$$

where $[X_{HF}]$ is sparse because two non-adjacent (aggregate) basis functions have disjoint support; each column has a number of non-zero terms independent of N. Note that one can use standard fast MoM codes to compute the vector-matrix products in (15). Very often the number M of aggregate basis functions is small enough to allow a direct solution for the compressed matrix Z_{HF} ; in all other cases, the above is used in the iterative solver. The compressive effect of the WBF produces a strong acceleration of the convergence.

Before proceeding further, we add that in most practical problems there will be sharp features (like the edge of a reflector) where the Ansatz (12) is questionable. This is solved in a simple manner by adding (unconstrained) elemental basis functions around these sharp features, which will add up to the count of the DOF like the unknowns associated to connection functions in SFX.

When the scatterer is flat or smooth and convex, PO is usually a good approximation for the phase; in this case, the above is directly applicable. The proposed algorithm, however, allows to go further. While a detailed description is beyond the scope of this work, the phase-tracking algorithm is outlined next in its salient traits.

One starts with the WBF with local PO phase. These will be zero-order WBF, ψ_k^0, described by coefficients $[U_k^{(0)}]$. Next, the radiation of all of these WBF$_0$ everywhere on the structure is considered; note that this is described by the product

$$\left[Z\right]\left[U_k^{(0)}\right]$$

that can be carried out by a fast matrix-vector multiplication. Because of the large support, the WBF radiate very narrow beams, and this is analogous to a beam shooting. The region(s) more intensely ”lit” will constitute the support for the first-order WBF, as pictorially shown in Fig. 4; their phase will be that of the field radiated by the 0-th order WBF. The procedure is repeated with WBF or order 1 acting as ”transmitter” to get the second-order WBF, and so on.

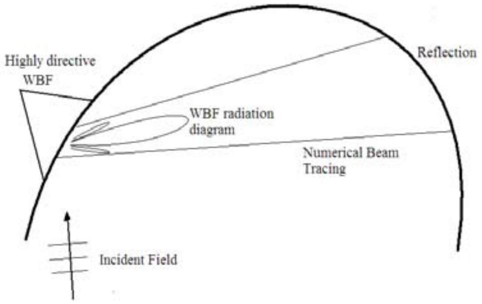

Fig. 4. Numerical Beam Tracing by iterating the operator of the EFIE.

2D tests of the method are reported in Sec. IV.2; in many instances it reduces the degrees of freedom to a very low value that is almost frequency independent, thus allowing a direct (iteration free) solution. Finally, we remark that a recent work [30] shares some of the objectives and approaches of this work.

III.4 Accuracy and DOF

It is often intuitive that a DOF reduction is possible when the solution is over-sampled. For example, in antenna problems one is often forced to employ mesh cells well below the λ/5−λ/10 rule employed in smooth scattering problems. It can thus be expected that a “smart” choice of the aggregate functions may tap into this redundancy to reduce the global DOF; for example, far interactions between aggregate functions will not need a fine detail to be accurately described. The above is correct, but it does not constitute the full picture.

A trivial, but somewhat revealing example is the following. If we take $M = 1$ and $\underline{\psi}_1$ to be the exact solution to the original problem, of course a 1-dimensional subspace is enough to allow the solution with compressive aggregate functions. No matter how trivial, this example points at the two key ingredients of a good compressive scheme: a) the aggregate basis functions must be related to the solution of the original boundary-value problem (hopefully, not in its entirety); b) the success of the method also depends on its ability in selecting the subspace of the aggregate-function solution in a way that depends on the properties of the forcing term (RHS).

In this perspective, one can observe that all compression schemes imply the use of aggregate basis functions that are ”Maxwellian”, in the sense that they are related to the (exact or asymptotic) solution of Maxwell’s equations with part of the original boundary conditions.

The methods like SFX, CBS, etc., rely on the solution of the problem in parts of the original structures, and these solutions are related to the original forcing field. It can be noted that this obviously comes at a (computational) cost, and in general the higher this cost (e.g. the larger the sub-domains), the more accurate the solution. The issue is finding an optimal way of achieving accuracy at a low cost.

The WBF method relies on the asymptotic approximation of the solution; this solution is not used in its entirety, and only the phase is employed. As already commented, this phase information essentially bounds the supbspace determination, and is key in ensuring a correct solution. The dependence on the forcing term in the construction of the solution subspace is more evident in this technique than in the explicit DD schemes like SFX and CBF. However, in both SFX and CBF the forcing field plays a role in the construction of the aggregate functions; in these case, one often considers a certain number of incident plane waves as ”natural sources”; in SFX and the case of an array, e.g., each block has its own natural source, which corresponds to considering all possible choices of port feeding.

Another vantage point can be gained by resorting to the SVD of the problems in (4) and (5):

$$\begin{aligned}\left[Z\right] &= \sum_{k=1}^{N} \zeta_k \left[u_k\right]\left[v_k\right]^H \\ \left[I^e\right] &= \sum_{k=1}^{N} \frac{1}{\zeta_k}\left[u_k\right]\left(\left[v_k\right]^H\left[B\right]\right)\end{aligned} . \qquad (16)$$

As well known, the above indicates that the most relevant singular values (SV) of [Z] are the smallest, in the sense that for a *generic* RHS the smallest (SV) are those who determine the solution accuracy. Considering now the compressed matrix,

$$[z]=[X]^H[Z][X]=\sum_{k=1}^{N}\zeta_k[X]^H[u_k][v_k]^H[X]. \tag{17}$$

one understands that the aggregate functions must ideally all reside in the span of the singular vectors associated to the most relevant (i.e. smallest) SV. Note that this criterion is essentially independent of the forcing term, and is the option most typically followed in approaches like SFX and CBF, less oriented to tailoring the solution subspace around a specific forcing term.

IV. NUMERICAL EXAMPLES

In this section numerical results are presented to clarify the application of SFX and WBF. All the reported examples have been simulated on standard PC, equipped with a Pentium4 processor, with 2.3GHz clock and 512MB RAM.

IV.1 SFX

The SFX method was employed to design the conformal broad-band GSM-UMTS base station antenna shown in Fig. 1. It was designed for adaptive (“smart”) operation. It is similar to, and inspired by the configuration in [31].

The structure has been chosen with the aim of applying the SFX method to a real-life geometry, and finally comparing simulation and measured results. The antenna requirements, design, and measurement procedure are outside the scopes of this paper; they are reported elsewhere, [32], [33] and in future communications; here we concentrate on the computational side and on the ensuing experimental validation.

The array antenna has 32 identical square stacked patches, in a 4 × 8 arrangement over an octagonal prism. Radiating elements are excited by proximity coupling with an L probe-strip structure, visible in the CAD model in Fig. 1. Excitation is modeled numerically via a voltage gap at the base of the probe, where it is connected to the (finite) ground. For SFX application, it is important to note that the underlying prism is a solid metal (the grounds of the facets are electrically connected).

In the full antennas, the 4 patches of each column are fed by a 1 : 4 equal-length, uniform-amplitude microstrip beam forming network printed below the ground plane; i.e., individual radiator are not accessible individually. One of the facets of the antenna in Fig. 1 (not shown there) was initially constructed with access to the four individual radiators; it will be used to compare simulation and measured results for S-parameters. The radiation results of the conformal array refer to operation with equal phase and amplitude over the eight columns (achieved via a commercial 1 : 8 uniform splitter).

At the center frequency, the antenna is about 3.1λ in height; the width of one facet is about 0.55λ while the average length of the edge of the stacked patches is of about 0.32λ. Its numerical model involves 24501 unknowns. We observe that no symmetry was used in the SFX simulation. A standard MoM solution in this case was unfeasible on the standard (32-bit) employed PC. The individual column, requiring 3010 unknowns, will thus be used for comparing SFX results to standard MoM.

Comparison between SFX and the standard MoM solution will be done with reference to the surface current relative error:

$$\varepsilon=\frac{\left\|I_{MoM}-I_{SFX}\right\|_2}{\left\|I_{MoM}\right\|_2}, \tag{18}$$

and directly on S-parameters or radiation pattern.

Analysis of the single column

The block partitioning of the facet is shown in Fig. 1c; it can be noted that there is one radiator per block, and that the block boundary cuts the (finite) ground, thus requiring the use of l-blocks and connection functions. It can be observed that the blocks are pairwise identical, the difference being on whether the block is central (bordering with one block per side) or on the edge. The coupling sources were placed on a regular grid on the (cubical) bounding box (not shown; an example of source distribution is shown for the full antenna below). The reported result refers to a total of 98 *coupling* sources on the block boundary for all blocks.

In counting SV and SF, it should be kept in mind that the present implementation employs real (as opposed to complex) response vectors, i.e. separating their real and imaginary parts prior to the SVD operation in (9); the reasons for this (not critical) choice are detailed in [7]). This makes the association between SF and sources to appear typically in pairs.

The SV sequences for the four blocks are shown in Fig. 7, and the associated convergence of the solution vs. SV truncation threshold *t* (in (10)) is shown in Fig. 8. The convergence for the radiation pattern is in Fig. 5. Comparison of S-parameters results for standard MoM and SFX are shown next in Fig. 6 for $t \approx 10^{-3}$.

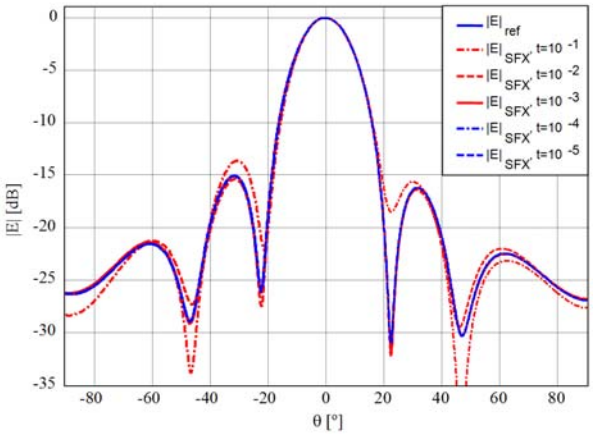

Fig. 5. Single column 4-patch array: radiation pattern convergence vs. SV truncation threshold *t*. The graph shows the cut along the array longitudinal axis. Solid blue line: reference; the other curves refer to the t value reported in the inset.

In order to interpret the results, we detail the relevant numbers for this case. We have one natural port on all blocks, i.e. $N_{nat}^{1,2} = 1$, while the number of connection functions is $N_{con}^{1} = 20$ and $N_{con}^{2} = 40$ on block 1 and 2 respectively. We have therefore Q_1 = 42 and Q_2 = 82 for the two types of blocks, having factored in the 2 factor for real/imaginary splitting; the position of these numbers in the SV sequences in Fig. 7 is indicated for further reference.

It is important to observe that the solution convergence is monotonic with respect to the number of considered SF; this is a guarantee of stable solution. The convergence analysis shows that keeping as many SF as natural plus all connection sources is a conservative estimate.

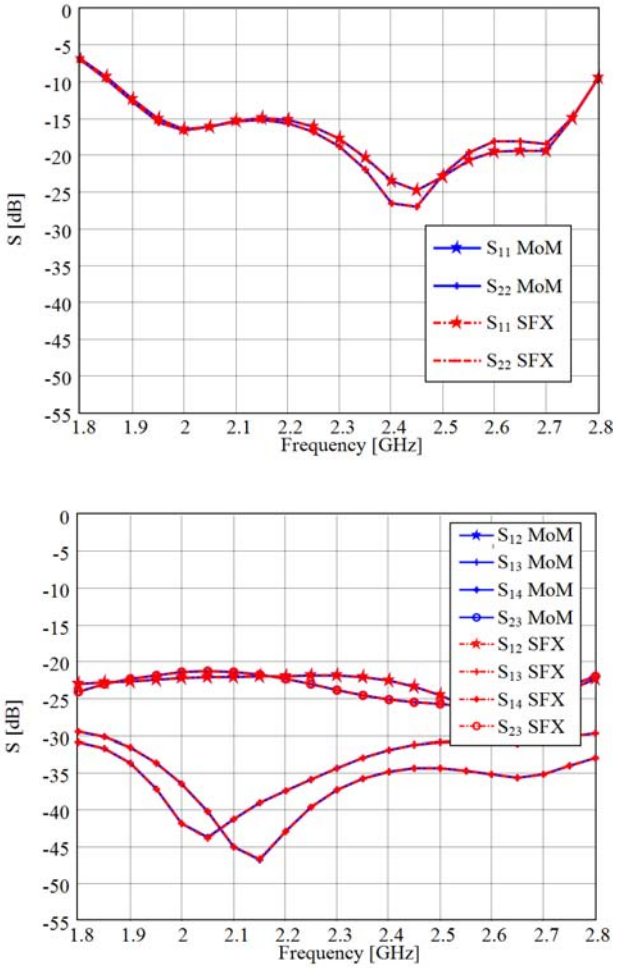

Fig. 6. Single column 4-patch array: Significant S parameters. Blue lines: standard MoM (reference); red lines: SFX.

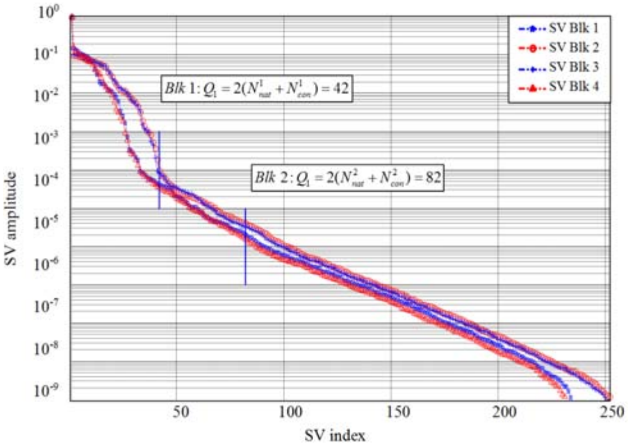

(a)

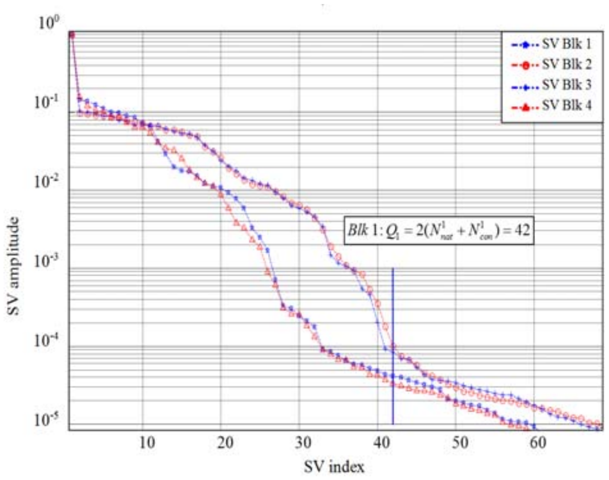

(b)

Fig. 7. Single column array (see Fig. 1): SV sequence. (a) Singular values sequence for the four s-blocks (superimposed); (b) Detailed view of the first part of the SV sequence. The vertical bars indicate the numbers Q.

Finally, Fig. 9 compares numerical and experimental results (reference MoM and SFX are undistinguishable); the agreement is very good (note that the slight shift in the resonance frequency happens below −20 dB in return loss).

As to numerical performances, using a $t \approx 10^{-5}$ threshold, the total dimension of the final linear equations system in the SFX basis has decreased to 658 unknowns (from 3010 unknowns in the RWG basis) and the solution time for this compressed system is of 4.9 seconds, which gives a cumulated solution time for all the 21 frequency steps of about 105 seconds. The necessary time for solving the 3010 unknowns linear equation system in the original RWG basis, for only one of the 21 frequency steps, is of 433.43 seconds. This means that the total solution time for all the 21 frequency steps in the original RWG basis is of 9102 seconds, 86 times the solution time in the SFX basis.

As the convergence results show, the $t = 10^{-5}$ value chosen for the SV threshold for this numerical simulation is very conservative. A higher compression of the final linear equation system, without significant changes in the accuracy of the final solution can be achieved also with $t = 10^{-3}$.

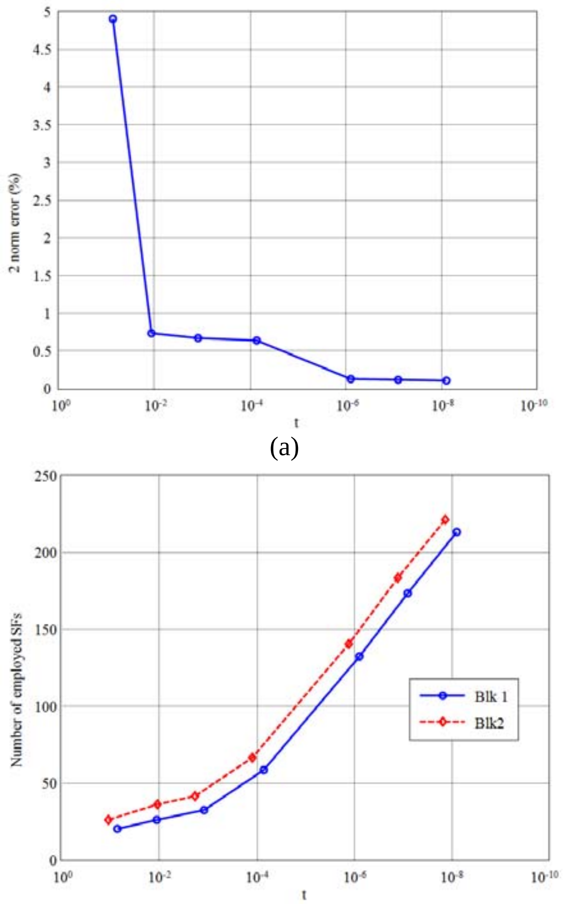

(a)

(b)

Fig. 8. Single column array (see Fig. 1). (a) Surface current error (18) with respect to SV threshold value t in (10); (b) Number of SFs corresponding to threshold values t; solid line: external blocks; dashed line: internal blocks.

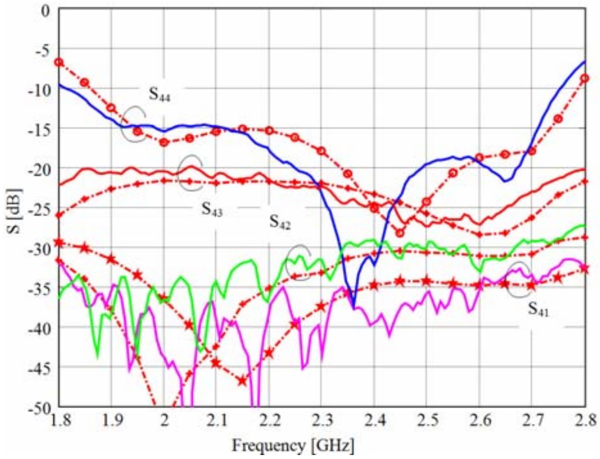

Fig. 9. Simulated vs. measured values for the S parameters of one column of the array considered in isolation; the curves without markers correspond to the measurements.

Analysis of the entire antenna

As alluded above, the only direct comparison between measured and simulated data is for the radiation pattern, yet including cross-pol. However, computed self- and mutual-impedances of the 32 radiating elements were employed in obtaining the radiation data; they were used to compute the excitation coefficients at all ports by solving the circuit problem with the S-matrix of the BFN splitters (data sheets and measured on prior breadboarding) and the S-matrix of the 32-element array.

The complete base station antenna in Fig. 1.a) was separated into the 16 blocks shown in Fig. 2 (exploded view of the mesh after block separation); each block contains two azimuthally neighboring radiating elements. Due to the symmetry of the structure and of the domain-decomposition, all blocks are identical to one of the two separately shown in Fig. 2, corresponding to internal or terminal location in the structure. Also in this case, we note that the block partitioning requires the cut of the continuous ground plane below the patches, i.e. the continuity of the current on it; this generates the need of connection functions and connection sources.

There are two natural responses for the block (4 natural SFs, arising from the separation into real and imaginary parts) originating from the port excitation of each one of the two radiating elements inside each block. In addition to natural and connection functions, a total of 56 coupling sources were used around each block.

The SV sequences for the different blocks are shown in Fig. 10, only for the two basic blocks shown in 2. The reported results refer to two threshold values: $T = 10^{-1}$ and $T = 10^{-2}$, the latter being very conservative. For $T = 10^{-1}$, the total number of SFX unknowns in the SFs basis was of 2354, and the solution time of about 204 seconds (about 3.4 minutes). With $T = 10^{-2}$ there were 4379 SFX unknowns, requiring 1358 seconds (about 22.6 minutes) to solve. The surface current distribution on the entire structure obtained for the higher accuracy SFX simulation is illustrated in Fig. 11.

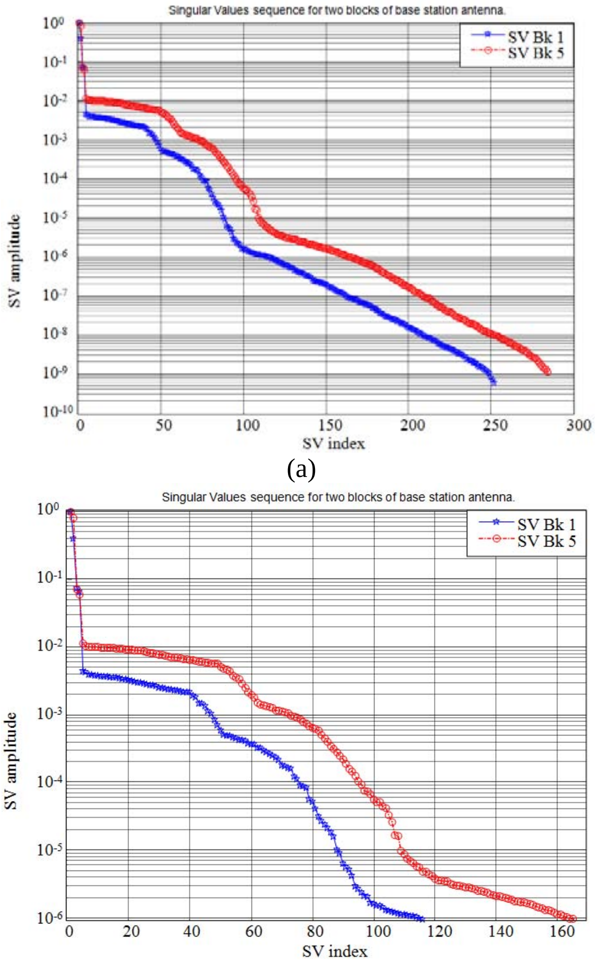

(a)

(b)

Fig. 10. (a) Singular values sequence for two blocks of conformal base station antenna; (b) detailed view of the first part of the SV sequence. For numbering see Fig. 2.

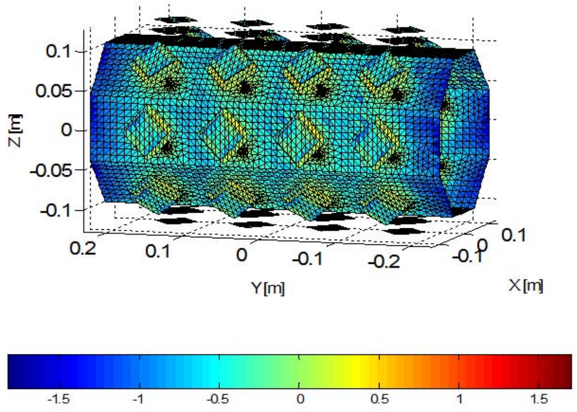

Fig. 11. Logarithmic plot for surface current on the base station antenna obtained by using the SFX technique.

The radiation patterns for the antenna were computed for the two sets of computed surface currents and reported in Fig. 12 for the co-polar and cross-polar components. The results for the two solutions show negligible differences. The radiation patterns were measured for eight elevation cuts (vertical planes, Fig. 13), one cut for each facet, and in the horizontal plane (azimuth cut, Fig. 14). Despite the structural symmetry, some differences are observed, and most likely due to feed cables (especially beyond 140◦) and mast in addition to fabrication tolerances in the radiating elements and BFNs.

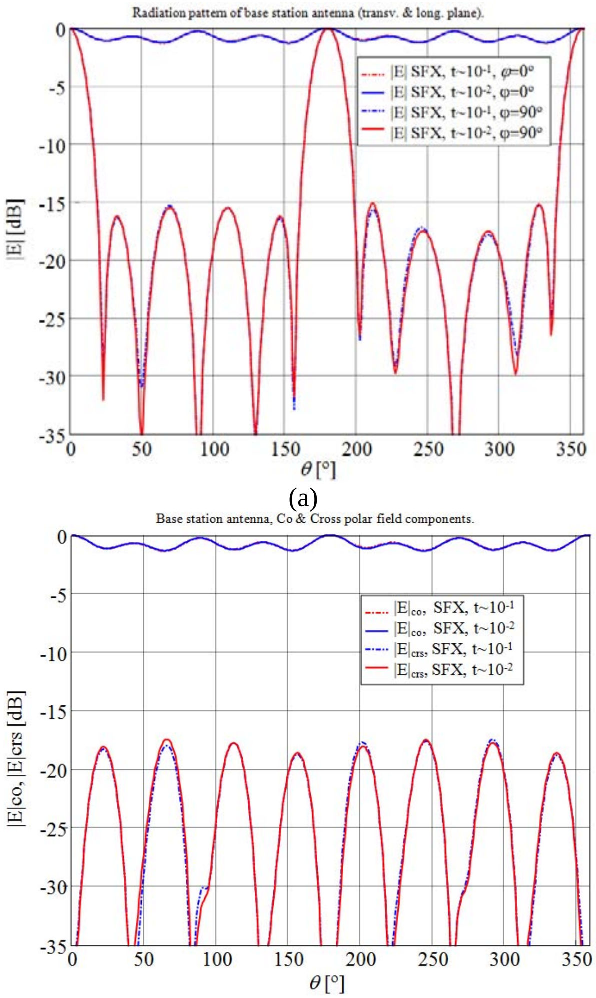

(a)

(b)

Fig. 12. SFX simulation results for base station antenna in Fig. 1; (a) radiation patterns in the two main planes for the base station antenna (solid line for $T \approx 10^{-2}$ threshold on SV sequence, dotted line for $T \approx 10^{-1}$ threshold); (b) Co- and cross-polar components (azimuthal cut) for the base station antenna (solid line for $T \approx 10^{-2}$, dotted line for $T \approx 10^{-1}$).

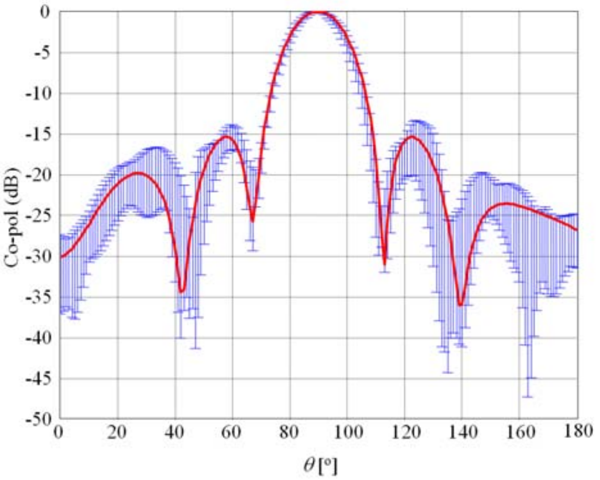

Fig. 13. Base station antenna: radiation pattern. The solid line shows computed results; the confidence bars display, for each angle, the min and max of the measured individual patterns for the 8 columns, in the plane orthogonal to each antenna facet.

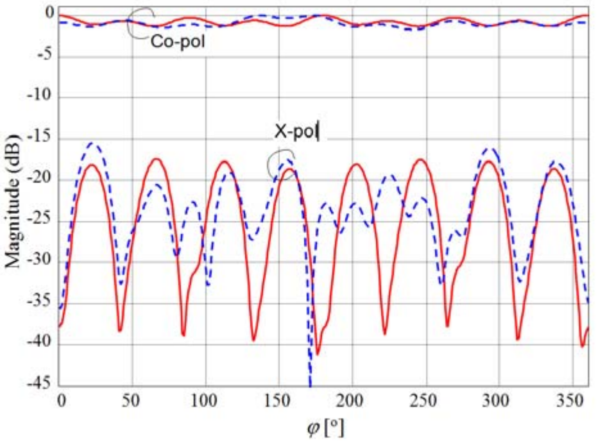

Fig. 14. Measured vs. simulated Co and Cross-polar components of the field for the entire array in azimuth cut.

IV.2 WBF

We will only consider simple examples so that we can use a simple fast 2D MoM algorithm due to the Toeplitz property of the resulting matrix. Nevertheless those easy examples contain all relevant difficulties to prove the method works, that is: concavity, multiple reflections, etc.. In all reported examples, we consider plane wave incidence along the directions indicated graphically in the relevant figures. The standard MoM (sub-wavelength) discretization uses triangular basis functions with $l = \lambda/10$ support; the number of associated basis functions will be denoted by N.

Scattering from flat strips were considered in [24]; here we discuss the case of scattering from a curved, concave strip; it is an arc of circle of angular aperture $\lambda/2$ and arc length L sketched in the inset of Fig. 15; the incidence is from the direction bisecting the opening angle ($\phi_{inc} = \pi/4$) in the concave part. Two cases were considered: $L = 360\lambda$, with $N = 3600$ and NWBF = 273, with support of about 6λ; and $L = 1440\lambda$, with $N = 14400$ but with the same NWBF as in the previous case, i.e. with aggregate function of about 24λ.

The error on the current, defined as in (18) (with SFX substituted for WBF), was 3.5% for the $L = 360\lambda$ case, and 1.8% for the larger, $L = 1440\lambda$ case. It is interesting to note that the number of necessary WBF terms is essentially independent of the frequency. This observation seems confirmed by [30]. The comparison for the radiated (far) field is shown in Fig. 15 for the case of $L = 1440\lambda$; panel (a) shows the overall pattern, and the following panels (b-h) report enlargement of various zones, to allow for a closer comparison. The figure allows to appreciate the accuracy of the WBF approach; the deviation from standard MoM is negligible almost everywhere, with small deviations in a low-amplitude region (panel d; well below -30dB).

V. CONCLUSION

We have discussed integral-equation methods that employ basis functions constructed by grouping standard ”elemental” basis functions (e.g. RWG); these basis functions are termed ”aggregate” throughout. The initial general setting includes both one-to-one basis change, that leave the number of unknowns unchanged, and compressive mappings, that reduce the overall number of necessary unknowns. In the former case, the reasons behind the basis change are typically centered around the spectral properties of the ensuing MoM matrix, like in the loop-tree decomposition used at low frequencies.

The discussion then has been focused on compressive aggregate-function methods. General considerations have been offered, and the specific examples of SFX and WBF methods employed to substantiate the general discussion. The SFX method belongs to the larger class of domain-decomposition methods, while WBF is based on high-frequency local solutions of Maxwell equations.

Compressive methods appear to be a mature technology in Computational EM; they can provide a simple ”boost” solution that re-uses existing MoM codes, but they can also be used to produce sophisticated tools. In particular, their combination with fast methods appears very promising, due to the complementary natures of the two approaches.

ACKNOWLEDGMENTS

The authors would like to acknowledge the cooperation with Prof. M. Orefice and Ing. G.L. Dassano for the design and measurement of the base station antenna employed as an application example in this paper.

This work has been partially developed in the Sixth Framework Program of the European Community within the Antenna Center of Excellence (ACE2). This work has been supported in part by the Spanish Ministerio de Educacion y Ciencia under the project TEC2004-04866-C04.

REFERENCES

[1] T. F. Eibert,“Iterative-solver convergence for loop star and loop-tree decomposition in method of moments solutions of the electricfield integral equation”, *IEEE Antennas Propagat. Mag.*, vol. 46, no. 3, pp. 80, pp. 2509−2521, 2004.

[2] S. Ooms and D. DeZutter, “A new iterative diacoptics based multilevel moments method for planar circuits”, *IEEE Trans. Microw. Theory Tech.*, vol. MTT-46, no. 3, pp. 280, pp. 2509−2521291, 1998.

[3] J. Heinstad, “New approximation technique for current distribution in microstrip array antennas”, *Electron. Lett.*, vol. 29, no. 21, pp. 1809−1810, 1993.

[4] E. Suter and J. Mosig, “A subdomain multilevel approach for the MoM analysis of large planar antennas”, *Microw. Opt. Technol. Lett.*, vol. 26, no. 4, pp. 270−277, 2000.

[5] V. V. S. Prakash and R. Mittra, “Characteristic basis function method: a new technique for efficient solution of method of moments matrix equation”, *Microw. Opt. Technol. Lett.*, pp. 95−100, 2003.

[6] L. Matekovits, G. Vecchi, G. Dassano, and M. Orefice, “Synthetic Function Analysis of Large Printed Structures: the Solution Space Sampling Approach”, *Digest of 2001 IEEE AP-S Soc. Int’l*

Symp., pp. 568−571, 8−13, July 2001, Boston, Massachusetts, USA.

[7] L. Matekovits, V. A. Laza, and G. Vecchi, “Analysis of Large Complex Structures with the Synthetic Functions Approach”, *IEEE Trans. Antennas and Propagat*., vol. 55, no. 9, pp. 2509−2521, 2007.

[8] K. F. Sabet, J. C. Cheng, and L. P. B. Katehi, “Efficient wavelet-based modelling of printed circuit antenna arrays”, *IEE Proc. Microwave Antennas Propagat.*, vol. 146, no. 4, pp. 298−304, 1999.

[9] R. Loison, R. Gillard, J. Citerne, G. Piton and H. Legay, “Optimised 2D multi-resolution method of moment for printed antenna array modelling”, *IEE Proc. Microwave Antennas Propagat.*, vol. 148, no. 1, pp. 1−8, 2001.

[10] P. Pirinoli, G. Vecchi, and L. Matekovits, “Multiresolution analysis of printed antennas and circuits: a dual−isoscalar approach”, *IEEE Trans. Antennas Propagat.*, vol. 49, no. 6, pp. 858−874, 2001.

[11] G. Schneider, G. Oberschmidt, and A. F. Jacob, “Efficient Implementation of a Wavelet Based Galerkin Scheme”, *IEEE Trans. Antennas Propagat.*, vol. 52, no. 9, pp. 2298−2304, 2004.

[12] F. Vipiana, P. Pirinoli, and G.Vecchi, “A Multiresolution Method of Moments for Triangular Meshes”, *IEEE Trans. Antennas Propagat.*, vol. 53, no. 7, pp. 2247−2258, 2005.

[13] Z. Baharav, Y. Leviatan “Analysis Of Scattering By Surfaces Using A Wavelet- Transformed Triangular-Patch Model”, *Microwave Opt. Tech. Lett.*, vol. 21, no. 5, pp. 359−365, 1999.

[14] W. C. Bandlow, G. Schneider, and A. F. Jacob, “Vector-valued wavelets with triangular support for method of moments applications”, *IEEE Trans. Antennas Propagat.*, vol. 53, no. 10, pp. 3340−3346, 2005.

[15] F. Vipiana, G. Vecchi, and P. Pirinoli, “A Multi-Resolution system of Rao-Wilton-Glisson functions”, *IEEE Trans. Antennas Propagat.*, vol. 55, no. 3, pp. 924−930, 2007.

[16] F. P. Andriulli, F.Vipiana, and G.Vecchi, “Hierarchical bases for non-hierarchic 3D triangular meshes”, *IEEE Trans. Antennas Propagat.*, vol. 56, no. 8, pp. 2288−2297, 2008.

[17] F. Vipiana, P. Pirinoli, and G.Vecchi, “Spectral properties of the EFIE-MoM matrix for dense meshes with different types of bases”, *IEEE Trans. Antennas Propagat*., vol. 55, no. 11, pp. 3229−3238, 2007.

[18] C. Craeye, “A Fast Impedance and Pattern Computation Scheme for Finite Antenna Arrays”, *IEEE Trans. Antennas Propagat*., vol. 54, no. 10, pp. 3030−3034, 2006.

[19] P. De Vita, A. Freni, L.Matekovits, P. Pirinoli, and G.Vecchi, “A combined AIM-SFX approach for complex arrays”, *Digest of 2007 IEEE APS Soc. Int’l Symp.*, pp. 3452−3455, Honolulu, Hawaii, USA, 10−15 June 2007.

[20] V. A. Laza, L. Matekovits, and G. Vecchi, “Synthetic Function Expansion with multi-grid approach”, *Proceedings of The First European Conference on Antennas and Propagation* (*EuCAP 2006*), ESA SP-626 CD Proceedings, pp. 386.1, Nice, France, 6−10 November 2006.

[21] F. C´atedra, E. Garca, C. Delgado, F. S. de Adana, and R. Mittra, “Development of an efficient rigorous technique based on the combination of CBFM and MLFMA to solve very large electromagnetic problems”, *Proc. Int’l Conf. Electromagnetics in Advanced Applications*, Torino, Italy, Sep. 2007.

[22] R. Maaskant, R. Mittra, and A. Tijhuis, “Fast Solution of Multi-Scale Antenna Problems for the Square Kilometre Array (SKA) Radio Telescope using the Characteristic Basis Function Method (CBFM) ”, *Applied Computational Electromagnetics Society Journal*, vol. 24, no. 2, 2009

[23] O. M. Bucci, and G. Franceschetti, “On the degrees of freedom of scattered fields”, IEEE Trans. Antennas and Propagat., vol. 37, no. 7, pp. 918−926, 1989.

[24] F. Vico, G. Vecchi, M. Ferrando, ”A New Sparsification And Compression Technique For High Frequency Mom By Means Of Wavefront Basis Functions”, *Proceedings of The First European Conference on Antennas and Propagation EuCAP, 2007.*

[25] K. R. Aberegg and A. F. Peterson, “Application of the Integral Equation-Asymptotic Phase Method to two-dimensional scattering”, *IEEE Trans. Antennas Propagat.*, vol. 43, no. 5, pp. 534−537, 1995.

[26] D. Kwon, R. J. Burkholder, and P. H. Pathak, “Efficient Method of Moments Formulation for Large PEC Scattering Problems Using Asymptotic Phasefront Extraction (APE)”, *IEEE Trans. Antennas Propagat*., vol. 49, no. 4, pp. 583−591, 2001.

[27] S. N. Chandler-Wilder, S. Langdon, “A Galerking Boundary Element Method for High Frequency Scattering by Convex Polygons”, *SIAM J. Numer. Anal*., vol. 45, no. 2, pp. 610−640, 2007.

[28] K. Tap, R. J. Burkholder, P. H. Pathak, and M. Albani, “Methods for Efficiently Computig the MoM Impedance Matrix for APEx Type Basis Functions”, *IEEE AP-S Soc. Int’l Symp.*, pp. 4119−4122, Albuquerque, *2006*.

[29] R. J. Burkholder, and T. Lee, “Adaptive Sampling for Fast Physical Optics Numerical Integration”, IEEE Trans. Antennas and Propagat., vol. 53, no. 5, pp. 1843−1845, 2005.

[30] C. P. Davis and W. C. Chew, “Frequency-Independent Scattering from a Flat Strip with TE_z-Polarize Fields”, *IEEE Trans. Antennas Propagat.*, vol. 56, no. 4, pp. 1008−1016, 2008.

[31] S. Raffaelli, M. Johansson, and B. Johannisson, “Cylindrical Array Antenna Demonstrator for WCDMA Applications”, *Proc. of ICEAA03*, Turin, Italy, 8−12 Sept. 2003.

[32] G. Vecchi, P. Nepa, G. Manara, A. Serra, M. Orefice, V. A. Laza, L. Matekovits, G. L. Dassano, and V. Kysrytsya, “Wideband Stacked-Patch Designs for Base Station Antenna”, *Wireless Reconfigurable Terminals and Platforms* (*WiRTeP*), pp. 241−245, Rome, Italy, 10−12 April 2006.

[33] G. Dassano, V. A. Laza, L. Matekovits, M. Orefice, and G. Vecchi, “Numerical and Experimental Characterization of a Wide- Band Conformal Base Station Antenna”, *Digest of 2006 IEEE AP-S Soc. Int’l Symp.*, pp.3735−3738, Albuquerque, New Mexico, 9−14 July 2006.

Ladislau Matekovits was born in Arad (Romania), on November 19, 1967. He received the degree in Electronic Engineering from Institutul Politehnic din Bucureşti, Bucureşti, Romania and the Ph.D. (Dottorato di Ricerca) in Electronic Engineering from Politecnico di Torino, Turin, Italy in 1992 and 1995 respectively. Since 1995 he has been with the Electronics Department of the Politecnico di Torino, first with a post-doctoral fellowship, then as a Research Assistant. He joined the same Department as Assistant Professor in 2001 and was appointed as Senior Assistant Professor in 2005. In late 2005 Ladislau Matekovits was Visiting Scientist at the Antennas and Scattering Department of the FGAN-FHR, Wachtberg, Germany. His main research interest is in the numerical analysis of printed antennas and in particular in the development of new, numerically efficient full-wave techniques to analyze large arrays, in metamaterials and in optimization techniques. Dr. Matekovits is recipient of many awards in international conferences, and is member of various conferences program committees. He was Assistant Chairman and Publication Chairman of the European Microwave Week 2002 (Milan, Italy). He serves as a reviewer for the various Journals in his fields of interest.

Giuseppe Vecchi received the Laurea and Ph.D. (Dottorato di Ricerca) degrees in electronic engineering from the Politecnico di Torino, Torino, Italy, in 1985 and 1989, respectively, with doctoral research carried out partly at Polytechnic University (Farmingdale, NY). He was a Visiting Scientist at the Polytechnic University from August 1989 to February 1990. In 1990, he joined the Department of Electronics, Politecnico di Torino, as an Assistant Professor (Ricercatore) where, from 1992 to 2000, he was an Associate Professor and, since 2000, he has been a Professor. He was a Visiting Scientist at the University of Helsinki, Finland, in 1992, and has been an Adjunct Faculty in the Department of Electrical and Computer Engineering, University of Illinois at Chicago, since 1997. His current research activities concern analytical and numerical techniques for analysis, design and diagnostics of antennas and devices, RF plasma heating, electromagnetic compatibility, and imaging.

Felipe Vico was born in Valencia, Spain, in 1981. He received the M.S in 2004 in telecommunication from the Polytechnic University of Valencia. From 2004 to 2005 he was with the Institute of Telecommunications and Multimedia Applications (iTEAM) as a Research Assistant. From 2005 to 2006 he was awarded with a Research Fellowship by the Spanish Ministry of Culture. Since 2007 he has been an Assistant Professor in the Communications Engineering Department, Polytechnic University of Valencia, where he is currently working toward the Ph.D degree. His research interests include numerical methods applied to scattering and radiation problems, asymptotic techniques, hybridization of high frequency and numerically rigorous methods and fast computational techniques applied to electromagnetics.

Diffraction-like Synthetic Functions to Treat the Scattering from Large Polyhedral Metallic Objects

Massimiliano Casaletti [1], Stefano Maci [1], and Giuseppe Vecchi [2]
[1] Department of Information Engineering
University of Siena, Siena, Italy
casaletti@dii.unisi.it , macis@dii.unisi.it

[2] LACE Department of Electronics
Politecnico di Torino, Torino, Italy
giuseppe.vecchi@polito.it

***Abstract*─** This paper presents an innovative procedure that allow for the Method of Moments (MoM) analysis of electrically large objects composed of flat faces, i.e. open or closed polyhedrons with or without attached plates. The method is framed within the category of iteration-free, compressive basis function approaches. Two kinds of diffraction-like basis functions are introduced to achieve drastic memory requirement compression; relevant results compared with those obtained employing standard RWG basis functions are presented.

***Index Terms*─** Method of Moment (MoM), large structures, Synthetic Functions (SFX), scattering.

I. INTRODUCTION

The Integral Equation (IE) approach combined with the Method of the Moment (MoM) discretization scheme is widely used in the prediction of the electromagnetic scattering from a large complex objects. The conventional MoM formulations have well-known limits to the problem size, because they lead to large, dense and sometimes ill-conditioned matrices, with a consequent huge memory occupation and CPU time consumption. In order to overcome these problems, different schemes have been presented in literature. Among these schemes, we mention the Fast Multipole Method (FMM), the Adaptive Integral Method (AIM), and the multilevel matrix decomposition algorithm.

An alternative route is taken in a family of methods that employ an “iteration free” approach [1], where standard (e.g. RWG) basis functions are aggregated into larger functions. This notably includes the Synthetic Function expansion (SFX) [2] and the Characteristic Basis Function (CBF) [3] methods. These aggregate basis functions are defined from the solution of smaller-size numerically-tractable problems, excited by appropriate sources, and then used in the MoM solution of the large problem. This allows one to incorporate the intermediate and macro-scale features of the structure, while maintaining a reduced number of unknowns. Thousand of wavelength structures can be treated with memory and CPU cost provided by a standard personal computer. Within this scheme, we proposed here a method to treat large portions of PEC planar objects containing edges; special cases include geometries with large polyhedral sub-surfaces, as frequently encountered in ships and especially in satellites. We will show that this appears a quite useful addition to the general framework of the iteration free methods.

The core of the proposed method is centered around the construction of the basis functions that describe the edge diffraction effects. As usual in compressive methods, the large-support basis functions derive from the (exact or approximate) solution of the EM problem on portions of the overall structure, for a set of suitable excitations. A key issue investigated here is the excitation mechanism employed to generate these basis functions. Two different approaches are investigated, and the relevant results critically compared: 1) spherical wave generated diffraction basis functions where the generating dipoles are located slightly displaced from the edge; 2) grazing plane-wave generated BF with different propagation directions.

The paper is structured as follows: in Section II, the iteration free synthetic function method is summarized to frame the present approach; the particular case of flat metallic portions and of the object within the Physical Optics interpretation is discussed. In Section III, the appropriate definitions of the two types of generating sources for defining the basis functions is presented. Section IV shows the procedure to select and construct the synthetic basis functions on the basis of the singular value decomposition, and the subsequent followed Section V illustrate the MoM spectral domain solution, with focus on the calculation of the impedance matrix entries. Numerical results are presented in Section VI.

II. THE SFX METHOD

In the following, we will start from the baseline SFX method. The first step is a geometrical domain-decomposition, that breaks down the conductor surface into portions, that we called surface blocks (s-blocks) S_i, whose collection reconstruct the entire surface S on which EFIE is applied. Each s-block is bounded by a boundary line ∂S_i. On each s-block S_i, one generates basis functions with support on the entire s-block, that are subsequently used as synthetic basis functions (SBF) for the analysis of the entire structure. Since the number of SBF functions is significantly smaller than those used in a conventional description [4], the overall number of unknowns is drastically reduced with a consequent gain in terms of memory and solution time. These basis functions defined over the entire domain S_i are called “Synthetic Functions” (SF), they are generated from the numerical solution of the electromagnetic problem for the block in isolation, under excitation by suitably defined “generating” sources. The synthetic functions are obtained from a linear combination of the responses to all sources via a procedure based on the Singular-Value Decomposition (SVD). Because of the strong reduction of the global number of unknowns, one can store the MoM matrix and afford a direct solution. In this sense, the method can be viewed as an ”iteration-free” alternative to so-called fast methods (like the Fast Multiple Method) that are based on iterative solvers for the MoM linear system, and on special techniques to avoid the storage of the full MoM matrix. The method is kernel-free, and can be implemented on top of existing MoM codes.

A. Flat Perfectly Conducting Portions of Complex Objects

Let us assume as an s-block a flat perfectly conducting portion of surface. If the geometrical decomposition conforms to the mesh of the entire structure the boundary line ∂S may result in zigzag lines to conform to the mesh edges (see surface S_i in Fig. 1). The way to treat interaction among blocks with non-straight contour ∂S mesh is described in [4] and will not be repeated here. For the sake of simplicity, we will assume here that the boundary line ∂S is composed by straight segments (see surface S_i in Fig. 1); this is not a restriction, except on the meshing algorithm (the meshing should follow the block subdivision and not vice-versa). As described for the general scheme [4], the s-block (flat polygonal face) is isolated from the rest of the structure by a (virtual) closed surface S^{eq} (bounding box), via the Equivalence Theorem. On this separation surface one then allows an equivalent current distribution that accounts for the external world. This equivalent current distribution may be defined by using several kinds of wave objects, like plane waves [3], point sources [4], or complex point sources. The SFX formulation *does not* use the coefficient of these wave objects as unknowns of the problem. Rather it use these sources as *generating sources* for the basis functions to be defined on for the s-block, called Synthetic Functions (SF). The set of EM responses to the generating sources constitutes the starting point for the generation of the SF set, in which a SVD is employed to orthogonalize and discriminate among the totality of the responses that might have scarce linear independence.

As mentioned before the choice of the generating sources is largely arbitrary [4], and different sets of (synthetic) basis functions arise from different choices of generating sources. The efficiency of each scheme, i.e. the number of necessary SF to represent the solution to the complete problem is actually associated to the ability of the generating sources to produce responses that well reconstruct the solution space, the latter being defined as the (sub) space spanned by all the possible solutions for the entire problem localized to the considered s-block.

B. Physical Optics SF

When addressing the internal part of the equivalence problem for the s-block, the (arbitrary) medium that can fill the external part is chosen in order to simplify as much as possible the Green's function of the internal region. The conventional choice is to fill the external region by a free-space medium. In this case, the SF basis functions f_n are derived by a MoM solution of a problem of the dimension of the surface block in isolation. Taking advantage from the fact that our s-block is a flat surface, the region external to S^{eq} is filled with the infinite continuation of the flat portion, to recover an infinite flat plate (see Fig. 1). This allows the construction of the SF f_i in exact closed form for each generating source, simply applying the image principle. The responses so obtained will be called "PO functions" in the following. Because of the simplicity of dealing with analytical expressions of PO functions, in the following we will use the PO functions as starting point for the generation of SF on flat polygonal plates. The usual SVD process [4] will be used on them to generate the actual SF.

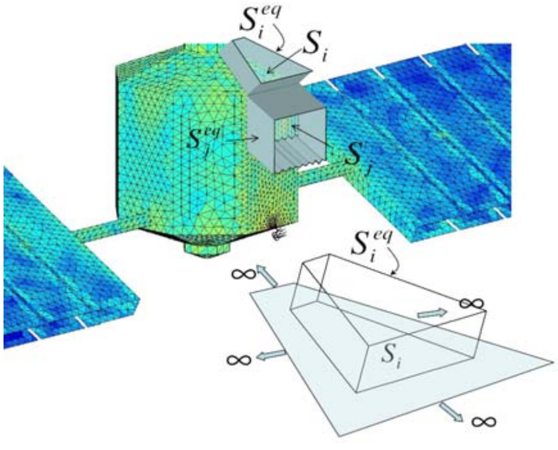

Fig. 1. Flat surface blocks on complex object. The surface block S_i is bounded by true edges; part of the contour of the surface block S_j matches the mesh edges. The surface blocks are isolated by equivalent surface S_i^{eq}; the exterior of this surface is filled by the infinite continuation of the flat surface to simplify the internal region.

As generating sources we will use and compare both grazing plane waves and point sources (dipoles); this is addressed in the next sections.

In order to avoid confusion, in the following we will always deal with a block subdivision in which the edges of the s-block correspond to actual edges in the overall structure. This is the sensible choice for this approach, but it is obviously different from the setting in [4], where large plates could be "torn" into smaller pieces to reduce the associated computational effort. The singular behavior of the field at these edges is therefore not an artifact of the procedure in this case.

III. GENERATING SOURCES AND THEIR SPACE AND SPECTRAL RESPONSES

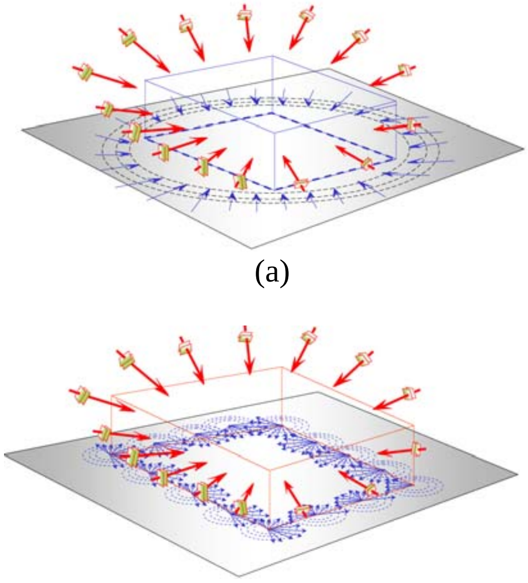
(a)

(b)

Fig. 2. Different schemes for generating PO synthetic basis functions. (a) Homogeneous plane waves plus nearly evanescent plane waves, (b) homogeneous plane waves plus spherical wave sources.

The choice of the generating sources is a key point for the correct reconstruction of the solution space. Let us subdivide conceptually the current solution J on the s-block in the sum of two contributions $J_0 + J_f$, where J_f are the "fringe" currents associated to the diffraction process at the true edge of the S-block, and J_0 is the remainder. Two schemes will be investigated here.

In a first scheme the solution space associated to the fringe currents J_f will be spanned by synthetic functions generated by *elementary dipoles* distributed close to the edges of the S-block. The synthetic functions to describe the remainder contribution J_0 are instead generated by *homogeneous plane waves* . In a second scheme, the contribution J_0 is still represented by SFs generated by homogeneous plane waves, while the fringe contributions are generated by *nearly-evanescent (near grazing) plane waves*. The two schemes differ in the way to describe the fringe contributions. We have set our focus on the diffraction effects, and therefore we limit our investigation here on the contribution J_f described by the two mentioned alternatives.

A. Spherical Wave Generation of Po Basis Functions

As prescribed in the framework of high frequency diffraction theory, the diffraction process may be described by equivalent spherical wave incremental contributions arising from the edge [5, 6]. Following this guideline, it seems adequate the use of (elementary) dipoles distributed close to the edge as generating sources of fringe currents. To this end, let us introduce a local reference system with the τ-axis along the considered edge of the surface, the η-axis orthogonal to the edge oriented toward the surface and z-axis normal to the surface, that lies at $z=0$ (see Fig. 3).

The generating electric dipoles are centered at a generic position τ' and displaced of $\lambda/10$ from the edge along both τ and η in order to avoid inappropriate singularities at the edge. To cover the two polarizations, pairs of dipoles parallel and orthogonal to the edge are used. The PO induced currents normalized with respect to the maximum values can be well approximated by the following expressions:

$$\begin{Bmatrix} \mathbf{f}_\tau(x',x,y) \\ \mathbf{f}_\eta(x',x,y) \end{Bmatrix} = \sum_m \frac{\alpha}{\pi\lambda} \frac{e^{-jkr_m}}{r_m}\left(1-\tfrac{1}{kr_m}\right)\chi(x,y) \cdot \begin{Bmatrix} \hat{\boldsymbol{\tau}}_m \\ \hat{\boldsymbol{\eta}}_m \end{Bmatrix}, \quad (1)$$

where: $\hat{\boldsymbol{\tau}}_m = \hat{\mathbf{s}}_m^- = \frac{(\mathbf{v}_{m+1}-\mathbf{v}_m)}{|\mathbf{v}_{m+1}-\mathbf{v}_m|}$, $\hat{\boldsymbol{\eta}}_m = \hat{\mathbf{z}} \times \hat{\mathbf{s}}_m^-$,

$$r_m = \sqrt{(\tau-\tau')^2 + (\eta-\lambda/10)^2 + (\lambda/10)^2},$$

$\hat{\mathbf{s}}_m^- = \frac{(\mathbf{v}_{m+1}-\mathbf{v}_m)}{|\mathbf{v}_{m+1}-\mathbf{v}_m|}$, $\mathbf{v}_m$ (m=1,.. N) are the position vectors of the s-block surface vertexes, α is the normalization constant that is taken to have maximum amplitude equal to unity, and $\chi(x,y)$ is the characteristic function of the s-block, that is unity inside the s-block and zero elsewhere. The basis functions are normalized in such a way that the maximum value of the amplitude (obtained for $\eta=0$, and $\tau=\tau'$) is equal to unity. The generating sources are placed along the polygonal contour of the surface with uniform steps, thus constructing a sequence of type:

$$\mathbf{f}_{n,\xi}(x,y) = \mathbf{f}_\xi(n\delta,x,y) = = \frac{25}{\pi\lambda}\sum_m \frac{e^{-jkr_n}}{r_n}\left(1-\tfrac{1}{kr_n}\right)\chi(x,y)\hat{\boldsymbol{\xi}}_m, \quad (2)$$

where: $\hat{\boldsymbol{\xi}}_m = \hat{\boldsymbol{\tau}}_m, \hat{\boldsymbol{\eta}}_m$

$$r_n = \sqrt{(\tau-n\delta)^2 + (\eta-\lambda/10)^2 + (\lambda/10)^2}.$$

Since the currents are devoted to reconstruct diffraction effects, these functions are herein after denoted as *Spherical wave generated-PO functions (SWG-POF)* . The step δ between contiguous generating sources will be chosen according to the SVD scheme presented in the subsequent section.

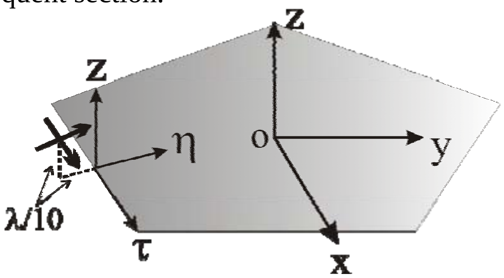

Fig. 3. Geometry for defining SWG-POF.

It is interesting to look at the Fourier transform

$$\tilde{\mathbf{F}}_{n,\xi}(k_x,k_y) = FT[\mathbf{f}_{n,\xi}(x,y)] \quad (3)$$

of the two types of PO-functions. Note that the spectrum is not available in closed form due to the presence of the truncation function $\chi(x,y)$; therefore an FFT has been used to calculate it. The typical spectral domain behavior of $\left|\tilde{\mathbf{F}}_{n,\xi}(k_x,k_y)\right|$

for the case of a flat metallic square s-block is shown in Fig. 4, while the space domain response is strongly concentrated in the area close to the generating dipole, the spectral amplitude is concentrated close in an angular spectral sector around the circular periphery of the visible region (Fig. 4). Note that the extension of the significant spectral region is different when the source is near a corner and when it is near a fault edge. These spectra can be simply explained (at least inside the visible region) by invoking the direct relationship between the far field radiated by each basis function and the spectrum of the same basis function. It is indeed evident that the PO field scattered by a metallic plate illuminated by a coplanar dipole is concentrated in the paraxial region, with an angular spread which is dictated by the metallic sector seen by the generating source in its actual position; it is also useful to recall that the boundary of the visible region in (k_x, k_y) corresponds to grazing directions. For instance, if the dipole is placed on a corner of the first quadrant of a square plate, the far field radiation density (spectrum amplitude) is concentrated in the opposite direction (third quadrant of the spectral plane) close to grazing aspect (boundary of the visible region) and along an angular range of 90°. If the source is placed at the center of the edge, the radiation is concentrated along an angular range of 180° in the opposite directions. The spectral density concentration will be used to derive a criterion to select the right number of generating sources to be placed around the s-block periphery (see Section IV).

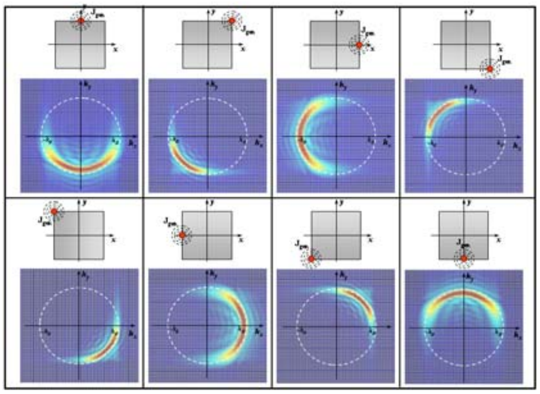

Fig. 4. Spectrum amplitude of the diffraction basis functions for a given position of the spherical wave generating sources.

B. Nearly Grazing Plane Wave Generation of PO Basis Functions

An alternative description of the diffraction contribution can be given in terms of basis functions generated by propagating nearly grazing plane waves. As a generating source we take TE or TM polarized plane waves characterized by the wave-vector $\mathbf{k}' = \mathbf{k}_t^{'} + \mathbf{z}\sqrt{k - \left(k_x^{'}\right)^2 - \left(k_y^{'}\right)^2}$, where $\mathbf{k}_t^{'} = k_x{'}\hat{\mathbf{x}} + k_y{'}\hat{\mathbf{y}}$ is the transverse to z part of $\mathbf{k}'$, and k is the free-space wave-number. The transverse wave-vectors $\mathbf{k}_t^{'}$ associated to the generating plane waves are chosen so that $k^2 \tilde{\lessgtr} \left(k_x^{'}\right)^2 + \left(k_y^{'}\right)^2$ (near grazing incidence) with a constant angular step; namely

$$\mathbf{k}_{tn}^{'} = k\left(\sin\left(n\Delta\phi\right)\hat{\mathbf{x}} + \cos\left(n\Delta\phi\right)\hat{\mathbf{y}}\right), \qquad (4)$$

where the step $\Delta\phi$ between contiguous wave-numbers will be chosen according to the SVD scheme presented in the next section and in a similar way as done for the selection of the spherical wave basis functions. The normalized PO currents associated to the above plane waves are given by

$$\begin{aligned} \mathbf{f}_{n,TM}(\mathbf{k}', x, y) &= \mathbf{k}_{tn}^{'} e^{-j(k_x{'}x + k_x{'}y)} \chi(x,y), \\ \mathbf{f}_{n,TE}(\mathbf{k}', x, y) &= \mathbf{k}_{tn}^{'} \times \hat{\mathbf{z}} e^{-j(k_x{'}x + k_x{'}y)} \chi(x,y), \end{aligned} \qquad (5)$$

where χ is the above-defined characteristic function of the polygonal surface. We note that in order to interpret the TE component in (5) as a normalized grazing wave PO current for TE polarization, we should apply a process to the limit for near grazing of the normalized currents. We note indeed that the non-normalized TE PO currents are zero for exact grazing incidence, but the TE component are essential to the completeness of the description. The spectrum of the above functions can be evaluated in a closed form for arbitrary polygonal flat surface with vertexes located at the position vectors $\mathbf{v}_m$ (m=1,.. N), as

$$\begin{aligned} \tilde{\mathbf{F}}_{n,TM}\left(k_x, k_y\right) &= -j\frac{\mathbf{k}_{tn}^{'}}{k\left|\mathbf{w}_n\right|^2}\sum_{m=1}^{N} T_{n,m}(k_x, k_y), \\ \tilde{\mathbf{F}}_{n,TE}\left(k_x, k_y\right) &= -j\frac{\mathbf{k}_{tn}^{'} \times \hat{\mathbf{z}}}{k\left|\mathbf{w}_n\right|^2}\sum_{m=1}^{N} T_{n,m}(k_x, k_y), \end{aligned} \qquad (6)$$

where

$$T_{n,m}(k_x,k_y) = \left(\mathbf{w}_n{}^* \cdot \mathbf{s}_m^-\right) e^{j\frac{k}{2}\mathbf{w}_n\cdot\mathbf{s}_m^+} \frac{\sin\left(\frac{k}{2}\mathbf{w}_n\cdot\mathbf{s}_m^-\right)}{\frac{k}{2}\mathbf{w}_n\cdot\mathbf{s}_m^-}, \quad (7)$$

in which

$$\begin{aligned} \mathbf{w}_n &= (\mathbf{k}_{tn}^{'} - \mathbf{k}_t)/k, \\ \mathbf{s}_m^{\pm} &= \left(\mathbf{v}_{m+1} \pm \mathbf{v}_m\right). \end{aligned} \quad (8)$$

The spectrum of each *plane wave generated PO functions* (PWG-POF) is concentrated along the boundary of the visible region and rotates at each angular increment $\Delta\phi$ in the direction of incidence of an equal spectral azimuthally step. Figure 5 illustrates the same case of a square plate used in for the spherical wave generation (Fig. 4). At difference with SWG-POF, here the spectral spot is azimuthally narrow, being the spectral density in both directions inversely proportional to the size of the domain in the corresponding spatial direction. This is well evident in case of a rectangular plate, because of the associated separable *sinc* spectral functions, and it holds in general.

Compared to the spherical wave functions, the present basis functions appear to be spectrally localized, while the previous functions were spatially localized; they are therefore complementary.

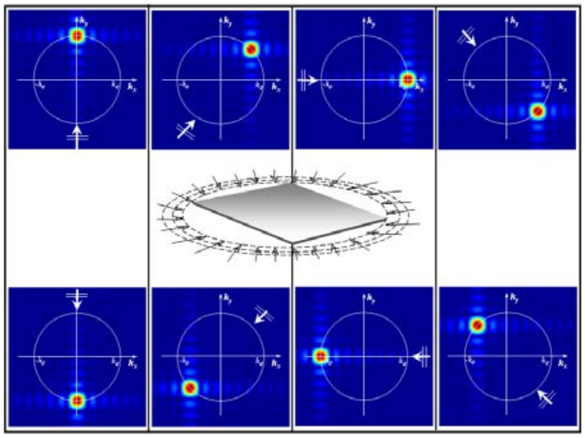

Fig. 5. Amplitude of the spectrum of the PO basis functions for a given direction of incidence of the plane wave generating sources for a four wavelength square plate. The associated plane wave direction is symbolically depicted in each same diagram.

IV. SINGULAR VALUE DECOMPOSITION (SVD) PROCESS

A. Selection of the Number of Generating Functions through SVD

The optimal number of basis functions is determined by evaluating the degree of independence of the entire domain functions both generated by near-edge dipoles and by near-grazing plane-waves via an iterated SVD-based procedure analogous to the one described in [4].

In the proposed procedure, we start with a given discretization in both schemes, i.e. with a given spatial (δ) or spectral ($\Delta\phi$) source density; the responses to the source sets are computed as indicated above, and processed by SVD as described in [4]. The number of the generating sources is incremented by reducing increasingly the parameter δ or $\Delta\phi$ with a linear law, and the SVD repeated. The process is stopped when the N most relevant SV do not change beyond a fixed ratio between the minimum and the maximum singular value, the latter can't be too small to avoid ill-conditioning.

At a difference with the procedure in [4], we adopt here a specialized implementation of the SVD generation process, that is very convenient for the present case. The procedure in [4] operates on the coefficients of the solution represented in terms of elemental, spatially localized functions (e.g. RWG), i.e. with spatial samples of the responses to the set of defining sources; in that case, the number of spatial samples is simply dictated by the mesh initially chosen to discretize the problem. In the present case, the (PO) responses are not subjected to an inherent spatial discretization, which is however a necessity when dealing with numerical operations. In the first place, then, we will choose a discretization for the PO responses to dipoles and plane waves; we will use $2N_s$ samples, being only constrained to be able to correctly represent the functions. In addition, we observe that in the present case it is meaningful and feasible to employ *spectral* samples instead of spatial samples of the responses. Indeed, the natural space sampling of the PO responses is not suitable since the s-block surface may extend over several wavelengths, thus leading to very large matrices. Furthermore, it has been shown in section III that both the spherical-and the plane-wave generation processes produce responses with spectral concentration around the boundary of the visible region. This suggest a spectral sampling of the PO response spectra in N_s equal-spaced points on the spectral circumference of radius k (Fig.6).

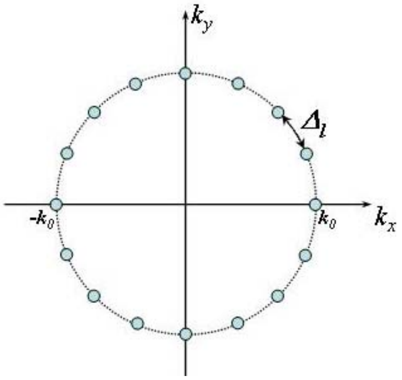

Fig. 6. Example of spectral samples for SVD computation.

We call N the number of employed sources, and we assemble the $2N_s$ samples (N_s samples for each polarization) of the ensuing N PO functions into the columns of the $2N_s \times N$ response matrix $\mathbf{R}$. This matrix represents the operator that maps the (N-dimensional) source spanned by linear combinations of the generating sources into the corresponding PO currents.

For spherical wave generating functions (dipole sources) the entries of the response matrix $\mathbf{R} = \left\{ r_{pq} \right\}_{\substack{p=1,2N_s \\ q=1,N}}$ are given by:

$$\begin{aligned} r_{2p'-1,2q'-1} &= \tilde{\mathbf{F}}_{q',\tau}(k_{sx}, k_{sy}) \cdot \hat{\mathbf{x}} \\ r_{2p',2q'-1} &= \tilde{\mathbf{F}}_{q',\tau}(k_{sx}, k_{sy}) \cdot \hat{\mathbf{y}} \\ r_{2p'-1,2q'} &= \tilde{\mathbf{F}}_{q',\eta}\left(k_{sx}, k_{sy}\right) \cdot \hat{\mathbf{x}} \\ r_{2p',2q'} &= \tilde{\mathbf{F}}_{q',\eta}\left(k_{sx}, k_{sy}\right) \cdot \hat{\mathbf{y}} \\ p' &= 1,\ldots,N_s, q' = 1,\ldots,\frac{N}{2}, \end{aligned} \tag{9}$$

where: $\tilde{\mathbf{F}}_{n,\xi}(k_x, k_y)$ is defined in (3), $k_{sx} = k_0 \cos\left(s\Delta\eta\right)$, $k_{sy} = k_0 \sin\left(s\Delta\eta\right)$, $\Delta\eta = 2\pi / N_s$ and $s = 1,\ldots,N_s$.

For near-grazing plane-wave sources they are given by:

$$\begin{aligned} r_{2p'-1,2q'-1} &= \tilde{\mathbf{F}}_{q',TE}\left(k_{px}, k_{py}\right) \cdot \hat{\mathbf{x}} \\ r_{2p',2q'-1} &= \tilde{\mathbf{F}}_{q',TE}\left(k_{px}, k_{py}\right) \cdot \hat{\mathbf{y}} \\ r_{2p'-1,2q'} &= \tilde{\mathbf{F}}_{q',TM}\left(k_{px}, k_{py}\right) \cdot \hat{\mathbf{x}} \\ r_{2p',2q'} &= \tilde{\mathbf{F}}_{q',TM}\left(k_{px}, k_{py}\right) \cdot \hat{\mathbf{y}} \\ p' &= 1,\ldots,N_s, \mathrm{q'} = 1,\ldots,\frac{N}{2}, \end{aligned} \tag{10}$$

where $\tilde{\mathbf{F}}_{n,TE}$ and $\tilde{\mathbf{F}}_{n,TM}$ are defined in (6). Note that this scheme strongly reduces number of samples with respect to those needed in a space domain sampling. The number of samples N_s has to be greater than N and sufficiently large to respect the Shannon sampling condition (correct representation of the spectral current functions); namely $N_s \geq \left\lfloor 2\pi k_0 / 2B \right\rfloor$, where B is the larger extension of the total surface.

Applying to the matrix $\mathbf{R}$ the SVD process yields the decomposition

$$\mathbf{R} = \mathbf{U}\Sigma\mathbf{V}^H, \tag{11}$$

where $\mathbf{U}$ and $\mathbf{V}$ are unitary matrix and Σ is the diagonal matrix containing the singular values $\sigma_1 \geq \sigma_2 \geq \cdots \geq \sigma_N$. The shape of this decomposition is visualized below for convenience of the reader

$$\boxed{\mathbf{R}} = \boxed{\mathbf{U}} \boxed{\begin{matrix} \sigma_1 & 0 & 0 & 0 \\ 0 & \sigma_1 & 0 & 0 \\ 0 & 0 & \ldots & \\ 0 & 0 & 0 & \sigma_N \end{matrix}} \boxed{\mathbf{V}^H}$$

The square matrices $\mathbf{U} = \left\{ u_{ij} \right\}_{\substack{i=1,2N_s \\ j=1,2N_s}}$ and $\mathbf{V} = \left\{ v_{nm} \right\}_{\substack{n=1,N \\ m=1,N}}$ have dimensions $2N_s$ and N, respectively, and the matrix Σ has and the same dimensions $2N_s \times N$ as $\mathbf{R}$. The matrix $\mathbf{V}^H = \left\{ v_{mn}^* \right\}_{\substack{n=1,N \\ m=1,N}}$ is the transpose conjugate of $\mathbf{V}$. The singular value sequence $\left\{ \sigma_i \right\}$ typically presents a decay beyond a certain value [7].

As indicated in [4], the normalized SV sequence σ_r / σ_1 indicates the relative independence of the r^{th} singular vector respect to the preceding subset, is a good indicator to select the necessary number of synthetic functions, upon the establishment of a threshold. For a given N, we increase iteratively the number of the generating sources, recomputing the SVD and stopping the process when the SV within the thresholding set of $\sigma_{\min}/\sigma_{\max}$ do not change anymore appreciably. A systematic implementation is based on the following iterative steps. One first fix an a priori value of $\sigma_{\min}/\sigma_{\max}$ on the basis of the conditioning number one can accept (let us say 10^{-4}). Next, one fix an initial number of generating sources $N = N_0$ on the basis of an initial guess for δ_0 (for SWG-BF) or $\Delta\phi_0$ (for PWG-POF). (for SWG-POF, $N_0 = P/\delta_0$ where P is the surface perimeter, for PWG-POF $N_0 = 360°/\Delta\phi_0$). As initial guess of the process we suggest $\delta_0 = \lambda/2$ and $\Delta\phi_0 = 30°$. Successively, the corresponding SV are determined trough (11). At the i^{th} iterative step the number of sources is increased to $N_i = 2N_{i-1}$ ($\delta_i = \delta_{i-1}/2$ or $\Delta\phi_i = \Delta\phi_{i-1}/2$) and the process is restarted obtaining a new SV sequence that is in general slightly different from that obtained at the previous step. The procedure is stopped when the SV sequence inside the fixed threshold $\sigma_{\min}/\sigma_{\max}$ does not change appreciably anymore. We note that to stabilize the process we need a number of generating sources N_I (with I number of iterations) which is higher than the number $\overline{N}$ to which the sequence meets the threshold. Examples of stabilized SV sequences for PWG and SWG basis functions are shown in Fig. 7 and Fig. 8, respectively. The sequences are relevant to the problem of a square flat metallic plate of side 0.9λ. The horizontal axis presents the index number of singular values and the vertical axis the relevant normalized SV’s. Fig. 7(a) are obtained sampling both TE- and TM-polarized waves at the same spectral locations. In Fig.7(b) only TE waves have been considered, with the evident outcome to reduce by a factor 2 the number of independent functions. Analogously, Fig. 8 are relevant to spherical generating dipoles both orthogonal and tangent to the edge (a) and only tangent to the edge (b). Again, the number of independent functions is reduced of a factor two in the second case. The final outcome of this analysis is that 60 PWG-POF are required to stabilized a sequence of 26 SV’s in the range $\sigma_{\min}/\sigma_{\max} = 10^{-4}$, while in the same range, the required SWG-POF are 40 to stabilize a sequence of 34 SV’s.

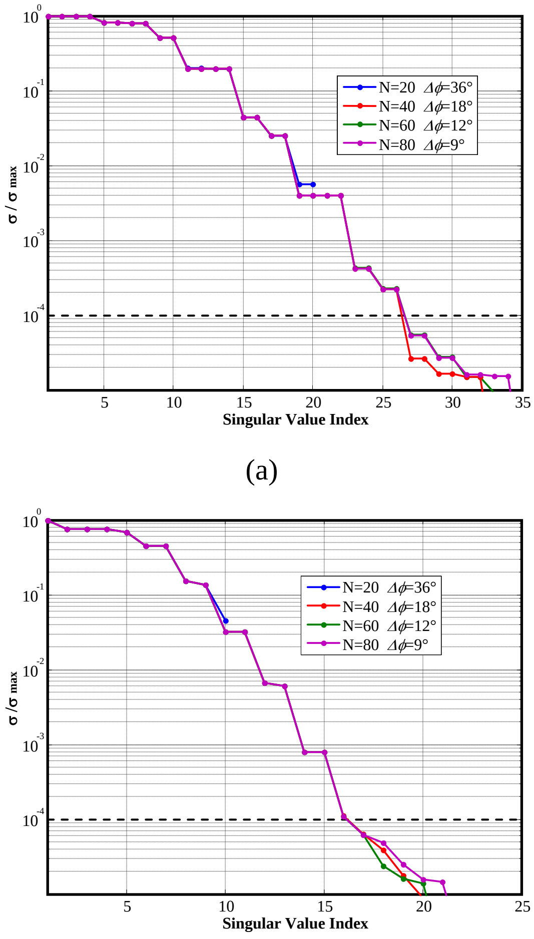

(a)

(b)

Fig. 7. Singular value sequences for PWG-POF defined over a square metallic plate of side length 0.9λ. The results are obtained using both polarization TE and TM (a) or using just the TE polarization (b). The spectral step $\Delta\phi$ is decreased till when each sequence is stabilized in the range $\sigma/\sigma_{\max} = 10^{-4}$. The final step $\Delta\phi$ obtained is $\Delta\phi = 12°$.

B. Generation of the Synthetic Functions

The final SVD obtained at the end of the iterative process contains information of an “orthogonal” set of synthetic functions in spectral (in the $\mathbf{U} = \left\{u_{ij}\right\}_{\substack{i=1,2N_s \\ j=1,2N_s}}$) and spatial (in the matrix $\mathbf{V} = \left\{v_{nm}\right\}_{\substack{n=1,N \\ m=1,N}}$) domain, where N is the number of generating sources used to stabilized the sequence.

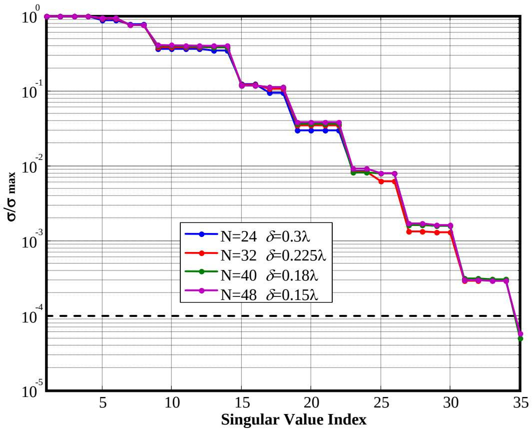

(a)

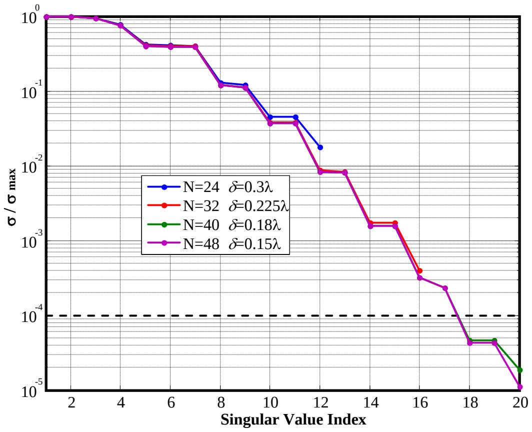

(b)

Fig. 8. Singular value sequences for SWG-POF defined over a squared metallic plate of side length 0.9λ obtained using both polarized dipoles as generating sources (a) or using only dipoles alignment to the edge (b). The space step δ is decreased till when each sequence is stabilized in the range $\sigma/\sigma_{\max} = 10^{-4}$. The finale δ-step obtained is 0.18λ.

In particular, the coefficients of the n^{th} column of $\mathbf{V}$ constitutes the coefficients of the PO-type functions that synthesize orthonormal *plane-wave generated synthetic basis functions* (PWG-SFX) or *spherical-wave generated synthetic basis functions* (SWG-SFX) in spatial domain:

$$\mathbf{d}_m(x,y) = \frac{1}{\sigma_m}\sum_{n'=1}^{N/2} v_{(2n'-1),m}\mathbf{f}_{n',\zeta_1}(x,y) + v_{2n',m}\mathbf{f}_{n',\zeta_2}(x,y) \quad (12)$$

$m = 1,\ldots,\bar{N}$,

$$\zeta_1 = \begin{cases} TE & \text{for PWG-SFX} \\ \tau & \text{for SWG-SFX} \end{cases},$$

$$\zeta_2 = \begin{cases} TM & \text{for PWG-SFX} \\ \eta & \text{for SWG-SFX} \end{cases}.$$

The number of synthetic functions $\bar{N}$ corresponds to the number of singular value inside the dynamic range (e.g. $\bar{N} = 26$ for PWG-SBF, and $\bar{N} = 35$ for SWG-SBF in case of Figs. 7 and 8). The spectrum of the selected synthetic functions can be easily obtained by linearity from the spectrum of the generating sources:

$$\tilde{\mathbf{D}}_{m,\zeta}(k_x,k_y) = \frac{1}{\sigma_m}\sum_{n'=1}^{N/2} v_{(2n'-1),m}\tilde{\mathbf{F}}_{n',\zeta_1}(k_x,k_y) + v_{2n',m}\tilde{\mathbf{F}}_{n',\zeta_2}(k_x,k_y) \quad (13)$$

$m = 1,\ldots,\bar{N}$.

We note that sampling the above equality on the boundary of the visible spectral region in the same N_s spectral points used for the SVD in (11) reconstructs the relation $\mathbf{RV} = \mathbf{U}\Sigma$ obtained by multiplying both sides of (11) by $\mathbf{V}$ (note that $\mathbf{V}^{-1} = \mathbf{V}^H$). We note that the spherical wave generation approach requires in general less number of sources to reach a stable value of the SV sequence wrt the plane wave generation , the latter really finally gives a lower number of SV's within the same threshold, after stabilization of the sequence.

V. MOM SOLUTION

The basis function selected by the SVD process are now used in a MoM-Galerkin solution scheme. Since the synthetic functions are extended over domains that could be electrically large, it is convenient the use of the inverse spectral-domain transform of the MoM matrix entries. Our investigation is limited here to coplanar basis functions, but the process should be easily extended to non coplanar surfaces [8, 9]. For a pair of two spectral synthetic functions $\tilde{\mathbf{D}}_{p,\zeta}$ and $\tilde{\mathbf{D}}_{q,\eta}$ the Galerkin MoM matrix entry is obtained as

$$Z_{pq}^{\zeta\sigma} = -\frac{\varsigma\kappa}{8\pi^2}\int_{-\infty}^{+\infty}\int_{-\infty}^{+\infty}\tilde{\mathbf{D}}_{p,\zeta}(k_x,k_y)\cdot\frac{1}{k_z}\left[\underline{\underline{I}} - \frac{\mathbf{kk}}{\kappa_0^2}\right]\cdot\tilde{\mathbf{D}}_{q,\sigma}(-k_x,-k_y)\,dk_x dk_y \quad (14)$$

$p,q = 1,\ldots,\bar{N}$,

where $\mathbf{k}=k_x\hat{x}+k_y\hat{y}+k_z\hat{z}$ in which $k_z=\sqrt{k^2-k_x^2-k_y^2}$ is the wave-vector and ς is the characteristic impedance of the medium. Using (13), (14) can be expressed as a function of the mutual impedances $Z_{pq}^{\zeta\eta,PO}$ of the PO-type basis functions via

$$Z_{pq}^{\zeta\sigma}=\frac{1}{\sigma_p}\frac{1}{\sigma_q}\sum_{n=1}^{N}\sum_{n'=1}^{N}v_{n'q}v_{np}Z_{pq}^{\zeta\sigma,PO}, \qquad (15)$$

$$Z_{pq}^{\zeta\sigma,PO}=-\frac{\varsigma\kappa}{8\pi^2}\int_{-\infty}^{+\infty}\int_{-\infty}^{+\infty}\tilde{\mathbf{F}}_{p,\zeta}\left(k_x,k_y\right) \qquad (16)$$

$$\cdot\frac{1}{k_z}\left[\underline{\underline{I}}-\frac{\mathbf{kk}}{\kappa_0{}^2}\right]\cdot\tilde{\mathbf{F}}_{q,\eta}\left(-k_x,-k_y\right)dk_x dk_y .$$

We stress that the integrand in (16) is calculated in a closed form for the plane wave generation approach and by FFT for the spherical wave generation approach.

VI. NUMERICAL RESULTS

As an example of application we consider a square flat plate of dimension $L=0.9\lambda$ illuminated by an electric dipole at a distance of a wavelength as shown in Fig. 9. The plate will be considered as a unique block in the iteration-free procedure. The SVD sequences associated to this block for both type of basis function introduced in this paper are those shown in Figs. 7 and 8.

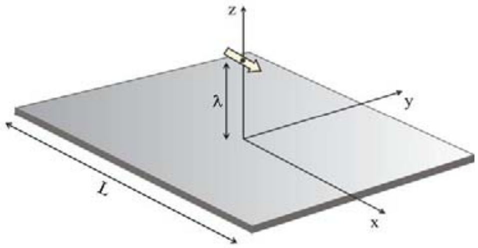

Fig. 9. Electric dipole radiating over a squared flat metallic plate.

The simulations have been carried out by using alternatively 26 PWG synthetic functions and 35 SWG synthetic basis functions, according to the sequence in Figs. 7a and 8a, respectively, and adding as a basis function a part the PO currents. The results compared with those provided by a commercial standard MoM (FEKO™) using 648 RWG basis functions. Figure 10 shows the amplitude of the induced currents on the plate in the E and H cut-planes. A reasonable good agreement has been seen except very close to the edge, where the SWG-SFX looks like more appropriate than PWG-SFX to represent the edge effect for the intrinsic space high resolution capability of the SWG-POF space functions.

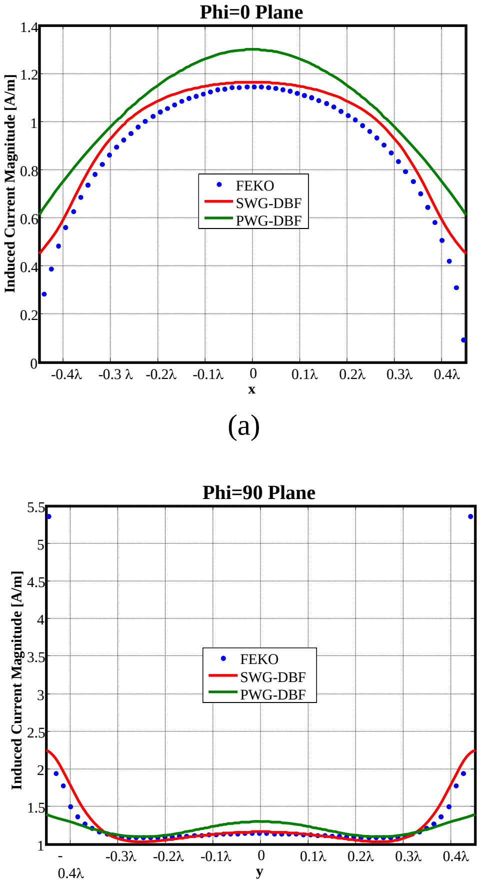

(a)

(b)

Fig. 10. Square plate, $L=0.9\lambda$; comparison of the induced currents on (a) E-plane and (b)H-plane cuts.

Figure 11 shows the comparison between the far field in E-plane (Fig. 11a) and H-plane (Fig. 11b); the agreement is satisfactory for both SWG-DBF and PWG-DBF.

We observe that the present procedure increases accuracy for increasing the plate dimensions. Let us consider the same scattering problem as shown in Fig. 9 for a plate side $L=4\lambda$. The simulations have been done by using 98 SWG-SFX and 80 PWG-SFX stabilized by using 120 SWG-POF and 100 PWG-POF, respectively; the relative SV sequences are shown in Fig. 12.

Figeurs13 and 14 shows the comparison of the far field and the induced current with a standard MoM (FEKO™) using 12800 RWG basis functions, as we can see using just respectively 98 SWG-SFX and 80 PWG-SFX it is possible to obtain a very good agreement between the results.

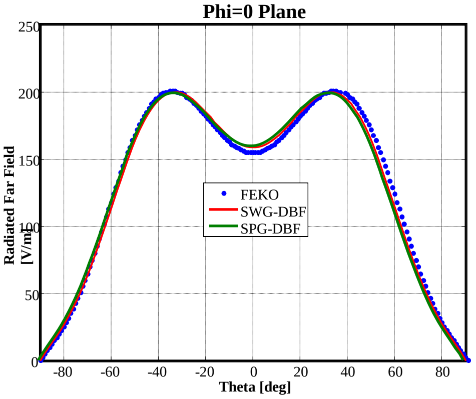

(a)

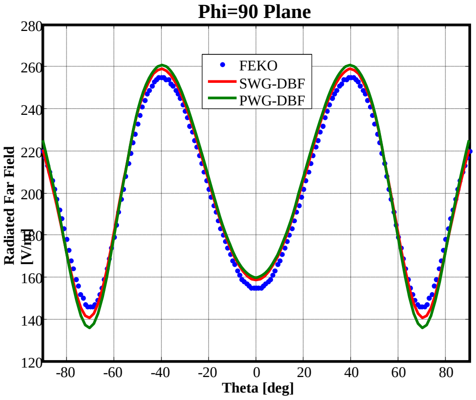

(b)

Fig. 11. Square plate, $L = 0.9\lambda$; far field comparison on (a) E-plane and (b) H-plane.

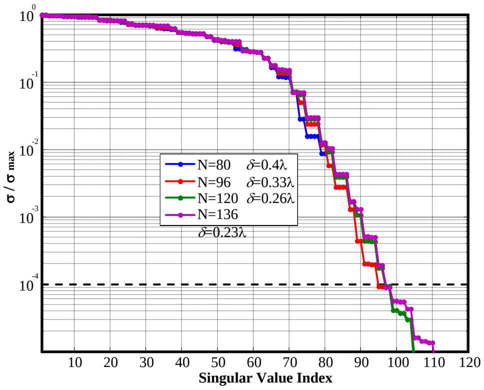

(a)

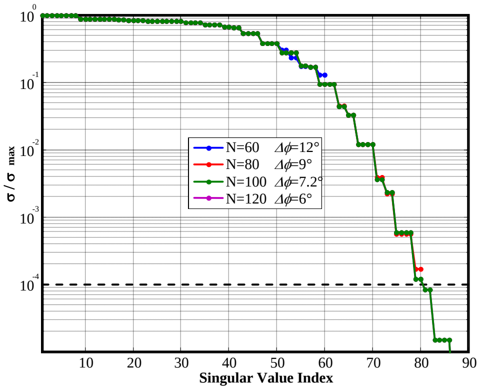

(b)

Fig. 12. SV stabilized sequences for a flat squared metallic plat with side length 4λ (a) Spherical-wave generation (final step $\delta = 0.26\lambda$) (b) Plane-wave generation (final step $\Delta\phi = 7.2°$).

VII. CONCLUDING REMARKS

We have presented a method to reduce the computational cost of the MoM analysis of large and complex structures that exhibits a large portion of flat metallic surfaces with edges. While the overall framework is the one presented in [1] the method is based on breaking down the overall structures into smaller parts, called “blocks,” and constructing entire-domain “synthetic” basis functions over these blocks making use of PO functions to span the solution space. The PO functions are generated by two alternative processes, namely, by using edge located spherical wave sources, or near grazing propagating plane waves. The most evident computational gain consists on a reduction of the MoM matrix size, that have a dimension proportional to the perimeter and not to the area of the plate (it is obvious that this property refers to the description of the edge mechanisms only, and leaves out of consideration the generating sources used for describing the external environment).

Comparison of the two different generating processes shows that the spherical wave generation approach is more accurate while the plane wave generation approach exhibits advantages of closed form spectral domain entries, with favourable capability in treating large structures in terms of wavelengths.

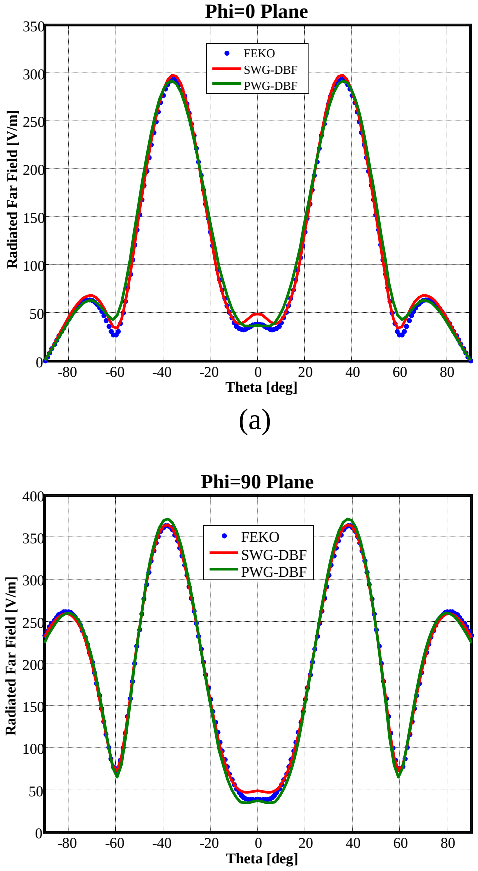

(a)

(b)

Fig.13. Square plate, $L = 4\lambda$ **;** far field comparison on E-plane (a) and H-plane (b).

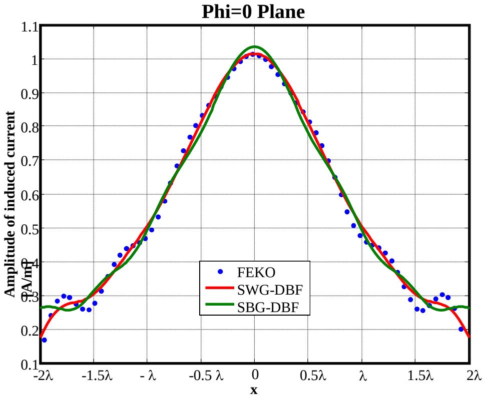

(a)

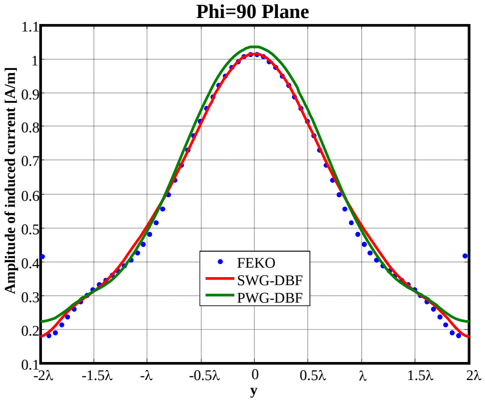

(b)

Fig. 14. Square plate, $L = 4\lambda$ **;** induced currents comparison on E-plane (a) and H-plane cut (b).

REFERENCES

[1] S. Maci, R. Mittra, and G. Vecchi, “A Unified Iteration-Free Approach to Solving Large Antenna and Scattering Problems,” *IEEE AP-S Symposium* Washington DC, July 2005, and *IEEE AP-S Symposium* Albuquerque, July 2006.

[2] P. Pirinoli, L. Matekovits, G. Vecchi, F. Vapiana, and M. Orefice, ”Synthetic functions: multiscale MoM analysis of arrays,” *Proc. of the 2003 IEEE Antennas Propagation Society Symposium*, vol. 4, pp. 799-802, Columbus, 22-27 June 2003.

[3] V. V. S. Prakash and R. Mittra, “Characteristic basis function method: A new technique for fast solution of integral equations,” *Micro. Opt. Tech. Lett.*, pp. 95–100, Jan. 2003.

[4] L. Matekovits, V. A. Laza, and G. Vecchi, “Analysis of Large Complex Structures With the Synthetic-Functions Approach” *IEEE Trans. Antennas Propagat.*, vol. 55, no. 9, pp. 2509-2521, Sep. 2007.

[5] S. Maci, M. Albani, and F. Capolino, “ITD Formulation for the Currents on a Plane Angular Sector,” *IEEE Trans. Antennas Propagat.*, vol. 46, no. 9, September. 1998.

[6] P. Y. Ufimtsev, *Fundamentals of the Physical Theory of Diffraction*, IEEE Press, Wiley Inter-science, 2007.

[7] O. M. Bucci and G. Franceschetti, "On the degrees of freedom of the scattered fields," *IEEE Trans. Antennas Propagat.*, vol. 37, no. 7, pp. 918-926, July 1989

[8] G. Tiberi, S. Rosace, A. Monorchio, G. Manara, and R. Mittra, “Electromagnetic scattering from large faceted conducting bodies by using analytically derived characteristic basis functions,” *IEEE Antennas Wireless Propagat. Lett.*, vol. 2, pp. 290- 293, 2003.

[9] M. Casaletti “Deterministic and Stochastic Methods for the Electromagnetic Analysis of Complex Structures,” Ph.D. Thesis, University of Siena, Department of Information Engineering, 2007.

Massimiliano Casaletti was born in Siena, Italy, in 1975. He received the Laurea degree in Telecommunications engineering and the Ph.D. degree in Information engineering from the University of Siena, Italy, in 2003 and 2007, respectively. From September 2003 to October 2005 he has been with the research center MOTHESIM, Les Plessis Robinson (Paris, FR), under a EU grant RTN-AMPER (RTN: Research Training Network, AMPER: Application of Multiparameter Polarimetry). Since 2006, he has been Research Associate at the University of Siena, Italy. His research interests include electromagnetic band-gap structures, polarimetric radar, rough surfaces and numerical methods for electromagnetic scattering and beam waveguides.

Stefano Maci was born in Rome in 1961. Since '98 he joined the University of Siena, Italy, where he presently is a Full Professor. His research interests include: theory of Electromagnetism, high-frequency techniques, integral equation methods, large phased array antennas, planar antennas and multilayer structures, reflector antennas and feed horns, metamaterials. He was a co-author of an Incremental Theory of Diffraction for the description of a wide class of electromagnetic scattering phenomena at high frequency, and of a diffraction theory for the high frequency analysis of large truncated periodic structures. On these subjects he was various times recipient of best paper award in international journals and conferences. In 2004 he was founder, and he presently is the coordinator, of the "European school of antennas" (ESoA), a post-graduate school comprising 12 course per year and 150 teachers coming from 20 European research centres. He was the responsible of several projects funded by the European Union (EU), by the European Space Agency (ESA-ESTEC) and by various European industries; he was work package leader in the Network of Excellence "Antenna Center of Excellence" (FP6, EU). He was associate editor of IEEE Transactions on EMC, and he is associate editor of IEEE Transaction on Antennas and Propagation. He is member of the Technical Advisory Board of the URSI Commission B, member of the Delegate Assembly of the European Association of Antennas and Propagation, member of a NATO panel on metamaterials and MEMS, member of the scientific board of the Italian Society of Electromagnetism (SIEM), and coordinator of the board of the Italian PhD school of Electromagnetism, member of the Board of Director of the European Association of Antennas nd Propagation. He is a Fellow (‘04) of IEEE, two times guest editor of special issues of IEEE Transaction on Antennas and Propagation. He is principal author or co-author of about 100 papers published in international journals, 8 book Chapters, and about 300 papers in proceedings of international conferences.

Giuseppe Vecchi received the Laurea and Ph.D. (Dottorato di Ricerca) degrees in electronic engineering from the Politecnico di Torino, Torino, Italy, in 1985 and 1989, respectively, with doctoral research carried out partly at Polytechnic University (Farmingdale, NY). He was a Visiting Scientist with Polytechnic University in 1989-1990. In 1990, he joined the Department of Electronics, Politecnico di Torino, as an Assistant Professor (Ricercatore) where, from 1992 to 2000, he was an Associate Professor and, since 2000, he has been a Professor. He was a Visiting Scientist at the University of Helsinki, Finland, in 1992, and has been an Adjunct Faculty in the Department of Electrical and Computer Engineering, University of Illinois at Chicago, since 1997. His current research activities concern analytical and numerical techniques for analysis, design and diagnostics of antennas and devices, RF plasma heating, electromagnetic compatibility, and imaging.

Fast Solution of Multi-Scale Antenna Problems for the Square Kilometre Array (SKA) Radio Telescope using the Characteristic Basis Function Method (CBFM)

Rob Maaskant [1], Raj Mittra [2], and Anton Tijhuis [3]
[1] The Netherlands Institute for Radio Astronomy (ASTRON),
P.O. Box 2, 7990 AA Dwingeloo, The Netherlands
maaskant@astron.nl

[2] Electromagnetic Communication Laboratories,
Pennsylvania State University, University Park, PA 16802, USA
mittra@engr.psu.edu

[3] Faculty of Electrical Engineering, Eindhoven University of Technology,
P.O. Box 513, 5600 MB Eindhoven, The Netherlands
a.g.tijhuis@tue.nl

***Abstract*—** We present a numerically efficient technique, called the Characteristic Basis Function Method (CBFM), for computing the scan impedances of antenna elements located inside an electrically large subarray, which is surrounded by (many) other actively phase-steered subarrays. We construct a reduced moment matrix for a single subarray, and modify its entries in a manner that accounts for the mutual coupling between the surrounding subarrays. This enables us to circumvent the difficult problem of having to deal with the entire large array geometry in one step and reduces the total solve time significantly. Furthermore, the reduced moment matrix can be constructed in a time-efficient manner by exploiting the translation symmetry between pairs of Characteristic Basis Functions (CBFs). However, since we propose an overlapping domain decomposition technique for arrays of electrically interconnected antenna elements, symmetry can only be exploited if the mesh partitioning facilitates a one-to-one mapping of CBFs. To fully utilize the translation symmetry, a strategy has been developed to mesh the structure and to take advantage of this geometrical property. A numerical example is presented for a large array of subarrays of Tapered Slot Antennas (TSAs). The proposed method has good accuracy, excellent numerical efficiency, and reduced memory storage requirement.

***Index Terms*—** Characteristic Basis Function Method, Moment Methods, Scan Impedance, Tapered Slot Antennas, Square Kilometre Array.

I. INTRODUCTION

The Square Kilometer Array (SKA) project is a world-wide project to design and construct a revolutionary new radio telescope with a collecting area which is on the order of 1 million square meters in the wavelength range from 3 m to 1 cm [1–3]. It will have receiver sensitivity orders of magnitude higher than the current radio telescopes in operation, and an unprecedented large instantaneous field-of-view (FOV). The Netherlands institute for radio astronomy (ASTRON) is engaged in the development of the aperture array concept, by designing and examining small-scale prototype arrays, thereby demonstrating the feasibility of the instrument [4]. Concurrently, the knowledge gained from the SKA design studies is being used to realize cost-effective solutions for inexpensive fabrication of the instrument [5]. An electromagnetic field simulation is required at each step to analyze the antenna impedance and radiation characteristics, which, in turn, facilitates the evaluation of the potentials of various array technologies [6, 7].

In some of these studies it is vitally important to accurately analyze electrically large – but finite – array antenna problems and associated truncation effects. Given the electrical size and geometrical complexity of such structures, the numerical analysis presents a severe computational burden when only limited computing resources are available [8]. In order to mitigate the computational burden, a vast number of numerically efficient techniques have been developed over the last few decades.

In the present paper, we only provide a brief overview of the literature relevant to the approach employed in this paper, namely, iteration-free integral-equation techniques. Moreover, while focusing in this paper on the challenging case of large arrays of strongly coupled TSAs, we point out that the radiation and scattering characteristics of such arrays have been considered by others as well. Much work has been performed on the edge truncation effects and the efficient computation of embedded element patterns and element impedances by the authors of [9], both in the time and the frequency domain. Furthermore, in [10], the Finite Element Method has been combined with an Integral-Equation technique (FEM-IE) to iteratively solve for the fields in TSA arrays that involve dielectric materials.

In this paper, we present an integral-equation-based technique, called CBFM, which enhances the conventional method of moments by compressing the moment matrix such that the resultant reduced matrix equation can be solved in an iterative-free manner, and simultaneously for multiple right-hand sides (MRHS) [11, 12]. The above compression is achieved by employing macro basis functions, which themselves are constructed as fixed combinations (aggregations) of subsectional basis functions [13, 14]. Hence; these macro domain functions can conform to arbitrarily shaped geometries, provided that the underlying subsectional basis functions also satisfy this geometrical property. An additional advantage in using these macro domain functions is that existing computer codes that employ subsectional basis functions can be reused with only minor modifications. Furthermore, in CBFM, the entire computational domain is subdivided into smaller subdomains, each of them supporting a set of numerically generated macro basis functions, referred to herein as CBFs. The inherent advantage of such a domain decomposition technique is that many algorithmic steps involved can be carried out in parallel, on supercomputers or on platforms with multiple processors [15]. Furthermore, the modular setting of a domain decomposition technique enables one to analyze/optimize the entire structure at minimal cost by only reconsidering the domains that have been altered [16].

The concept of reducing the matrix equation by employing numerically generated macro basis functions, and decomposing the problem into smaller problems, has also been widely exploited in other recently developed iterative-free methods for solving large-scale problems. For instance, the Synthetic-Functions Approach (SFX) [17, 18], the Sub-Entire-Domain Basis Function Method (SED) [19], the eigencurrent approach [20], and a subdomain multilevel approach [21]. Although the above methods all have similar objectives, namely to reduce the matrix equation and to solve it in an iterative-free manner, the differences between these methods can be considerable. For example, within the framework of each of these methods, a variety of techniques have been proposed to numerically generate the macro basis functions. Among these, it is possible to distinguish between two categories, namely the overlapping and non-overlapping domain decomposition techniques. Furthermore, different methods have been proposed to ensure that the surface current at the interfaces between adjacent domains are smoothly varying functions without the presence of truncation effects [17, 22]. Obviously, the accuracies of the aforementioned iterative-free methods depend upon the type of domain decomposition employed. In each of these methods, several techniques have been proposed to arrive at a computationally efficient implementation.

For electrically large problems, the overall solution time of CBFM is governed by the time it takes to construct the reduced matrix equation, as opposed to solving it. The construction of the reduced matrix involves the calculation of reaction integrals between pairs of CBFs, for many of which the computation time can be reduced significantly, especially for those that are well-separated. Various acceleration techniques have been proposed to reduce the matrix construction time, including; multipole approaches [23, 24]; the Adaptive Cross Approximation (ACA) technique [25]; a multi-level decomposition approach [26]; and the Adaptive Integration Method (AIM) [27]. These methods all rely on the fact that the electric field, generated by a macro basis function, is a relatively smoothly varying function over the support of the macro test function. Obviously, the electric field function becomes increasingly smoother over the support of the macro test function, for increasingly large separation distances. Hence, for electrically large antenna and scattering problems, many of the reduced matrix entries (CBF reactions) can be computed rapidly.

In addition to these acceleration techniques, the reciprocity theorem is often used to compute only the upper triangular part of the reduced matrix, and this saves approximately a factor of two in the total fill time. More importantly, and also for array antennas with electrically interconnected antenna elements, a significant degree of translation symmetry exists when the elements are positioned on a uniform grid. This can be understood by realizing that many reactions between (groups of) CBFs are replicated elsewhere in the array. Thus, even though the moment matrix may not have a full block Toeplitz symmetry, many entries (even blocks) of the reduced matrix are identical and, hence, can simply be copied during the matrix construction process. Depending upon the array geometry, the computational complexity of the matrix filling may even be of linear order.

The structure of this paper is as follows. First, we provide a brief description of the CBFM and the steps that are involved in the process of generating a reduced matrix equation, as well as the CBFs for antenna-type problems. Second, we focus on an overlapping domain decomposition technique and describe a strategy for meshing a large array structure efficiently to optimally exploit the translation symmetry between the CBFs. Third, in accordance with the SKA concept of using disjoint phased-array tiles, we outline an approximate technique for an efficient solution for the computation of the scan impedance of antenna elements, located within an electrically large subarray and surrounded by (many) other actively phase-steered subarrays. Results will be presented for a 576 TSA element array, which is subject to several different scanning scenarios, showing that the proposed approximate method is first-order accurate for these types of problems and therefore represents a viable alternative to a full CBFM solution. The significant savings realized in memory and computation time will be described.

II. OUTLINE OF CBFM

A. Domain Decomposition and Matrix Equation Reduction

Let S denote the perfectly conducting surface of an antenna array. In CBFM, we subdivide the entire domain S into N smaller subdomains. N is typically chosen to be equal to the number of antenna elements. If the nth subdomain is denoted by S_n, then

$$S = \bigcup_{n=1}^{N} S_n \, . \tag{1}$$

Since we propose an overlapping domain decomposition technique, $S_p \bigcap S_q \neq 0$, in general, for $p, q \in \{1, 2, \ldots, N\}$. However, in our approach, we require that S_p and S_q overlap only if the corresponding antenna elements p and q are electrically interconnected. Furthermore, the overlap is restricted to the adjacent antenna element only. Each subdomain S_n is geometrically represented by an adequate number of triangular patches that are subsequently grouped into pairs to form the Rao-Wilton-Glisson (RWG) vector basis functions used to represent the surface current distribution [28]. Note that as subdomains overlap, some triangular patches, as well as the corresponding RWG basis functions, are common to multiple subdomains. Let N_n denote the number of RWG basis functions on the nth subdomain S_n. Typically, N_n is chosen to be at least 10 RWGs/wavelength in order to achieve a high phase accuracy of the final surface current solution. Moreover, N_n may be governed by tiny geometrical details that need to be represented with sufficient accuracy. Also, let the n^{th} subdomain S_n support a set of K_n CBFs, each of which is expanded using the N_n RWG basis functions. The generation of these CBFs is discussed in Sec. II B. Furthermore, let $\mathbf{J}_n$ be a column-augmented matrix, whose k_n^{th} column vector represents the RWG expansion coefficients of the k_n^{th} CBF on the n^{th} subdomain. Then, if the uncompressed matrix block $\mathbf{Z}_{pq}^{RWG}$ represents the mutual reaction matrix between the source and test RWGs belonging to domains q and p, respectively, the reduced matrix block $\mathbf{Z}^{CBF}_{pq}$ is readily computed as

$$\mathbf{Z}^{CBF}_{pq} = \left\langle \mathbf{J}^{T}_{p}, \mathbf{Z}^{RWG}_{pq}\mathbf{J}_{q} \right\rangle, \tag{2}$$

where T denotes the transposition operator, and $\langle \cdot,\cdot \rangle$ denotes a symmetric product. Note that the size of the reduced matrix block $\mathbf{Z}^{CBF}_{pq}$ is $K_p \times K_q$, whereas the uncompressed matrix block $\mathbf{Z}^{RWG}_{pq}$ is of size $N_p \times N_q$.

Similarly, if the uncompressed RWG excitation vector for the pth subdomain is denoted by $\mathbf{V}^{RWG}_{p}$, and its size is $N_p \times 1$ (single excitation), the reduced excitation vector $\mathbf{V}^{CBF}_{p}$ is of size $K_p \times 1$, and is computed by evaluating

$$\mathbf{V}^{CBF}_{p} = \left\langle \mathbf{J}^{T}_{p}, \mathbf{V}^{RWG}_{p} \right\rangle. \tag{3}$$

Finally, after constructing all the reduced matrix blocks, as well as the reduced excitation vectors for all subdomains, we obtain a reduced matrix equation that has the form

$$\mathbf{Z}^{CBF}\mathbf{I}^{CBF} = \mathbf{V}^{CBF}, \tag{4}$$

which can be solved directly for the unknown CBF expansion coefficient vector $\mathbf{I}^{CBF}$, in an iteration-free manner, provided that the size of $\mathbf{Z}^{CBF}$ is sufficiently small. In fact, depending upon the type of problem and required solution accuracy, the size of vector $\mathbf{I}^{CBF}$ can be a factor 50-500 smaller than $\mathbf{I}^{RWG}$.

B. Generation and Windowing of CBFs

A rather attractive feature of the physics-based CBFM is the way CBFs are generated. We will briefly describe this procedure for an overlapping domain decomposition approach, applied to antenna array problems. The details can be found in several previously published works [12, 22] and [25].

For large antenna array problems, we first extract several distinct and relatively small subarrays from the fully meshed array, typically from the center, corners and edges of the array. The subarray sizes are chosen such that the direct electromagnetic environment for the center, corner and edge elements of the corresponding subarrays closely resemble their original electromagnetic array environment. For instance, Fig. 1b illustrates two subarrays that are extracted from a 4 × 3 × 2 dual-polarized Vivaldi array[1]. These two subarrays represent a corner and center element along with their interconnected neighboring elements, respectively.

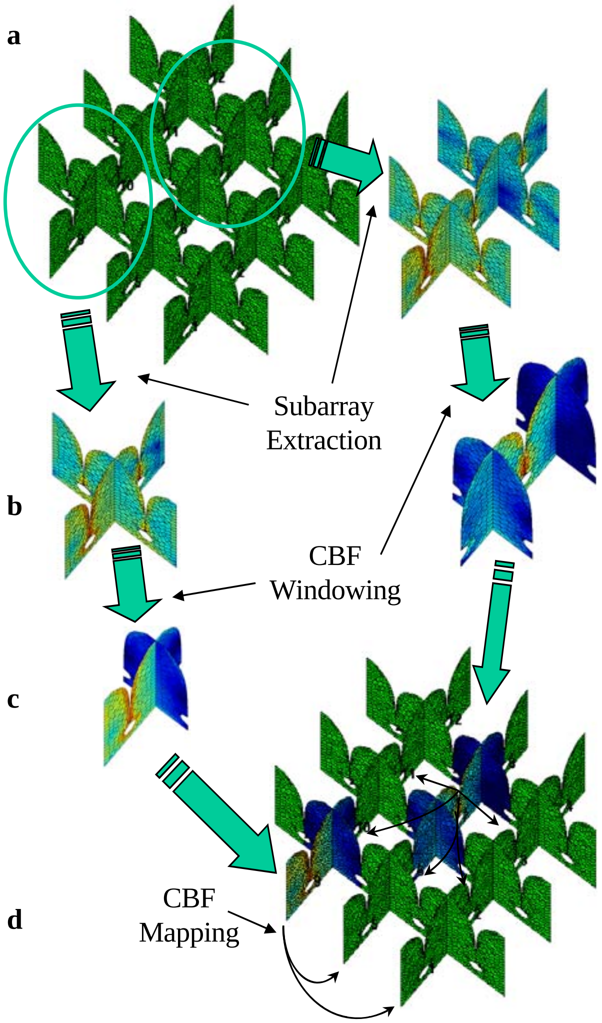

Fig. 1. Approach to generate and window primary CBFs. (i) Subarray extraction and generation of primary CBFs, (ii) Trapezoidal post-windowing of CBFs, (iii) One-to-one mapping of CBFs throughout the array lattice.

Next, we solve for a set of surface currents induced in each of the subarrays, by sequentially exciting the antenna terminals of the corresponding subarray (Fig. 1b). Hence, for our example, 4 primary CBFs are generated for the subarray comprising the corner element, and 7 primary CBFs for the subarray comprising the center element.

---

[1] 4 elements in the E-plane, 3 elements in the H-plane, and 2 polarizations.

Next, we apply a (trapezoidal) post-windowing function to the sets of primary CBFs to suppress the undesired edge-truncation effects by reducing the support of the so-generated primary CBFs (Fig. 1c). In essence, the RWG expansion coefficients making up the CBFs are post-multiplied with suitable weights. Note that the partially overlapping windowing functions have to add up to unity, so that the tapered CBFs add up in a correct manner as well, particularly in the overlapping regions. In our specific example (Fig. 1), the support extends to one-half of the neighboring elements, though this can be changed in a manner discussed in [22]. For instance, in [25], very good accuracy has been realized with only a one-cell overlap.

Finally, the set of CBFs are mapped, one-to-one, onto the corresponding edge and center elements so that each array-element/subdomain will have its own set of CBFs (Fig. 1d). Note that for our example, 6 subarrays have to be extracted in total so as to accommodate CBFs on all the array elements (3 subarrays per polarization, i.e., 2 subarrays for the opposite edge elements, and 1 for a center element).

The number of CBFs on array elements can be enlarged in order to model surface currents on array elements that can have a large degree of freedom, namely, by appending a set of secondarily generated CBFs to the already existing set of primary CBFs [12]. This is accomplished by taking the primary CBFs as distant current sources to the subarrays, which then induce extra surface currents on these subarrays after which these newly generated currents are truncated/windowed again and added to the primary set of CBFs.

Regarding the generation of CBFs, it is instructive to consider how the CBFs differ from eigencurrents employed in the eigencurrent approach [20]. In CBFM, the induced surface current on each subarray is computed for a certain excitation vector $\mathbf{V}$ by solving the corresponding matrix equation $\mathbf{ZI} = \mathbf{V}$ for the unknown RWG expansion coefficient vector $\mathbf{I}$. The complex symmetric moment matrix $\mathbf{Z} = \mathbf{Z}^T$ is assumed to be nondefective and diagonalizable by its eigenvectors. Hence, an eigenvalue decomposition of $\mathbf{Z}$ exists and is herein expressed through the block factorization

$$\mathbf{Z} = \mathbf{UDU}^{-1}, \tag{4}$$

where the n^{th} diagonal entry ν_n of diagonal matrix $\mathbf{D}$ is the *n*th eigenvalue of $\mathbf{Z}$, and where the *n*th column $\mathbf{u}_n$ of $\mathbf{U}$ is the *n*th eigenvector of $\mathbf{Z}$. Hence, the unknown coefficient vector $\mathbf{I}$ can be expressed in terms of the eigenvectors $\mathbf{u}$, eigenvalues ν, and excitation vector $\mathbf{V}$ as

$$\mathbf{I} = \sum_{n=1}^{N} \frac{1}{\nu_n} \left\langle \mathbf{u}_n, \mathbf{V} \right\rangle \mathbf{u}_n . \tag{5}$$

In the eigencurrent approach [20], the eigencurrents $\mathbf{u}$ of $\mathbf{Z}$ are used as macro-domain basis functions. Essentially, the set of eigencurrents forms a fingerprint of the physical structure and simultaneously forms a complete orthonormal basis for the currents that can exist on this structure. Accurate solutions have been obtained for arrays of disconnected antenna elements, by using only an (incomplete) subset of $\mathbf{u}$. However, this reduced orthonormal basis does not include information about the port position of the antenna element or excitation field applied to the actual problem, and therefore will, in general, not lead to the most optimal/smallest basis. On the contrary, in CBFM, a representative excitation field $\mathbf{V}$ is applied to each subarray to generate CBFs, implying that we identify the left-hand-side of (5) as a basis. This can be advantageous, because when an antenna port of a subarray is excited, the induced surface current (and thus the CBF) naturally accounts for a possibly asymmetrical port position, and may therefore represent the final surface current quite well even when we employ only a limited number of the above macro-domain basis functions. However, one major drawback in generating macro basis functions in this manner is that these CBFs will not be mutually orthogonal in general. As a remedy, one would need to orthonormalize the CBFs, and retain only a minimal number of them. This can both be accomplished with the aid of a Singular Value Decomposition (SVD) and a thresholding procedure on its singular values [29, 30].

III. EXPLOITING TRANSLATION SYMMETRY

Once each (extended) subdomain supports a set of CBFs, the reduced moment matrix can be constructed efficiently by exploiting the translation symmetry. As an example, Fig. 2

graphically exemplifies that the reduced matrix block $\mathbf{Z}_{pq}^{CBF}$ equals $\mathbf{Z}_{p+1;q+1}^{CBF}$, because both blocks represent reactions between identical, though translated, set of CBFs.

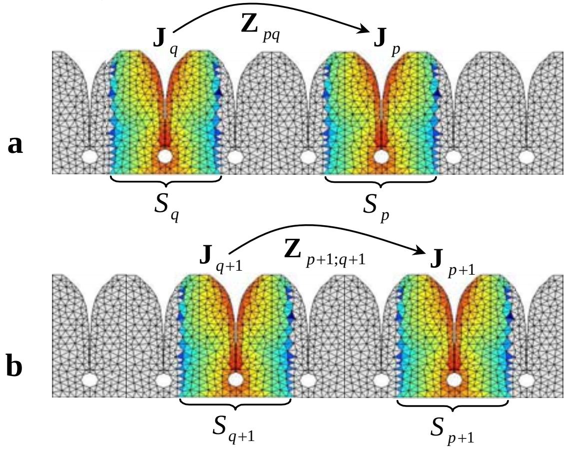

Fig. 2. Construction of identical reduced matrix blocks $\mathbf{Z}_{pq}^{CBF}$ and $\mathbf{Z}_{p+1;q+1}^{CBF}$.

Therefore,

$$\mathbf{Z}_{pq}^{CBF} = \left\langle \mathbf{J}_p^T, \mathbf{Z}_{pq}^{RWG} \mathbf{J}_q \right\rangle = \mathbf{Z}_{p+1;q+1}^{CBF}, \qquad (6)$$

provided that the extended subdomain S_q (Fig. 2a), that supports a set of source CBFs, maps one-to-one onto the one-element translated subdomain S_{q+1} (Fig. 2b). Furthermore, the testing CBFs supported by the subdomain S_p have to map one-to-one onto the subdomain S_{p+1} when the same translation vector is used. However, this requires a consistent triangulation as well as a consistent partitioning of the RWGs of all subdomains (and thus array elements) as further clarified with the aid of Fig. 3.

A. Array Meshing Method

The entire array mesh can be efficiently constructed from a few elementary meshed array elements, called the base elements. The geometry of each base element is discretized by a number of polygonal facets of which the outlines are described by a set of boundary nodes. Figure 3 (Step I) shows a discretized TSA base element comprising of 3 polygonal surfaces (two tapered fins and one tiny port polygon across the slotline), where the polygonal boundary nodes are designated by (red) dots. Every polygonal facet is supplied by a non-uniform grid of internal nodes and subsequently triangulated (in a 2-D plane) using a Delaunay meshing routine [31, 32]. The internal grid is distributed such that the elementary triangles are very nearly equilateral. Subsequently, nodes and triangles are added along the boundaries to ensure that the triangulations will be consistent with those of the electrically interconnected adjacent elements when these base elements are placed in the array environment. Next, triangulated base elements are equipped with the RWGs. Step I (Fig. 3) shows a possible RWG polarity distribution, visualized by vectors that join the common edges of each pair of triangles to form an RWG.

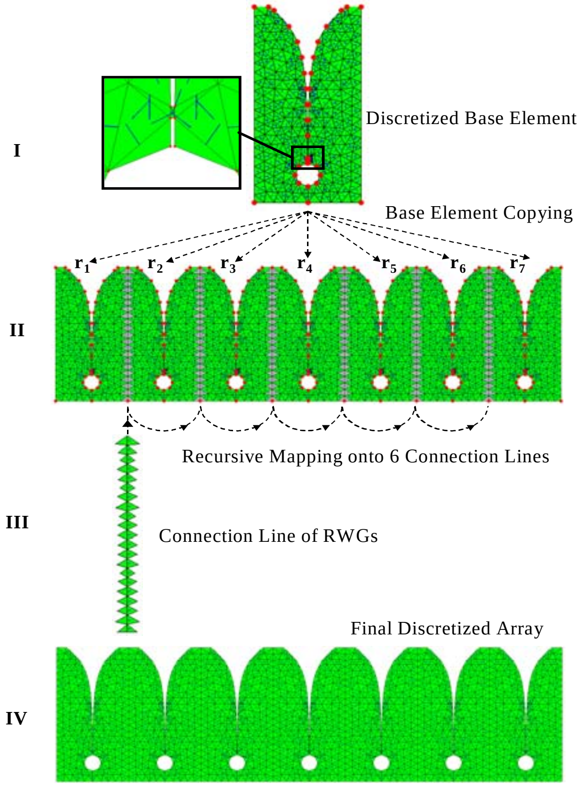

Fig. 3. Efficient and consistent meshing of the antenna array structure to fully exploit translation symmetry.

Step II illustrates a one-to-one replication of the discretized base element at array element locations $\boldsymbol{r}_1 \ldots \boldsymbol{r}_7$. Note that, at this stage, the RWGs ensuring the electrical connection between array elements have not yet been defined. This is accomplished in Step III, where the triangles along a connection line are separately equipped with RWGs and subsequently mapped (recursively) onto the various corresponding connection lines that remain to be equipped with RWGs. For this purpose, we utilize the array symmetry as detailed in the next section. A pseudo code of the recursive-mapping algorithm is included in App. A using Matlab's notation.

Finally, a full meshing of the array geometry (Step IV) facilitates a one-to-one mapping of the CBFs, even though each supporting subdomain extends beyond the outer boundaries of an array element, as shown in Fig. 2.

B. Array Symmetry Extraction Method

For the full array geometry, the degree of translation symmetry between pairs of subdomains, each of which supports a set of CBFs, can be determined as explained below. Following the generation of the boundary nodes for the array in a manner shown in Fig. 3 of Step-II where we replicate the boundary nodes of the base element(s) at their respective array positions, we can determine which array elements are electrically interconnected. Furthermore, when using multiple base elements, such as in the case of dual-polarized arrays, one can also keep track of the type of base element that is interconnected. Let the element interconnection and the corresponding base element type be stored in two separate matrices. Then, for our example, using only one type of base element (Fig. 3), we have:

$$\begin{bmatrix} 1 & 2 & 0 \\ 2 & 1 & 3 \\ 3 & 2 & 4 \\ 4 & 3 & 5 \\ 5 & 4 & 6 \\ 6 & 5 & 7 \\ 7 & 6 & 0 \end{bmatrix} \quad \text{and} \quad \begin{bmatrix} 1 & 1 & 0 \\ 1 & 1 & 1 \\ 1 & 1 & 1 \\ 1 & 1 & 1 \\ 1 & 1 & 1 \\ 1 & 1 & 1 \\ 1 & 1 & 0 \end{bmatrix}$$

where the first rows of the left- and right-hand matrices indicate that element-1 is connected to element-2, and that they are both base elements of type-1 (ignore the zero entries).

Also, for each array element, one can determine the relative positions of the electrically interconnected elements surrounding it. Upon comparing the groups of relative position vectors in conjunction with the corresponding base element types (rows of second matrix), one can readily determine which subdomains (and therefore corresponding set of CBFs) are identical. For our example, subdomains {2, 3, 4, 5, 6}; {1}; and {7} form 3 unique groups. As explained in Section II B, we need to only generate one set of CBFs per unique subdomain, in this case for subdomains 1, 7 and 4, where subdomain 4 is chosen from the first group as the most centralized element. Elements 1, 7 and 4 are extracted from the fully meshed array, together with their neighboring array elements (within a specified radius), to form the resulting three subarrays that are used to generate the CBFs. Note that, after windowing these CBFs, the CBFs supported by subdomain 4 are mapped onto the subdomains 2, 3, 5 and 6.

After determining the unique subdomains (1, 4 and 7), from which the CBFs are mapped, we also compute the relative element array position vectors between all the array elements and store these in a matrix form. For our example, we have

$$\begin{bmatrix} \mathbf{r}_1 - \mathbf{r}_1 & 1 & 1 \\ \mathbf{r}_1 - \mathbf{r}_2 & 1 & 4 \\ \mathbf{r}_1 - \mathbf{r}_3 & 1 & 4 \\ \vdots & \vdots & \vdots \\ \mathbf{r}_7 - \mathbf{r}_5 & 7 & 4 \\ \mathbf{r}_7 - \mathbf{r}_6 & 7 & 4 \\ \mathbf{r}_7 - \mathbf{r}_7 & 7 & 7 \end{bmatrix},$$

where the first column holds the 49 relative array position vectors between element pairs, and the last two columns denote the corresponding two array elements that support the same set of CBFs from which they were initially mapped, namely either 1, 4 or 7. By comparing the rows, one can readily determine which element/subdomain pairs are identical in terms of the sets of CBFs supported by them (last two columns), as well as their mutual orientation and separation distance (first column). Upon selecting the unique rows, the minimal number of impedance matrix blocks that need to be filled can be determined (out of the 49 possible combinations). For convenience, we create a new matrix showing how the reduced matrix is built-up from only a limited number of unique matrix blocks. For our example, the structure of the 7x7 block matrix is:

$$\begin{array}{c|ccccccc} \textit{Subdomain \#} & \mathbf{1} & \mathbf{2} & \mathbf{3} & \mathbf{4} & \mathbf{5} & \mathbf{6} & \mathbf{7} \\ \hline \mathbf{1} & 1 & 2 & 3 & 4 & 5 & 6 & 7 \\ \mathbf{2} & & 8 & 9 & 10 & 11 & 12 & 13 \\ \mathbf{3} & & & 8 & 9 & 10 & 11 & 14 \\ \mathbf{4} & & & & 8 & 9 & 10 & 15 \\ \mathbf{5} & & & & & 8 & 9 & 16 \\ \mathbf{6} & & & & & & 8 & 17 \\ \mathbf{7} & & & & & & & 18 \end{array}$$

where only 18 out of 49 non-redundant mutual impedance blocks have been identified, since we also exploited reciprocity (only the upper triangular part of the matrix is required). Note that, for this example, the matrix entry 11 denotes that the reactions between the CBFs supported by subdomains 2 and 5 are identical to the reactions between the CBFs supported by subdomains 3 and 6, as we can verify by using Fig. 3.

In summary, symmetry can be exploited for arrays of electrically interconnected elements to reduce the complexity of the matrix filling process. For the present example (Fig. 3), the computational complexity becomes linear when the symmetry is exploited.

Furthermore, symmetry can also be used to efficiently compute the array far-field pattern function $\mathbf{f}^{tot}$ by expanding $\mathbf{f}^{tot}$ in terms of M known CBF far-field patterns $\mathbf{f}^{CBF}$ as follows (see also [23]):

$$\mathbf{f}^{tot}(\theta,\varphi) = \sum_{m=1}^{M} I_m^{CBF} \mathbf{f}_m^{CBF}(\theta,\varphi), \qquad (7)$$

where I_m^{CBF} is the mth expansion coefficient for the mth CBF. The coefficient vector $\mathbf{I}^{CBF}$ is computed via the CBFM for a certain array excitation. Because many of the subdomains support the same set of CBFs, the respective CBF patterns are identical as well, apart from a phase correction due to their translated position. For instance, we can write

$$\mathbf{f}_p^{CBF} = \mathbf{f}_q^{CBF} e^{-jk\langle \mathbf{r}_{pq}, \hat{\mathbf{r}}(\theta,\varphi)\rangle}, \qquad (8)$$

where the p^{th} CBF pattern is derived from the qth one by accounting for the translation vector $\mathbf{r}_{pq}$. The unit vector $\hat{\mathbf{r}}(\theta,\varphi)$ denotes the direction of observation, and k the free-space wavenumber of the medium. Note that, for our example (Fig. 3), we only need to explicitly compute the CBF patterns for the sets of CBFs supported only by the subdomains 1, 4 and 7. The remaining CBF patterns are obtained simply via translation.

IV. ARRAYS OF ELECTRICALLY LARGE SUBARRAYS

A rigorous full-wave analysis of phased arrays, each of them surrounded by a number of other disjoint actively phased-steered arrays, becomes computationally prohibitive for a large number of electrically large subarrays. Despite the fact that the computational complexity of solving the matrix equation can be reduced by a large factor by employing a relatively small number of CBFs, the numerical analysis of a much larger array of subarrays will inevitably pose a computational burden, along with an increase in the number of unknowns beyond a certain point. Conventional infinite array approaches may be accurate and fast for an extremely large array of subarrays, although the subarrays have to be electrically small and positioned over a uniform (possibly skewed) rectangular lattice.

In the method proposed herein, the CBFM is used to construct a reduced moment matrix for only one of the subarrays, and the matrix entries are modified so as to account for the mutual coupling by using the characterization of the actively phase-steered surrounding subarrays. Towards this end, we enforce the final surface current solution to be identical on every subarray, apart from a phase difference depending on the scan angle and position vector of a subarray, whereas within each subarray, surface currents may differ per element.

Computing the fields in a given region of a periodic structure, while assuming that they are identical in other regions is a perturbation approach, has also been exploited by Skrivervik and Mosig [33, 34]. The first exposes a spectral-domain approach, the latter shows a spatial-domain approach. In its implementation, the latter is closer to the approach considered in this paper; the main difference being that in the Skrivervik and Mosig papers, the region referred to above is one (microstrip) antenna, while in this paper, it corresponds to a sub-array.

Basically, the CBFM is used at antenna element level, whereas an infinite array approach is used at subarray level. The concept of combining infinite array approaches with macro-domain basis-functions have been examined before in similar methods, e.g., in [35] and [36].

The use of an infinite array assumption at the subarray level obviates the need to solve for all the subarrays at once, and reduces the total solve-time significantly. Obviously, such an approximate method is exact for infinite arrays of mutually coupled subarrays, as well as for finite arrays of non-coupled subarrays (isolated subarrays), or for mutually coupled subarrays where the end-effects of bordering subarrays do not disrupt the impedance characteristics of the subarray under study. Hence, for a finite and all-excited array, the active mutual coupling (or active mutual scan impedance) between the subarrays is one of the primary factors that determines the approximation error of the proposed method. Generally, the accuracy of the approximate method depends upon the scan angle, number of surrounding subarrays, the electrical distance between the subarrays, the electrical size of a subarray, and the type of the antenna element.

Let us refer to Fig. 4, in which we depict the scheme for computing the scan impedance matrix of the six antenna elements that comprise the central subarray. Basically, the scan impedance matrix is obtained by adding the phase-shifted coupling impedance matrices of the surrounding subarrays to the array impedance matrix of the central subarray.

As we impose the condition that the final surface current solutions among the various subarrays be identical, except for a phase shift, we are led to conclude that the corresponding CBF expansion coefficients have to be equal, though phase shifted as well. Figure 4a illustrates how the (active) reduced matrix block $\mathbf{Z}_{pq}^{CBF}$ is computed by testing the electric field, which is generated not only by the source CBF $\mathbf{J}_q$, but also by the respective phase-shifted neighboring source CBFs $\mathbf{J}_q e^{j\phi}$ and $\mathbf{J}_q e^{-j\phi}$ (coupling terms), where the phase shift ϕ depends on both the scan direction $\hat{\mathbf{r}}(\theta,\varphi)$ and the relative position of the subarray w.r.t. the central subarray.

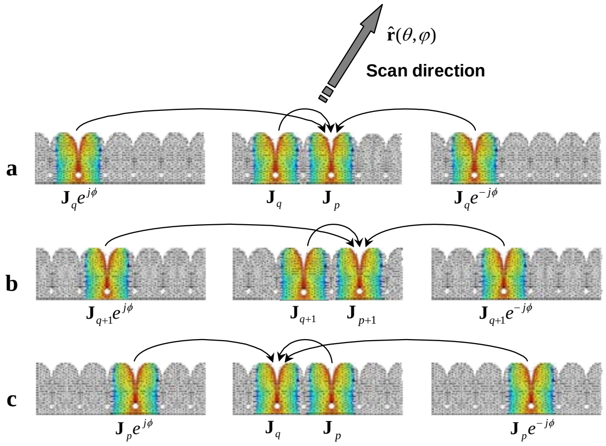

Fig. 4. Reduced matrix construction for the central subarray while accounting for the coupling with the actively phase-steered surrounding subarrays.

In the process of computing all the mutual reactions, the translation symmetry can again be exploited for fast construction of the $\mathbf{Z}^{CBF}$. This can be observed by comparing Fig. 4a to Fig. 4b (see also Sec. III), where an identical though one-element translated reaction between the CBFs is visualized.

Finally, for an off-broadside scan direction, one can easily verify that the active reduced matrix block $\mathbf{Z}_{pq}^{CBF} \neq \left(\mathbf{Z}_{qp}^{CBF}\right)^T$. This is depicted in Fig. 4c, where the source and test domains on the central subarray have been interchanged with respect to the domains shown in Fig. 4b. Consequently, the final active reduced matrix $\mathbf{Z}^{CBF}$ will be non-symmetric; therefore, both the upper- and lower-triangular part of the matrix must be computed, at least partially.

V. NUMERICAL RESULTS

The numerical accuracy and efficiency of the modified CBFM approach, relative to a direct CBFM approach, will be evaluated in this section for an array of disjoint subarrays of TSA elements. The anomalous antenna impedance effects, associated with the (resonant) gaps/slots between disjoint subarray tiles, have been reported in [37, 38] and will therefore not be discussed in this paper. These gaps may need to be introduced for servicing purposes, so that, e.g., individual subarrays can be installed and/or removed as modular units. Furthermore, the transport and manufacturability of relatively small units may be advantageous.

Unless specified otherwise, a threshold of 10^{-2} is used both for the SVD procedure in CBFM, and in the Adaptive Cross Approximation Algorithm [25]. These parameter settings are chosen to be equal for both the direct and modified CBFM approach and we will exploit the translation symmetry for all the cases that are studied, which enables us to make relative comparisons.

All the computations have been carried out by using double-precision arithmetic on a Dell Inspiron 9300 Notebook, equipped with an Intel Pentium-M processor operating at 1.73 GHz, and 2.0 GB of RAM.

The TSA element geometry has been adopted from [22] and [25], and serves here as a reference case for further study.

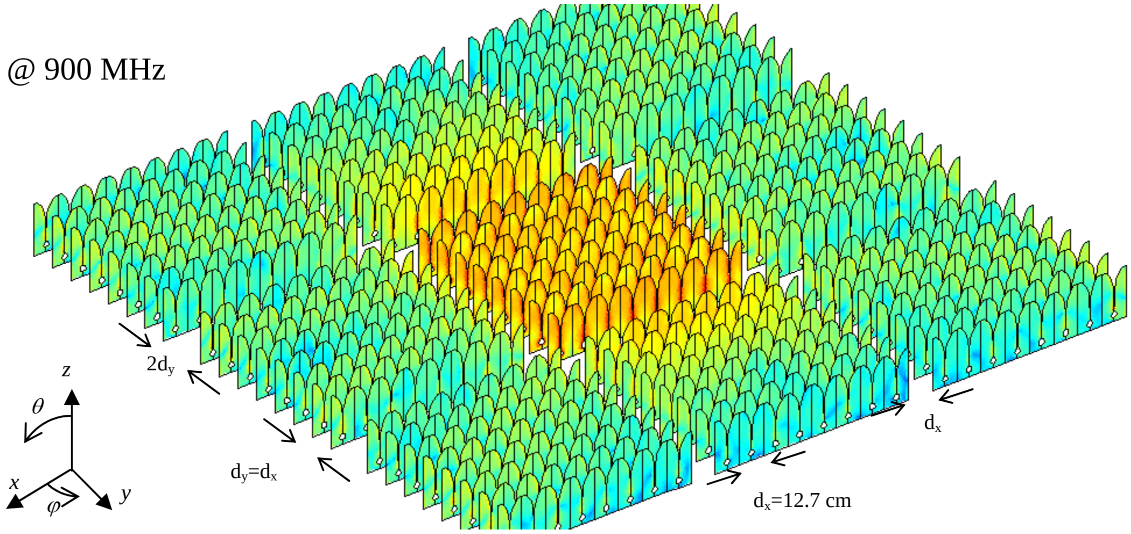

Fig. 5. Array of 9 subarrays (3x3), each of them composed of 64 TSA elements (8x8). To illustrate coupling effects, the active antennas within the central tile are excited by a voltage-gap generator placed over the slot of each TSA element. The central tile scans to broadside (end-fire direction), whereas the TSAs of the surrounding tiles are short-circuited. The magnitude of the surface current distribution is shown (log scale) as computed by a direct CBFM approach.

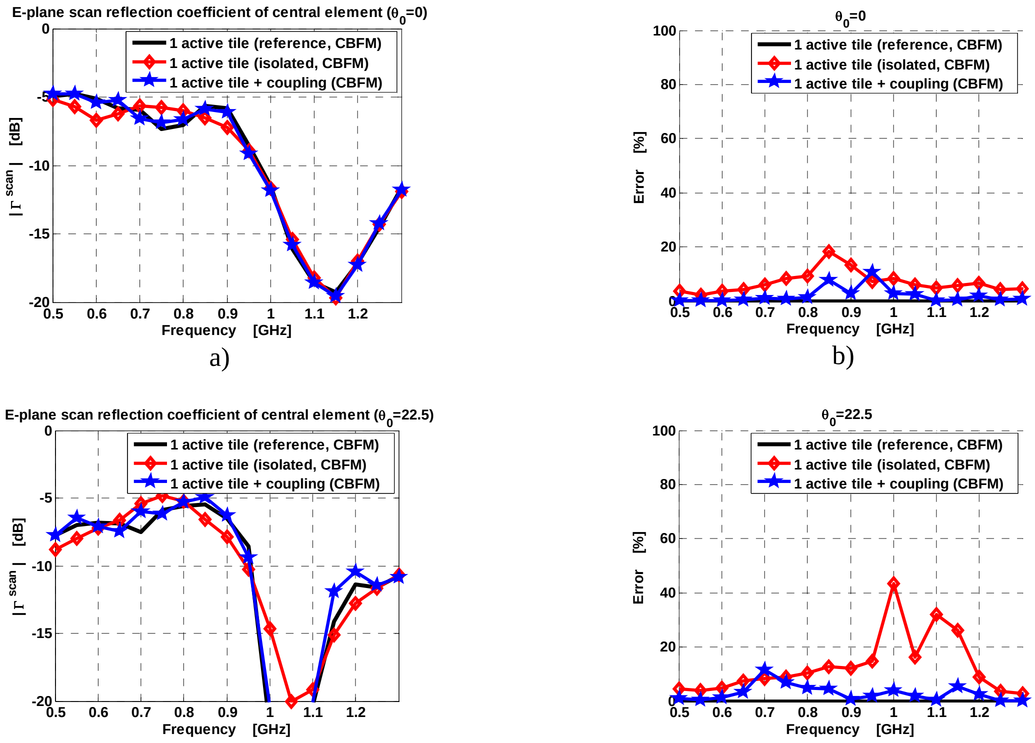

a) b)

c) d)

Fig. 6. (a) Scan reflection coefficient of the central element of the central subarray for broadside scan; (b) Average relative error of all the scan reflection coefficients of the central tile\subarray, for broadside scan; (c) Scan reflection coefficient of the central element of the central subarray for a 22.5 Deg E-plane scan; (d) Average relative error of all the scan reflection coefficients of the central tile\subarray, for a 22.5 Deg E-plane scan.

@ 900 MHz (θ_0=0)	# RWGs	# CBFs	# MoM Blocks	# MoM Blocks (Symmetry)	Time to build MoM blocks	Total Execution Time
9 Tiles	375192	4320	331776	8394	144 m. 29 s.	209 m. 25 s.
1 Isolated Tile	41688	464	4096	294	3 m. 54 s.	11 m. 45 s.
1 Tile + Coupling	41688	480	4096	294	8 m. 42 s.	16 m. 48 s.

Figure 5 illustrates an array of 9 TSA subarrays (3×3) for which a total of 375,192 RWG basis functions have been employed. We compute the antenna impedance matrix of the 576 TSA elements by using a direct CBFM approach, and then go on to derive the scan reflection coefficient for each TSA element (150Ω source-reference impedance). These scan reflection coefficients are taken as references for further comparison. It should be noted that the scan impedances (or scan reflection coefficients) are not only of interest for the characterization of transmit antennas, but can also be used to evaluate noise coupling in receive antennas [39, 40].

Let the scan reflection coefficient of the *n*th antenna element be denoted as Γ_n^{scan}, and the total number of the central subarray elements be N_{sub}. Then, within the central subarray, the average relative error between the actual and approximated scan reflection coefficients can be defined as

$$Error = \frac{\sum_{n}^{N_{sub}} |\Gamma_n^{scan,ref}(\theta_0,\varphi_0) - \Gamma_n^{scan,approx}(\theta_0,\varphi_0)|^2}{\sum_{n}^{N_{sub}} |\Gamma_n^{scan,ref}(\theta_0,\varphi_0)|^2} \times 100\%, \quad (9)$$

where θ_0 and φ_0 designates the scan direction. For the sake of comparison, the error in the scan reflection coefficients has been computed for a single isolated subarray, as well as for a single subarray where we account for the coupling effects with the neighboring subarrays (Sec. IV). Figures 6a and 6c show the scan reflection coefficient of the central element of the central subarray, obtained by using the direct CBFM (reference solution). The same figures also plot the results obtained by using both the single isolated subarray configuration and the subarray configuration with coupling. The corresponding average relative errors for the two scan directions have been plotted in Figs. 6b and 6d as a function of the frequency for the reference case; the isolated array case; and, for the approximate method as proposed in this paper.

As compared to the single isolated subarray case, the accuracy of the scan reflection coefficients is higher for the one-tile array with coupling, particularly for off-broadside scan directions. Obviously, a relatively good accuracy can be obtained for a solve time that is comparable to the time required to solve a single isolated subarray problem (~17 min. versus ~12 min.). The larger solve time is due to the overhead required to construct the reduced matrix while accounting for the coupling terms with neighboring subarrays. Despite this overhead, the overall solve time is about 12 times shorter than the total time required when we use the CBFM approach.

VI. CONCLUSIONS AND FUTURE WORK

In this paper we have outlined a strategy for meshing arrays of electrically interconnected antenna elements in a manner that optimally exploits the translation symmetry between the groups of Characteristic Basis/Testing Functions. As a consequence, the reduced matrix has a block Toeplitz structure and can therefore be constructed in a numerically efficient manner by realizing that many matrix blocks are identical and, hence, can be simply copied during the matrix generation process. The complexity of the matrix-filling process can be reduced to linear order, for 1-D arrays of interconnected single-polarized antennas, by exploiting the Toeplitz symmetry.

In addition, an approximate method has been presented for computing the antenna scan impedances of elements within a subarray, which is surrounded by (many) disjoint phased-steered subarrays. The reduced matrix is constructed only for one of the subarrays, while the coupling between the adjacent subarrays is accounted for explicit in the process of constructing the reduced matrix. Numerical results have been shown for the central subarray of an array of 9 subarrays of 64 tapered slot antennas each. It was shown that the scan reflection coefficients of a single isolated tile resemble those of a central tile which is surrounded by 8 phase-steered subarrays. However; a higher accuracy was obtained for the proposed approximate technique, where a single subarray has been considered while accounting for the coupling with the neighboring subarrays. As expected, the accuracy remains reasonably good (error is less than 10%) for off-broadside scan directions. The total solve time is approximately 12 times faster than that of the direct CBFM approach, though the result has to be recomputed for each scan angle. It should be noted that the scan impedances (or scan reflection coefficients) are not only of interest for the characterization of transmit antennas, but can also be used in the evaluation of noise coupling in receive antennas [39, 40].

In this paper we enforce the condition that the final surface current solution be identical on each subarray, apart from a phase difference depending upon the scan angle and position vector of a subarray, though the surface currents may differ per element within each subarray. It is conjectured that the solution accuracy can be further increased by post-correcting the amplitude level of the initially computed solution of the current per subarray, while maintaining their shapes. For our example, we then have to solve a system of 9 unknowns (per scan angle) in order to accurately synthesize the edge effects in current amplitudes of bordering subarrays.

APPENDIX

The mapping of the 6 consecutive connection lines of RWGs (Fig. 3, step III) is straightforward when we use the array symmetry as described in Sec. III B. For this procedure, a recursive mapping algorithm is employed, which has been developed and summarized below using a pseudo Matlab notation.

Essentially, the main program is executed to construct a list of connection RWGs, termed *ConnRWGList*, which holds the final set of connection RWGs for all lines. To build this list, we first iterate over all RWG connection lines that have been identified (6 identical lines in Fig. 3, although, in general, many more lines may exist that are different from one another). During each iteration, we select a line that is free of RWGs, then equip this line with RWGs, and map this line onto the corresponding translated lines that are yet to be equipped with RWGs, and in a recursive manner by invoking the function *MapRWGLine*.

Main program to build a list of all connection RWGs:

```
ConnRWGList=[];
for n=1:NumberOfConnectionLines
         if triangles along nth line without RWGs?
     -    Equip these connection triangles with
          ConnectionRWGs;
     -    rOffsetGlobal=rOffsetList=[0 0 0];
     -    Call recursive function:
          [ConnectionRWGs, rOffsetList]=MapRWGLine
          (rOffsetGlobal, ConnectionRWGs, rOffsetList,
          ConnRWGList);
     -             Append ConnectionRWGs to
  ConnRWGList;
         end
end
```

The recursive function *MapRWGLine* (detailed on second last page) determines which subdomains are sharing the present RWG connection line at hand. We iterate over the pertaining subdomains and determine, for each subsequent subdomain, which other subdomains are equal, in the sense that they support the same set of CBFs. Within this first loop, we then also iterate over the equal subdomains and, during each iteration, compute the corresponding relative position vector of the corresponding identical subdomain. Within this second loop, we translate/map the RWG line under consideration using the same relative position vector, except if we have mapped this line to the same position before. After the mapping has been successfully completed, we recall the recursive function at this newly mapped position.

The total recursion depth is approximately equal to the total number of maps that have to be made. When the procedure returns from the deepest recursion, most of the maps have been carried out so that the double loops within each recursion are not as time-demanding as one may think at a first glance, because identical maps are skipped. However, the double loop is required to ensure that one also maps the RWG connection line onto the left-hand-side of element 7 (Fig. 3) for instance, which is not obvious by only considering the identical subdomains that belong to subdomain 2.

Recursive function `MapRWGLine`:

```
[ConnRWGList, rOffsetList]=MapRWGLine
(rOffsetGlobal, ConnectionRWGs, rOffsetList, ConnRWGList)
    -    Determine subdomains/elements attached to the
         connection line under consideration;
    for m=1:NumberOfAttachedSubDomains
         - Determine list of subdomains that are
           equal to this mth attached subdomain;
                  for k=1:NumberOfEqualSubDomains
             -   Compute rel. pos. vector rOffset
                 between mth attached subdomain and kth
                 equal subdomain;
             -   rOffsetGlobalNew = rOffsetGlobal +
                                    rOffset;
             if rOffsetGlobalNew not in rOffsetList?
                   -   Append rOffsetGlobalNew to
                       rOffsetList;
                   -   Map ConnectionRWGs using rOffset,
                       yielding MappedRWGs;
                   -   Append MappedRWGs to ConnRWGList;
                   -   Call the recursive function:
                  [ConnRWGList, rOffsetList]=MapRWGLine
                  (rOffsetGlobalNew, MappedRWGs,
                  rOffsetList, ConnRWGList)
             end
        end
    end
```

ACKNOWLEDGEMENT

We are grateful to Prof. A. Boryssenko from Amherst University (UMASS) for his advices and suggestions regarding the implementation of a MATLAB mesher.

REFERENCES

[1] P. J. Hall, "The square kilomtere array: an engineering perspective," Reprinted from *experimental astronomy*, vol. 17, no. 1-3, 2004, ISBN: 1-4020-3797-x, Springer 2005.

[2] A. B. Smolders and M. P. van Haarlem, "Perspectives on radio astronomy: technologies for large antenna arrays," *Conf. Proc., ASTRON*, ISBN: 90-805434-2-x, April 1999.

[3] Website: http://www.skatelescope.org/

[4] A. van Ardenne and C. M. de Vos, "EMBRACE (Electronic Multi-Beam Radio Astronomy ConcEpt) an update 2005," SKA meeting, Pune, India, 2005.

[5] R. Maaskant, M. Popova, and R. van de Brink, "Towards the design of a low cost wideband demonstrator tile for the SKA," *Proc. European Conf. on Antennas and Propag. EUCAP*, Nice, France, 2006.

[6] R. Maaskant, R. Mittra, and W. van Cappellen, "Efficient numerical analysis of prototype antennas for the Square Kilometer Array (SKA) using the Characteristic Basis Function Method (CBFM)," *IEEE AP-S International Symposium USNC/URSI Meeting*, Albuquerque, New Mexico, Jul. 9-14, 2006.

[7] R. Maaskant, M. Ivashina, R. Mittra, W. Yu, and N. T. Huang, "Parallel FDTD modeling of a focal plane array with Vivaldi elements on the highly parallel LOFAR Bluegene/L supercomputer," *IEEE AP-S International Symposium*, Albuquerque, New Mexico, pp. 3861-3864, July 2006.

[8] R. Mittra, "A look at some challenging problems in computational electromagnetics," *IEEE Antennas Propag. Mag.*, vol. 46, no. 5, pp. 18-32, Oct. 2004.

[9] C. Craeye, A. O. Boryssenko, and D. H. Schaubert, "Analysis of infinite and finite arrays of tapered-slot antennas for SKA," *Proc. EUMC*, Milan, Italy, pp. 1003-1006, 2002.

[10] M. N. Vouvakis, S. C. Lee, K. Zhao, and J. F. Lee, "A symmetric FEM-IE formulation with a single-level IE-QR algorithm for solving electromagnetic radiation and scattering problems," *IEEE Trans. Antennas Propag.*, vol. 52, no. 11, pp. 3060-3070, Nov. 2004.

[11] V. Prakash and R. Mittra, "Characteristic basis function method: A new technique for efficient solution of method of moments matrix equations," *Micro. Opt. Tech*. vol. 36, pp. 95-100, Jan. 2003.

[12] J. Yeo, V. Prakash, and R. Mittra, "Efficient analysis of a class of microstrip antennas using the Characteristic Basis Function Method (CBFM)," *Micro. Opt. Tech*. vol. 39, pp. 456-464, Dec. 2003.

[13] G. A. E. Vandenbosch and A. R. Van de Cappelle, "Use of combined expansion scheme to analyze microstrip antennas with the method of moments," *Radio Sci.*, vol. 27, pp. 911-916, Nov. /Dec. 1992.

[14] J. Heinstadt, "New approximation technique for current distribution in microstrip array antennas," *Micro. Opt. Tech*. vol. 29, pp. 1809-1810, Oct. 1993.

[15] E. Lucente and A. Monorchio, "A parallel iteration-free MoM algorithm based on the Characteristic Basis Functions Method," *Proc. int. URSI Commission B, EMTS 2007*, Ottawa, Canada, July 26-28, 2007.

[16] A.M. van de Water, B. P. de Hon, M. C. van Beurden, A. G. Tijhuis, and P. de Maagt, "Linear Embedding via Green's operators: A modeling technique for finite electromagnetic band-gap structures," *Phys. Rev. E*, vol. 72, p. 056704, 2005.

[17] L. Matekovits, V. A. Laza, and G. Vecchi, "Analysis of large complex structures with the synthetic-functions approach," *IEEE Trans. Antennas Propag.*, vol. 55, no. 9, pp. 2509-2521, Sep. 2007.

[18] L. Matekovits, G. Vecchi, G. Dassano, and M. Orefice, "Synthetic function analysis of large printed structures: the solution space sampling approach," *IEEE AP-S International Symposium*, Boston, Massachusetts, pp. 568-571, July 2001.

[19] W. B. Lu, T. J. Cui, Z. G. Qian, X. X. Yin, and W. Hong, "Accurate analysis of large-scale periodic structures using an efficient Sub-Entire-Domain basis function method," *IEEE Trans. Antennas Propag.*, vol. 52, no. 11, pp. 3078-3085, Nov. 2004.

[20] D. J. Bekers, S. J. L. van Eijndhoven, A. A. F. van de Ven, P. Borsboom, and A. G. Tijhuis, "Eigencurrent analysis of resonant behavior in finite antenna arrays," *IEEE*

Trans. Micro. Theory Tech., vol. 54, no. 6, pp. 2821-2829, June 2006.

[21] E. Suter, J. R. Mosig, "A subdomain multilevel approach for the efficient MoM analysis of large planar antennas," *Micro. Opt. Tech.* vol. 26, no. 4, pp. 270-277, Aug. 2000.

[22] R. Maaskant, R. Mittra, and A. G. Tijhuis, "Application of trapezoidal shaped Characteristic Basis Functions to arrays of electrically interconnected antenna elements," *Proc. Electromagnetics in Advanced Applications*, ICEAA, pp. 567-571, 17-21 Sept. 2007.

[23] C. Craeye, "A fast impedance and pattern computation scheme for finite antenna arrays," *IEEE Trans. Antennas Propag.*, vol. 54, no. 10, pp. 3030-3034, Oct. 2006.

[24] E. Garcia, C. Delgado, F. S. de Adana, F. Cátedra, and R. Mittra, "Incorporating the Multilevel Fast Multipole Method into the Characteristic Basis Function Method to solve large scattering and radiation problems," *IEEE AP-S International Symposium*, Honulullu, Hawaii, pp. 1285-1288, June 2007.

[25] R. Maaskant, R. Mittra, and A. G. Tijhuis, "Fast analysis of large antenna arrays using the Characteristic Basis Function Method and the Adaptive Cross Approximation algorithm", *IEEE Trans. Antennas Propag.*, vol. 56, no. 11, pp. 3440-3451, Nov. 2008.

[26] I. Stevanovic, and J. R. Mosig, "Subdomain multilevel approach with fast MBF interactions," *IEEE AP-S International Symposium*, Monterey, California, pp. 367-370, June 2004.

[27] P. De Vita, A. Freni, L. Matekovits, P. Pirinoli, and G. Vecchi, "A combined AIM-SFX approach for large complex arrays," IEEE AP-S International Symposium, Honulollu, Hawaii, pp. 3452-3455, June 2007.

[28] S. Rao, D. Wilton, and A. Glisson, "Electromagnetic scattering by surfaces of arbitrary shape," *IEEE Trans. Antennas Propag.*, vol. 30, no. 3, pp. 409-418, May 1982.

[29] G. H. Golub and C. F. van Loan, *Matrix Computation*, Baltimore, MD: John Hopkins Univ. Press, 1989.

[30] C. Delgado, F. Catedra, and R. Mittra, "A numerically efficient technique for orthogonalizing the basis functions arising in the solution of electromagnetic scattering problems using CBFM," *IEEE AP-S International Symposium*, Honulollu, Hawaii, pp. 3608-3611, June 2007.

[31] B. Delaunay, "Sur la sphère vide," *Izvestia Akademii Nauk SSSR, Otdelenie Matematicheskikh i Estestvennykh Nauk*, vol. 7, pp. 793-800, 1934.

[32] Personal communication with Prof. A. Boryssenko regarding the implementation of a MATLAB mesher, UMASS, 2004.

[33] A. K. Skriverik and J. R. Mosig, "Analysis of finite phase arrays of microstrip patches," *IEEE Trans. Antennas Propag.*, vol. 41, no. 8, pp. 1105-1114, Aug. 1993.

[34] A. K. Skriverik, and J. R. Mosig, "Analysis of printed array antennas," *IEEE Trans. Antennas Propag.*, vol. 45, no. 9, pp. 1411-1418, Sept. 1997.

[35] C. Craeye, A. G. Tijhuis, and D. H. Schaubert, "An efficient mom formulation for finite-by-infinite arrays of two-dimensional antennas arranged in a three-dimensional structur," *IEEE Trans. Antennas Propag.*, vol. 51, no. 9, pp. 2054-2056, Sep. 2003.

[36] A. Neto, S. Maci, G. Vecchi, and M. Sabbadini, "A truncated floquet wave diffraction method for the full wave analysis of large phased arrays - part II: Generalization to 3-D cases," *IEEE Trans. Antennas Propag.*, vol. 48, no. 3, pp. 601-611, Mar. 2000.

[37] D. H. Schaubert, and A. O. Boryssenko, "Subarrays of Vivaldi antennas for very large apertures," *Proc. 34th European Microwave Conference*, Amsterdam, pp. 1533-1536, 2004.

[38] D. H. Schaubert, S. Kasturi, M. W. Elsallal, and W. van Cappellen, "Wide bandwidth Vivaldi antenna arrays - some recent developments," *Proc. European Conf. on Antennas and Propag.*, Nice, France, 2006.

[39] R. Maaskant and B. Woestenburg, "Applying the Active Antenna Impedance to Achieve Noise Match in Receiving Array Antennas", *Antennas and Propagation Symposium*, Hawaii, USA, pp. 5889-5892, June 2007.

[40] C. Craeye, Personal communication.

Rob Maaskant received the M.Sc. degree (*cum laude*) in electrical engineering from the Eindhoven University of Technology, The Netherlands, in 2003. Since then, he has been an antenna research engineer at the Netherlands Foundation for Research in Astronomy (ASTRON) where his research is carried out in the framework of the Square Kilometre Array (SKA) radio telescope project. He is currently working toward the Ph.D. degree in the field of numerically efficient integral-equation techniques for large finite array antennas. Besides, his research includes the characterization and design of antenna array receiving systems.

Raj Mittra (S'54–M'57–SM'69–F'71–LF'96) is a Professor in the Electrical Engineering Department, Pennsylvania State University, University Park. He is also Director of the Electromagnetic Communication Laboratory, which is affiliated with the Communication and Space Sciences Laboratory of the Electrical Engineering Department. Prior to joining Penn State, he was a Professor in the Electrical and Computer Engineering Department, University of Illinois, Urbana-Champaign. He is President of RM Associates, State College, PA, a consulting organization that provides services to industrial and governmental organizations, both in the U.S. and abroad. He has published more than 700 technical papers and more than 30 books or book chapters on various topics related to electromagnetics, antennas, microwaves, and electronic packaging. He has received three patents on communication antennas. He has advised more than 85 Ph.D. students and about an equal number of M.S. students, and has mentored approximately 50 postdoctoral research associates and visiting scholars in the EMC Laboratory. Prof. Mittra received the Guggenheim Fellowship Award in 1965, the IEEE Centennial Medal in 1984, IEEE Millennium Medal in 2000, the IEEE/AP-S Distinguished Achievement Award, the AP-S Chen-To Tai Distinguished Educator Award in 2004, and the IEEE Electromagnetics Award in 2006. He is a past President of AP-S and was an Editor of the IEEE Transactions on Antennas and Propagation.

Anton G. Tijhuis (M'88) was born in Oosterhout N.B., The Netherlands, in 1952. He received the M.Sc. degree in theoretical physics from Utrecht University, Utrecht, The Netherlands, in 1976, and the Ph.D. degree (*cum laude*) from the Delft University of Technology, Delft, The Netherlands, in 1987. From 1976 to 1986 and 1986 to 1993, he was an Assistant and Associate Professor with the Laboratory of Electromagnetic Research, Faculty of Electrical Engineering, Delft University of Technology. In 1993, he became a Full Professor of electromagnetics with the Faculty of Electrical Engineering, Eindhoven University of Technology, Eindhoven, The Netherlands. He has been a Visiting Scientist with the University of Colorado at Boulder, the University of Granada, Granada, Spain, the University of Tel Aviv, Tel Aviv, Israel, and with McDonnell Douglas Research Laboratories, St. Louis, MO. Since 1996, he has been a Consultant with TNO Defence, Security, and Safety, The Hague, The Netherlands. His research interests are the analytical, numerical, and physical aspects of the theory of electromagnetic waves. In particular, he is involved with efficient techniques for the computational modeling of electromagnetic fields and their application to detection and synthesis problems from several areas of electrical engineering.

Application of the Characteristic Basis Function Method for the Electromagnetic Analysis of Electrically Large and Complex Bodies

Carlos Delgado [1], Eliseo García [2], Felipe Cátedra [1], and Raj Mittra [3]
[1] Department of Computer Science
University of Alcalá, Edificio Politécnico, Alcalá de Henares 28871, SPAIN
carlos.delgado@uah.es , felipe.catedra@uah.es

[2] Department of Automatics
University of Alcalá, Edificio Politécnico, Alcalá de Henares 28871, SPAIN
eliseo.garcia@uah.es

[3] Department of Electrical Engineering
Pennsylvania State University, University Park, PA 16802, USA
Mittra@engr.psu.edu

***Abstract*—** An overview of a parallel implementation of the Characteristic Basis Function Method combined with the Multilevel Fast Multipole Algorithm is presented. This approach allows an accurate analysis of very large electromagnetic problems. The geometry is described by means of Non-Uniform Rational B-Splines, and the macro-basis functions are expressed in terms of subsectional functions totally conformed to the original geometry. A number of representative examples are considered in order to show the performance of the proposed approach.

***Index Terms*—** Method of Moments, Macro-Basis Functions, Characteristic Basis Function Method (CBFM).

I. INTRODUCTION

Due to the great improvement of the computational efficiency during the last decade, many problems for which high-frequency approaches (such as Physical Optics [1] or the Geometrical Theory of Diffraction [2]) or hybrid methods [3-6] were the only possible choices are now amenable to simulation via rigorous techniques. Also, the development of architectures and paradigms for the parallelization of computer codes [7] are playing a very important role in the expansion of the scope of rigorous analysis methods. However, the most important contribution to this new scenario is given by the development of improved numerical techniques carried out by numerous research groups worldwide. Even though the heterogeneous underlying strategies define different features for each of these developments, we can classify them into different categories, according to the treatment of the electromagnetic problem.

The Method of Moments (MoM) [8] is nowadays a strong reference against which the new frequency-domain approaches can be compared. Since in the MoM the unknowns are distributed over the surface of the objects, it is widely used for the analysis of scattering or radiation problems involving geometries with one or several layers of homogeneous materials. Many of the new approaches maintain a MoM-based formulation and add new improvements that allow us to expand its application range. The main drawback of the MoM is the size of the coupling matrix that determines the linear system to be solved later. Owing to a fine discretization of the object geometry, typically 10 per λ in the conventional MoM, the matrix size becomes large relatively quickly as the object size becomes electrically large, and this, in turn, places a heavy burden on the CPU, both in terms of solve time and memory. A widely well-known approach to overcome this difficulty consists of using the Fast

Multipole Method (FMM) [9] or the Multilevel Fast Multipole Algorithm (MLFMA) [10], that reduce the computational complexity from $O(N^2)$ to $O(N^{3/2})$, or even to $O(N\log N)$ for the latter approach. The use of these approaches entails the storage of only the near-field terms of the coupling matrix and computing the far-field interactions efficiently via fast matrix-vector products in the iterative solution process. There are a number of techniques that also take advantage of the efficient evaluation of these products in the iterative solution of large problems, such as the Complex Multipole Beam Approach (CMBA) [11], the Impedance Matrix localization (IML) technique [12] or the Adaptive Integral Method (AIM) [13].

A different strategy which has been proven to decrease the computational complexity of the conventional MoM is based on the fact that the submatrices that contain the coupling between moderately distant blocks (about a few wavelengths, usually) are rank-deficient or, in other words, the number of degrees of freedom is smaller than the number of samples used. Therefore, these submatrices can be compressed using some of the techniques available in the literature, like those based on the Modified Gram-Schmidt procedure (MGS) [14, 15], the Adaptive Cross Approximation (ACA) [16, 17] or the Matrix Decomposition Algorithm [18]. It is worthwhile to remark that these approaches make use of purely algebraic manipulations of the original matrices.

A third group of methods, among which the presented work can be situated, is based on a strategy that utilizes a domain-decomposition scheme and reduces the number of unknowns by replacing the subdomain-type basis functions with a set of macro-basis functions. We can mention here the Synthetic Function Expansion technique (SFX) [19] or the Characteristic Basis Function Method (CBFM) [20].

The CBFM models the current on an arbitrarily shaped target by means of a set of macro-basis functions, called Characteristic Basis Functions (CBFs), defined over geometrical blocks in which the geometry is subdivided. Instead of being limited to a predetermined and/or fixed shape, the CBFs are generated taking into account the physics of the problem, so they are tailored to the geometrical properties of each block, and their use leads to a “reduced” matrix whose size is considerably smaller than that of the original impedance matrix based on subdomain functions (e.g. Rao-Wilton-Glisson functions [21] or rooftops [22]). Each CBF, in turn, can be seen as an aggregation of low-level basis functions whose weights are fixed when each CBF is generated. The reduction in matrix size achieved by the CBFM enables us to use direct solvers for some problems where, previously, an iterative solver represented the only possible choice because of the size of the impedance matrix. However, for very large problems the reduction achieved in the number of unknowns may still be insufficient as to resort to a direct solver. In this situation, an iterative solution process can be utilized by combining the CBFM with the MLFMA approach [23].

We will consider in this work a geometric representation based on Non-Uniform Rational B-Splines (NURBS) [24], due to its flexibility to model arbitrary geometries and the fact that this format has become widespread in the world of Computer Aided Geometric Design (CAGD). The CBFs are represented in terms of modified rooftop functions defined along the u or v directions over a parametric domain, totally conformed to the NURBS patches, so the discretization error is minimized.

This paper is structured as follows. In Section 2, we discuss the procedure for obtaining the Characteristic Basis Functions from rigorous or asymptotic solutions of smaller problems where each block is isolated from the rest of the geometry. Section 3 deals with a particular implementation of the CBFM, used in this work, where the low-level basis functions employed are modified rooftops placed over the parametric domain of NURBS patched and totally conformed to the surface, and the low-level testing functions are razor blades also located directly over the parametric domain of the patch. In Section 4 the applicability of the CBFM is enlarged by including the MLFMA formulation, so that the computational requirements of very large problems are now affordable by using the CBFM-MLFMA. In section 5 we discuss the details of the parallelization of the proposed approach in order to optimize the balance of the computational load between different computing nodes. Finally we present some conclusions derived from this work.

II. GENERATION OF THE CHARACTERISTIC BASIS FUNCTIONS

Previous to the generation of the CBFs, which will model the current over the structures under analysis, we set up a partitioning of the geometry into blocks. It is important to note that the size of these blocks can go up to a few thousands low-level basis functions. The CBF generation process takes into account the shape of each block. In order to incorporate the physics of the problem into the CBFs we obtain these functions from the current solutions of the isolated block. The approach shown in [20] considers a scheme where the CBFs are grouped into two categories: the primary CBFs, due to the currents induced by the incident field on each block (obtained by isolating the block), and the secondary CBFs, obtained by assuming that the incident field on a block is due to the field radiated by the currents that the external field induces on another block. Thus, a set of CBFs (one primary and several secondary CBFs) is assigned to each block. However, by following this approach the reduced matrix depends on the external field, which can be undesirable in some cases. In order to overcome this problem, there is a different technique, more appropriate for scattering problems with multiple right hand sides, consisting on obtaining the CBFs from a set of plane waves (Plane Wave Spectrum, PWS) which impinge on the scatterer from different angles, and considering both polarizations (θ and φ). By following this procedure we eliminate the primary and secondary classification of the CBFs. Fig. 1 depicts this approach in a 2D scenario. The different plane waves that surround the surface are separated by an angular step $\Delta\theta$. The number of plane waves to be considered obviously depends on the size of the block. In fact, having a large enough number of currents with different shapes based on approximate solutions with which build the new basis functions (i.e., the CBFs) is more important than having a few extremely accurate solutions of the currents due to several plane waves. It is also interesting to remark that the accuracy obtained in the modelization of evanescent fields can be controlled by increasing the discretization density (i.e. the size of the subdomains). The evanescent behaviour of the CBFs is seen after obtaining the currents induced by the plane waves on the block with the MoM. Therefore, it is not necessary to consider a sampling of plane waves outside of the visible spectrum in order to obtain CBFs with fast amplitude variations. Thus, simply by choosing an angular separation in the θ and φ spherical components between consecutive plane waves depending on the block size is enough for obtaining good results. Specifically, we use a separation of 10º for block sizes whose maximum side length is below 2λ, 5º when the block size is up to 4λ and 3º for larger blocks.

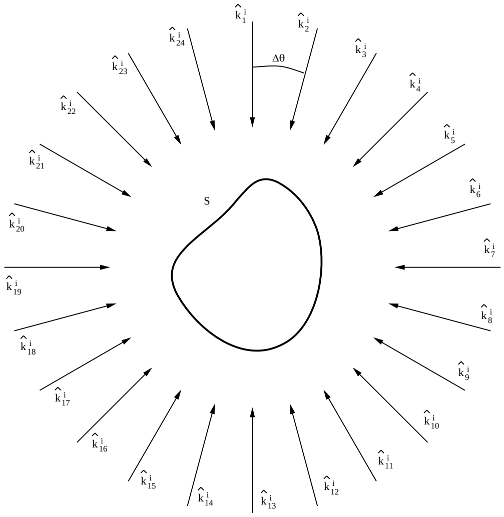

Fig. 1. 2D scheme of the PWS surrounding the target object for the CBF generation.

There are different possibilities for obtaining the currents induced by the plane waves on the block under consideration. For example, the conventional Method of Moments can be used for this purpose. If we are considering P different incident waves, it would be necessary to solve the following set of MoM problems [20,25]:

$$[Z]^i [J]_k^i = [V]_k^{inc},\ k = 1,\dots,P, \tag{1}$$

where $[Z]^i$ is the coupling matrix for block-*i*, $[J]_k^i$ indicates the current vector for block-*i* and the k^th plane wave excitation, and $[V]_k^{inc}$ represents the k^{th} excitation vector. Due to the fact that we are isolating the block from the rest of the geometry, in order to mitigate the artificial edge behaviour of the currents it is convenient to compute the currents over an extension of the original block, usually considering a fraction of wavelength as the size of this extension [20]. Only the currents that are inside the original block are retained and stored as the CBFs after being orthogonalized. Obviously, we do not need to follow this procedure if we are using PO to calculate the induced currents instead of the MoM. The size of the extension depends on the type of low-level basis functions considered. We have found that with the scheme described in [28], which utilizes rooftops, no extension is required to get accurate results, because of the use of connection strips which effectively dovetail the subdomains in which the low-level basis functions are defined. For an RWG-based scheme, accurate results are obtained by extending the original blocks by approximately 0.3λ. If no extensions are considered, a noticeable degradation of the results has been observed in a number of test cases simulated.

It is also possible to use high-frequency approaches for the computation of the currents induced by the incident plane wave, when the block being analyzed is smooth. The PO approach can be used to bypass the solution of (1) for different plane wave excitations. The expansion of the current over the block-*i* in terms of subdomain functions due to the k-th incident plane wave can be expressed as:

$$\begin{aligned} B_k^i(u,v) = 2\sqrt{\frac{\mu_0}{\varepsilon_0}} \sum_{n=1}^{N_i} \left\{ \hat{n}(u_{0n},v_{0n}) \times \left[\hat{k}_k^i \times \vec{E}_0 \right] \cdot \right. \\ \exp\left[-jK\left(\hat{k}_k^i \cdot \vec{r}(u_{0n},v_{0n}) \right) \right] \cdot T_n(u,v), \end{aligned} \tag{2}$$

where (u_{0n},v_{0n}) designates the point on the nth rooftop where the current is sampled, and corresponds to the center of the associated parametric contour, $\hat{n}$ is the normal vector and $\vec{r}$ is the spatial point. The function $T_n(u,v)$ is the n$^{\text{th}}$ rooftop located in block-*i*, and N_i is the total number of rooftops within this block. Our experience shows that PO currents can be used to construct the Characteristic Basis Functions even for relatively small block sizes (one wavelength or even less). One can find that in some cases the PO-derived CBFs cannot model appropriately the fast current variations in the free edges of the geometry. The scheme shown in [26] solves this problem by defining a special type of blocks with a reduced width near these edges.

After generating the induced current vectors corresponding to each one of the plane wave excitations for block-*i*, the associated CBFs can be obtained by performing the orthogonalization of these vectors. The Singular Value Decomposition (SVD) [14] is used for this purpose. If we denote as M the total number of plane waves considered, we can arrange all the calculated currents in a $M \times N$ matrix form, where N is the number of low-level basis functions on the block. After calculating the SVD of this matrix, we obtain a new orthogonal set of basis vectors which can be identified with the singular vectors resulting from the SVD operation [27]. However, it is not necessary to retain the complete set of singular vectors as the new macro-basis functions. Those singular vectors which correspond to singular values with a negligible magnitude can be discarded without losing accuracy in the final results. In other words, we set a threshold γ, relative to the largest singular value, and retain only the singular vectors corresponding to those singular values above γ times the strongest singular value. We recommend γ in the range from $2 \cdot 10^{-3}$ to10^{-3}. It is important to remark that the number of orthogonal vector retained after the SVD is usually several times lesser than the number of original plane wave currents, due to the linear relations of dependence of these in the block surface. The induced current solutions used to represent the CBFs need only be approximate solutions at this stage, since the final solution will be derived later by adjusting the coefficients of these basis functions. In other words, as long as we introduce a sufficiently large number of plane waves for the CBF generation, the final current distribution will be satisfactorily modelled. The truncated SVD technique referenced in the manuscript is not an exact decomposition of the original matrix, but it is a very useful and close approximation to the original matrix achieved by a matrix of reduced rank (optimal approximation considering the Frobenius norm). In the practical applications we observe a very rough decrease of the amplitude of the singular values. In most cases setting the threshold higher that the reference value given in the manuscript does not affect significatively the number of resulting CBFs. The threshold values proposed in this work allow us to obtain very good results (in the sense that the resulting set of CBFs can model the currents very accurately) and do not depend on the shape or the size of the block.

In Fig. 2 we have depicted the evolution of the magnitude of the singular values for two different block types and sizes. We show in the figure the singular values obtained for a plane block with a side length of two wavelengths and for a block with the shape of a spherical quadrant with a radius of one wavelength. It can be seen that the magnitude of these values decays very fast. The contribution of those CBFs whose singular values have a very small magnitude can be considered negligible, so that they can be discarded.

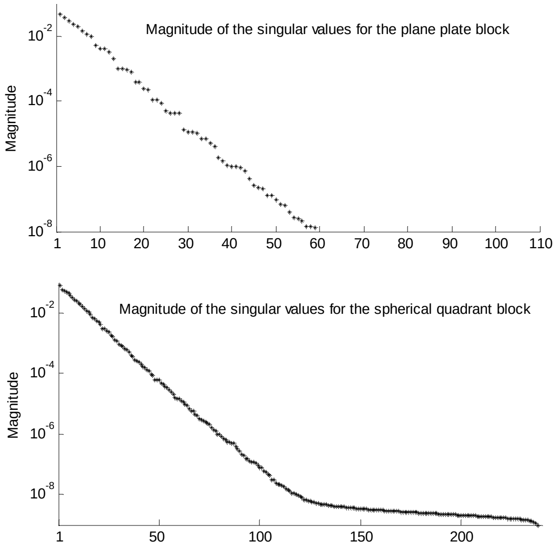

Fig. 2. Magnitude of the singular values after calculating the currents induced by the plane waves on the block for a plane plate case (top) and a spherical quadrant case (bottom).

III. THE COMBINATION OF THE CBFM AND NURBS SURFACES

As previously indicated, the CBFM is independent from the type of low-level subsectional basis functions chosen for the expansion of the CBFs. In this work, we consider a generalization of the planar rooftops introduced by Glisson and Wilton in [22] as the low-level basis functions. These functions are located over a region of the NURBS patch where they belong. To do this, the parametric domain associated to the NURBS surface is divided in order to generate a mesh of rectangular subdomains. Each one of the contour segments between two consecutive subdomains is then associated with a basis and a testing function. It is necessary to define two sets of rooftops, for modeling the *u*- and *v*-components of the current over the patch. The testing functions selected are razor-blades, also be separated into two groups. For the Electric Field Integral Equation (EFIE) formulation we place the razor blades perpendicular to the contour shared by each pair of subdomains, while they should be parallel to the contour for the case of the Magnetic Field Integral Equation (MFIE). Note that these basis and testing functions are totally conformed to the NURBS surface. Figure 3 shows a scheme of an arbitrary surface with its control points, and the set of subdomains obtained when we divide its parametric domain into regions. Also, we show in the figure how a basis function along the *v*-direction and a testing function along the *u*-direction are placed. Note that this testing function corresponds to the EFIE formulation, according to the above explanation (perpendicular to the contour shared between two subdomains). Further details can be consulted in [28-30].

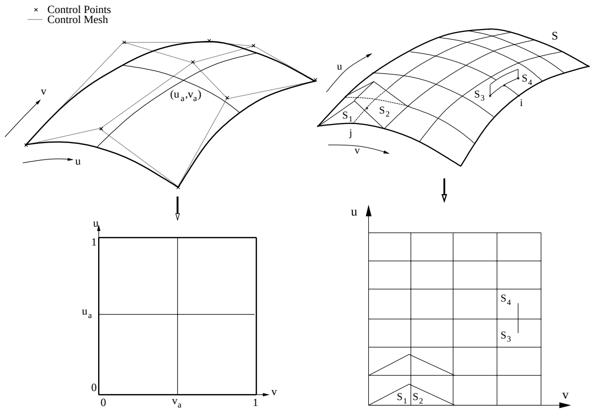

(a) (b)

Fig. 3. (a): Arbitrary NURBS patch and control points; (b): Discretization of the surface in the parametric domain and collocation of basis and testing functions.

As a validation of the CBFM approach described so far in this work, we consider a PEC cube with two square facets parallel to each canonical plane (*XY*, *XZ* and *YZ*). The length of each side is 1 meter, and a frequency of 900 MHz has been set for the simulations. We have obtained monostatic RCS values and we have compared them with those returned by the conventional MoM, for the θ-θ and φ-φ polarizations. Figures 4 and 5 show a good agreement between the results obtained using both methods. The number of unknowns required by the Method of Moments has been 11532, while the CBFM has needed 1140 unknowns. Each one of the six faces of the cube was identified as one CBFM block, so we obtained 190 CBFs for each block. The CBFs have been obtained from a set of incident plane waves considering $\Delta\theta=\Delta\varphi=7^o$. The MoM CPU time is 44022 seconds; the CBFM CPU-time is 3526 seconds. Both results have been obtained using a SUN Fire V65 workstation (2 Xeon 3GHz processors with 8 Gbytes of RAM).

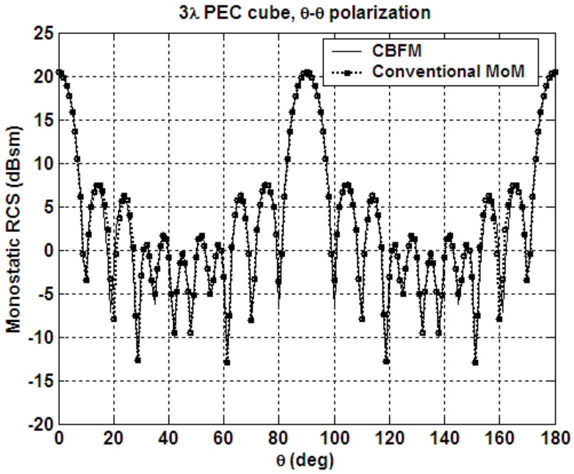

Fig. 4. θ-θ polarization results for the PEC cube monostatic RCS analysis.

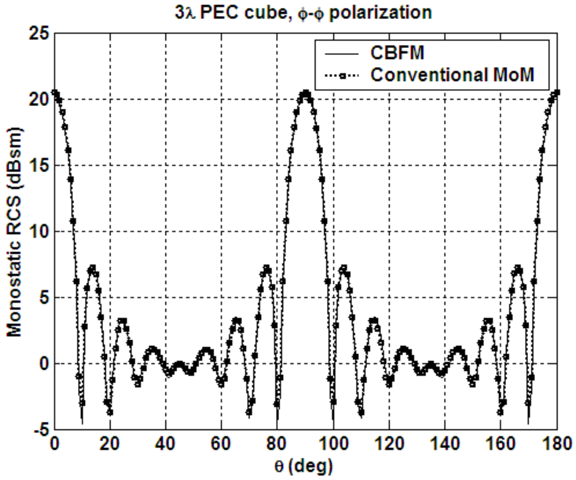

Fig. 5. φ-φ polarization results for the PEC cube monostatic RCS analysis.

In the following test case we consider the COBRA cavity with a flap (Fig. 6), modeled using 24 NURBS surfaces. In figures 7 and 8 we show the monostatic RCS results obtained for an angular sweep with a fixed value of $\varphi=0^o$ and $\theta=0^o$ to 90^o with an angular step of 1^o at a frequency of 10 GHz with the proposed method, compared with the values given by the Finite Element-Boundary Integral method in [31]. From the discretization process, 59147 unknowns arise considering the standard sampling rate of $\lambda/10$. An angular step of 5^o has been considered in this case for the CBF computation. Only 4711 high-level functions have been retained after orthogonalizing the PO-derived induced currents. The simulation has been carried out in 65966 seconds using an Opteron processor at 2.4 GHz with a total RAM of 64 Gbytes

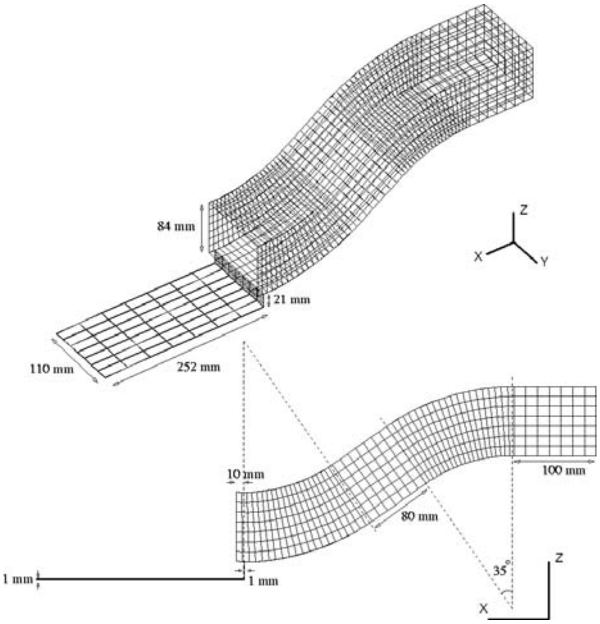

Fig. 6. Geometrical scheme of the COBRA cavity with a flap.

The next example consists of a PEC almond-shaped target (Fig. 9), similar to the NASA almond [32], but with a different size. The total length of the object is 2.5 meters with a total surface area of 4 m^2. The geometry is defined by the equations:

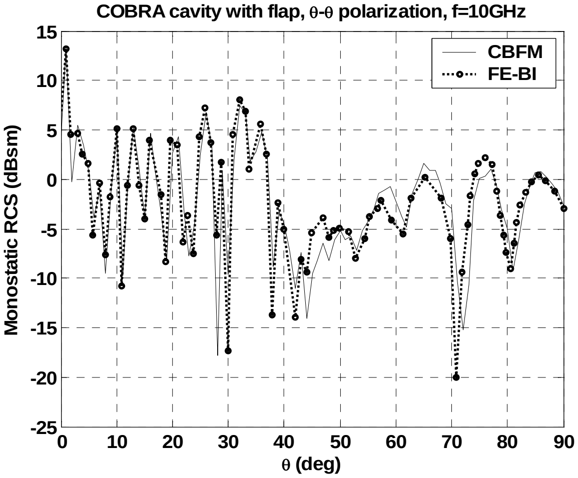

Fig. 7. *θ-θ* polarization results for the COBRA cavity with a flap.

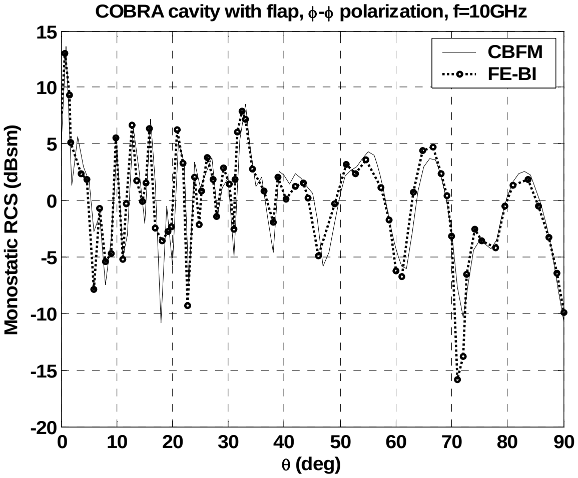

Fig. 8. *φ-φ* polarization results for the COBRA cavity with a flap.

$$
\left.\begin{aligned}
x &= d\,t\\
y &= 0.193333\,d\left[\sqrt{1-\left(\frac{t}{0.416667}\right)^2}\,\right]\cos\psi\\
z &= 0.06444\,d\left[\sqrt{1-\left(\frac{t}{0.416667}\right)^2}\,\right]\sin\psi\\
&-\pi < \psi < \pi
\end{aligned}\right\}\text{, for } -0.416667 < t < 0 \tag{3}
$$

$$
\left.\begin{aligned}
x &= d\,t\\
y &= 4.833450\,d\left[\sqrt{1-\left(\frac{t}{2.083350}\right)^2}-0.96\right]\cos\psi\\
z &= 1.611148\,d\left[\sqrt{1-\left(\frac{t}{2.083350}\right)^2}-0.96\right]\sin\psi\\
&-\pi < \psi < \pi
\end{aligned}\right\}\text{, for } 0 < t < 0.583333 \tag{4}
$$

where d is the length of the almond, 2.5 m.

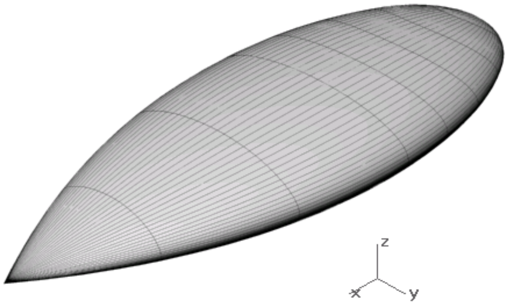

Fig. 9. “Almond” test case.

Figures 10 and 11 show the bistatic RCS results at a frequency of 2 GHz for the *θ-θ* and *φ-φ* polarizations, respectively. We have compared the MoM results with those obtained by utilizing the CBFM with PO-derived CBFs. We have considered 181 observation directions ranging from *φ*=0º to *φ*=180º, for an incidence angle given by *θ* =90º and *φ*=180º. The number of unknowns is 55460 when using the MoM, while 5801 CBFs are retained in the CBFM approach. The almond is modeled using 8 NURBS patches which, in turn, are identified as 8 CBFM blocks, so the average number of CBFs and low-level unknowns per block are 725 and 6932, respectively. Both cases show good agreement. The total time needed to solve this case example has been 12123 seconds using the same machine as in the previous cases.

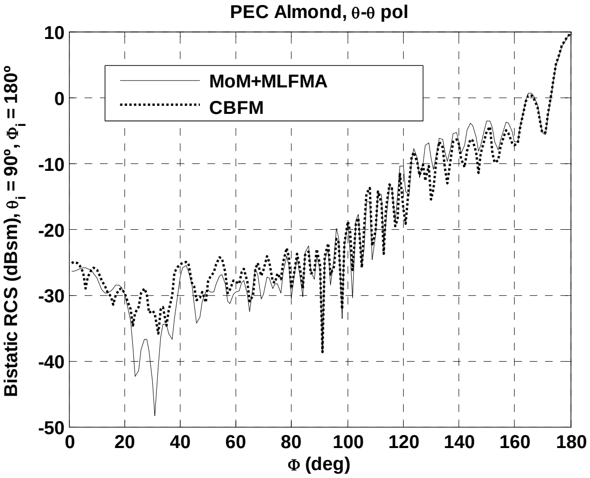

Fig. 10. Bistatic RCS results for the almond test case, *θ*-*θ* polarization.

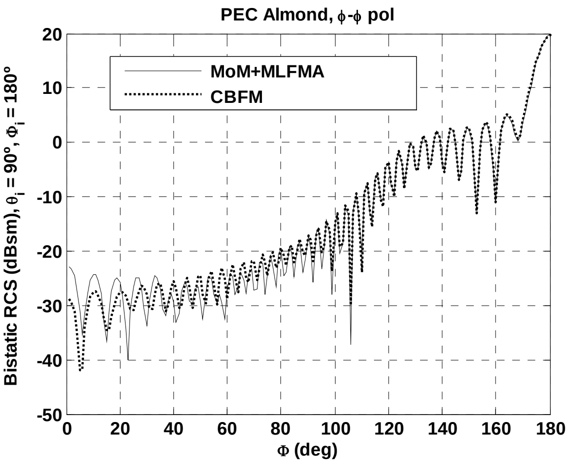

Fig. 11. Bistatic RCS results for the almond test case, *φ*-*φ* polarization.

IV. COMBINATION OF MLFMA AND CBFM

In previous sections, we showed the advantages of CBFM in terms of the reduction of the number of unknowns, leading to a coupling matrix whose size is much smaller than that obtained in the conventional Method of Moments. As a consequence, direct solvers can be applied to solve medium size problems, which could be addressed in the past by relying upon iterative techniques.

However, when the size of the scatterer becomes very large, the CBFM system matrix can become so large as to preclude its solution without resorting to iteration, despite a significant reduction in the matrix size realized via the CBFM. Additionally, the memory needed to store the reduced matrix can present a problem as well. One of the most common approaches to easing the burden on the computational resources entails the storing of only the near-field terms of the coupling matrix and computing the far-field interactions via the Fast Multipole Method, or its multilevel implementation, MLFMA. The use of the MLFMA avoids the need of calculate and store the coupling terms between near elements in the reduced matrix, thereby optimizing the memory storage requirements. In addition, the MLFMA improves the CPU-time required to solve the system via an efficient evaluation of the matrix-vector product operations in an iterative solution process. In the application of the MLFMA we compartmentalize the whole geometry into several first-level cubical groups which, in turn, generate higher-order cubes as they are grouped. A first-order group size of a quarter of wavelength is recommended [10], and the aggregation point of every cube is chosen to be its geometrical centre. For the first level, the cubes include a few basis functions, and the coupling between basis functions associated to geometrically close cubes is calculated in a rigorous way and stored for later use. Figure 12 depicts the volumetric distribution of these cubical volumes, given a generic geometry.

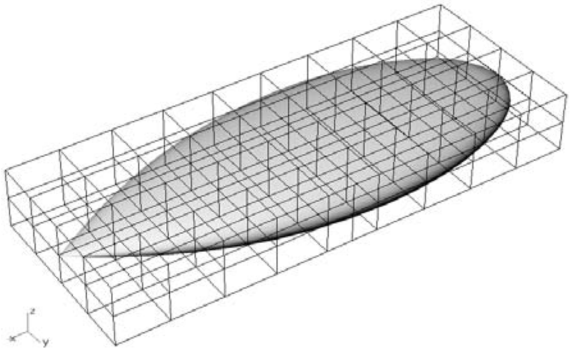

Fig. 12. Compartmentalization of the target geometry into cubical groups.

The application of the FMM/MLFMA entails the storage of only the near-field terms of the coupling matrix and the efficient computation of the far-field interactions in the iterative process. This is achieved by computing the matrix-vector products as shown in (5). For both the EFIE and MFIE cases we have:

$$A_{ji} = \int V_{mj}^{\left\{ {AGG-EFIE \atop AGG-MFIE} \right\}}(\hat{k})\,\tau_{mm'}(\hat{k},\vec{r}_{mm'})\,V_{m'i}^{\left\{ {DIS-EFIE \atop DIS-MFIE} \right\}}(\hat{k})\,d^{2}\hat{k}\,, \quad (5)$$

where $V_{mj}^{AGG}(\hat{k})$ represents the aggregation term, computed as follows for each formulation:

$$\begin{aligned} V_{mj}^{AGG-EFIE}(\hat{k}) &= \sum_{k=1}^{N_m}\int_u\int_v e^{-j\hat{k}\cdot\vec{r}_{jm}}(\bar{I}-\hat{k}\hat{k})T_k(u,v)\,du\,dv \\ V_{mj}^{AGG-MFIE}(\hat{k}) &= -\hat{k}\times\sum_{k=1}^{N_m}\int_u\int_v e^{-j\hat{k}\cdot\vec{r}_{jm}}\left[T_k(u,v)\times\hat{n}(u,v)\right]du\,dv \end{aligned}\,, \quad (6)$$

where N_m is the number of subdomain functions within the cubical group, and $\vec{r}_{j,m}$ represents the vector that extends from the sampling point to the aggregation point. Analogously, the dissagregation term can be computed as:

$$V_{m'i}^{DIS-EFIE}(\hat{k}) = \sum_{k=1}^{N_m} \int_u \int_v e^{j\hat{k}\cdot\overrightarrow{r_{im'}}} (\bar{I} - \hat{k}\hat{k}) R_k(u,v)\,dudv \quad , \qquad (7)$$
$$V_{m'i}^{DIS-MFIE}(\hat{k}) = \sum_{k=1}^{N_m} \int_u \int_v e^{j\hat{k}\cdot\overrightarrow{r_{im'}}} R_k(u,v)\,dudv$$

and the translation term between points *m* and *m'* is given by:

$$\tau_{mm'}(\hat{k}, \vec{r}_{mm'}) = \frac{jk}{4\pi} \sum_{l=0}^{L} j^l (2l+1) h_l^{(1)}(kr_{mm'}) P_l(\hat{r}_{mm'} \cdot \hat{k})\text{'} \qquad (8)$$

where $h_l^{(1)}(x)$ is a spherical Hankel function of the first kind and $P_l(x)$ is a Legendre polynomial.

The first step in the computation of the far-field interactions embodies calculating the aggregation terms for each first-level cube, according to (6). These terms represent the outgoing wave expansions of each cube. For each higher-level cube, the aggregation is obtained by taking into account the aggregation terms of the lower-level cubes contained in it, and by using shifting and interpolation in order to reduce the computational resources. After the aggregation stage, translation between well-separated cubes that belong to the same level is performed.

The last step of the algorithm consists of the disaggregation process, in which all the cubes have received the contributions from the rest of the cubes belonging to the same level, and these contributions are released to their children cubes, via shifting and anterpolation. If the parent cube is a first-level cube, the contribution released to the subdomain functions is given by (7).

Following the MLFMA strategy, the scatter geometry is compartmented into several first-level groups and higher-order cubes are generated. Each high-level cube groups several cubes in the lower level and so on. According to this idea, a tree structure is created from the highest level to the first one.

Next, the CBFM blocks are defined and the macro-basis functions are obtained via SVD as it was shown in previous sections. Each CBF included in a block extends over the entire block, so its size is usually much larger than the size of the subdomains. Therefore, it is common that a CBF can be defined over several MLFMA groups.

It shall be pointed out that the size of the groups and the corresponding number of levels in the application of the MLFMA can be different when we are dealing with CBFs instead of low-level basis functions. In the conventional MoM-MLFMA application, it is recommended to maintain a size of about 0.25 λ for the first level groups. However, in the presented scheme (CBFM-MLFMA) the size of the groups of the first level should be as small as possible, but with the restriction that it is not much smaller than the size of the blocks (the surfaces over which the CBFs extend). From our experience, the best choice for the size of the groups at the first level is between the half and the whole size of the CBF block. If a block extends over many small groups we would require a large amount of memory usage, since each group included in a block must store the multipole information for all the CBFs in that block.

The reduced matrix is calculated containing only the coupling terms between near blocks, which are on or close to the diagonal of the matrix. The reaction terms corresponding to distant are efficiently calculated using the MLFMA. Considering the EFIE formulation, we compute the aggregation for the CBF j inside the block m as follows:

$$V_{mj}^{AGG-EFIE}(\hat{k}) = \sum_{n=1}^{N_n} \alpha_{j,n} V_{m,n}^{AGG-EFIE} = \quad , \qquad (9)$$
$$\sum_{n=1}^{N_n} \alpha_{j,n} \int_u \int_v e^{-j\hat{k}\cdot\overrightarrow{r_{jm}}} (\bar{I} - \hat{k}\hat{k}) T_n(u,v)\,dudv$$

where $\alpha_{j,n}$ is the coefficient of the CBF-*j* associated to the n^{th} basis function T_n, and $V_{m,n}^{AGG-EFIE}$ is the aggregation term for the n^{th} basis function inside the block *m*. Analogously, the dissagregation term can be computed as:

$$V_{m'i}^{DIS-EFIE}(\hat{k}) = \sum_{n=1}^{N_n} \alpha_{j,n} V_{m,n}^{DIS-EFIE} = \quad , \qquad (10)$$
$$\sum_{n=1}^{N_n} \alpha_{i,n} \int_u \int_v e^{j\hat{k}\cdot\overrightarrow{r_{im'}}} (\bar{I} - \hat{k}\hat{k}) R_n(u,v)\,dudv$$

and the translation term between points *m* and *m'* is calculated according to (8).

For the MFIE formulation, the aggregation and disaggregation terms for the CBFs are computed as:

$$V_{mj}^{AGG-MFIE}(\hat{k}) = \sum_{n=1}^{N_n} \alpha_{j,n} V_{m,n}^{AGG-MFIE} = \sum_{n=1}^{N_n} \alpha_{j,n} \int_u \int_v e^{-j\hat{k}\cdot\overrightarrow{r_{jm}}} T_n(u,v)dudv \quad , \qquad (11)$$

$$V_{m'i}^{DIS-MFIE}(\hat{k}) = \sum_{n=1}^{N_n} \alpha_{j,n} V_{m,n}^{DIS-MFIE} = \sum_{n=1}^{N_n} \alpha_{i,n} (-\hat{k} \times \int_u \int_v e^{j\hat{k}\cdot\overrightarrow{r_{im'}}} R_n(u,v) \times \hat{n}dudv) \quad . \qquad (12)$$

The previous expressions can be used for solving the problem employing an iterative algorithm. The coupling terms corresponding to geometrically close blocks can be calculated by means of direct matrix-vector products, while far-field coupling terms can be computed through the MLFMA. As a consequence, the CPU-time is reduced, while simultaneously optimizing the memory storage requirements, since the number of CBFs is much smaller than the number of subdomains. It is important to note that the aggregation and disaggregation terms are computed for the CBFs, which allows the analysis of electrically larger problems. Obviously, the CBF generation process increases the preprocessing CPU-time, as will be seen in the numerical examples shown below. However, as the electrical size of the problem increases the preprocessing time is smaller compared to the CPU-time required for the system solution, which in turn involves a higher efficiency of the presented approach when compared to the MoM-MLFMA technique.

It is also interesting to make a remark about the appropriate group and block size in the CBFM-MLFMA combination. The reduction in the number of unknowns depends only on the block size, as the memory requirements depends on the group and block size. From the experience obtained in this work and previous ones, we conclude that block sizes from λ to 2λ and group sizes from 0.5λ to λ constitute a good compromise.

The first test case considered for the validation of the CBFM-MLFMA approach is the COBRA cavity with a cap previously depicted in Fig. 6. We have obtained monostatic RCS values at a frequency of 10 GHz for an angular sweep θ from 0º to 90º with a fixed value of φ=0º. Results for both the $\theta-\theta$ and $\varphi-\varphi$ polarizations are showed in Figures 13 and 14, respectively, in which we compare the MoM-MLFMA technique, the conventional CBFM and the CBFM-MLFMA approach. The conventional MoM-MLFMA approach required about 304000s for the θ-θ polarization and 456000s for the φ-φ polarization using the EFIE formulation and the BiCGStab solver without any preconditioner. As indicated in a previous section, the conventional CBFM CPU-time was 65966 seconds for each polarization. The presented CBFM-MLFMA approach required 23821s for the θ-θ polarization and 27544s for the φ-φ polarization with the same solver used for the MoM-MLFMA case. All the simulations have been performed using an Opteron processor at 2.4 GHz with a total RAM of 64 Gbytes.

The next case consists of two parallel square plates with a size of 32λ and a separation of 16λ between them. The frequency considered is 2.4 GHz. Bistatic RCS values for an incidence direction defined by θ=0º and φ=0º and a sweeping θ from 0º to 180º for the θ-θ polarization have been obtained. Figure 15 shows the results obtained compared with the MoM -MLFMA, and Table 1 contains the corresponding CPU-times and the resulting number of unknowns considered. Regarding the memory comparision between MoM-MLFMA and CBFM-MLFMA, the former approach needs 9.9 Gbytes of RAM while the latter only requires 6.7 Gbytes, for a group size of λ.

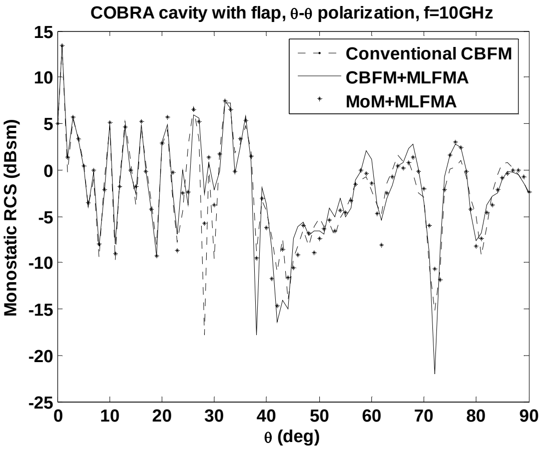

Fig. 13. θ-θ polarization results for the COBRA cavity with a flap.

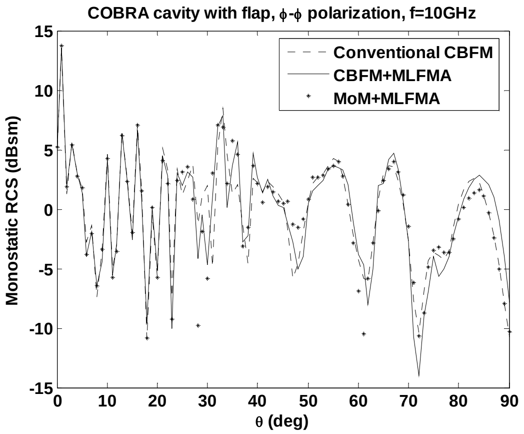

Fig. 14. *φ*-*φ* polarization results for the COBRA cavity with a flap.

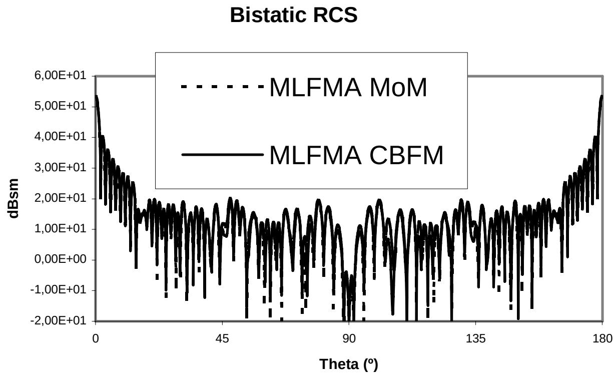

Fig. 15. Bistatic RCS values at 2.4 GHz for the two-plate test case.

Table 1: Analysis of the RCS of the two-plate test case at 2.4 GHz

Method	Block size	Group size	N. Unknowns	Pre-process time (seconds)	Time per direction (seconds)
MoM		0.25	405320	14715	30240
CBFM	1	0.5	105856	22394	5432
CBFM	2	0.5	56832	47357	5213
CBFM	1	1	56832	50695	3105

V. PARALLELIZATION OF THE MLFMA-CBFM APPROACH

It is also important to recognize that currently the parallelization of computer codes plays a very important role, because it enables the code to run on multiple processors, resulting in considerable time-saving if the algorithm scales efficiently as the number of processors is increased progressively [32]. In order to take advantage of these clusters, it is necessary to modify the initial code, following a parallel-computation standard. The Message Passing Interface (MPI) paradigm [7] is at the present time widely used for the parallelization of codes based on the use of computer clusters.

The design of the parallel CBFM-MLFMA follows the so called data-parallel approach [33]. In this approach the data is partitioned among the processes, and each process executes approximately the same set of commands on its data. This approach usually leads to more scalable programs.

In the design of the parallel approach, all the groups are distributed between the processors [34]. Each group is assigned to a processor, which manages the information about all the coupling terms of the CBFs located in that group. In the delivering process, it is essential to apply load-balancing for the near-field. Each processor computes the near-field terms that correspond to the associated CBFs, and it obtains the rigorous coupling terms with the rest of CBFs by sharing information with other processors. Each processor calculates the aggregation and disaggregation terms of its assignated CBFs, and it exchanges this information at the corresponding level with those processors which require it.

In order to improve the efficiency of a parallelized program, the communication between processors and duplicated computations must be minimized. In a simple parallelization technique [32], we can obtain the highest level at which the MLFMA cubes are coupled. Next, we distribute and assign equally the cubes of that level to the processors, and, for the lower levels, if a cube in the higher-level belongs to a processor, then all its sub-cubes are also assigned to the same processor. By following this procedure, the aggregation and disaggregation steps from the bottom of the hierarchical tree up to the higher-coupling level can be performed without any communication.

This scheme avoids the communication between processors in the aggregation and disaggregation process, but it can lead to an inefficient speed-up in some cases. When the geometry of the scatter is irregular, by applying the higher-coupling level distribution a processor can be in charge of cubes that have a low number of non-empty low-level cubes, so the processor can wait for long periods of time.

To overcome this disadvantage, a new strategy in the distribution of the cubes has been developed. We fixed the level of the distribution of the cubes to be different to the highest-coupling level. To avoid communication between processors in the aggregation and disaggregation processes for the cubes at a level above the distribution level, it is allowed that these cubes can be duplicated in different processors. For this cubes, each processor computes the aggregation of its sub-cubes, and adds its partial contribution in the translation process, so the contributions from different processors are combined automatically for the duplicated cubes. Applying this new strategy, the speed-up is improved for geometries with irregular shapes [35].

In Fig. 16 the speed-up for the COBRA cavity with a flap is shown. All the simulations have been performed using dual-core Opteron processors at 2.4 GHz with a total shared RAM of 64 GBytes. Table 2 shows the CPU-times for both polarizations using the presented approach, and a comparison between CBFM-MLFMA and MoM-MLFMA using the same parallelization scheme. The conventional CBFM CPU-time was 65966 seconds for each polarization with a single processor.

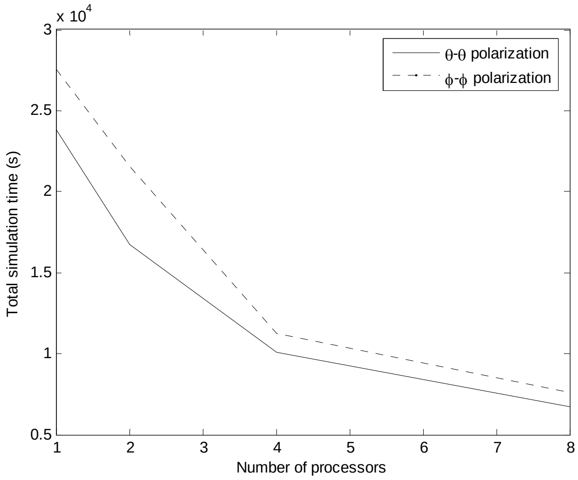

Fig. 16. Evolution of the CPU simulation time as a function of the number of processors.

Table 2. CPU-times for the simulations

Method	Polarization	N. of processors	Total CPU time	Preprocess time	Solver time
CBFM	Theta	1	23821 s	10567 s	13254 s
CBFM	Theta	2	16698 s	5276 s	11422 s
CBFM	Theta	4	10056 s	4146 s	5910 s
CBFM	Theta	8	6736 s	2401 s	4335 s
CBFM	Phi	1	27544 s	10650 s	16894 s
CBFM	Phi	2	21584 s	5353 s	16231 s
CBFM	Phi	4	11216 s	4195 s	7021 s
CBFM	Phi	8	7621 s	2417 s	5204 s
MoM	Theta	1	304443 s	743 s	303700 s
MoM	Theta	8	79095 s	177 s	78918 s
MoM	Phi	1	456756 s	743 s	456013 s
MoM	Phi	8	137154 s	177 s	136976 s

VI CONCLUSIONS

We have presented an overview of a very efficient, recently developed technique (CBFM), based on the definition of macro-basis functions which can be generated using different approaches. Also, we have presented an implementation of the CBFM combined with the MLFMA. The conventional MoM memory requirements are highly reduced due to the reduction of the number of unknowns via the CBFM and to the reduction in the size of the reduced matrix via MLFMA. Also the CPU-time is smaller due to the reduction of the size of the linear problem to be solved and to the efficiently computed matrix-vector products in the iterative solution process.

ACKNOWLEDGEMENT

This work has been supported in part by the University of Alcala and the Madrid Community Project CCG07-UAH/TIC-2058 and S-0505/TIC/0255. and by the Spanish Department of Education and Science Projects Ref. TEC2006-03140, TEC 2007-66164 and CONSOLIDER-INGENIO Nº CSD-2008-0068

REFERENCES

[1] G. T. Ruck, D. E. Barrick, W. D. Stuart, and C. K. Krichbaum, *Radar Cross Section Handbook*, Vol. 1, Plenum Press, 1970.

[2] D. A. McNamara, C. W. I. Pistorius and J. A. G. Maherbe, *Introduction to the Uniform Geometric Theory of Diffraction*, Norwood, MA: Artech House, 1990.

[3] U. Jakobus and F.M. Landstorfer: “Improved PO-MM hybrid formulation for scattering from three-dimensional perfectly conducting bodies of arbitrary shape”, *IEEE Trans. Antennas Propagat.*, vol. 43, pp. 162-169, Feb. 1995.

[4] G. A. Thiele and G. A. Newhouse, “A Hybrid Technique for Combining Moment Methods with the Geometrical Theory of Diffraction”, *IEEE Trans. Antennas Propagat.*, vol. 23, pp. 551-558, July 1975.

[5] W. D. Burnside, C. L. Yu, and R.J. Marhefka: “A technique to combine the geometrical theory of diffraction and the moment method”, *IEEE Trans. Antennas Propagat.*, AP-23, pp. 551-558, July 1975.

[6] E. P. Ekelman and G. A. Thiele: “A hybrid technique for combining the moment method treatment of wire antennas with the GTD for curved surfaces”, *IEEE Trans. Antennas Propagat.*, AP-28, pp. 831-839, November 1980.

[7] W. Gropp, E. Lusk, and A. Skjellum, *Using MPI*, MIT Press, October 1994.

[8] R. F. Harrington, *Field Computation by Moment Methods*, New York, McMillan, 1968.

[9] N. Engheta, W. D. Murphy, V. Rokhlin, and M. S. Vassiliou, “The Fast Multipole Method (FMM) for Electromagnetic Scattering Problems”, *IEEE Trans. Antennas Propagat.*, vol. 40, no. 6, pp. 634-641, June 1992.

[10] W. C. Chew, J. Jin, E. Michielssen, and J. Song, *Fast and Efficient Algorithms in Computational Electromagnetics*, Artech House Inc., 2001.

[11] A. Boag and R. Mittra, “Complex multipole beam approach to electromagnetic scattering problems,” *IEEE Trans. Antennas Propagat.*, vol. 42, pp. 366-372, Mar. 1994.

[12] F. X. Canning, “The Impedance Matrix Localization (IML) Method for Moment-Method Calculations”, *IEEE Anntenas Propagat. Mag.*, vol. 32, no. 5, pp. 18-30, Oct 1990.

[13] E. Bleszynski, M. Bleszynski, and T. Jaroszewicz, "AIM: Adaptative Integral Method for Solving Large Scale Electromagnetic Scattering and Radiation Problems", *Radio sci.*, vol. 31, no.5, pp. 1225-1251, 1996.

[14] Gene H. Golub and Charles van Loan, *Matrix Computations*, Johns Hopkins University Press, 1989.

[15] R.J. Burkholder and J.F. Lee, “Fast Dual-MGS Block-Factorization Algorithm for Dense MoM Matrices”, *IEEE Trans. Antennas Propagat.*, Vol-52, NO. 7, pp. 1693-1699, July 2004.

[16] M. Bebendorf, “Approximation of boundary element matrices”, *Numer. Math.*, vol. 86, no. 4, pp. 565–589, 2000.

[17] K. Zhao, M. Vouvakis, and J. F. Lee, “The adaptive cross approximation algorithm for accelerated method of moment computations of EMC problems”, *IEEE Trans. Electro. Comp.*, vol. 47, no. 4, pp. 763–773, Nov. 2005.

[18] E. Michielssen and A. Boag, “A multilevel matrix decomposition algorithm for analyzing scattering from large structures”, *IEEE Trans. Electro. Comp.*, vol. 44, no. 8, pp. 1086–1093, Aug. 1996.

[19] L. Matekovits, V. A. Laza, and G. Vecchi, “Analysis of Large Complex Structures With the Synthetic-Functions Approach”, *IEEE Trans. Antennas Propagat.*, vol. 55, no. 9, pp. 2509-2521, September 2007.

[20] V. V. S. Prakash and R. Mittra, “Characteristic Basis Function Method: A New Technique for Efficient Solution of Method of Moments Matrix Equation”, *Micro. Opt. Tech. Lett.*, vol. 36, no. 2, pp. 95-100, Jan. 2003.

[21] S. M. Rao, D. R. Wilton, and A. W. Glisson, “Electromagnetic scattering by surfaces of arbitrary shape”, *IEEE Trans. Antennas Propagat.*, vol. 30, pp. 409-412, May 1982.

[22] A. W. Glisson and D. R. Wilton, “Simple and Efficient Numerical Methods for Problems of Electromagnetic Radiation and

Scattering from Surfaces", *IEEE Trans. Antennas Propagat.*, vol. 28, no. 5, pp. 593-603, Sept. 1980.

[23] E. García , C. Delgado, I. González , and F. Cátedra, "An iterative solution for electrically large problems combining the Characteristic Basis Function Method and the Multilevel Fast Multipole Algorithm", *IEEE Trans. Antennas Propagat.*, accepted for publication.

[24] G. Farin, *Curves and Surfaces for Computer Aided Geometric Design: A Practical Guide*, Boston, Academic Press, 1998.

[25] E. Lucente , A. Monorchio, and R. Mittra, "An Iteration-Free MoM Approach Based on Excitation Independent Characteristic Basis Functions for Solving Large Multiscale Electromagnetic Scattering Problems", *IEEE Trans. Antennas Propagat.*, vol. 56, no. 4, pp. 999-1007, April 2008.

[26] C. Delgado, R. Mittra, and F Cátedra, "Accurate Representation of the Edge Behavior of Current when Using PO-Derived Characteristic Basis Functions", *IEEE Antennas and Wireless Propagat. Lett.*, vol. 7, pp. 43-45, March 2008.

[27] G. Tiberi, M. Degiorgi, A. Monorchio, G. Manara, and R. Mittra, "A Class of Physical Optics-SVD Derived Basis Functions for Solving Electromagnetic Scattering Problems", *Antennas and Propagation Society Int. Symposium*, Washington D.C, USA, July 2005.

[28] C. Delgado, F. Cátedra, and R. Mittra: "Application of the Characteristic Basis Function Method Utilizing a Class of Basis and Testing Functions Defined on NURBS Patches", *IEEE Trans. Antennas Propagat.*, vol. 56, no. 3, pp. 784-791, March 2008.

[29] L. Valle, F. Rivas, and M. F. Cátedra, "Combining the Moment Method with Geometrical Modelling by NURBS Surfaces and Bézier Patches", *IEEE Trans. Antennas Propagat.*, vol. 42, no. 3, pp 373-381, March 1994.

[30] M. F. Cátedra, F. Rivas, and L. Valle: "A Moment Method Approach Using Frequency Independent Parametric Meshes", *IEEE Trans. Antennas Propagat.*, vol. 45, no. 10, pp. 1567-1568, October 1997.

[31] J. Liu and J. Jin, "Scattering Analysis of a Large Body with Deep Cavities", *IEEE Trans. Antennas Propagat*, Vol. AP-51, Issue 5, pp 1157-1167, June 2003.

[32] A. K. Dominek, H. Shamanski, R. Wood, and R. Barger, "A Useful Test Body", *in Proceedings Antenna Measurement Techniques Association*, September 24, 1986.

[33] Özgür Ergül and Levent Gürel, "Efficient Parallelization of Multilevel Fast Multipole Algorithm". *Proceedings of the European Conference on Antennas and Propagation: EuCAP 2006.* Nice, France, November 2006.

[34] P. S. Pacheco, *Parallel Programing with MPI*, Morgan Kaufmann Publishers Inc., 1997.

[35] W. C. Chew, J. Jin, E. Michielssen, and J. Song, *Fast and Efficient Algorithms in Computational Electromagnetics,* Artech House Inc., 2001.

[36] E. García, C. Delgado, I. González, and F. Cátedra "A Parallel CBFM-MLFMA Implementation for the Analysis of Complex Problems" *ACES 2008 Meeting*, April 2008.

Carlos Delgado was born in Guadalajara, Spain, in 1979. He received the MS degree in Telecommunications Engineering from the University of Alcalá, Spain, in 2002, and the Ph. D. in Telecommunications Engineering in 2006. He is currently an Associate Professor in the Computer Science Department, Universidad de Alcalá, Spain. He was a visiting scholar during fall 2005 and a visiting postdoctoral fellow during spring and summer 2007 at the Electromagnetic Communication Laboratory of the Pennsylvania State University. His research interests include numerical methods applied to scattering and radiation problems, hybridization of high frequency and numerically rigorous methods and fast computational techniques applied to electromagnetics.

Eliseo García was born in Madrid, Spain, in 1977. He received the B.S., M.S. and Ph.D. degrees in telecommunication engineering from the University of Alcalá, Spain, in 1999, 2001 and 2005, respectively.Since 2005, he worked at the University of Alcalá, first as Assistant Professor and since 2006 as Associated Professor in the Automatic Department. His research interests include numerical methods applied to scattering and radiation problems, parallel computing and fast computational techniques applied to electromagnetics.

Manuel F. Catedra received his M.S. and Ph. D. degrees in Telecommunications Engineering from the Polytechnic University of Madrid (UPM) in 1977 and 1982, respectively. From 1976 to 1989 he was with the Radiocommunication and Signal Processing Department of the UPM. He has been Professor at the University of Cantabria from 1989 to 1998. He is currently Professor at the University of Alcalá, in Madrid, Spain. He has worked on about 80 research projects solving problems of Electromagnetic Compatibility in Radio and Telecommunication Equipment, Antennas, Microwave Components and Radar Cross Section and Mobile Communications. He has developed and applied CAD tools for radio-equipment systems such as Navy ships, aircraft, helicopters, satellites, the main contractors being Spanish or European Institutions such as EADS, ALCATEL, CNES, ALENIA, ESA, DASA, SAAB, INTA, BAZAN, INDRA, and the Spanish Defence Department. He has directed 16 Ph. D. dissertations, has published about 55 papers (IEEE, Electronic Letters, etc), two books, about 10 chapters in different books, has given short courses and has given more than a hundred and thirty presentations in International Symposia.

Raj Mittra is Professor in the Electrical Engineering department of the Pennsylvania State University. He is also the Director of the Electromagnetic Communication Laboratory, which is affiliated with the Communication and Space Sciences Laboratory of the EE Department. Prior to joining Penn State he was a Professor in Electrical and Computer Engineering at the University of Illinois in Urbana Champaign. He is a Life Fellow of the IEEE, a Past-President of AP-S, and he has served as the Editor of the Transactions of the Antennas and Propagation Society. He won the Guggenheim Fellowship Award in 1965, the IEEE Centennial Medal in 1984, the IEEE Millennium medal in 2000, the IEEE/AP-S Distinguished Achievement Award in 2002, the AP-S Chen-To Tai Distinguished Educator Award in 2004 and the IEEE Electromagnetics Award in 2006. He has been a Visiting Professor at Oxford University, Oxford, England and at the Technical University of Denmark, Lyngby, Denmark. He has also served as the North American editor of the journal AEU. His professional interests include the areas of Communication Antenna Design, RF circuits, computational electromagnetics, electromagnetic modeling and simulation of electronic packages, EMC analysis, radar scattering, frequency selective surfaces, microwave and millimeter wave integrated circuits, and satellite antennas.He has published over 900 journal and symposium papers and more than 40 books or book chapters on various topics related to electromagnetics, antennas, microwaves and electronic packaging. He also has three patents on communication antennas to his credit. He has supervised 90 Ph.D. theses, 90 M.S. theses, and has mentored more than 50 postdocs and Visiting scholars. He has directed, as well as lectured in, numerous short courses on Computational Electromagnetics, Electronic Packaging, Wireless antennas and Metamaterials, both nationally and internationally.

Characteristic Basis Function Method (CBFM) - An Iteration-free Domain Decomposition Approach in Computational Electromagnetics

Raj Mittra
EMC Lab, Penn State University,
319 EE East, University Park, PA 16802, USA
rajmittra@ieee.org

Abstract**─** In this paper we review a novel Domain Decomposition (DD) approach, called the Characteristic Basis Function Method (CBFM), which tackles large-scale electromagnetic problems by generalizing the concept of principle of localization that forms the cornerstone of asymptotic methods. The paper shows that the problem of having to deal with large matrices that arise in the conventional formulation of large problems with the Method of Moments (MoM) can be obviated, by dividing the original large problem into a number of smaller sub-problems that are more manageable to handle. However, unlike the conventional DD approaches that typically rely upon iteration algorithms to account for the inter-coupling between the subdomains, the CBFM tackles the problem with direct solvers instead. It is possible to do this in the context of CBFM, because it reduces the original large system matrix into one whose size is orders of magnitude smaller, and is appropriately called the "reduced matrix." Furthermore, an important salutary feature of CBFM is that the algorithm is naturally parallelizable, an attribute that distinguishes it from many other CEM solvers, and makes it well suited for parallel platforms that have become ubiquitous in recent years. This, in turn, enables us to take advantage of the power of these platforms and to solve, numerically efficiently, large problems that were well beyond our reach in the past. The paper also shows that the basic concepts of CBFM are quite general, and they not only apply to MoM, but can also be tailored for both FEM and FDTD.

Index Terms**─** Characteristic Basis Function Method (CBFM), Domain Decomposition, Method of Moments (MoM), Finite element Method (FEM), Finite Difference Time Domain (FDTD).

I. INTRODUCTION

Solutions of large problems that are described by a large number of Degrees of Freedom (DoFs) are of considerable interest in Computational Electromagnetics. Presently, iterative techniques, coupled with fast matrix-vector multipliers, form the backbone of leading Method of Moment (MoM) solvers, for instance, the Fast Multipole Method (FMM) and similar techniques [1-4] that are used for such problems. Historically, the asymptotic methods, such as the GTD [5] dominated the electromagnetics scene for several decades, and were the only viable options available to us when we wanted to tackle problems, whose dimensions were very large when compared to the wavelength. However, it is well known that while the asymptotic methods can handle smooth, perfectly conducting objects with relative ease—regardless of how large they may be—the methods do suffer from several inherent limitations, especially when dealing with arbitrarily shaped, inhomogeneous, and multiscale objects. Some of these limitations are: the GTD diffraction coefficients are available only for a limited number of canonical geometrical shapes, such as PEC wedges and smooth surfaces with large radii of curvature; resonant structures, for instance re-entrant cavities, or Frequency Selective Surfaces (FSSs), are not amenable to convenient analysis via asymptotic methods, regardless of their size; and, multiscale and material inhomogeneities are always problematic because they do not lend themselves to asymptotic analysis owing to the fact that the wave phenomena in

1054-4887 © 2009 ACES

these structures do not satisfy the ansatz upon which the asymptotic methods are based. Attempts to modify the GTD, either by using techniques such as the Physical Theory of Diffraction PTD [6], or by hybridizing it with rigorous numerical methods [7], have met varying degrees of success. This is because either these approaches do not fully overcome the fundamental limitations of the GTD—alluded to above—or they are not sufficiently robust.

In this paper we review a novel Domain Decomposition (DD) approach, called the Characteristic Basis Function Method (CBFM) [8-10], which tackles large-scale electromagnetic problems by generalizing the concept of principle of localization that forms the cornerstone of asymptotic methods. For instance, in Physical Optics (PO) we simply use the local property of the surface in the neighbourhood of a "bright point" to compute the field reflected from the surface, instead of solving a large dense matrix equation arising in MoM, which assumes that each of the subdomain basis functions fully couples to all other similar basis functions in a global sense. One consequence of this is that, for large problems, the system matrix arising in MoM is large as well as fully populated, and burdens both the CPU time and the memory. As shown in this paper, this problem can be obviated, however, by dividing the original large problem into a number of smaller sub-problems that are more manageable to handle. However, unlike the conventional DD approaches that typically rely upon iteration to account for the inter-coupling between the subdomains, the CBFM tackles the problem with direct solvers instead. It is possible to do this in the context of CBFM, because it reduces the original large system matrix into one whose size is orders of magnitude smaller, and is appropriately called the "reduced matrix." Furthermore, an important salutary feature of CBFM is that the algorithm is naturally parallelizable, an attribute that distinguishes it from many other CEM solvers, and makes it well suited for parallel platforms that have become ubiquitous in recent years. This, in turn, enables us to take advantage of the power of these platforms and to solve, numerically efficiently, large problems that were well beyond our reach in the past. We also mention that the basic concepts of CBFM are quite general, and they not only apply to MoM, but can also be tailored for both FEM and FDTD. Although CBFM was originally developed for MoM solution of microwave circuit problems [9], and has been applied to quasi-static problems in the context of FEM [11], we restrict our attention in this paper solely to scattering and radiation problems.

The organization of this review paper is as follows. In Sec. 2 we present the details of CBFM for MoM problems to lay the foundations of the method. We show how we can use the concepts of domain decomposition and high-level or macro basis functions to significantly reduce the size of the MoM matrix, which can then be solved directly, without resorting to iteration. Next, in Sec. 3, we present two numerical examples of the application of CBFM. Following this, in Sec. 4, we describe the basic steps of parallelization of the CBBOR (Characteristic Basis Body of Revolution) code. The next section, Sec. 5, discusses an efficient technique for handing locally modified objects in the context of CBFM. Adaptations of the CBFM concept to FEM and FDTD, are presented in Secs. 6 and 7, respectively, which have their own unique features. Finally, we refer to some recent developments in CBFM and present some summary conclusions in Sec. 8.

II. CBFM FOR MOM PROBLEMS

Let us begin by describing the principle of localization as it is incorporated in CBFM. Suppose we have an arbitrary scatterer illuminated by a plane wave, as shown in Fig. 1.

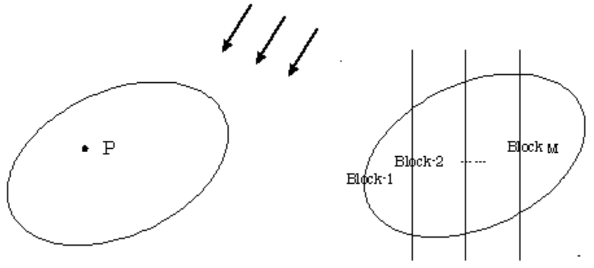

(a) (b)

Fig. 1. (a) Arbitrary scatter illuminated by a plane wave; (b) Dividing original object into blocks.

Let us consider the behavior of the induced current at a point P, which resides on the surface of the object. Then, we could approximate the current at *P* by invoking the PO, which says that this current can be approximately expressed as $2\hat{n}\times\bar{H}^i$, provided the principle radii of curvature of the surface are large. If the point *P* is located on an edge, we can use the GTD to find the field scattered from *P*, again by using the properties of the edge in the vicinity of *P*, and making suitable approximations if the geometry there is not one of the canonical shapes for which we can derive the diffraction coefficients. (Note: If we desire to find the approximate induced current near *P*, we have to employ the PTD instead.) We can either move the point *P* around to determine the induced current on the entire body by following the above procedure, or we can simply go directly to the far scattered field by using the ray theory approach, rather than by integrating the induced current on the scatterer. The procedure, just described, is an extreme limit of localization, which works well at very high frequencies, provided we are dealing either with smooth bodies, or with those that have canonical edge geometries and are amenable to ray type of analysis. If, however, these conditions are violated by the geometry of the object, then the ray theories do not provide a systematic way to generalize the analysis, or enable us to handle arbitrary objects whose geometries may have multiscale features. The CBFM generalizes the above concept, by first using DD to break up the original object into "blocks," and then viewing entire subdomains as the local regions upon which macro basis functions are defined in a manner explained below. Following this, the interactions between the blocks are accounted for not via the use of iteration, as is the case in conventional DD procedures, but by rigorously incorporating them in the formulation by using the Galerkin's method to generate a reduced matrix, as is further explained below. The procedure described above is very general, and is capable of handling arbitrarily shaped objects, which can even be multiscale.

Let us now describe the CBFM in a little more detail. Its formulation starts with the conventional MoM procedure, whereby the mixed potential integral equation is discretized into a matrix equation:

$$\mathbf{Z}\cdot\mathbf{I}=\mathbf{V}, \tag{1}$$

where Z denotes the conventional MoM impedance matrix; I is the unknown current vector; and, V is the excitation voltage vector. Typically, the desired solution *I* is represented in terms of the RWG basis functions using a discretization of λ/10; hence, the number of unknowns grows rapidly with the increase in the size of the object being analyzed. This, in turn, forces us to resort to iterative techniques, which often offer the only viable option for handling large scatterers. However, the CBFM circumvents this problem by working with high-level basis functions I_i (i=1,…,N), called the Characteristic Basis Functions (CBFs), and representing I as:

$$\mathbf{I}=\sum_{i=1}^{N}c_i\mathbf{I}_i\ , \tag{2}$$

where c_i's denote the weights of these currents. Note that each I_i would have non-zero entries only at the positions belonging to a sub-block. When I_i is normalized, the value of c_i provides a measure of the coupling effects between the currents induced on the blocks. This observation is useful in determining *N*, the total number of characteristic bases that would be needed to yield an accurate solution to the problem at hand.

The primary bases are computed by solving a series of smaller matrices, arising from the application of the MoM procedure to the sub-blocks, using a spectrum of plane wave excitations as incident waves. This is done by anticipating the fact that we would be solving the scattering problem for multiple excitations anyway, and arguing that we might as well formulate the reduced matrix in a way such that, once generated, it can be re-used for different excitations without modification. This is also a powerful feature of the CBFM, which can solve the multiple incidence problems very efficiently, once the reduced matrix has been L-U factored. This is in contrast to iterative techniques, which must start the procedure from the beginning each time the RHS is changed. (Note: A slightly modified version of this procedure is used in Microwave circuits, where the secondary (see [9]) and even tertiary basis functions have been proposed, instead of just the primaries.)

As mentioned earlier, we begin by dividing the geometry of the object to be analyzed into blocks, for instance M in number (see Fig. 1b). Next, we derive the primary characteristic basis functions by illuminating the isolated blocks with plane waves, say $\mathrm{N}_{\mathrm{PWS}}$ in number (see Fig. 2), which impinge upon the object at intervals of θ and φ, say every 20 degrees, for two orthogonal polarizations.

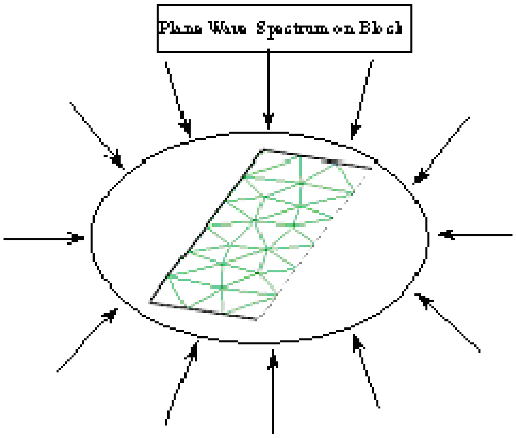

Fig. 2. Spectrum of Plane Waves incident on a single block.

We can be flexible in choosing the number of these incident waves, and can also include a part of the invisible range of the spectrum—if desired—since the SVD will downselect the number of basis functions to remove the redundancy and will retain only as many as needed to represent the unknown current with a certain degree of accuracy, determined by the level of the SVD threshold we set. In addition, the decomposition of the object into blocks is also somewhat arbitrary, and there is no limitation on the number and size of the blocks. The upper size is bounded by the available RAM needed for the unknowns in the self-blocks that are solved to generate the CBs. Typically, the block size ranges from a few hundred to a few thousand sub-domain type of unknowns. As pointed out earlier, the advantages of following this procedure is that it enables us to solve for multiple excitations using the same reduced matrix with a significant time-saving, since only the RHS of the reduced system needs to be computed for a new excitation.

For the sake of illustration, we consider a thin plate which is divided into 25 blocks, shown in Fig.3. Although, in general, the blocks can have different sizes, we assume that they have approximately the same dimension Nb in terms of number of unknowns. To mitigate the problem of spurious edge effects in the CBs, introduced by the truncation, we extend all blocks by a fixed amount (typically 0.2λ to 0.4λ) in all directions, except when the boundaries are free edges.

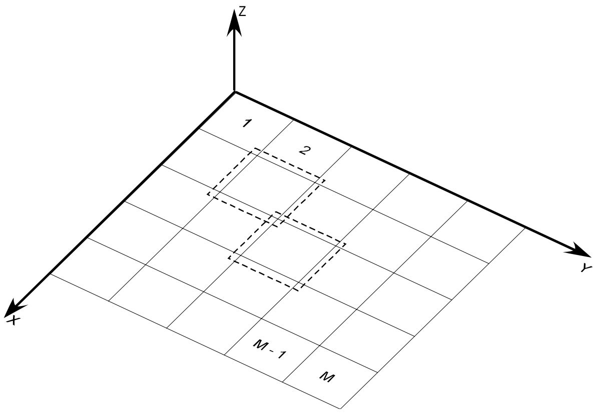

Fig. 3. Geometry of a PEC plate divided into 25 blocks. Extended blocks are duplicated by dashed lines.

The final step is to generate the reduced $KM \times KM$ MoM matrix for the KM unknown complex coefficients ck by following the usual Galerkin procedure in the context of the Method of Moments. Once the induced surface current distribution for the entire structure has been derived, the electrical parameters such as RCS, scattered field, etc., can be computed in the usual manner.

The most computationally intensive steps of the proposed method are associated with the generation of the primary CBs and the construction of the reduced matrix reduction, though the latter task can be speeded up by invoking the symmetry of the matrix.

Once we have generated the reduced matrix, we proceed to factorize it. Note that generation of CBs is one of the time-consuming and memory-demanding tasks. It requires the filling the self-impedance matrix Zii for the extended block and its factorization in an LU form. Since the CBs are independent of the incident angles, this factorization needs to be performed only once, and the resulting primaries can be reused for multiple incident angle directions. This implies that the final reduced matrix (5) is independent of the excitation, and this fact enables us to handle a problem involving multiple excitations by only solving the reduced system for the new RHS (excitation). Moreover, we can store the reduced matrix on the hard disk, and reuse it whenever we need to analyze a new excitation. Furthermore, if the geometry within a particular block is modified, only the CBs belonging to this block need to be recomputed.

The technique described above realizes a saving in the CPU running time and RAM requirement compared to the conventional MoM technique. The memory requirement is now proportional to the square of the self impedance matrix of the extended block, and this is different from that in the conventional MoM where the storage requirement is related to the square of the dimension of the entire impedance matrix. Moreover, we realize a consistent saving in the execution time, which reduces to $O(M(Nbe)3)$ instead of $O(N3)$.

As mentioned earlier, the generation of CBs is one of the most computationally intensive tasks in CBFM. We will now briefly discuss two techniques for reducing this time, both of which are physics-based.

The first approach [12] is best suited for geometries that are relatively smooth ─ though they may have edges ─ but are not multiscale. In this approach we simply use the P.O. solutions for different incident angles as the characteristic basis functions, totally bypassing the matrix solution that we would employ in the conventional procedure for CB generation. An added advantage of using this approach is that these PO/CBs no longer suffer from the spurious edge effects ─ even after the SVD ─ as do the CBs generated by matrix methods. We point out that even if the geometry under consideration has true edges, we can still accommodate this situation by using relatively small-size blocks near the edges. This is because a superposition of these basis functions can still pick up the edge behavior of the current, despite the fact that none of the individual basis functions possess this behavior.

The second method [13], which is more general than the one we just described above, works with a sparsified version of the matrix for the subdomain that we need to solve to generate its CBs. In this approach, we simply use a threshold value to discard the matrix elements that fall below this value. This operation obviously sparsifies the matrix, and not only enables us to employ a sparse-LU factorization scheme, but to also reduce the storage requirement significantly.

In the next section we present some numerical examples to illustrate the application of CBFM to scattering problems.

III. NUMERICAL RESULTS DERIVED WITH CBMOM (CHARACTERISTIC BASIS METHOD OF MOMENTS)

3.1 Plane wave scattering by a 4λ radius PEC Sphere

To validate the accuracy of the method we will compare the CBFM solution with the analytical one for a PEC sphere of radius 4λ, at a frequency of 300 MHz. The object is excited by a normally incident (θ=0, ϕ=0) theta-polarized plane wave. The discretization is carried out by using triangular patches with a mean edge length of 0.1λ, resulting in a problem with 85155 unknowns. The geometry is divided into 16 blocks with an average size of 8000 unknowns. Each block is extended by Δ=0.4λ in all directions, and analyzed for a spectrum of plane waves incident from $0^O \le \theta < 180^O$ and $0^O \le \phi < 360^O$, with $N_\theta = N_\phi = 20$. These results in a total of 800 CBs; but, after the SVD, only 310 are retained in each block. The 85155×85155 MoM matrix is then reduced to only 4925×4925, which is solved directly.

As we mentioned earlier, the construction of the CBs can be speeded up, with little loss of accuracy, by using a sparsified version of the self-blocks—that retain only the near-region interactions—rather than working with the full versions of these blocks. It should be realized that we are only generating the basis functions at this point and, hence, they themselves need not be the rigorous solutions of the self-block problems, so long as they span the solution space, they need not strictly be solutions of the original self-blocks. To validate this concept, we have analyzed the problem at hand by using both dense and sparse matrix approaches. The use of the latter allows us to reduce the computational cost by a factor of approximately 4. The bi-static E- and H-plane RCS results are presented in Figs. 4(a) and 4(b), respectively, using the dense and sparse approaches, as well as the MIE series. The agreement is seen to be good for all scattering directions, including the grazing angles.

Next, we turn to some example problems involving bodies of revolution (BORs), to which the CBFM has been successfully applied. The BOR geometry offers the advantage that we can factor out the azimuthal variation and thereby reduce a 3-D/BOR problem into a number of 2-D ones. Thus we can easily solve problems with very large dimensions ─ that are hundreds if not thousands of wavelengths. In Fig. 5 we show a finite-length cylinder, which is subdivided into two blocks to illustrate the partitioning scheme.

Figure 6 shows the flowchart of the CBF_BOR code, which combines the CBF algorithm with the BOR code. The above code includes five steps: (i) Data entry--input data, input (generate) structure, define indices for vectors; (ii) Call “Split structure” subroutine--split the original structure into a number of smaller blocks; (iii) Call “Generate CBFs” subroutine: the CBFs for each mode of each block are obtained and stored; (iv) Call “Generate reduced matrix” subroutine--compute the reduced matrix for each mode; (v) Call “Solve reduce matrix” subroutine--solve the reduced matrix system for each mode and sum the results for all modes to derive the final results.

3.2 Numerical Example of CBF_BOR Code

We now present some numerical examples obtained by using the CBF_BOR code for the test geometry of a PEC sphere. The relevant parameters are:

- Radius of the sphere = 6.755 wavelengths
- Overlap region between blocks = 1 wavelength
- Number of incident angles for generating the CBFs = 100
- Threshold for SVD = 1000 (ratio of largest to smallest singular values retained).

Comparisons with the results obtained by using the non-CBF version (single block) code are included for the purpose of validation of the CBF result, and demonstrating that it is not sensitive to the number of blocks in which the object is divided. Both the induced current distributions and the far field results are presented in Figs. 7a through 7d for the threshold value of 1000.

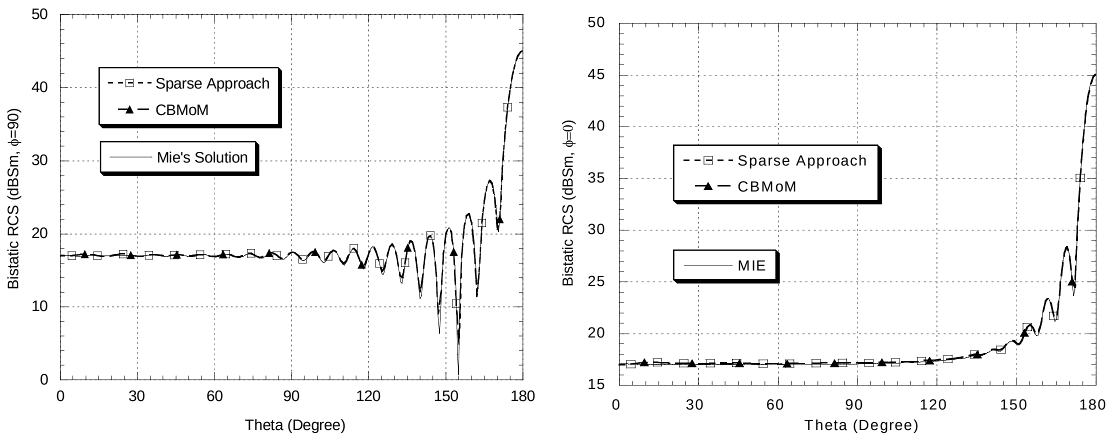

(a) (b)

Fig. 4. RCS of radius PEC sphere at 0.3GHz: (a) E-plane; (b) H-plane.

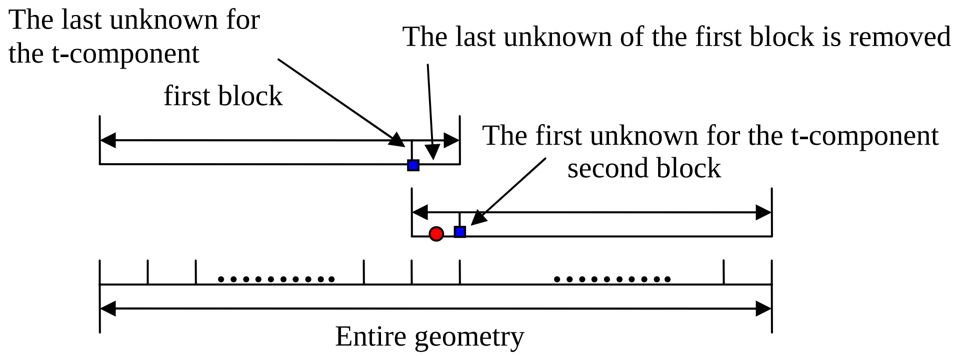

Fig. 5. BOR geometry of a finite cylinder and the partitioning scheme for two blocks.

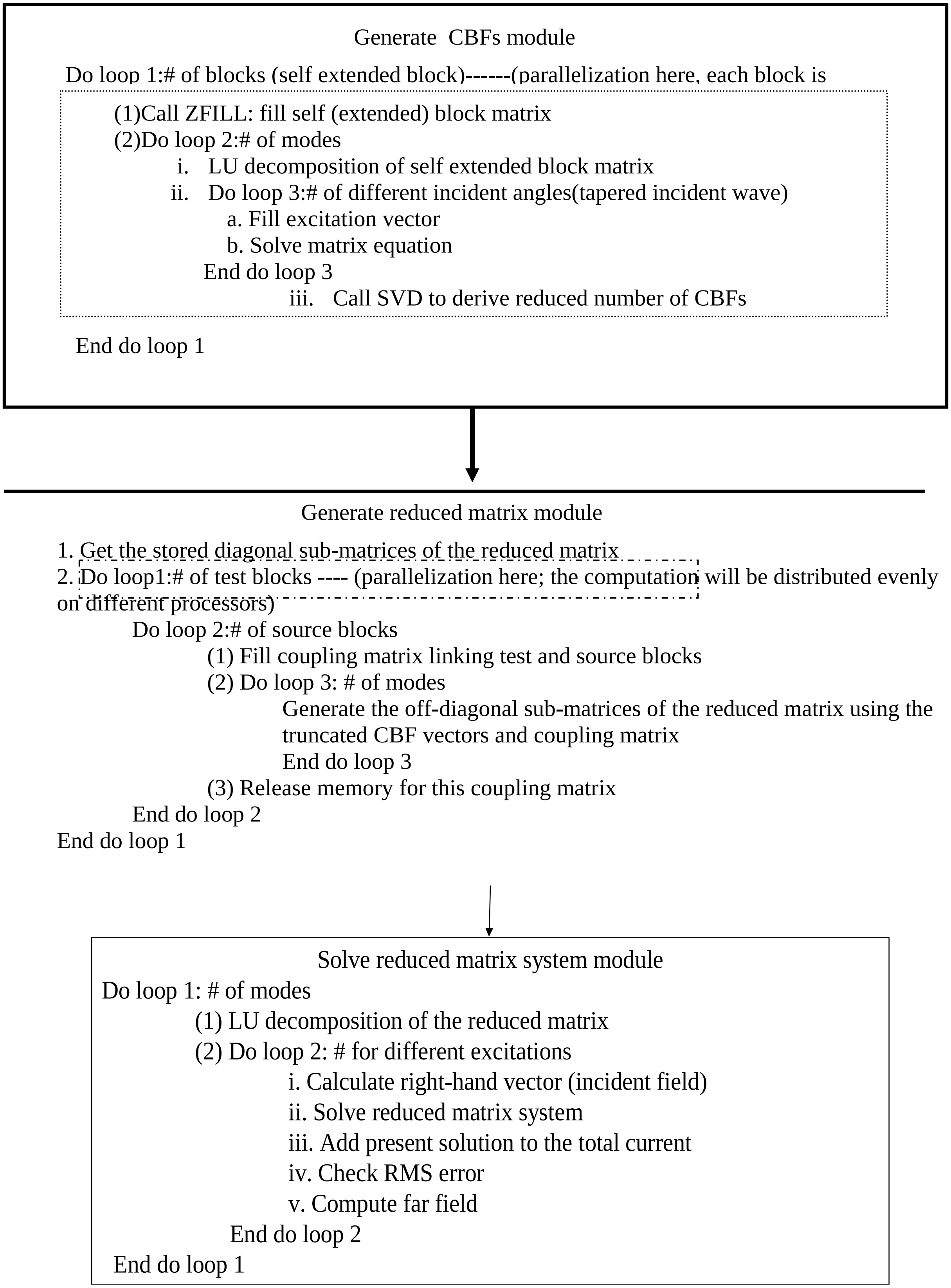

```
Generate  CBFs module
Do loop 1:# of blocks (self extended block)------(parallelization here, each block is
    (1)Call ZFILL: fill self (extended) block matrix
    (2)Do loop 2:# of modes
        i.   LU decomposition of self extended block matrix
        ii.  Do loop 3:# of different incident angles(tapered incident wave)
                a. Fill excitation vector
                b. Solve matrix equation
             End do loop 3
        iii. Call SVD to derive reduced number of CBFs
End do loop 1

Generate reduced matrix module
1. Get the stored diagonal sub-matrices of the reduced matrix
2. Do loop1:# of test blocks ---- (parallelization here; the computation will be distributed evenly
on different processors)
    Do loop 2:# of source blocks
        (1) Fill coupling matrix linking test and source blocks
        (2) Do loop 3: # of modes
                Generate the off-diagonal sub-matrices of the reduced matrix using the
                truncated CBF vectors and coupling matrix
                End do loop 3
        (3) Release memory for this coupling matrix
    End do loop 2
End do loop 1

Solve reduced matrix system module
Do loop 1: # of modes
    (1) LU decomposition of the reduced matrix
    (2) Do loop 2: # for different excitations
            i. Calculate right-hand vector (incident field)
            ii. Solve reduced matrix system
            iii. Add present solution to the total current
            iv. Check RMS error
            v. Compute far field
        End do loop 2
End do loop 1
```

Fig. 6. Flowchart for the CBF_BOR code.

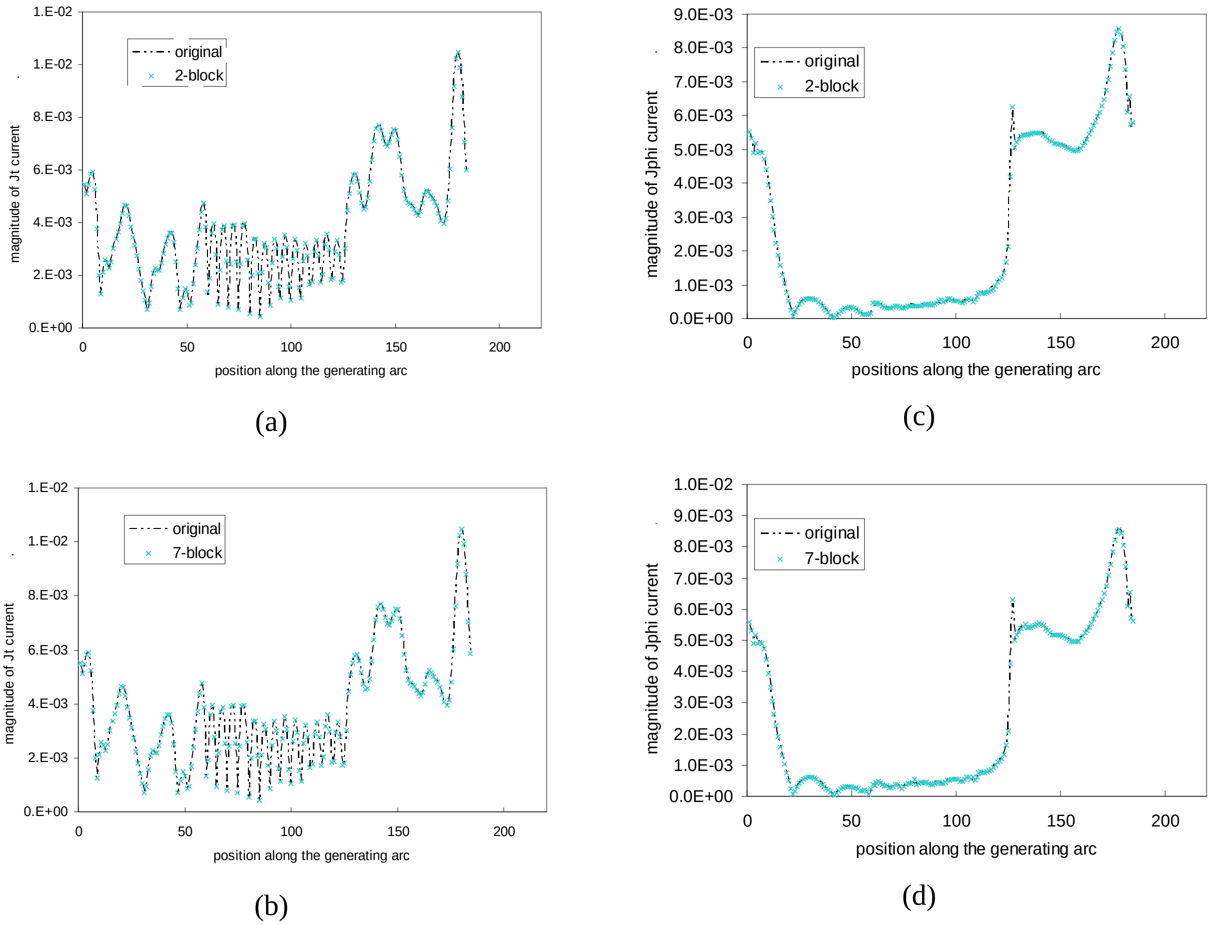

(a) (c)

(b) (d)

Fig. 7. The J_t current on the cylinder in Fig. 5 due to theta excitation. Axial incidence (a) 2-block, (b) 7-block. The J_{phi} current on the cylinder in Fig. 5 at ϕ =90 due to θ excitation. Axial incidence (c) 2-block. (d) 7-block.

Next, we illustrate the effect of changing the SVD threshold on the accuracy of the results. In Fig. 8 we show the results of progressively varying this threshold value, beginning from 100 and moving upward, steadily improving the accuracy of the current distribution in the process. We notice from these plots, which compare the direct solution with those obtained by using the CBF/BOR code, that a value of 1,000 marked in the figures as original is adequate for achieving numerical convergence. Of course, the far-field is more forgiving, and we can probably use a somewhat lower value for the threshold, without compromising the accuracy of the far field pattern noticeably, as may be seen from Fig. 9.

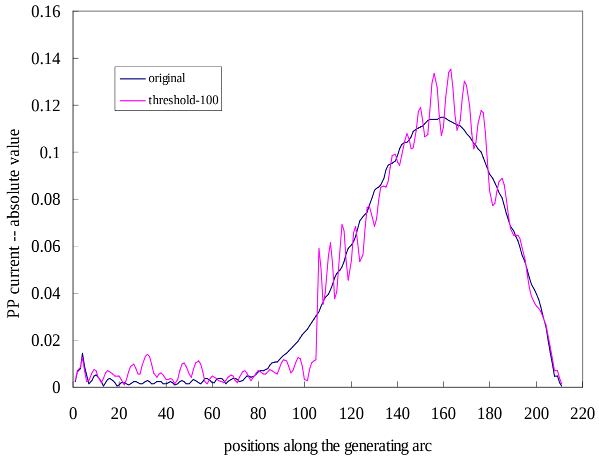

(a)

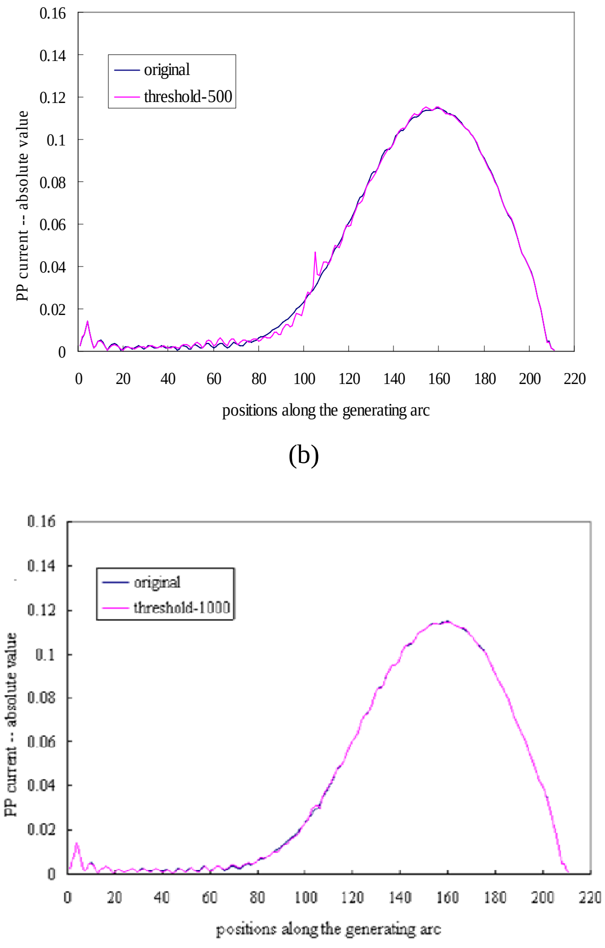

(b)

(c)

Fig. 8. The ϕ-ϕ current on a sphere along the generating arc for axial incidence. (a)Threshold value for SVD is 100. (b) Threshold valuefor SVD is 500. (c) Threshold value for SVD is 1000.

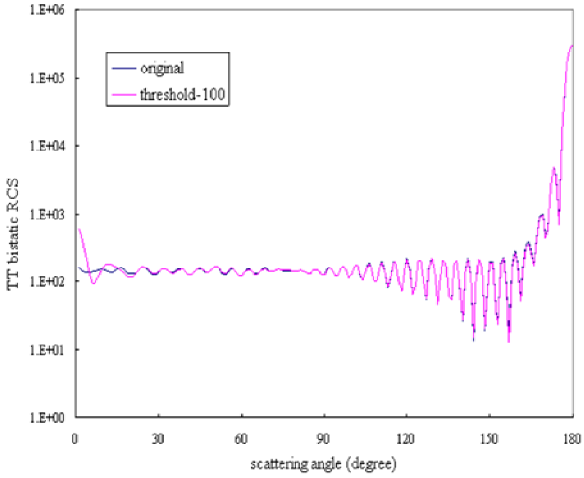

(a)

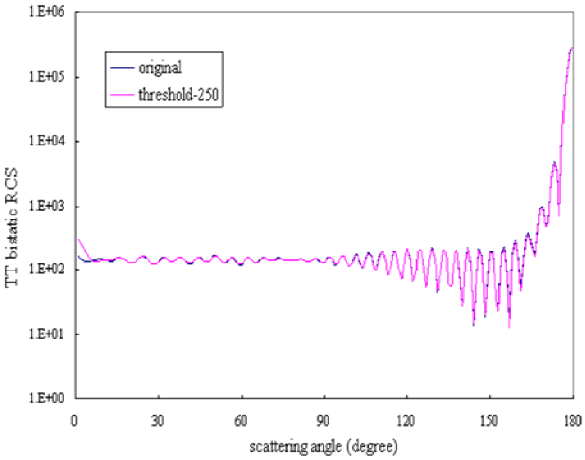

(b)

Fig. 9. The θ-θ bistatic RCS of a sphere. (a)Threshold for SVD is 100. (b) Threshold for SVD is 250.

Obviously, lowering the threshold increases the number of CBs we retain and, hence, the size of the reduced matrix and the associated computational burden. Numerical experiments involving a variety of different problems have shown that a good choice for the SVD threshold is the value we have mentioned above, namely 1000.

Table 1: First five letters of the Greek alphabet

Threshold Value	Name
100	33
250	43
500	51
1000	54
2000	55
5000	58

We will now describe the parallel implementation of CBF/BOR, which involves four steps, as detailed below.

IV. STRATEGY FOR PARALLEL IMPLEMENTATION OF CBBOR

As mentioned earlier, one of the important attributes of the CBFM is that the algorithm is easily parallelizable. Although we do not present the details of the parallelization algorithm in this review work, we outline just the basic steps here. First, we recognize that the generation of the CBs can proceed independently, on separate processors, since these processors do not need to communicate with each other at this step. Once the CBs have been generated, the next step is to construct the reduced matrix by using the Galerkin approach, which entails matrix-vector multiplications involving the CBs, and the self- as well as off-block matrices. A bulk of these processes can also be readily parallelized, because, at no point we need to deal with the entire MoM matrix concurrently.

We now briefly review the parallelization process for the CBF_BOR code which basically includes four steps:

(i) generating and splitting geometry;
(ii) generating CBFs;
(iii) generating reduced matrix;
(iv) solving the reduced matrix system.

The parallelization is implemented in parts (ii) and (iii), with computation burden evenly distributed among different processors.

1) Generating and splitting the geometry

All processors participate in the tasks of geometry generation and splitting, so that they will have the needed parameters and geometry data, obviating the need for communication among processors.

2) Generating CBFs

If the number of blocks is less than the number of available processors, each processor will perform the computation for one block. In each processor, the extended self-block matrix is filled and the matrix system is solved to generate the CBFs for this block. The diagonal sub-matrix of the reduced matrix for this block is then obtained by using the self-block matrix and CBFs. The memory for the self-block matrix is then released. Next, the CBFs for this block are broadcast to every processor. The diagonal sub-matrix of the reduced matrix is sent to only one master processor. Figure 10 illustrates the implementation of this procedure. Of course, if the number of blocks is larger than the number of available processors, then each processor would perform the computation for several blocks

3) Generating the reduced matrix

The generation of the reduced matrix entails the linking of the test and source blocks to obtain the off-diagonal elements of the reduced matrix, and a parallel implementation of this process is carried out in accordance with Fig. 11 Each processor computes the coupling matrices in a row. The off-diagonal sub-matrices of the reduced matrix in one row are then obtained by using these coupling matrices and the CBFs matrices for all blocks on this processor. These off-diagonal sub-matrices are then sent to the master processor.

4) Solving the reduced matrix system

The reduced matrix system is solved only on the master processor. The far field calculation and data output operations are also handled by this processor.

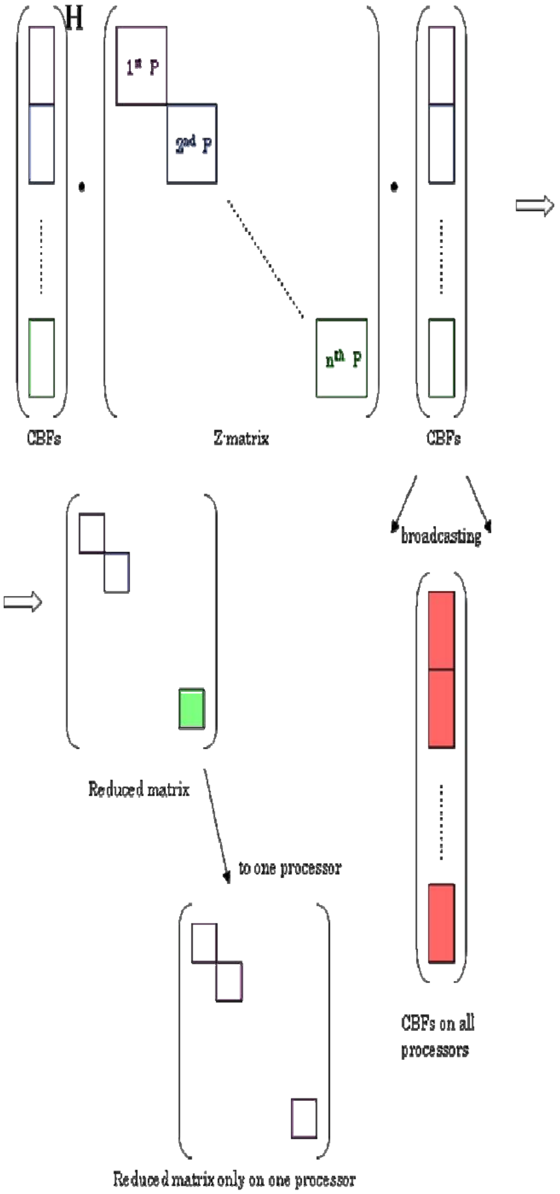

Fig. 10. Parallel implementation for the generation of CBFs for BOR problem.

V. LOCALLY MODIFIED CBFM

Recall that the most computationally intensive task in CBFM algorithm is associated with the generation of the CBFs, which entails the filling and LU factorization of the MoM impedance matrix associated with the various blocks. To generate the high-level basis functions for a given block, the CBFM localizes the problem to the particular macro-domain of that block; hence, it does not need to account for the interaction among the various blocks at this stage. This feature offers great flexibility when modelling targets whose geometries are modified only locally, for instance to reduce (or enhance) its RCS. Consequently, this feature of CBFM has an important advantage over the conventional MoM or FMM, which must analyze the modified problem a new essentially from the very beginning even if only a small part of the geometry is altered. In contrast to the conventional methods, the CBFM only needs to re-work the block that is being modified to obtain a new set of CBFs for it, while bypassing this step for the other blocks whose macro-bases are stored in a file, and are reused to generate the reduced matrix. Furthermore, we can achieve consistent time-saving even during the process of generating the reduced matrix, because only the matrix elements that link the modified block to the rest of the structure need be re-computed.

Below we delineate the steps involved in the implementation of the CBFM to handle a locally-modified object, which is depicted, symbolically in Fig. 12. The steps for modifying the blocks are presented in Fig. 13.

As an example we consider a plate problem which is locally modified, as shown in Fig.14, by introducing a hemispherical “bump” on the right side of the plate.

In Fig. 15 we present the bistatic RCS results for both cases, computed by using the conventional and LM/CBFM algorithms. We note from the above plot that the two results are virtually indistinguishable.

VI. CHARACTERISTIC BASIS FUNCTION FOR FEM

To the best of our knowledge, a CBFM-type of procedure that leads to a reduced matrix generated by using characteristic basis functions—tailored to individual—sub-domains has not been employed in the past for the Finite Element-Method (FEM), until quite recently. Space does not permit us to discuss the procedure in minute details in this review paper on CBFM, and we refer the reader to [14] where they can be found. Here we only show a representative example of scattering by a sphere, and point out some important difference between the implementations of CBFM in MoM and FEM.

Figure 16(a) illustrates the CBFM procedure implemented in FEM. Let us assume that we decompose the original scattering problem into two blocks, as shown in Fig. 16(b). To generate the CBs for these domains we use fictitious dipoles residing on the surface of the object (see Fig. 16(c)), which is a sphere in this example though it could be arbitrary in general.

The incident fields at the interfaces of the sub-domains are radiated by the dipoles in the absence of the scatterer. Note that this step is different from that followed in the MoM implementation of CBFM.

Next, as before, we apply the SVD procedure to retain only the non-redundant CBFs. The third step is to compute the CBFs in the various sub-domains; by using the interface-based CBFs ─which we just derived in the previous step─ for the incident fields. Following this, we apply the SVD procedure once again to select the post-SVD CBFs which we wish to retain. Finally, we construct the “reduced” matrix, using the Galerkin’s procedure, similar to that followed in CBMoM (Characteristic Basis Method of Moments).

We will now present the results for a test example, that of a sphere, which has been solved on a parallel platform. We remark here -without going into the details- that, in common with the MoM, CBFEM also tends itself to convenient parallelization. As shown in Fig. 17, the computational domain for the problem geometry in Fig. 16 is divided into 16 blocks.

The number of elements we have after using a uniform $\lambda/10$ discretization is 241,765 and the associated DOFs number of edge is 313,958. The final reduced matrix is only 16,016 and the result for the bistatic RCS, computed by using the above matrix, are shown in Fig. 18. The above are also compared with those derived by using the Mie series, as well as via an alternate numerical approach called the Backward-forward Domain Decomposition method [15].

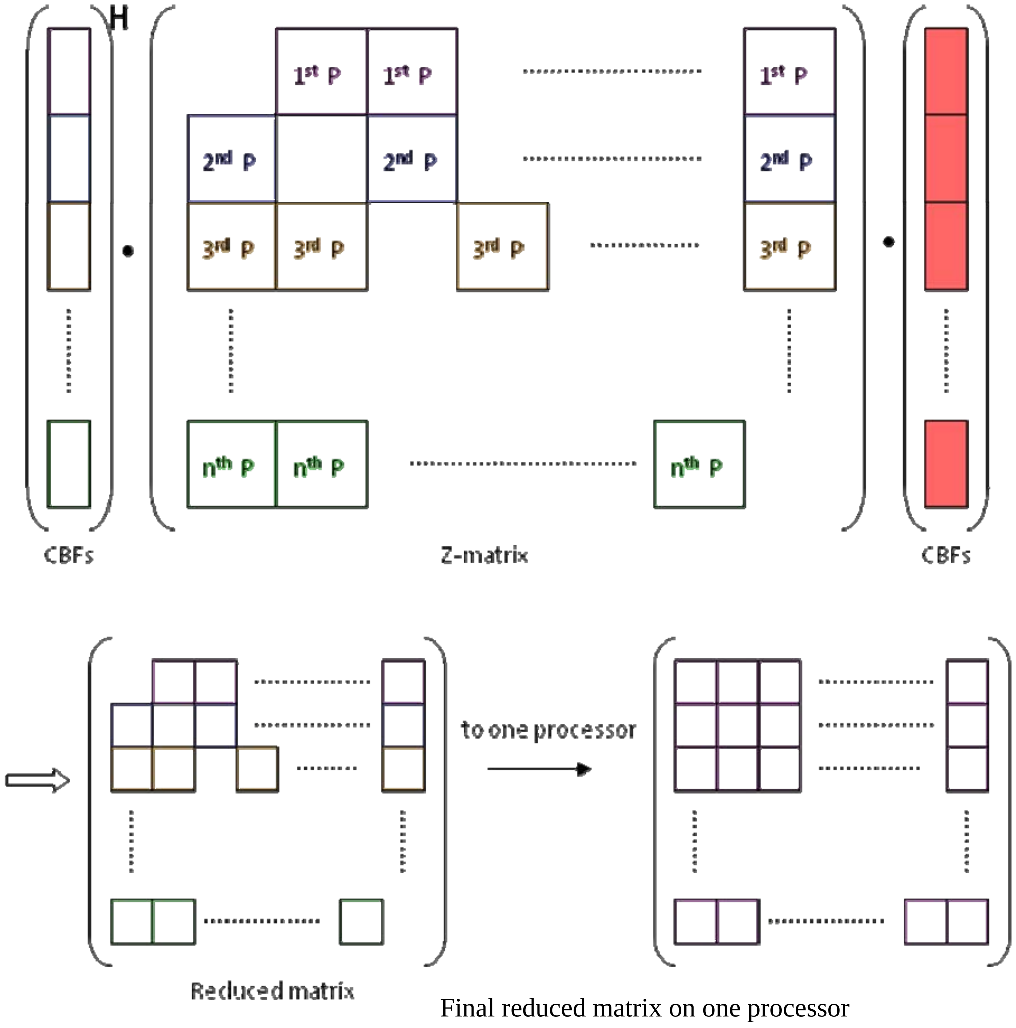

Fig. 11. Parallel implementation of reduced matrix generation.

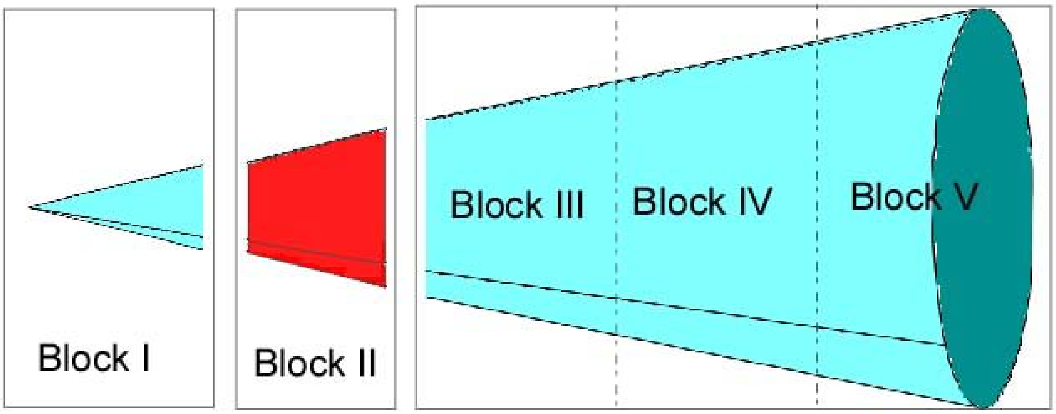

Modified geometry: Block II is being modified

Fig. 12. Geometry of an object, one of whose (Block-II) is being modified.

Load Project:
1) Read block file (each block has an option field)
2) Option value must be 1->Redo, 0->Already done
3) If all option fields are equal to 1 then a new excitation is being analyzed
4) All new block's definitions, not previously present, must be placed last

Split Structure:
1) If the block has already been analyzed, then load geometrical info only
2) If the block has been modified, then obtain the new mesh

Self Block Analysis:
1) If the block has already been analyzed, then load the number of post-SVD CBFs
2) If the block has been modified, then obtain the new set of CBFs

Reduced-RHS Generation:
1) Compute the reduced right-hand sides anew. The user might have added some new excitations

Reduced-Matrix Generation:
1) If all blocks have the option field equal to 1, then load the previously computed reduced-matrix
2) If some blocks have been modified, then computed the relative row and column in the reduced matrix. Note: Since we compute the reduced-matrix by forcing symmetry, particular care must be exercised to avoid duplicated jobs.
3) If some blocks have been modified, then load the previous reduced-matrix and modify it with the new entries. The modified block(s) can be placed in the middle of the reduced-matrix and the number of post-SVD used to generate these blocks can be different from that in the previous simulation. This results in a different size for the reduced-matrix and its indices are shifted.

Fig. 13. Steps for CBMOM modification.

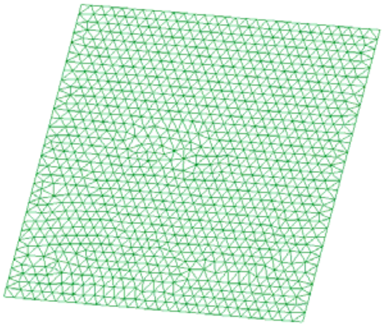

(a)

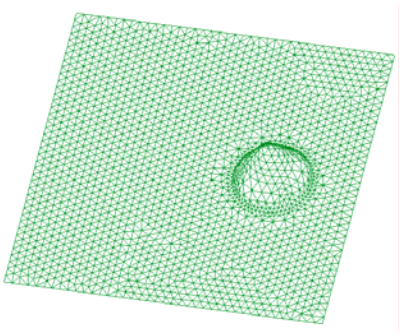

(b)

Fig. 14. (a) Plate Geometry. (b) Local Modification of the plate.

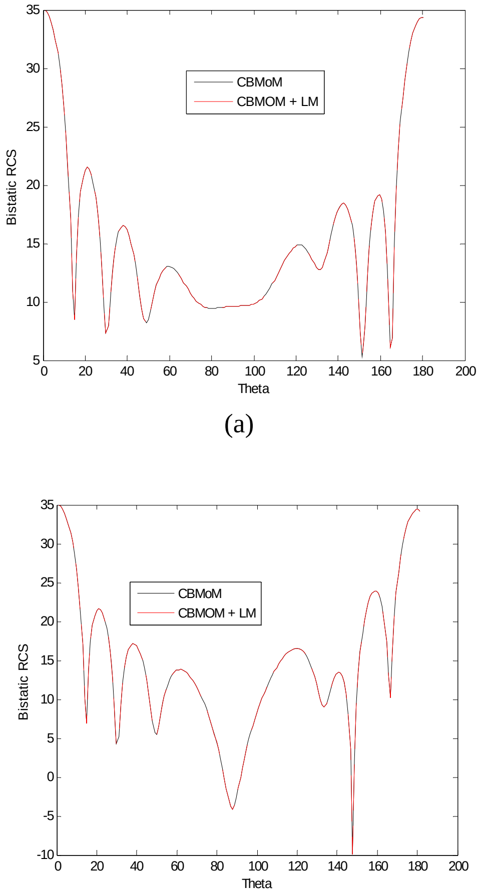

(a)

(b)

Fig. 15. Bistatic RCS of the locally modified plate compared by asing the conventional and locally modified CBFMs.

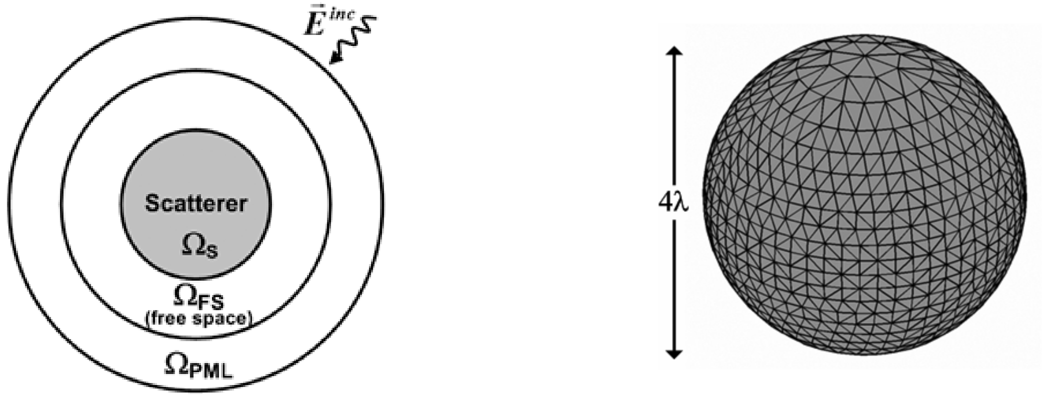

(a)

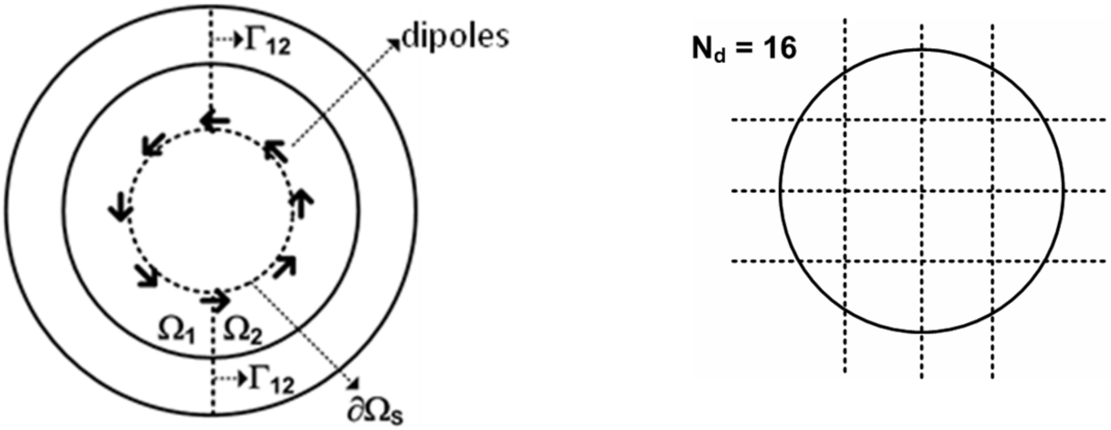

(b)

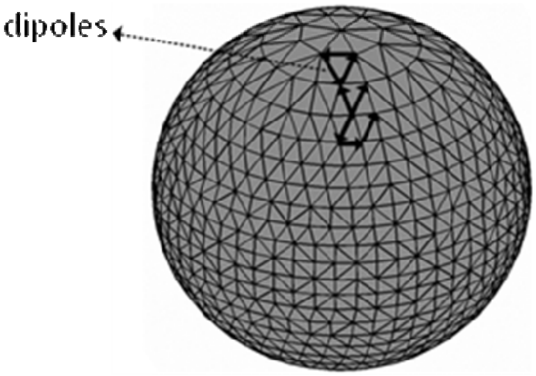

(c)

Fig. 16. (a) Original scattering problem of scattering by a 4λ diameter sphere. (b) CBFEM approach. (c) Dipole positions on the surface of the sphere.

Input Parameters:

Diameter	4 λ
Incident Field	$\vec{E}^{inc} = \hat{a}_x \exp(-jkz)$
Element Size	λ/10 λ/20 (on boundary)
Number of elements	114,304
Number of edges (unknowns)	240,465
Initial number of dipoles	45,996
SVD Threshold	10^{-5}
Number of subdomains (N_d)	16
Number of interfaces	45

Analysis Parameters:

		Pre-SVD	**Post-SVD**
Number of CBFs in each domain	Ω_1	1,733	1,221
	Ω_2	1,907	1,515
	Ω_3	1,914	1,502
	Ω_4	1,739	1,228
	Ω_5	2,128	1,348
	Ω_6	1,371	989
	Ω_7	1,383	994
	Ω_8	2,108	1,370
	Ω_9	2,120	1,327
	Ω_{10}	1,369	972
	Ω_{11}	1,383	971
	Ω_{12}	2,108	1,337
	Ω_{13}	1,729	1,224
	Ω_{14}	1,914	1,517
	Ω_{15}	1,918	1,517
	Ω_{16}	1,739	1,229
Size of the final reduced Schur matrix (Total number of CBFs on interfaces)	**14,135**		

Fig. 17. Relevant parameters for the CBFEM solution of the 4λ diameter sphere.

VII. DOMAIN DECOMPOSITION IN FDTD

Finally, we will present a novel approach [16] to solve large problems using the domain decomposition in the context of FDTD. The strategy here differs significantly from that utilized in MOM or FEM, because it is unique to the time domain alone. We should point out that this is approach, which is tailored for large problems, is not suitable for problems in which there exist significant multiple interactions between the subdomains, as for instance when the object size is relatively small, of course such an object can be solved directly, without resorting to domain decomposition.

We begin by subdividing the geometry of the large object into smaller blocks, as in the past, but only in one dimension, say *x*, as shown in Fig. 19. We make sure that there is an overlapping or buffer region between two adjacent sub-domains (see Fig. 19). Next, we begin to analyze the problem from one end, say the left, and proceed in much the same way as we would in a TDR (time domain reflectometer). Specifically, we track the E and H fields as they traverse from left to right, including only the local interactions within a sub-domain and not the mutual effects between two sub-domains at this point. (To do this, we terminate the interface of the sub-domain on the right with a PML.) We then proceed to interface-1, and record the time domain signatures of the tangential fields at the interface with the wave impinging upon it from the left. We then use this information to excite the sub-domain to the right, which is again terminated with a PML on its right. We repeat this procedure until we reach the end.

In many large problems, such as for instance in the case of two large antenna arrays separated by a large distance, we can terminate the procedure after just one pass, once we have reached the end. This is because the coupling between the two arrays is relatively weak and, hence, the level of the signal reflected from the second array is very small, i.e., essentially negligible.

However, we can have a different scenario, such as the one depicted in Fig. 20, where we wish to estimate the coupling of unwanted signals into a room with electronic devices, e.g., computers. In this case, we find that it becomes necessary to account for the reflected signal, at least through one round-trip, in order to improve the accuracy of the results. The results for the fields, computed by using the DD/FDTD approach, are shown in Figs 21a and Fig. 21b, where they are also computed with the direct solution (see Fig. 21b). We note that the comparison is quite good.

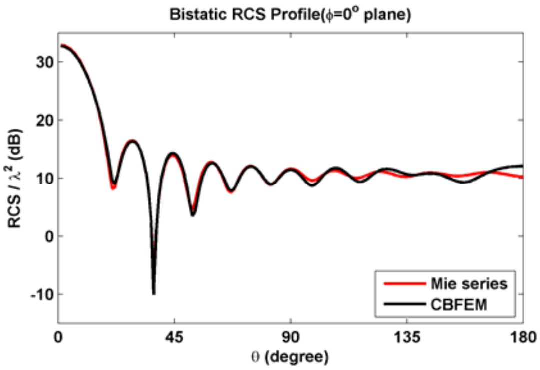

(a)

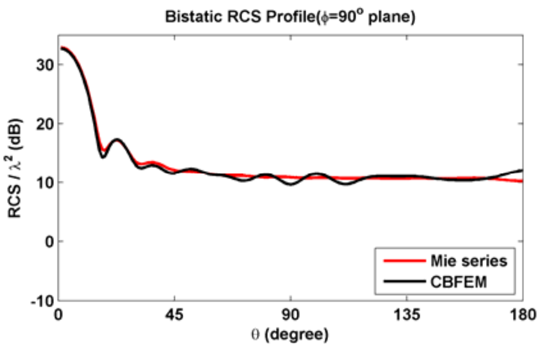

(b)

Fig. 18. Comparison of CBFEM and Mie series r for the 4λ sphere problem. (a) Phi=90°. (b) Phi=0°.

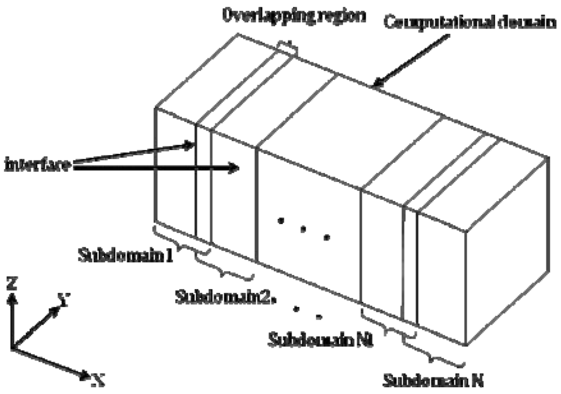

Fig. 19. Domain decomposition scheme in the context of the FDTD.

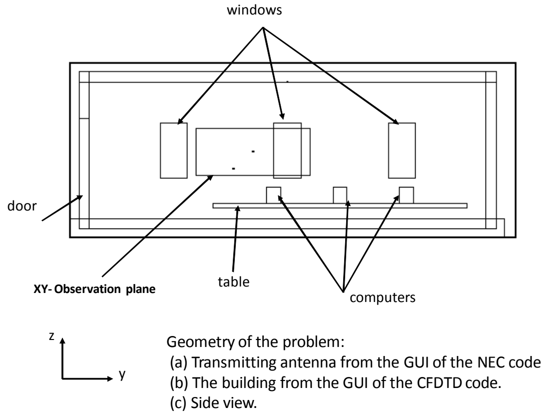

Fig. 20. Geometry of the problem.

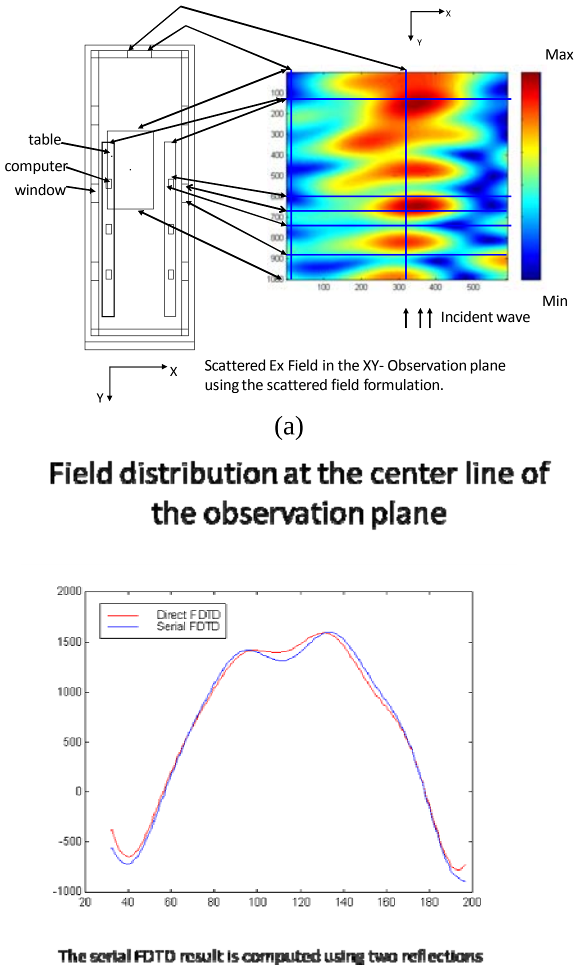

(a)

(b)

Fig. 21. (a) Scattered E_x Field in the XY-Observation plane. (b) Field distributions at the center line of the observation plane Computed by using two reflections In the Domain Decomposition sc.

We observe that this type of approach can be quite useful for modelling the problem of remotely tracking the movements of targets in a room with brick walls, which can easily fall into the “large” problem category and, hence, is likely to benefit from the application of the DD/FDTD analysis.

VIII. CONCLUSION AND FUTURE WORK

In this paper, we have reviewed a technique, based on the domain decomposition approach, for solving large problems, unlike the conventional domain decomposition schemes, which rely on iterative procedures, and hence often suffer from convergence problems. The characteristic basis function method (CBFM) yields a reduced-size matrix, which is solved directly. Yet another important attribute of the technique is that it is general in nature, and can be tailored to apply to integral equation method as well as to FEM and FDTD algorithms. Finally, the CBFM is naturally parallelizable, which enables us to solve even larger problem in an efficient manner.

The method itself is still evolving and is currently an active research topic. Space does not permit us to discuss the various embellishments of the method, and we only provide a bibliography [17-53] that lists some of the contributions on the subject that have inspired the preparation of this paper.

REFERENCES

[1] R. Coifman, V. Roklin and S. Wandzura, “The fast multipole method for the wave equation: a pedestrian prescription,” *IEEE Antennas Propagat. Mag.*, vol. 35, pp. 7–12, Jun. 1993.

[2] J. Song, C. Lu and W. C. Chew, “Multilevel Fast Multipole Algorithm for Electromagnetic Scattering by Large Complex Objects”, *IEEE Trans. Antennas Propagat.*, vol. AP-45, pp. 1488-1493, Oct. 1997.

[3] E. Michielssen, and A. Boag, “Multilevel evaluation of electromagnetic fields for the rapid solution of scattering problems,” *Microwave Opt. Tech. Lett.*, vol. 7, 790-795, Dec. 5, 1994.

[4] F. X. Canning, “Solution of IML form of moment method problems in 5 iterations,”, *Radio Sci*., vol. 30, no. 5, 1371-1384, Sept./Oct. 1995.

[5] P. Y. Ufimtsev, *Fundamentals of the Physical Theory of Diffraction*, Wiley Interscience, 2007 (Book).

[6] J. B. Keller, “Geometrical Theory of Diffraction”, *J. Opt. Soc. Am*, vol. 52, no. 2, pp. 116-130, Feb. 1952.

[7] G.A. Thiele and G. A. Newhouse, “A hybrid technique for combining moment methods with the geometrical theory of diffraction,” *IEEE Trans Antennas Propagat.*, vol. AP-23, pp. 551-558, July 1975.

[8] V. V. S. Prakash and R. Mittra, “Characteristic Basis Function Method: A New Technique for Efficient Solution of Method of Moments Matrix Equation,” *Micr. Opt. Tech. Lett.*, vol. 36, no. 2, pp. 95-100, Jan. 2003.

[9] S. J. Kwon, K. Du and R. Mittra, “Characteristic basis function method: A numerically efficient technique for analyzing microwave and RF circuits,” *Micro. Opt. Tech. Lett.*, vol. 38, No. 6, pp. 444-448, Sept. 2003.

[10] J. Yeo, V. V. S. Prakash and R. Mittra, “Efficient analysis of a class of microstrip antennas using the characteristic basis function method (CBFM),” *Micro. Opt. Tech. Lett.*, vol. 39, No. 6, pp. 456-464, Dec. 2003.

[11] O. Ozgun , R. Mittra, and M. Kuzuoglu, “CBFEM-MPI: A Parallelized Version of Characteristic Basis Finite Element Method for Extraction of 3D Interconnect Capacitances”, (to appear).

[12] C. Delgado, F. Catedra, and R. Mittra, “Accurate Representation of the Edge Behavior of Current when Using PO-Derived Characteristic Basis Functions”, Submitted for publication on *Antennas and Wireless Propag. Lett.*, Manuscript# AWPL 0307-2007.

[13] E. Lucente, A. Monorchio and R. Mittra, “Generation of Characteristic Basis Functions by Using Sparse MoM Impedance Matrix for Large Scattering and Radiation Problems,” I*EEE AP-S International Symposium USNC/URSI National Radio Science Meeting*, Albuquerque, New Mexico, July 9-14, 2006.

[14] O. Ozgun, R. Mittra, and M. Kuzuoglu ,”Parallelized Characteristic Basis Finite Element Method (CBFEM-MPI) — A Non-iterative Domain Decomposition Algorithm for Electromagnetic Scattering Problems,” (to appear).

[15] O. Ozgun and M. Kuzuoglu, “Forward-backward domain decomposition method for finite element solution of boundary value problems,” *Micro. Opt. Tech. Lett.*, vol. 49, no. 10, pp. 2582-2590, 2007.

[16] R. Mittra, H. Abd-El-Raouf, and N. Huang, “A Serial-Parallel FDTD Approach for Modeling the Coupling Problem between Two Large Arrays,” *ACES Special Issue on Phased Arrays*, vol. 21, no. 3, Nov. 2006.

Additional Bibliography

[17] E. Garcia, C. Delgado, F. S. de Adana and R. Mittra, "Development of an efficient rigorous technique based on the combination of CBFM and MLFMA to solve very large electromagnetic problems", *Electromagnetics in Advanced Applications, ICEAA*, pp. 579-582, Sep. 17-21, 2007.

[18] R. Maaskant, R. Mittra and A. G. Tijhuis, "Fast Solution of Large-Scale Antenna Problems Using the Characteristic Basis Function Method and the Adaptive Cross Approximation Algorithm", Submitted for publication on *IEEE trans. Antenna propagat.*

[19] J. Laviada, M. R. Pino, F. Las-Heras and R. Mittra, "Mitigation of the Truncation Problem in the Characteristic Basis Function Method via a Novel Cell-Stretching Approach," *IEEE Antennas Propagat. and URSI meeting*, San Dieogo, CA, July 5-8, 2008.

[20] J. Laviada, M. R. Pino, F. Las-Heras and R. Mittra, "Efficient Calculation of the Reduced Matrix in the Characteristic Basis Functions Method," *IEEE Antennas and Propagation and URSI meeting*, San Dieogo, CA, July 5-8, 2008.

[21] C. Delgado, E. García, F. Cátedra and R. Mittra, "Hierarchical Scheme for the application of the Characteristic Basis Function Method Based on a Multilevel Approach," *IEEE Antennas Propagat. and URSI meeting*, San Dieogo, CA, July 5-8, 2008.

[22] G. Tiberi1, E. Lucente1, A. Monorchio1, G. Manara1 and R. Mittra, "A Characteristic Basis Function Method (CBFM) for analyzing the EM scattering by large structures having slots," *IEEE Antennas Propagat. and URSI meeting*, San Dieogo, CA, July 5-8, 2008.

[23] O. Ozgun, R. Mittra, and M. Kuzuoglu, "Characteristic Basis Finite Element Method (CBFEM) — A Non-iterative Domain Decomposition Finite Element Algorithm for Solving Electromagnetic Scattering Problems," *IEEE Antennas Propagat. and URSI meeting*, San Dieogo, CA, July 5-8, 2008.

[24] N. Farahat, R. Mittra and N. Huang, "Modeling Large Phased Array Antennas Using the Finite Difference Time Domain Method and the Characteristic Basis Function Approach", *ACES*, vol. 21, no. 3, pp. 218-225, Nov. 2006.

[25] R. Mittra, H. E. Abd-El-Raouf and N. Huang, "A Serial-Parallel FDTD Approach for Modeling the Coupling problem between Two Large Arrays", *ACES*, vol. 21, no. 3, pp. 267-275, Nov. 2006.

[26] M. Kuzuoglu, and R. Mittra, "Fast solution of Electromagnetic Boundary Value Problems by the Characteristic Basis Functions/FEM Approach" *IEEE Antennas Propagat. Society International Symposium/URSI*, Columbus, Ohio, pp. 1071-75, June 2003.

[27] J. Yeo, and R. Mittra "Numerically Efficient Analysis of Microstrip Antennas using the Characteristic Basis Function Method (CBFM)," *IEEE Antennas Propagat. Society International Symposium/URSI*, Columbus, Ohio, vol. 4, pp. 85-88, June 2003.

[28] R. Mittra and V. V. S. Prakash, "The Characteristic Basis Function Method (CBFM) – An Alternative to FMM for a class of Antenna and Scattering Problems," *IEEE Antennas Propagat. Society International Symposium/URSI*, Columbus, Ohio, June 2003.

[29] V. V. S. Prakash, "RCS computation over a frequency band using the characteristic basis and model order reduction method," *IEEE Antennas Propagat. Society International Symposium/URSI*, Columbus, Ohio, June 2003.

[30] V. V. S. Prakash, and R. Mittra, "Fast Computation of Radar Cross Section for Multiple Incident Angles by using Characteristic Basis Functions (CBFs)," *IEEE Antennas Propagat. Society International Symposium/URSI*, Columbus, Ohio, June 2003.

[31] T. Su, L.C. Ma, N. Farahat and R. Mittra, "Modeling of a Large Slotted Waveguide Phased Array Using the FDTD and Characteristic Basis Function (CBF) Approaches," *IEEE Antennas Propagat.*

Society International Symposium/URSI, Columbus, Ohio, June 2003.

[32] G. Tiberi, A. Monorchio, G. Manara and R. Mittra, “Hybridizing Asymptotic and Numerically Rigorous Techniques for Solving Electromagnetic Scattering Problems using the Characteristics Basis Functions (CBFs),” *IEEE Antennas Propagat. Society International Symposium/URSI*, Columbus, Ohio, June 2003.

[33] R. Mittra, “Solution of Large Array and Radome Problems using the Characteristic Basis Function Approach,” *IEEE Antennas Propagat. Society International Symposium/URSI*, Columbus, Ohio, June 2003.

[34] Y. Sun, C. H. Chan, R. Mittra and L. Tsang, “Characteristic Basis Function Method for Solving Large Problems Arising in Dense Medium Scattering,” *IEEE Antennas Propagat. Society International Symposium/URSI,* Columbus, Ohio, vol. 2, pp. 1068-1071, June 2003.

[35] R. Mittra, J. Yeo and V. V. S. Prakash, “Efficient Generation of Method of Moments Matrices using the Characteristic Function Method,” *IEEE Antennas Propagat. Society International Symposium/URSI,* Columbus, Ohio, vol. 2, pp. 1068-1071, June 2003.

[36] R. Mittra, “A Proposed New Paradigm for Solving Scattering Problems Involving Electrically Large Objects using the Characteristic Basis Functions Method,” *Proceedings of the International Conference on Electromagnetics in Advanced Applications (ICEAA) 2003*, Turin, Italy, pp. 621-624, Sept. 2003.

[37] K. F. Chan, K.W. Lam, C.H. Chan and R. Mittra, “Modeling of Microstrip Reflectarrays Using the Characteristic Basis Function Approach,” *2004 International Symposium on Electromagnetic Theory (URSI-EMT’04)*, Pisa, Italy, May 23-27, 2004.

[38] G. Tiberi, S. Rosace, A. Monorchio, G. Manara and R. Mittra, “Electromagnetic Scattering from Large Faceted Conducting Bodies by Using Analytically Derived Characteristic Basis Functions,” *IEEE Antennas and Wireless Propagat. Lett.*, vol. 2, pp. 290-293, 2004.

[39] R. Mittra, T. Zhao, J. Yeo and S. Koksoy, “Solution of Large Radiation and Scattering Problems Without Iteration Using the Fast Matrix Solver (FMS) and the Characteristic Basis Function Method (CBFM),” *IEEE AP-S International Symposium and USNC/URSI National Radio Science Meeting*, *APS/URSI,* Monterey, CA, pp. 33, June 19-25, 2004,

[40] R. Mittra, and V. V. S. Prakash, “The Characteristic Basis Function Method: A New Technique for Fast Solution of Radar Scattering Problem,” *Special Issue on CEM of Computer Modeling in Engineering & Sciences,* vol. 5, no. 5, pp. 435-442, 2004.

[41] J. F. Ma, and R. Mittra, “Analysis of Scattering Characteristics of Electrically Large Objects Using a CBFM-Based Procedure,” *IEEE International Symposium on Antennas and Propagation and USNC/URSI National Radio Science Meeting (AP-S’05)*, Washington DC, Digest vol. 3A, pp. 105-108, July 3-8, 2005.

[42] N. Farahat, R. Mittra and N. T. Huang, “Modeling Large Phased Array Antennas Using the Finite Difference Time Domain Method and the Characteristic Basis Function Approach,” *the ACES 2006 conference,* Miami, Florida, March 12-16, 2006.

[43] C. Delgado, R. Mittra and F. Cátedra, “Analysis of Fast Numerical Techniques Applied to the Characteristic Basis Function Method,” *the IEEE AP-S International Symposium USNC/URSI National Radio Science Meeting*, July 9-14, 2006, Albuquerque, New Mexico, pp. 4031-4034.

[44] G. Tiberi, A. Monorchio, G. Manara and R. Mittra, “A Spectral Domain Integral Equation Method Utilizing Analytically Derived Characteristic Basis Functions for the Scattering From Large Faceted Objects,” *IEEE Trans. Antenna propagate.*, vol. 54, no. 9, pp. 2508-2514, Sept. 2006.

[45] E. Lucente, A. Monorchio and R. Mittra, “Generation of Characteristic Basis Functions by using Sparse MoM Impedance Matrix to Construct the Solution of Large Scattering and Radiation Problems,” *IEEE AP-S International Symposium and*

USNC/URSI National Radio Science Meeting, *APS/URSI*, Albuquerque, New Mexico, pp. 4091–4094, July 9-14, 2006.

[46] G. Tiberi, A. Monorchio, M. Degiorgi, G. Manara and R. Mittra, "An Efficient Method to Calculate the Convolution Based Reaction Integral Using the Analytical Fourier Transform, " *IEICE transactions on Electronics*, vol. E90-C, No. 2, pp. 231-234, Feb. 2007.

[47] G. Tiberi, A. Monorchio, G. Manara and R. Mittra, "A Numerical Solution for Electomagnetic Scattering from Large Faceted Conducting Bodies by Using Physical Optics-SVD Derived Bases," *IEICE transactions on Electronics*, vol. E90-C, no. 2, pp. 252-257, Feb. 2007.

[48] E. Lucente, A. Monorchio and R. Mittra, "Fast and Efficient RCS Computation over a Wide Frequency Band Using the Universal Characteristic Basis Functions (UCBFs)," *IEEE International Symposium on Antennas and Propagation*, Honolulu, Hawaii, June 10-14, 2007.

[49] C. Delgado, F. Catedra and R. Mittra, "A Numerically Efficient Technique for Orthogonalizing the Basis Functions Arising in the Solution of Electromagnetic Scattering Problems using the CBFM," *IEEE International Symposium on Antennas and Propagation*, Honolulu, Hawaii, June 10-14, 2007.

[50] R. Mittra, H. Abdel-Raouf and N. T. Huang, "CBFDTD--A New Extension of the FDTD Algorithm for Solving Large Radiation, Scattering and EMI/EMC Problems," *International Conference on Electromagnetics in Advanced Applications and European Electromagnetic Structures Conference, ICEAA'05*, September 12-16, 2005, pp. 1045-1048, Torino, Italy, May 2005.

[51] E. Garcia, C. Delgado, F. S. de Adana, F. Catedra and R. Mittra, "Incorporating the Multilevel Fast Multipole Method into the Characteristic Basis Function Method to Solve Large Scattering and Radiation Problems," *IEEE International Symposium on Antennas and Propagation*, Honolulu, Hawaii, June 10-14, 2007.

[52] R. Maaskant, R. Mittra and A. G. Tijhuis, "Application of Trapezoidal-Shaped Characteristic Basis Functions to Arrays of Electrically Interconnected Antenna Elements," *Electromagnetics in Advanced Applications*, *ICEAA*, pp. 567-571, Sep 17-21, 2007.

[53] A. Yagbasan1, C. A. Tunc, V. B. Erturk, A. Altintas and R. Mittra, "Use of Characteristic Basis Function Method for Scattering from Terrain Profiles," *ELEKTRIK* (to appear).

[54] R. Mittra, "Characteristic Basis Function Method--A Novel approach to Incorporating Concepts of Asymptotic Techniques into Rigorous Numerical Methods," *IEEE International Symposium on Antennas and Propagation*, Honolulu, Hawaii, June 10-14, 2007.

Raj Mittra (S'54–M'57–SM'69–F'71–LF'96) is a Professor in the Electrical Engineering Department, Pennsylvania State University, University Park. He is also Director of the Electromagnetic Communication Laboratory, which is affiliated with the Communication and Space Sciences Laboratory of the Electrical Engineering Department. Prior to joining Penn State, he was a Professor in the Electrical and Computer Engineering Department, University of Illinois, Urbana-Champaign. He is President of RM Associates, State College, PA, a consulting organization that provides services to industrial and governmental organizations, both in the U.S. and abroad. He has published more than 700 technical papers and more than 30 books or book chapters on various topics related to electromagnetics, antennas, microwaves, and electronic packaging. He has received three patents on communication antennas. He has advised more than 85 Ph.D. students and about an equal number of M.S. students, and has mentored approximately 50 postdoctoral research associates and visiting scholars in the EMC Laboratory. Prof. Mittra received the Guggenheim Fellowship Award in 1965, the IEEE Centennial Medal in 1984, IEEE Millennium Medal in 2000, the IEEE/AP-S Distinguished Achievement Award, the AP-S Chen-To Tai Distinguished Educator Award in 2004, and the IEEE Electromagnetics Award in 2006. He is a past President of AP-S and was an Editor of the IEEE Transactions on Antennas and Propagation.

Efficient Numerical Analysis of Arrays of Identical Elements with Complex Shapes

Christophe Craeye, David González-Ovejero, and Xavier Dardenne
Université catholique de Louvain,
Communications and Remote Sensing Laboratory,
Place du Levant 2, 1348 Louvain-la-Neuve, Belgium,
{christophe.craeye, david.gonzalez, xavier.dardenne}@uclouvain.be

***Abstract*—** A fast method-of-moments approach is proposed for the solution of finite arrays of complex identical elements, involving both metal and finite dielectric parts. The method is based on the use of Macro Basis Functions (MBF), also named “Characteristic” Basis Functions, among which interactions are computed very fast with the help of a Multipole approach. Fast evaluation of array patterns or embedded element patterns is obtained through decomposition into a finite series of pattern multiplication problems. Examples are provided for finite arrays of bowtie antennas embedded in dielectric boxes. For periodic arrays, results are compared with infinite-array solutions. The method is also extended to non-periodic structures, for which the Multipole approach appears very useful for interactions outside the near-field region. We show that interactions in the near-field region can benefit from an interpolation procedure.

***Index Terms*—** antenna arrays, method of moments, multipoles, macro basis functions.

I. INTRODUCTION

The numerical simulation of large finite arrays of antennas remains a challenge when the elements are of complex shapes and involve finite dielectric components and metallic parts. Examples of such radiators are ultra-wideband antennas embedded in finite dielectric boxes, which serve for instance as supporting material or as material allowing to reduce the size of the radiating elements. When dealing with piecewise homogeneous media, as is generally the case in antenna technology, integral-equation approaches, like the Method of Moments make sense, since unknowns can be limited to the interfaces between media. However, for the geometries referred to above, the description of currents or equivalent currents may anyway require several hundreds, and sometimes thousands, of coefficients per antenna, even if the latter is smaller than the wavelength.

Several efficient methods have already been developed for periodic structures; however, for the configurations of interest, they suffer from several drawbacks. When the total number of unknowns is larger than a few thousands, iterative methods that rely on fast matrix-vector multiplications can be used, they are based either on multipole decompositions [1], on Fast Fourier Transforms [2] or on QR decompositions [3]. In those cases, when based on Krylov subspace methods, convergence is theoretically guaranteed; however, the number of iterations is difficult to predict and relatively fast convergence generally requires preconditioners, whose performances are also difficult to predict. Besides this, some cases of divergence, generally attributed to effects of numerical round-off, are sometimes observed.

This is mainly why several authors have been trying to circumvent these difficulties by devising non-iterative methods in which elementary decomposition functions are aggregated into *Macro Basis Functions* (MBF’s), which would make sense from a physical point of view (they are then named *Characteristic*) [4]-[7]. The determination of the MBFs themselves is a research sub-topic on its own and will not be studied here. Besides the references above, a method is proposed in [8], where aggregations similar to the MBF approach are exploited in an iterative scheme based on multipole decompositions. For the challenging case of electrically connected antennas, specific schemes are presented in [9], [10] and [11]. In the latter, the Array Scanning Method [12], based on infinitearray solutions, is exploited to generate theMBFs.

1054-4887 © 2009 ACES

In this paper, we will concentrate on the computation of fast interactions between Macro Basis Functions (MBF), for the case of complex antennas fully embedded in dielectric blocks, assuming that all the elements of the array are identical, and with an extension to non-periodic arrays. The proposed method relies on a technique initially presented in [13] for the case of radiation by arrays made of metallic elements and in [14] for the case of scattering by finite arrays of homogeneous dielectric objects. The method is based on a combination of the Macro Basis Function (MBF) approach and of the Multipole method. In [15], this method has been extended by placing metallic elements inside finite dielectric objects. Examples were shown in [15] for dipoles embedded in dielectric quasi-spheres. In this paper, further results are shown for wideband bowtie elements embedded in dielectric boxes. It will also be recalled that, in the framework of the MBF approach, the array pattern can strictly be written as a series of pattern multiplication problems, for which the FFT can be exploited. The method will then be extended to the case of non-periodic arrays, for which the acceleration of interactions is even more crucial. Finally, we will also show that the FFT still can be exploited for pattern evaluation of irrergular arrays, provided that a specific interpolation procedure be applied.

This paper is organized as follows. In Section 2, the mathematical formulation is provided. In Section 3, simulation results are shown for bowtie antennas embedded in dielectric volumes. First for the case of a small 2×2 array, for comparison with a brute-force solution; then for a 10×10 array, with a comparison with the infinite-array solution. Finally, in Section 4, the methodology is extended to non-regular arrays. Conclusions are drawn in Section 5.

II. FORMULATION

Besides the currents j_m on the metallic part of the antenna, unknown equivalent electric and magnetic currents, j_s and m_s, are considered on the surface S_d of the dielectric objects. Hence, in this Method-of-Moments (MoM) formulation, the metallic part of the antenna couples with the exterior medium and with other antennas only through the equivalent currents on the surface S_d. Following the MBF (also called *Characteristic Basis Function*) methodology, the current distribution on a given cell is obtained as the linear superposition of distributions obtained while solving small problems:

$$\{\mathbf{j_m}, \mathbf{j_s}, \mathbf{m_s}\} = \sum_{p=1}^{P} C_p \ \{\mathbf{j^\circ_{m,p}}, \mathbf{j^\circ_{s,p}}, \mathbf{m^\circ_{s,p}}\}, \quad (1)$$

where $j^o_{x,p}$ and $m^o_{x,p}$ are the vectors of coefficients describing macro basis function *p*, and C_p is a constant to be determined. Here, these small problems are made either of an isolated transmitting cell (*primary* MBF), or of a receiving cell (*secondary* MBF, [6]), illuminated by the fields radiated by the transmitting cell. The interactions between MBFs are computed as the discretized approximation of:

$$I = \iint \left(\vec{J}_t^* . \vec{E}_s + \vec{M}_t^* . \vec{H}_s \right) dS \ , \quad (2)$$

where $\vec{J}_t$ and $\vec{M}_t$ currents can be either on the metallic or dielectric surfaces, while $\vec{E}_s$ and $\vec{H}_s$ are the fields radiated by a given macro basis function in the region of interest. The (*) superscript stands for complex conjugation, while the *t* index refers to testing functions. For MBFs associated with the same antenna or with neighboring antennas, interaction *I* can be computed with the help of the block of the MoM impedance matrix standing for interaction between those antennas [6]. When pairs of antennas located further away are considered, the computation of interaction I can be carried out much more efficiently, with the help of a multipole formulation. Using the plane-wave expansion of the free-space scalar Green's function, which can be found in [16], we obtain:

$$I = \frac{k}{(4\pi)^2} \iint \left(P_e + P_h \right) T\left(k, \vec{r}_{mn}, \hat{u}\right) dU \ , \quad (3)$$

where *T* is the Multipoles translation function [16], $\hat{u}$ is a unit vector in the direction of integration, and P_e and P_h are specific products of patterns of macro basis functions and of their divergences:

$$\begin{aligned} P_e &= \vec{\mathcal{F}}_t \, . \left(-\omega\, \mu \, \vec{\mathcal{F}}_b^\star - k\, \hat{u} \times \vec{\mathcal{G}}_b^\star \right) \\ &\quad + \frac{1}{\omega\, \epsilon} \, \mathcal{DF}_t \, \mathcal{DF}_b^\star \qquad , \end{aligned} \quad (4)$$

$$\begin{aligned} P_h &= \vec{\mathcal{G}}_t \, . \left(-\omega\, \epsilon \, \vec{\mathcal{G}}_b^\star + k\, \hat{u} \times \vec{\mathcal{F}}_b^\star \right) \\ &\quad + \frac{1}{\omega\, \mu} \, \mathcal{DG}_t \, \mathcal{DG}_b^\star \qquad , \end{aligned} \quad (5)$$

where the *b* index denotes the basis functions. In the following, to avoid too heavy notations, the *b* and *t* indices will be omitted.

$$\vec{\mathcal{F}} = \sum_{n=1}^{N} j_s^{\circ,\star}(n)\,\vec{F}_n;\ \mathcal{DF} \tag{6}$$

$$= \sum_{n=1}^{N} j_s^{\circ,\star}(n)\,DF_n \tag{7}$$

$$\vec{\mathcal{G}} = \sum_{n=1}^{N} m_s^{\circ,\star}(n)\,\vec{F}_n;\ \mathcal{DG} \tag{8}$$

$$= \sum_{n=1}^{N} m_s^{\circ,\star}(n)\,DF_n \tag{9}$$

where $\vec{F}_n$ is the pattern of the n^{th} subsectional basis function $\vec{f}_n$:

$$\vec{F}_n = \iint \vec{f}_n(\vec{r})\,e^{jk\hat{u}.\vec{r}}\,dS\ , \tag{10}$$

and DF_n is the pattern of its divergence. In the formulas above, k is the free-space wavenumber, ω is the radian frequency and ε and μ are the permittivity and permeability of free space. The formulas above can be delineated from [13] and from the well-known expressions of MoM-matrix entries for dielectric materials [17]. Detailed developments, along with slight variations on the formulation, will be given in [18].

The radiation patterns of the finite structure can be obtained very fast by decomposing the problem into a finite series of pattern multiplication problems. In this series, the contribution from a given MBF can be written as $F_{p,x}(\hat{u})\,A_p(\hat{u})$, where $F_{p,x}(\hat{u})$ is the element pattern of the current distribution described by the p^{th} macro basis function, computed with the help of the equivalent currents $\mathrm{j}^{\mathrm{o}}_{\mathrm{s,p}}$ and $\mathrm{m}^{\mathrm{o}}_{\mathrm{s,p}}$ on S_d, and which have already been obtained in the course of the MBF+Multipole computations. The index x stands for the polarization of the computed fields. The factor A_p corresponds to the array factor resulting from the array excited with the coefficients associated with the p^{th} macro basis function. Hence, we have:

$$F_x(\hat{u}) = \sum_{p=1}^{p=P} A_p(\hat{u})\,F_{p,x}(\hat{u})\ , \tag{11}$$

with

$$A_p(\hat{u}) = \sum_{mn} C_{mnp}\,e^{jk\left(u_x m\, a + u_y n b\right)} \tag{12}$$

$$= -j\omega\mu M\ N\ \mathrm{IFFT2}\Big(C_{mnp}\left(-1\right)^{m+n}\Big) \tag{13}$$

$$= A_p\left(r,\,s\right)\ , \tag{14}$$

where u_x and u_y are the horizontal projections of the unit vector $\hat{u}$ which indicates the direction of observation:

$$u_x\left(r\right) = \lambda/a\left(-1/2 + r/M\right), \tag{15}$$

$$u_y\left(r\right) = \lambda/b\left(-1/2 + s/N\right), \tag{16}$$

with (M, N) the dimension of the two-dimensional inverse FFT, $0 \le r \le N$ and $0 \le s \le M$, while a and b are the array spacings along x and y.

In [15], the method has been validated by comparison with a brute-force solution for a 5×5 array of broadband dipoles embedded in dielectric quasispheres and by comparison with infinite-array results for very large arrays. In the following, results will be shown for bowtie antennas inside dielectric blocks and an extension to non-regular arrays will be provided.

III. NUMERICAL EXAMPLES

The unit cell is sketched in Fig. 1. It is made of a bowtie antenna embedded in a parallelipipedic volume with relative permittivity equal to 4, represented here with 268 RWG-type [19] basis functions. The bowtie antenna is meshed with the help of 112 RWG and one rooftop basis functions. The antennas are terminated with a 100 Ohm load. The size of the box is 1.2 cm and the spacing between elements is 1.25 cm. The array configuration is shown in Fig. 2.

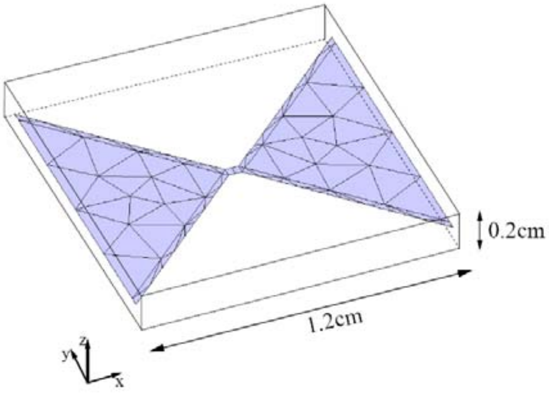

Fig. 1. Mesh of bowtie antenna embedded in dielectric volume.

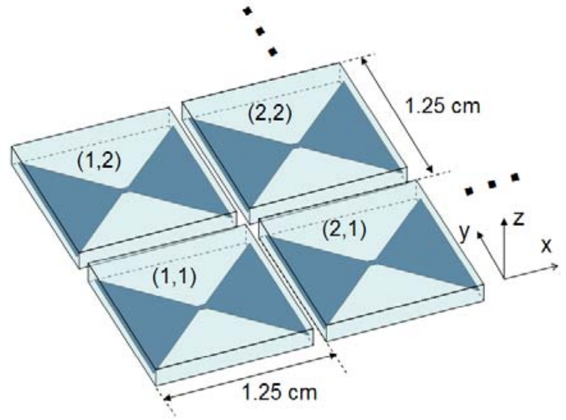

Fig. 2. Array geometry and element numbering.

Table 1. Coupling coefficients (amplitude and phase) in 2×2 array terminated with 100 Ohm loads, expressed in terms of induced currents, normalized w.r.t. excited element (1,1). Wavelength: 5 cm.

Index	(1,1)	(1,2)	(2,1)	(2,2)
B.F.(dB)	0.0	-14.944	-11.986	-27.370
MBF(dB)	0.0	-14.922	-12.002	-27.477
B.F.(rad)	0.0	1.351	-2.756	0.241
MBF(rad)	0.0	1.357	-2.754	0.255

Simulations have first been carried out at the element level, for a wavelength of 5 *cm*. We verified that, for lossless dielectrics, the power delivered to the antenna corresponds to the radiated power. This verification does not provide ultimate validation but appears as a useful check. Correspondence has been achieved within 0.1 percent of relative error. The array computations have been carried out while considering one primary MBF, corresponding to an isolated excited element and eight secondary MBFs, obtained as the field induced on the eight surrounding elements, due to the incident field radiated by the primary (this way of choosing MBFs was first proposed in [6]). First, still for a 5 cm wavelength, a very small array, made of 2×2 elements has been simulated, in order to see to what extent the MBF approach (so far without the Multipole acceleration) compares with the brute-force solution. In this case, the comparison is provided in terms of coupling coefficients and in terms of embedded element patterns. The coupling coefficients are provided as the currents induced on the 100 Ohm loads of the antennas when one of them is excited with a unit voltage and a 100 Ohm series impedance. Table 1 provides those coupling coefficients in the 2×2 array, expressed in dB with respect to the currents on the series impedance of element (1,1), which is excited. As for the magnitude, the first line stands for the brute-force (B.f.) solution, while the second line stands for the MBF solution. As for the phase, corresponding results are provided in third and fourth lines. It can be seen that the error levels are very low.

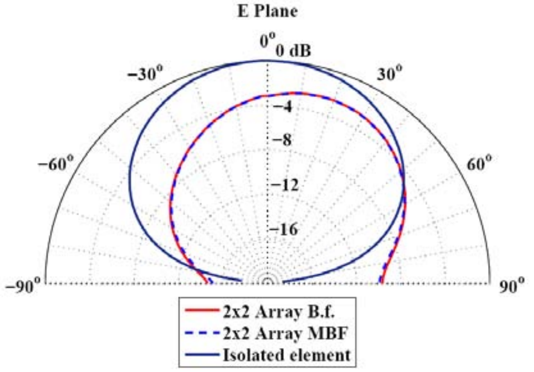

Fig. 3. E-plane cut in embedded element pattern for element (1,1) excited in 2×2 array, compared with pattern of isolated antenna. Wavelength: 5 cm.

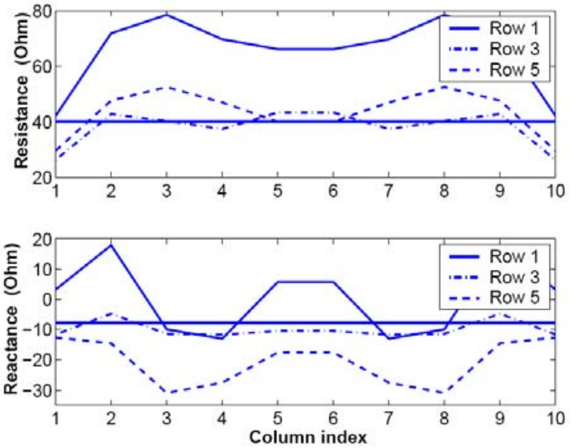

Fig. 4. Active input impedances in 10×10 array and in infinite array (horizontal lines) for broadside scan. Wavelength: 5 cm. Rows are along y in Fig. 2.

A major advantage of the MBF approach is that, once the reduced MoM impedance matrix is inverted, solutions are readily obtained for all possible excitations. Characteristics of major interest are the embedded element patterns, obtained with one element excited and all other elements passively terminated. On receive for instance, such a pattern fully describes the sensitivity at a given port of the array. For the 2×2 array referred to above, an E-plane cut of the embedded element pattern of element (1,1) is compared in Fig. 3 with the pattern obtained for an isolated element, as well as with the embedded element pattern obtained in the brute-force case. It can be seen that the MBF approach allows us to estimate with high accuracy the strong effects of mutual coupling on the embedded element patterns. In this case, in view of the very small size of the array, multipoles have not been used to compute the interactions between MBFs.

Other simulations have been carried out for a 10×10 array, with uniform excitations. This leads to (113+ 2×268)×100 = 64.900 surface unknowns on the finite- array structure. 900 unknowns are obtained in the reduced system of equations. The total computation time is of the order of 230 seconds on a 1.6 GHz laptop computer, 100 of which are dedicated to the computation of the MBFs themselves, 90 for computation of interactions in the near-field and 40 for all far-field interactions. The multipole approach has been used for interactions between MBFs as soon as the distance between antennas on which they are residing is larger than a wavelength. Once the reduced impedance matrix is obtained, all coupling coefficients, as well as all embedded element patterns can be computed almost instantly (a few seconds). Examples are provided here for uniform excitation. Fig. 4 shows results obtained for active input impedances on several rows along $\hat{x}$. The horizontal lines stand for the active input impedance obtained with the infinite-array approximation. The latter has been computed with the help of the Method of Moments [20], exploiting a rapidly converging scheme for the periodic Green's function and its gradient (the latter is necessary for the treatment of the dielectric material). It can be seen that, near the middle of the array, active impedances start resembling the infinite-array solution. However, in view of the relatively small size of the array (each array side is 2.5 wavelengths only), and given the oscillatory effects of array truncation on port currents, the infinite-array solution is a relatively poor approximation [21], such that the elements in the middle of the array are not necessarily the closest to the infinite-array solution.

Figure 5 shows the array pattern in the E-plane, obtained with the help of the FFT approach. To emphasize the effects of mutual coupling, we also show the array pattern obtained as a product between the array factor for uniform excitation and the element pattern obtained from the currents corresponding to the infinite-array solution for broadside scan. A 0.5 dB error appears at broadside and the error increases rapidly for successive side-lobes.

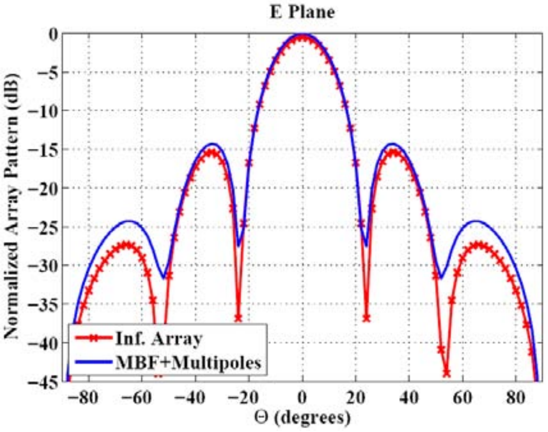

Fig. 5. Array pattern in E-plane, obtained with MBF+Multipole+FFT approach for 10×10 array and broadside scan, compared with solution assuming infinite-array currents. Wavelength: 5 cm.

IV. EXTENSION TO IRREGULAR ARRAYS

The method referred to above has been extended to irregular arrays. If N is the number of surface unknowns on the dielectric-air interface, the multipole approach presented above allows us to compute the interactions between macro basis and testing functions with complexity of the order of N instead of N^2, at least if the spacings between elements is larger than about one wavelength. If M is the number of antennas, for regular arrays, the number of different spacings to be considered for the interaction between a given pair of macro basis and testing functions is of the order of $4M$, thanks to redundance in the periodic structure. However, in general, for the irregular array, this number of interactions is again of the order of M^2, which underscores the importance of computing the interactions very fast. Besides this, for the array pattern (or embedded element pattern) evaluation, the FFT approach presented in Section 2 cannot be used directly. This point will be treated further below.

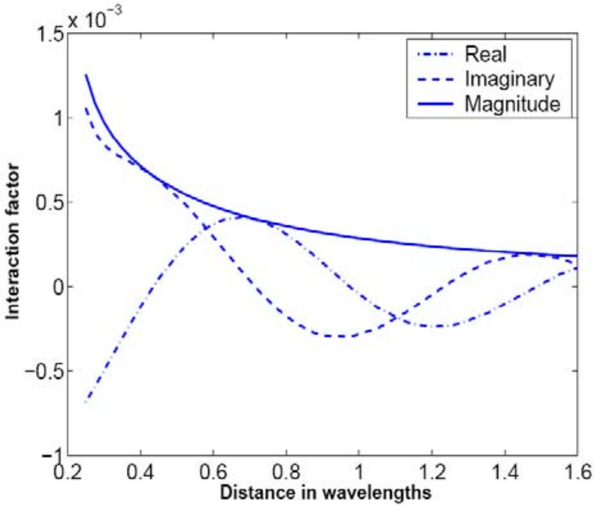

Fig. 6. Interaction factor I between two primary MBFs versus distance along y.

The Multipole approach has been applied for all pairs of elements separated by at least one wavelength, while an approach based on MoM impedance matrix calculations [6] has been used for elements placed closer to each other. For irregular arrays, this still may concern a large fraction of the pairs to be considered. Such interactions concern almost about a fourth of the interactions in the array considered below and take 20 seconds each, which is prohibitive. However, it is interesting to note that the interactions between MBFs on different antennas are a smooth function of the distance between antennas. This is illustrated in Fig. 6 for the interaction between two primaries at increasing distances along $\hat{y}$. It can be seen that this function is particularly smooth, which opens important perspectives for further acceleration of near-field interactions. A method fully exploiting this smooth behavior of near-field interactions versus distance has been initiated in [22] for the case of metallic antennas, and a more advanced version of this technique will be described in a separate publication. Active input impedances for the array configuration depicted in Fig. 7 have been computed for broadside scan at 6 GHz; results are shown in Fig. 8. The horizontal lines again stand for the infinite-array solution with 1.25 cm spacings.

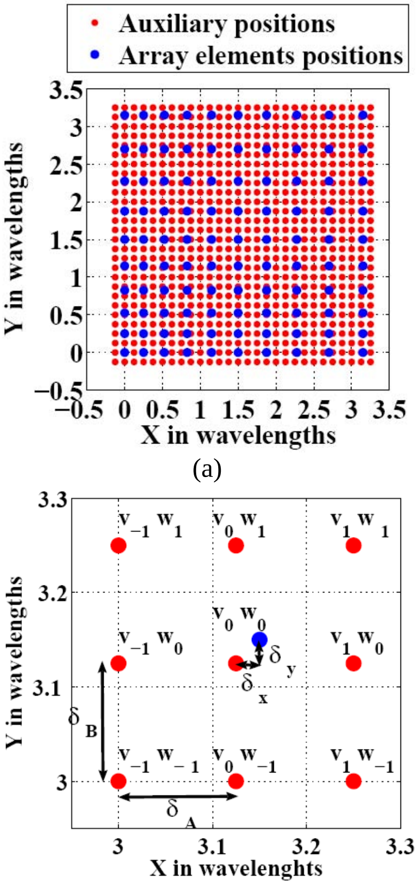

(a)

(b)

Fig. 7. Positions of elements in irregular array, and underlying finer grid used for NFFT-based pattern computations.

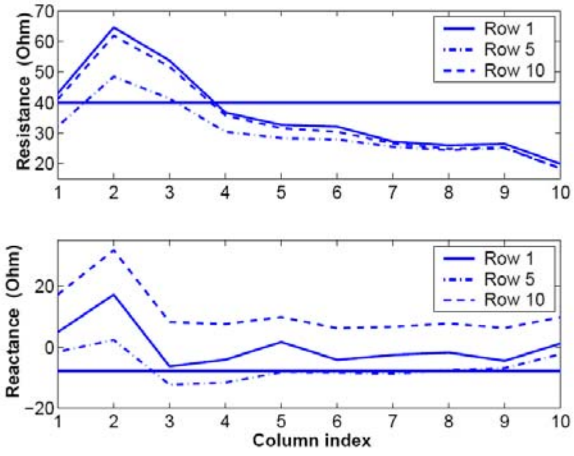

Fig. 8. Active impedances in 10×10 irregular array scanned at broadside. Horizontal lines stand for infinite-array solution. Wavelength: 5 cm. Rows are along y in Fig. 2.

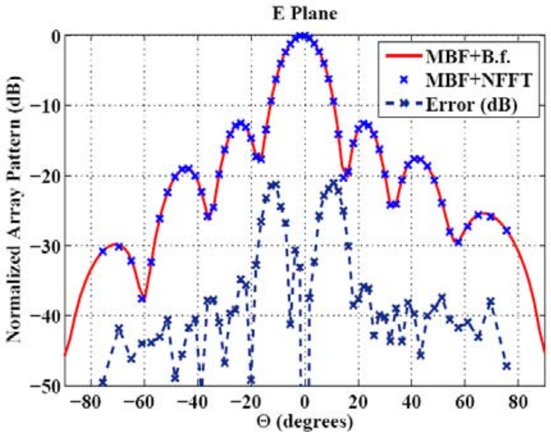

Fig. 9. Pattern of the 10×10 irregular array scanned at broadside, computed with brute-force approach and with the help of NFFT approach. The lower curve shows the errors incurred by use of NFFT with λ/8 grid and second order separable interpolation rule.

As for the pattern computations, we try to describe an equivalent uniform array for the irregular problem, such that the FFT approach still can be used in a straightforward manner. This approach can be connected to NFFT methods also applied to radar processing and medical imaging [24]. Here, a simple interpretation, inspired from interpolation methods, will be used. The phase factor associated with each element in the array factor expression depends on the element's position. In the following, it will be estimated as a linear combination, described with weights u_{ij}, of its value at a few points located around the antenna, on a regular grid. Hence, this problem is similar to a standard interpolation technique. The method amounts to distributing, for each element in the array, the MBFs coefficients onto a set of auxiliary neighbor elements located on a regular grid, as shown in Fig. 7(b), where 9 neighboring elements are considered. The distribution rule simply corresponds to the set of weights u_{ij}. The procedure to obtain the weights on the auxiliary elements with the help of a 1-D quadratic interpolation technique is illustrated in Fig. 7(b). The weight u_{ij} can be expressed as a product $u_{ij} = v_i w_j$. The weights $v_i(\delta_x)$ are computed as $v_{-1} = \delta_x^0\left(1-\delta_x^0\right)/2$,

$v_0 = 1-\left(\delta_x^0\right)^2$,

and $v_1 = \delta_x^0\left(1+\delta_x^0\right)/2$; similar expressions are used to define $\omega_j(\delta y)$. In those formulas, $\delta_x^0 = \delta_x/\delta_A$ and $\delta_y^0 = \delta_y/\delta_B$ are incremental positions on the regular grid, normalized w.r.t. the grid spacings. More sophisticated techniques may be employed to perform the aforementioned distribution [23], [25] but their evaluation is outside the scope of this paper.

Once the new coefficients and the regular grid are obtained, expression (14) can be employed again for the pattern computation. Performing the IFFT over for the auxiliary grid implies a higher computational cost, in view of the use of a finer grid: the $N\log_2 N$ complexity now becomes $CN\log_2 CN$, with C the ratio between the number of points in the fine grid and the number of antennas. However, for large arrays, this will remain competitive with the brute-force approach with complexity of the order of N^2. The proposed technique has been applied to the 10×10 array of Fig. 7(a), considering a fine grid with spacing λ/8. Results are shown in Fig. 9, together with the error incurred by the interpolation. For this example, the bruteforce solution applied to the pre-calculated MBF patterns takes 12.44 s, while the NFFT approach takes 2.23 s. Much larger time savings are expected for larger arrays.

V. CONCLUSION

A fast numerical approach, combining Macro Basis Functions and Multipole approaches, has been presented for arrays comprising dielectric elements that contain metallic parts. Once the macro basis functions have been computed, the complexity of the method no longer depends on the number of unknowns in the unit cell. The accuracy of the method has been demonstrated by comparison with a full-wave approach for a very small array. Besides this, we explained how the FFT can be exploited for the very fast estimation of radiation patterns (array patterns or embedded element patterns). This is possible thanks to the fact that the MBF approach allows us to decompose the full array pattern into a finite superposition of pattern multiplication problems. Finally, we showed that the method can be extended to the analysis of irregular arrays. In this case, more interactions need to be computed and we underscored the possibility of further acceleration by illustrating the smoothness of such interactions versus inter-element distance; we also illustrated the effectiveness of the NFFT for the fast pattern computation in the case of irregular arrays.

REFERENCES

[1] T. J. Cui, W. C. Chew, G. Chen, and J. M. Song, "Efficient MLFMA, RPFMA and FAFFA algorithms for EM scattering by very large structures," *IEEE Trans. Antennas Propag.*, vol. 52, pp. 759–770, Mar. 2004.

[2] P. Janpugdee, P. H. Pathak, P. Mahachoklertwattana, and R. J. Burkholder, "An accelerated DFT-MoM for the analysis of large finite periodic antenna arrays," *IEEE Trans. Antennas Propagat.*, vol. 54, pp. 279–283, Jan. 2006.

[3] K. Zhao and J. F. Lee, "A single-level dual rank IE-QR algorithm to model large microstrip antenna arrays," *IEEE Trans. Antennas Propagat.*, vol. 52, pp. 2580-2585, Oct. 2004.

[4] E. Suter and J. R. Mosig, "A subdomain multilevel approach for the efficient MoM analysis of large planar antennas," *Microwave Opt. Tech. Lett.*, vol. 26, pp. 270–277, Aug. 2000.

[5] L. Matekovits, G. Vecchi, G. Dassano, and M. Orefice, "Synthetic function analysis of large printed structures: The solution space sampling approach," *2001 IEEE Antennas Propagat. Soc. Int. Symp.*, Boston, pp. 568–571, Boston, June 2001.

[6] J. Yeo, V. Prakash, and R. Mittra, "Efficient analysis of a class of microstrip antennas using the Characteristic Basis Function Method (CBFM)," *Microwave Opt. Tech. Lett.*, vol. 39, pp. 456–464, Dec. 2003.

[7] X. Wan, J. Lei, and C. H. Liang, "An efficient analysis of large-scale periodic microstrip antenna arrays using the characteristic basis function method," *Prog. Eletromagn. Res.*, vol. 50, pp. 61–81, Aug. 2005.

[8] W. B. Lu, T. J. Cui, H. Zhao, "Acceleration of Fast Multipole Method for large-scale periodic structures with finite sizes using subentire- domain Basis Functions," *IEEE Trans. Antennas Propagat.*, vol. 52, pp. 414-421, Feb. 2007.

[9] L. Matekovits, V. A. Laza, and G. Vecchi, "Analysis of large complex structures with the synthetic-functions approach," *IEEE Trans. Antennas Propagat.*, vol. 55, pp. 2509-2521, Sept. 2007.

[10] R. Maaskant, R. Mittra, and A. G. Tijhuis, "Application of trapezoidal-shaped characteristic basis functions to arrays of electrically interconnected antenna elements," *Proc. of Int. Conf. Electromagn. Advanced Applications*, pp. 567-571, Torino, Sept. 17-21, 2007.

[11] C. Craeye and R. Sarkis, "Finite array analysis through combination of macro basis functions and array scanning methods," *J. of* Applied Comput. Electromagnetics Soc., vol. 23, no. 3, Sep. 2008.

[12] B. A. Munk and G. A. Burrell, "Plane-wave expansion for arrays of arbitrarily oriented piecewise linear elements and its application in determining the impedance of a single linear antenna in a lossy half-space," *IEEE Trans. Antennas Propagat.*, vol. 27, pp. 331-343, May 1979.

[13] C. Craeye, "A fast impedance and pattern computation scheme for finite antenna arrays," *IEEE Trans. Antennas Propagat.*, vol. 54, pp. 3030-3034, Oct. 2006.

[14] C. Craeye and Th. Gilles, "Combination of multipole and macro basis function approaches for the analysis of finite arrays with dielectric elements," *Proc. of 1st European Conf. Antennas Propagat.*, Nice, Nov. 2006.

[15] C. Craeye and X. Dardenne, "Fast numerical analysis of finite arrays of antennas in finite dielectric volumes," *Proc. of Int. Conf. Electromagn. Advanced Applications,* pp. 583- 586, Torino, Sept. 17-21, 2007.

[16] R. Coifman, V. Rokhlin, and S. Wandzuraz, "The fast multipole method for the wave equation: a pedestrial prescription," *IEEE Antennas Propagat. Mag.*, vol. 35, pp. 7-12, June 1993.

[17] P. Yla-Oijala, M. Taskinen, and J. Sarvas, "Surface integral equation method for general composite metallic and dielectric structures with junctions," *Progress Electromagn. Research,* vol. 52, pp. 81-108, 2005.

[18] C. Craeye, Th. Gilles and X. Dardenne, “Efficient full-wave characterisation of arrays of antennas embedded in finite dielectric volumes,” Submitted to Special Issue of *Radio Science* on 2008 EMTS Symp. in Ottawa, Dec. 2008.

[19] S. Rao, D. Wilton, and A. Glisson, “Electromagnetic cattering by surfaces of arbitrary shape,” *IEEE Trans. Antennas Propagat.*, vol. 30, pp. 409-418., May 1982.

[20] X. Dardenne, N. Gu´erin, C. Craeye, “Efficient MoM Analysis of Metamaterials Involving Dielectric Structures,” *Proc. of 23rd Ann. Rev. of Prog. Applied Comput. Electromagnetics,* Verona, March 19-23, 2007.

[21] H. Holter and H. Steyskal, “On the size requirement for finite phased-array models,” *IEEE Trans. Antennas Propagat.,* vol. 50, pp. 836-840, June 2002.

[22] D. Gonz´alez Ovejero and C. Craeye, “Fast computation of macro basis functions interactions in non uniform arrays,” *Proc. of 2008 IEEE AP Symposium*, San Diego, July 2008.

[23] A. Dutt and V. Rokhlin,“Fast Fourier transforms for nonequispaced data,” *SIAM J. Sci. Stat. Comput.,* vol. 14, no. 6, pp. 1368-1393, 1993.

[24] P. J. Beatty, D. G. Nishimura and J. M. Pauly, “Rapid gridding reconstruction with a minimal oversampling ratio,” *IEEE Trans. Med. Imag.*, vol. 24, pp. 799-808, June 2005.

[25] G. Steidl, “A note on fast Fourier transforms for nonequispaced grids,” *Adv. Comput. Math.,* vol. 9, no. 3, pp. 337-353, 1998.

Christophe Craeye was born in Belgium in 1971. He received the Electrical Engineer and bachelier in Philosophy degrees in 1994, from the Université catholique de Louvain (UCL). He received the Ph.D. degree in Applied Sciences from the same university in 1998. From 1994 to 1999, he was a teaching assistant at UCL and carried out research on the radar signature of the sea surface perturbed by rain, in collaboration with ESA and the Rain-sea interaction facility of NASA, Wallops Island (VA). From 1999 to 2001, he stayed as a post-doc researcher at the Eindhoven University of Technology, the University of Massachusetts and the Netherlands Institute for Research in Astronomy, where he worked on the numerical analysis of wideband phased arrays devoted to new generation radio telescopes (SKA project). Since 2002, C. Craeye is an Associate Professor (Chargé de Cours) at the Université catholique de Louvain. His research interests are finite antenna arrays, multiple antenna systems and numerical methods for fields in periodic media. He currently is an Associate Editor of the IEEE Transactions on Antennas and Propagation.

David Gonzalez-Ovejero was born in Gand´ıa (Valencia), Spain, in 1982. He received the Telecommunication Engineering degree from Universidad Politecnica de Valencia, in December 2005. From Jan. 2006 to Sep. 2007, he was with the Electromagnetic Radiation Group, Universidad Politecnica de Valencia, where he worked in the development of millimetre band radar antennas for IFF systems. In October 2007 he joined the Communications and Remote Sensing Lab at the Universit´e catholique de Louvain, where he is currently working toward the Ph.D. degree. His main research interests include computational electromagnetics and design of arrays for near-field detection.

Xavier Dardenne received the M.S. degree in Electrical Engineering from the Université catholique de Louvain (UCL), Louvain-la-Neuve, Belgium, in 2001. His research interests are computational electromagnetics, antenna arrays and low-profile high-gain antennas based on metamaterials. He was awarded the Ph.D. degree at UCL in March 2007 and has been working on the analysis of antenna arrays devoted to car traffic control till March 2008. He is now working with Altran Technology and Innovation Consulting.

A Mode Matching - Finite Element - Spectral Decomposition Approach for the Analysis of Large Finite Arrays of Horn Antennas

Alice Pellegrini, Stefano Bertini, Agostino Monorchio and Giuliano Manara
Microwave and Radiation Laboratory, Department of Information Engineering
University of Pisa, Italy
alice.pellegrini@iet.unipi.it, stefano.bertini@iet.unipi.it, a.monorchio@iet.unipi.it,
g.manara@iet.unipi.it

***Abstract*—** In this paper a Mode Matching / Finite Element / Spectral Decomposition (MM/FE/SD) approach is applied to the analysis of finite but large arrays of horn antennas. The proposed methodology retains advantages from the three involved techniques: the SD reduces the finite problem to a superposition of infinite periodic ones, whereas the flexibility of the FE method allows us to model complex irregular structures providing a very high degree of generality. A key step in the analysis consists of resorting to a stepped waveguide model of the longitudinal inner profile of the elementary horn antenna. The numerical efficiency of the MM procedure ensures the continuity of transverse fields over each waveguide discontinuity and over the radiating aperture. The methodology presented here is applied to array with elements arranged in polygonal shape.

***Index Terms*—** Mode Matching (MM), Spectral Decomposition (SD), Horn antenna array.

I. INTRODUCTION

A periodic array of horn antennas consists of a large number of identical radiating elements arranged in a double periodic grid. In this paper, a hybrid numerical technique, based on the Spectral Decomposition (SD) and Mode Matching/Finite Element (MM/FE) [1]-[5] method is presented for the analysis of a periodic array of horn antennas. The SD approach is used to reduce the finite large problem to a summation of infinite periodic problems through a Fast Fourier Transform (FFT) technique or by means of a Fourier closed form solution [6]. The Floquet's expansion of the electromagnetic field enables us to reduce the analysis to a single elementary radiating element and derive the solution for the other elements of the array by a proper phase shift. The longitudinal profile of the horn antenna is discretized into a series of waveguide discontinuities including the free space transition. The MM procedure provides an accurate and effective numerical modal analysis and is employed to impose the continuity of the fields at the discontinuous interfaces. Both Floquet modes and TE/TM waveguide modes have been exploited to evaluate the Generalized Scattering Matrix (GSM) of the radiating element including the radiating aperture. A two-dimensional FE with tangential vector interpolation basis functions is employed to solve the eigenvectors and eigenvalues problem. The FE method allows us to model complex and irregular structures, providing a very high degree of generality. The hybrid MM/FE/SD approach combines the three methods in order to retain the advantages of all. Comparison with available reference and other electromagnetic solver demonstrates the effectiveness of the method. This methodology reveals to be very useful when the number of elements of the array is large and full-wave three-dimensional methods become impractical due to their high numerical effort.

II. SPECTRAL DECOMPOSITION APPROACH

The MM/FE/SD method can be summarized in some fundamental main steps:

- confine the excitation in space where it exists (source windowing);
- decompose the windowed source in spectral samples via a DFT (or FFT) algorithm or by means of a closed form solution for the Fourier transform;
- solve the doubly-periodic (infinite) problem for each spectral sample with the MM/FEM approach (infinite array configuration);

- combine the above results in order to obtain the solution of the finite problem (finite array configuration).

Let us consider an array of horn antennas radiating in a given direction, where N_x and N_y represent the number of horn antennas along the $\hat{i}_x$ and $\hat{i}_y$ directions, respectively (see Fig. 1). The grid spacings are denoted by d_x and d_y, so that the total dimensions of the array are $L_x = N_x\ d_x$ and $L_y = N_y\ d_y$. Unlike the infinite array, the truncated array is no longer periodic, and it is not possible to invoke the Floquet's theorem to analyze a single elementary radiating element. In order to circumvent this difficulty, we employ the SD approach, which enables us to synthesize the solution of a finite array problem by superposing the solutions of several corresponding infinite array configuration problems.

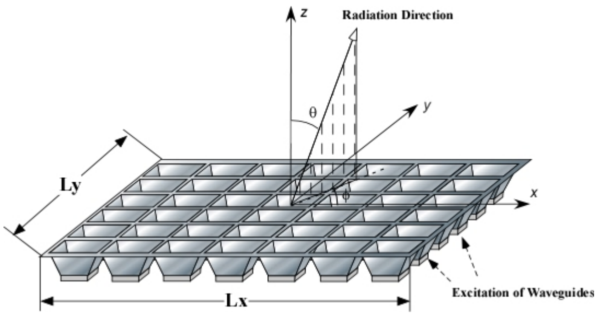

Fig. 1. Geometry and characteristic parameters of the finite array.

To this aim, the problem of a plane wave impinging on the finite array is replaced by the equivalent problem of the infinite array illuminated with an excitation confined in the working space of the array (Fig. 2). The equivalence between the above stated problem and the original one, although not strictly exact from a theoretical point of view, reveals very accurate especially when the array becomes larger and larger.

The excitation is easily represented by a two-dimensional rectangular (or polygonal) gate function $g(x,y)$ in the spatial domain. In order to apply the SD, the spectrum of the excitation $G(\beta_{kx}, \beta_{ky})$ is calculated and its numerical representation is derived via a DFT (or FFT) algorithm:

$$G(\beta_{kx},\beta_{ky})=\frac{1}{N_{Tx}N_{Ty}}\sum_{m=0}^{N_{Tx}-1}\sum_{n=0}^{N_{Ty}-1} g(x_m)g(y_n)\, e^{-j\frac{2\pi k}{N_{Tx}\Delta x}x_m} e^{-j\frac{2\pi k}{N_{Ty}\Delta y}y_n} \quad , \tag{1}$$

where $\beta_{ku}=k/(N_{Tu}\ \Delta u)$ is the discretized spectral frequency, Δu $(u=x,\ y)$ denotes the sampling interval into the spatial domain, N_{Tu} the number of samples and $u_n=n\Delta u$ represents the discretized spatial coordinate. We also note that the methodology can be extended to finite arrays with polygonal shape. In fact, when the antennas are arranged within a planar N-sided polygonal shape, the spectrum of the excitation is available in closed-form:

$$G(\beta_{ku},\beta_{kv}) = \sum_{n=1}^{N} e^{j\vec{w}\cdot\vec{\gamma}_n}\left[\frac{\hat{n}\times\hat{\alpha}_n\cdot\hat{\alpha}_{n-1}}{(\vec{w}\cdot\hat{\alpha}_n)(\vec{w}\cdot\hat{\alpha}_{n-1})}\right], \tag{2}$$

where $\vec{w}=\hat{i}_x\beta_{ku}+\hat{i}_y\beta_{kv}$, $\vec{\gamma}_n = x_n\hat{i}_x + y_n\hat{i}_y$ is the vector from origin O to corner n^{th}, $\hat{n}=\hat{i}_z$,and $\hat{\alpha}_n = \vec{\gamma}_{n+1}-\vec{\gamma}_n \big/ \left|\vec{\gamma}_{n+1}-\vec{\gamma}_n\right|$ is the tangential vector. For the sake of clarity, in Fig. 3 we represent the N-sided planar polygon.

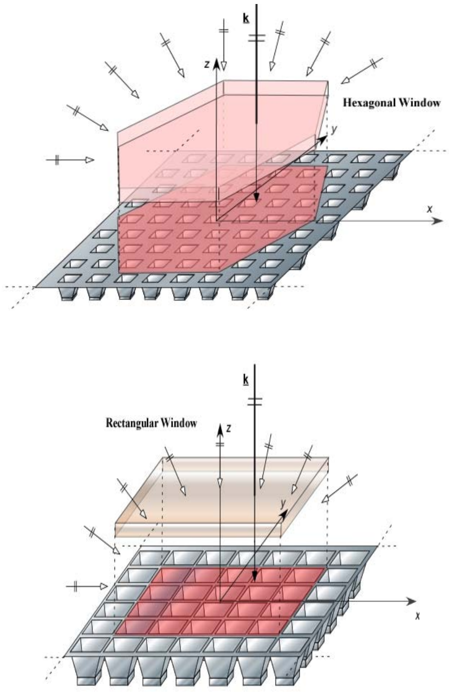

Fig. 2. Some examples of windowing functions applied to the excitation.

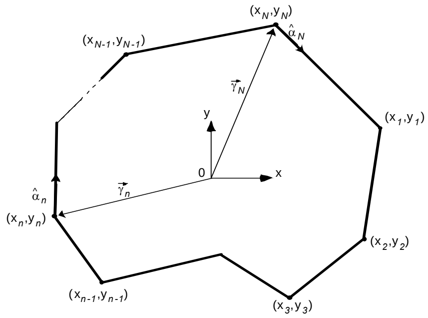

Fig. 3. *N*-sided planar polygon; $\hat{\alpha}_n$ is the tangential vector and $\hat{\gamma}_n$ describes the position of the n^{th} corner.

Each sample of the spectrum can be interpreted as an excitation of the infinite array with uniform amplitude and phase shift β_{ku}. The active reflection coefficients of the elements of the finite array can be obtained from the analysis of N_{Tu} different problems, each one corresponding to a spectral sample. The number of problems is determined by selecting the minimum number of samples required for the reconstruction of the windowing function, while avoiding the aliasing problem.

The active reflection coefficient, related to each horn antenna of the finite array, can be retrieved by applying the contribution of N_{tu} different samples as follows:

$$R(x,y) = C\sum_{i=0}^{N_{Tx}-1}\sum_{j=0}^{N_{Ty}-1} G(k_{i_x} k_{j_y}) r(k_{i_x} k_{j_y})\, e^{-jk_{i_x}x} e^{-jk_{i_y}y}, \quad (3)$$

where C denotes a normalization factor inversely proportional to the energy of the spectrum and the exponentials account for the different positions of the single horns within the array. The reflection coefficient $r(k_{ix}, k_{iy})$, relative to the elementary radiating element of the infinite array, is obtained by applying the MM/FE procedure for each incident spectral sample and accounts for all the scattering phenomena that occur over the aperture and within the inner part of the horn.

The far field radiation pattern of the entire array is evaluated as a summation of the fields radiated by each element resorting to radiation equation. To this aim, according to [7], accounting for the single infinite problem, the radiating aperture can be replaced by an equivalent magnetic surface current density radiating in unbounded free space. The magnetic surface current density for the elementary radiating horn excited by the generic sample of the spectrum of the excitation, is obtained as a weighted superimposition of the single magnetic current distributions generated by the selected N_M TE/TM Floquet's modes over the aperture:

$$\vec{M}\left(k_{i_x}, k_{i_y}\right) = \begin{cases} -2\sum_{n=1}^{N_M} t_n\left(k_{i_x}, k_{i_y}\right)\left[\hat{i}_n \times \vec{e}_n\left(\vec{p}\right)\right] & \vec{p} \in S_{Ap} \\ 0 & \vec{p} \notin S_{Ap} \end{cases}, \quad (4)$$

where S_{Ap} is the surface of the aperture, $\vec{e}_n$ is the transverse electric field related to the Floquet's mode. The weighting coefficients t_n are evaluated from the GSM of the entire radiating element, supposing that only fundamental mode is excited in the feeding waveguide section of each array element. Referring to Eq. 3-4, the distribution of the radiating surface magnetic current density for a generic m^{th} element of the array follows:

$$\vec{M}_m\left(\vec{p}\right) = \begin{cases} \sum_{i=0}^{N_{Tx}-1}\sum_{j=0}^{N_{Ty}-1} G\left(k_{i_x}, k_{j_y}\right)\vec{M}\left(k_{i_x}, k_{j_y}\right) e^{-jk_{i_x}x_m} e^{-jk_{i_y}y_m} & \vec{p} \in S_{Ap_m} \\ 0 & \vec{p} \notin S_{Ap_m} \end{cases}, \quad (5)$$

The radiated fields are then computed according to [8].

The analysis of finite arrays by means of the Spectral Decomposition method provides accurate and reliable results even if the solution is solved as a scalar 2-D problems. However, if one is interested to the solution of the radiated fields outside the principal planes as well as to the field polarization, a vector 3D problem must be considered. To this aim, a generalization to the 3D case can be derived by considering the proper polarization of the incident field. In order to ensure the correct reconstruction of the incident electromagnetic field, each spectral sample, which defines a plane wave, can be seen as a superposition of TE and TM plane waves. Then, appropriate depolarization coefficients are introduced [9], which determine a projection of the waves along the *x*, *y* and *z* axes according to the direction of the impinging wave. The active reflection coefficients depend now on both the polarization of the samples and the Floquet's expansion.

III. MODE MATCHING / FINITE ELEMENT APPROACH FOR A SINGLE HORN

Mode Matching technique is employed to efficiently compute the scattering behavior of the elementary horn antennas. A fundamental key step is the capability of MM to reduce the original three-dimensional problem into a cascaded of two-dimensional problems with a great reduction of the numerical effort. Longitudinal continuous profile is discretized into a series of subsequent waveguide discontinuities including the free space transition. As suggested in [10], a length of the waveguide sections equals to λ/32 has demonstrated as a sufficient bound to correct interpolate the continuous inner profile of the horn. At each discontinuity of the stepped waveguide model TE/TM fields are matched to evaluate the related GSM. All the matrices are then cascaded in a conventional manner in order to obtain the GSM of the inner guided part of the antenna. To account for the radiating aperture, for each sample of the spectrum of the excitation waveguide modes are matched with Floquet modes to compute scattering parameters. The coupling of the previous GSMs furnishes the scattering behavior of the elementary antenna horn taking into account the mismatch between waveguide and free space propagation regions.

IV. NUMERICAL RESULTS

As previously mentioned, the proposed approach can efficiently take into account complex configurations and devices with large dimensions considerably reducing the computational time with respect to fully three-dimensional approach. In order to demonstrate the effectiveness of the method, a comparison is made with the results obtained through the commercial software ANSOFT HFSS$^{v10.1}$ as well as some results found in open literature. As a first example, we propose a comparison with the results obtained with the Truncated Floquet Wave Full-Wave (T(FW)^2) [11]. The data are relevant to a 20×20 array of open-ended rectangular waveguides with periodicities T_x=18.84 *mm* and T_y=8.7 *mm* (TE polarization case). The elements have dimension a=17.142 *mm*, b=7.62 *mm* and the analysis is performed at frequency f=10 *GHz*. In Figs. 4 and 5 the active reflection coefficient and the radiation pattern on E-plane are shown respectively. In the case of array of open-ended truncated waveguides MM procedure is performed only over the radiating aperture.

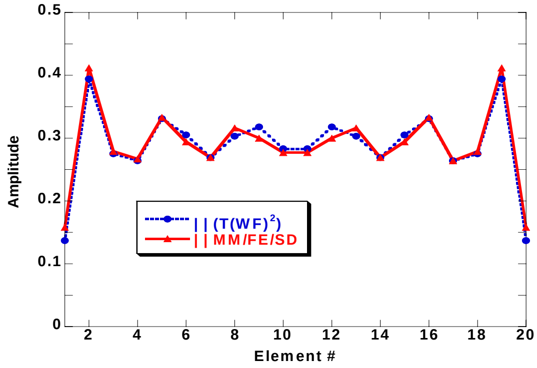

Fig. 4. Array of 20×20 open-ended rectangular waveguides compared with [11]: amplitude of active reflection coefficient relevant to one of the two central columns of the array.

Good accordance is obtained for reflection coefficient, while the far field pattern shows a mismatch especially for wide scan angles. This is probably due to a not correct reconstruction of the fringe currents by the MM/FE/SD approach. Indeed, in the presented procedure there is not any contribution or correction factor taking into account the diffraction effects produced by the edges or corners.

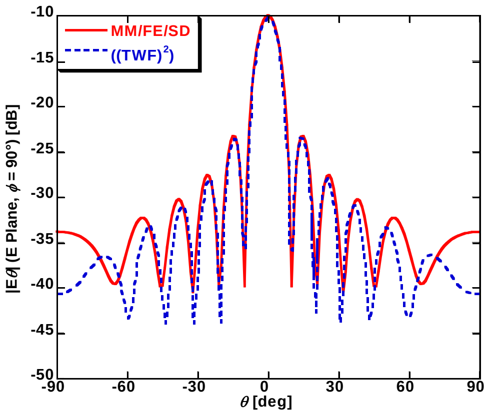

Fig. 5. Array of 20×20 open-ended rectangular waveguides compared with [11]: E-plane radiation pattern.

In Fig. 6 and Fig. 7, results are proposed for an array of previously mentioned truncated rectangular waveguides now arranged in a 6×6 spatial grid. The dimensions of the single unit element are the same as in the previous example.

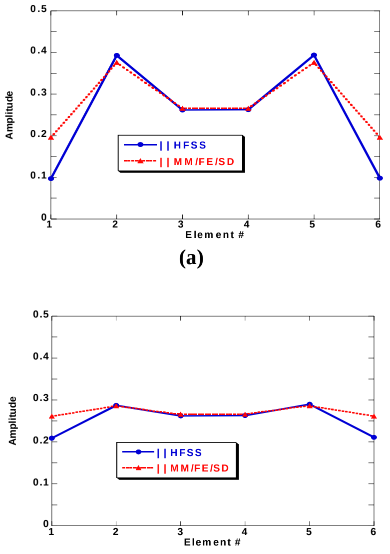

(a)

(b)

Fig. 6. Amplitude of active reflection coefficient for array of 6×6 open-ended waveguides compared with Ansoft HFSS: a) one of the two central columns, b) one of the two central rows.

Results show a good match with simulations performed by HFSS, proving the effectiveness of the proposed approach in the analysis of smaller array configurations.

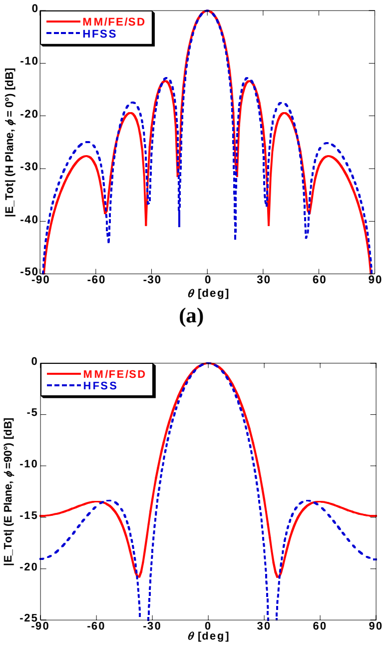

(a)

(b)

Fig. 7. Normalized radiation patterns of the 6×6 open-ended rectangular waveguide array compared with Ansoft HFSS: a) H-plane pattern, b) E-plane pattern.

If horn antennas are now considered as radiating elements the overall procedure is modified only by extending the MM procedure to the scattering analysis of the inner profile of the elementary horn antenna. As a first example the analysis has been performed at a frequency $f=15\,GHz$, and the data are relevant to a 6×6 array of pyramidal horn antennas arranged with periodicities $T_x=18.84\,mm$ and $T_y=8.7\,mm$. The feeding waveguides have dimensions $a_1=11.428\,mm$ and $b_1=5.08\,mm$ and the radiating apertures have dimensions $a_2=17.142\,mm$ and $b_2=7.62\,mm$, the longitudinal length $l=20\,mm$ (Fig. 8). The continuous internal shape has been arranged in a 32 cascaded waveguide discontinuities and only the fundamental exciting mode TE_{10} has been considered in the feeding waveguide section.

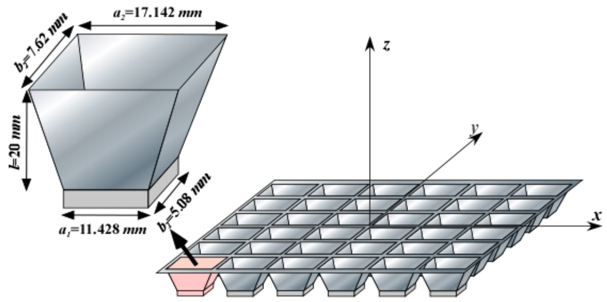

Fig. 8. Geometry of the array and dimensions of the elementary radiating element.

In Fig. 9, the magnitude of the active reflection coefficient evaluated along one of the two central columns of the array is shown. In Fig. 10, the normalized radiation patterns over principal planes are reported, all the results are compared with Ansoft HFSS, showing good agreement in the main beams region and the previous mentioned mismatch for wide scan angles.

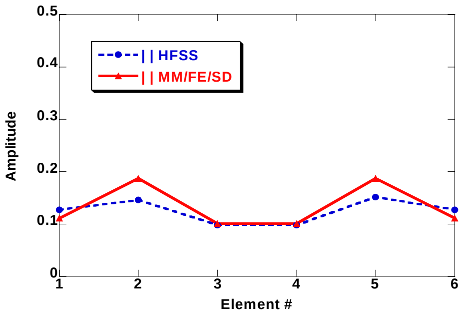

Fig. 9. Comparison with Ansoft HFSS: active reflection coefficient along one of the two central columns for the 6×6 array of pyramidal horns.

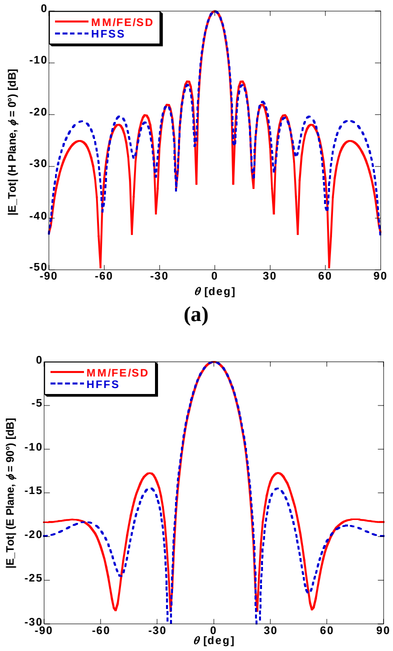

(a)

(b)

Fig. 10. Normalized radiation patterns of the 6×6 pyramidal horn array compared with Ansoft HFSS: a) H-plane pattern, b) E-plane pattern.

Another example shows the active reflection coefficient evaluated for an hexagonal array of horn antennas, operating at a frequency of 15 *GHz*. The geometry of the structure is depicted in Fig. 11. The radiating horns have the same dimensions of the previous example. The periodicity is T_x=28.57 *mm* and T_y=17.142 *mm* with a skewness angle α=50.194°. Due to the geometrical symmetry of the structure, the active reflection coefficient is shown in Fig. 11, only for the apertures belonging to the first quadrant.

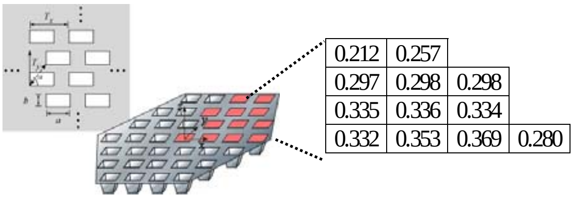

0.212	0.257		
0.297	0.298	0.298	
0.335	0.336	0.334	
0.332	0.353	0.369	0.280

Fig. 11. Geometry of the hexagonal array and magnitude of the active reflection coefficients belonging to the first quadrant.

Finally, in Table I we show the computational time and the memory usage for the proposed MM/FE/SD technique compared against Ansoft HFSS $^{v10.1}$ for the array cases proposed in Fig. 6 and Fig. 8, respectively. Simulations have been performed on a PC with AMD ATHLON XP2400 2.4 *GHz* processor with 2 GB RAM. As apparent, the proposed MM/FE/SD technique permits a time saving of more than 50% in both cases and a considerable memory saving.

Table 1: Comparison between computational time and memory usage for the proposed MM/FE/SD and Ansoft HFSS $^{v10.1}$.

	MM/FE/SD (Time/ Memory)	**HFSS** (Time/ Memory)
Array of 6×6 truncated rectangular waveguides (Fig. 6)	75 min./11.3 MB	164 min./1.29 GB
Array of 6×6 pyramidal horns (Fig. 8)	75 min./11.3 MB	205 min./1.394 GB

V. CONCLUSION

A hybrid Mode Matching / Finite Element / Spectral Decomposition (MM/FE/SD) approach for analyzing finite but large arrays of horn antennas has been presented in this paper. The SD approach enabled us to analyze the finite problem by a superposition of equivalent infinite periodic ones. For each infinite problems Floquet's theorem allowed us to compute the GSM of the elementary radiating element, accounting the radiating aperture, by employing a MM/FE technique. The problem where horn antennas are present, has been addressed by discretizing the longitudinal continuous profile into a series of subsequent waveguide discontinuities including the free space transition. A step of λ/32 has been chosen in order to ensure the correct reconstruction of the inner profile. Several representative numerical examples have been presented to demonstrate the accuracy and efficiency of the method.

REFERENCES

[1] M. A. Gonzales de Aza, J. A. Encinar and J. Zapata, "Radiation pattern computation of cavity-backed and probe-fed stacked microstrip patch arrays, " *IEEE Trans. Antennas Propagat.*, vol. 48, no. 4, pp. 502-509, April 2000.

[2] J. Rubio, M.A. Gonzalez, and J. Zapata, "Generalized-scattering-matrix analysis of a class of finite arrays of coupled antennas by using 3-D FEM and spherical mode expansion," *IEEE Trans. Antennas Propagat.*, vol. 53, no. 3, pp. 1133–1144, March 2005.

[3] P. Grassi, D. Arena, A. Monorchio, and G. Manara, “Analysis of inhomogeneously filled waveguide devices by a hybrid mode matching-finite element technique,” *Proc. of 2003 IEEE APS Intern. Symp.*, June 22-27, vol. 2, pp. 161-164, 2003.

[4] D. Arena, M. Ludovico, G. Manara, and A. Monorchio, “Analysis of waveguide discontinuities using edge elements in a hybrid mode matching/finite elements approach,” *IEEE Micro. Wireless Comp. Lett.*, vol. 11, no. 9, pp. 379-381, Sept. 2001.

[5] A. Monorchio, P. Grassi, and G. Manara, “A hybrid mode-matching finite-elements approach to the analysis of thick dichroic screens with arbitrarily shaped apertures,” *IEEE Antennas Wireless Propagat. Lett.*, vol. 1, no. 5, pp. 120-123, 2002.

[6] S. Lee and R. Mittra, “Fourier transform of a polygonal shape function and Its application in electromagnetics,” *IEEE Trans. Antennas Propagat.*, vol. 31, no. 1, pp. 99-103, Jan. 1983.

[7] C. A. Balanis, *Advanced Engineering Electromagnetics*, John Wiley & Sons, Chapter 7, pp. 329-334, 1989.

[8] C. A. Balanis, *Advanced Engineering Electromagnetics*, John Wiley & Sons, Chapter 6, pp. 285-291, 1989.

[9] V. V. S. Prakash and R. Mittra, “Convergence studies of plane-wave spectral expansion technique for analyzing truncated frequency selective surfaces,” Microwave and Optical Technology Letters, vol. 34, no. 6, pp. 417–421, September 2002.

[10] K. Liu, C. A. Balanis, C. R. Birtcher, and G. C. Barber, “Analysis of pyramidal horn antenna using moment methods,” *IEEE Trans. Antennas Propagat.*, vol. 41, no. 10, pp. 1379-1389, Jan. 1983.

[11] A. Cucini, M. Albani, and S. Maci, “Truncated Floquet wave Full-wave (T(FW)2) analysis of large periodic arrays of rectangular waveguides,” *IEEE Trans. Antennas Propagat.*, vol. 51, no. 6, pp. 1373-1385, June 2003.

Alice Pellegrini received the Master Degree in Telecommunication Engineering at University of Pisa (Italy), in 2005. She is currently enrolled in the “Information Technology” PhD program at the Microwave and Radiation Laboratory, Department of Information Enginnering, at the same University of Pisa. From March to July 2008, she was a Visiting Ph.D Researcher at the Electromagnetic Communication Laboratory, Penn State University, State College. Her primary research interests include numerical GSM-based methods for the electromagnetic analysis and design of truncated periodic structures.

Stefano Bertini received the Laurea degree in telecommunication engineering from the University of Pisa, Pisa, Italy in 2005. In October 2005, he joined the Microwave and Radiation Laboratory, Department of Information Enginnering, University of Pisa, where he is currently enrolled in the Ph.D program. From March to July 2008, he was a Visiting Ph.D Researcher at the Electromagnetic Communication Laboratory, Pennsylvania State University, University Park. His reasearch interests include frequency domain numerical methods for solving aperture antennas electromagnetic problems and high-frequency derived approach for electromagnetic propagation in complex environments.

Agostino Monorchio received the Laurea degree in electronics engineering and the Ph.D. degree in methods and technologies for environmental monitoring from the University of Pisa, Pisa, Italy, in 1991 and 1994, respectively. During 1995, he joined the Radio Astronomy Group, Arcetri Astrophysical Observatory, Florence, Italy, as a Postdoctoral Research Fellow, working in the area of antennas and microwave systems. He has been collaborating with the Electromagnetic Communication Laboratory, Pennsylvania State University (Penn State), University Park, where he is an Affiliate of the Computational Electromagnetics and Antennas Research Laboratory. He has been a Visiting Scientist at the University of Granada, Spain, and at the Communication University of China in Beijing. He is currently an Associate

Professor in the School of Engineering, University of Pisa, and Adjunct Professor at the Italian Naval Academy of Livorno. He is also an Adjunct Professor in the Department of Electrical Engineering, Penn State. He is on the Teaching Board of the Ph.D. course in "Remote Sensing" and on the council of the Ph.D. School of Engineering "Leonardo da Vinci" at the University of Pisa. His research interests include the development of novel numerical and asymptotic methods in applied electromagnetics, both in frequency and time domains, with applications to the design of antennas, microwave systems and RCS calculation, the analysis and design of frequency-selective surfaces and novel materials, and the definition of electromagnetic scattering models from complex objects and random surfaces for remote sensing applications.

Giuliano Manara was born in Florence, Italy, on October 30, 1954. He received the Laurea (Doctor) degree in electronics engineering (*summa cum laude*) from the University of Florence, Italy, in 1979. Currently, he is a Professor at the College of Engineering of the University of Pisa, Italy. Since 2000, he has been serving as the President of the Bachelor and the Master Programs in Telecommunication Engineering at the same University. Since 1980, he has been collaborating with the Department of Electrical Engineering of the Ohio State University, Columbus, Ohio, where, in the summer and fall of 1987, he was involved in research at the ElectroScience Laboratory. His research interests have centered mainly on the asymptotic solution of radiation and scattering problems to improve and extend the uniform geometrical theory of diffraction. In this framework, he has analyzed electromagnetic wave scattering from material bodies, with emphasis on the scattering from both isotropic and anisotropic impedance wedges. He has also been engaged in research on numerical, analytical and hybrid techniques (both in frequency and time domain), scattering from rough surfaces, frequency selective surfaces (FSS), and electromagnetic compatibility. More recently, his research has also been focused on the design of microwave antennas with application to broadband wireless networks, and on the development and testing of new microwave materials (metamaterials). Prof. Manara was elected an IEEE Fellow in 2004 for "contributions to the uniform geometrical theory of diffraction and its applications." Since 2000, he has been serving as the Secretary/Treasurer of the Italian Society on Electromagnetics (Società Italiana di Elettromagnetismo, SIEm). Since 2002, he has been working as a member of the IEEE Italy Section Executive Committee. In May 2004, Prof. Manara co-chaired the International Symposium on Electromagnetic Theory of Commission B of the International Union of Radio Science (URSI). He also served as a Convenor for several URSI Commission B international conferences, and URSI General Assemblies. In August 2008, he has been elected Vice-Chair of the International Commission B of URSI.

Iterative Physical Optics for Radar Scattering Predictions

Robert J. Burkholder [1], Çağatay Tokgöz [2], C. J. Reddy [2], and William O. Coburn [3]
[1] Department of Electrical and Computer Engineering
The Ohio State University, Columbus, OH 43212, USA
burkholder.1@osu.edu

[2] Applied EM, Inc., Hampton, VA 23666, USA
cagatay@appliedem.com, cjreddy@appliedem.com

[3] U. S. Army Research Laboratory, Aberdeen Proving Ground, MD, USA
wcoburn@arl.army.mil

***Abstract*—** The iterative physical optics (IPO) method is applied to compute the radar cross section of electrically large and realistically complex targets. The method is based on iterative refinement of the first-order physical optics currents to include multiple interactions up to a specified order. Unlike other high-frequency asymptotic methods, no ray tracing is required, and spurious diffraction effects from non-physical shadow boundaries are avoided. Numerical results are presented to demonstrate convergence, accuracy, efficiency and robustness.

***Index Terms*—** Physical optics, radar cross section, iterative methods, integral equations, high-frequency methods.

I. INTRODUCTION

The prediction of the radar cross section (RCS) of realistic targets remains a computational challenge due to the large size and complexity of aircraft, ships and ground vehicles. It is of considerable interest to develop efficient, robust and accurate computational electromagnetic (EM) methods to address this problem. In this article, the iterative physical optics (IPO) technique, previously developed for jet inlet scattering, is adapted to more general computer-aided design (CAD) geometries [1-3].

In the past, both numerical and ray tracing methods have been applied to RCS prediction. Numerical methods such as the method of moments (MoM) and the finite element-boundary integral (FE-BI) method are very accurate and reasonably robust for analyzing faceted CAD geometries [4,5]. However, the computational cost becomes extremely high for the electrically large problems that are typically of interest for radar scattering. For example, a fighter-size aircraft is on the order of a thousand wavelengths in length at X-band frequencies. A surface mesh of such a target requires upwards of 10 million unknowns. This size of problem has been solved by using the multi-level fast multi-pole algorithm, but requires massive parallel computing resources and a highly sophisticated software implementation [6]. Similarly, a volume mesh for finite element based methods typically requires hundreds of millions of unknowns. While domain decomposition methods for the FEM have come a long way in providing sparser matrices [7] and some very large problems have been solved [8], such solutions are still far from routine for most RCS engineers.

Physical optics (PO) based methods have provided engineers with a useful alternative to numerical methods for generating fast results, but at the cost of decreased accuracy. First-order PO includes the direct reflection and diffraction by the target from the PO approximation of the induced surface currents, as illustrated in Fig. 1(a). Only the optically lit part of the geometry has non-zero currents. It is noticed from Fig. 1(a) that this introduces abrupt shadow boundaries that, when integrated, give rise to false edge diffraction effects. It is also noticed that the strong double-bounce from the dihedral corner reflector is not included in the first-order PO.

1054-4887 © 2009 ACES

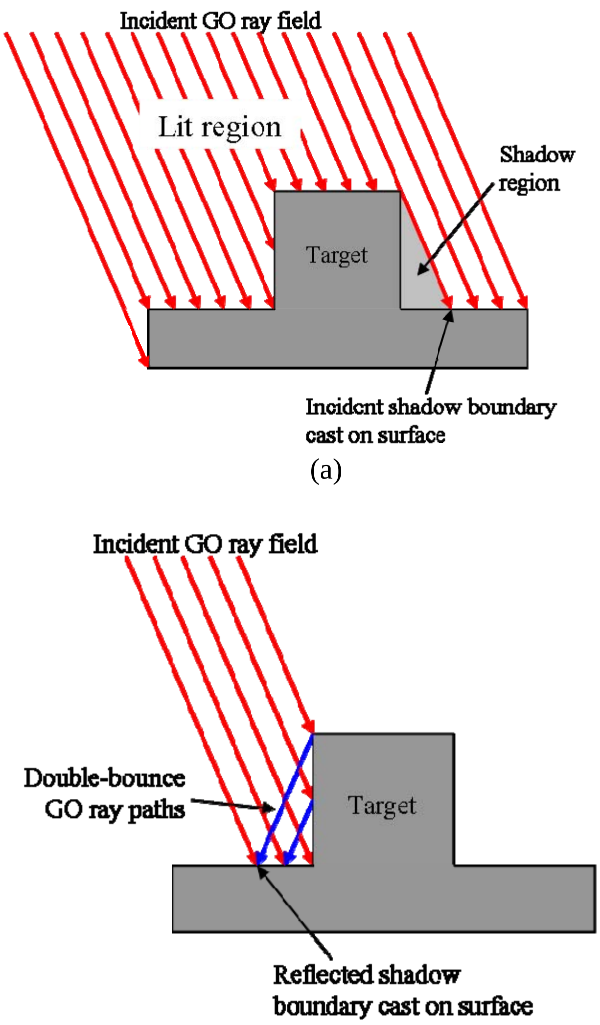

(a)

(b)

Fig. 1. GO/PO illumination of a multi-bounce RCS target: (a) First-order PO ray paths due to plane wave illumination on an RCS target. (b) Double-bounce ray paths associated with an RCS target.

To add multi-bounce effects, geometrical optics (GO) has been combined with PO in the shooting and bouncing ray (SBR) method [9], or GO/PO [10-12]. It is interesting to note that the SBR method was also originally developed for cavity scattering, similar to IPO. The incident field is represented as a set of GO rays which are launched at the target and traced through multiple reflections. At each bounce point, the ray footprint is integrated via PO [13]. This is the method used in the popular Xpatch suite of codes [14]. Figure 1(b) illustrates the strong double-bounce mechanism associated with the target which would be included by using SBR. However, it is noticed that the first GO bounce gives rise to another abrupt shadow boundary on the second surface which also gives rise to a false diffraction. In reality, these shadow boundaries are smoothed out by the continuous nature of the EM field as explained by the uniform geometrical theory of diffraction (UTD) [15]. The false diffractions in the SBR method can be misinterpreted as real scattering centers by target recognition algorithms [16].

IPO provides a way to include multi-bounce while not introducing false shadow boundaries. It does not use ray tracing and can be applied to general faceted CAD geometries. It is not quite as efficient as ray based methods since it requires integration, but it is far more efficient than numerical methods because the mesh density is coarser, only a certain percentage of the total surface area will be excited and simultaneous solution of matrix equations is not required. The basic approach is to start with first-order PO currents ignoring shadowing effects, and iteratively integrating the currents by using a simple facet visibility check. The iteration is halted after a prescribed number of bounces is reached or the IPO currents converge. The algorithm is described in Section II and implementation techniques are discussed in Section III. The convergence and accuracy of the method are demonstrated in the numerical results of Section IV.

II. THE IPO ALGORITHM

As its name implies, IPO iteratively refines the PO currents to account for multiple reflections and diffractions within the high-frequency asymptotic assumptions of PO. It is assumed that the target is a perfect electric conductor (PEC), but the formulation can be easily modified for impenetrable material surfaces [3,17]. In the following, an $e^{j\omega t}$ harmonic time convention is assumed and suppressed where ω is the radian frequency of the incident EM wave. The ambient medium is free space with EM wave number, $k = \omega / c$, where c is the speed of light in free space.

Consider the plane wave scattering problem shown in Fig. 2(a). The PO approximation is based on the magnetic field integral equation [4]. The equivalent current at a point $\mathbf{r}$ on the surface S of the target is found by solving the following MFIE,

$$\mathbf{J}(\mathbf{r}) = 2\hat{\mathbf{n}} \times \mathbf{H}^i(\mathbf{r}) + 2\hat{\mathbf{n}} \times \mathbf{H}(\mathbf{J}), \qquad (1)$$

where $\mathbf{H}^i(\mathbf{r})$ is the incident magnetic field and $\hat{\mathbf{n}}$ is the outward-pointing unit normal vector. **H**(**J**) is the principal value magnetic field radiation integral given by,

$$\mathbf{H}(\mathbf{J}) = \mathrm{P}\int_S \mathbf{J}(\mathbf{r}') \times \hat{\mathbf{R}}' \frac{e^{-jkR'}}{4\pi R'}\left(jk + \frac{1}{R'}\right) dS', \qquad (2)$$

where $\mathbf{R}' = \mathbf{r} - \mathbf{r}'$, $R' = |\mathbf{R}'|$ and $\hat{\mathbf{R}}' = \mathbf{R}'/R'$. The primed quantities represent variables of integration. Figure 2(b) shows the equivalent current representation of the scattering problem. The currents radiate the scattered fields $(\mathbf{E}^s, \mathbf{H}^s)$ in free space.

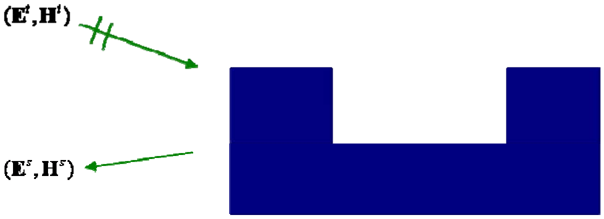

(a) Plane wave scattering problem.

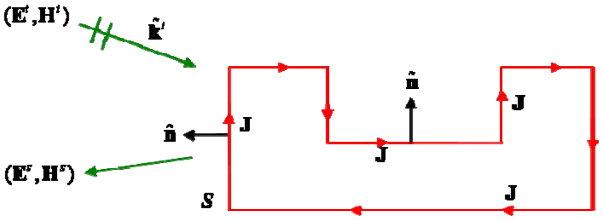

(b) Equivalent currents radiating in free space.

Fig. 2. Equivalent current representation of the plane wave scattering from a simple concave geometry.

The first-order PO approximation used here is,

$$\mathbf{J}^{(0)}(\mathbf{r}) = \begin{cases} 2\hat{\mathbf{n}} \times \mathbf{H}^i(\mathbf{r}) : \hat{\mathbf{n}} \cdot \hat{\mathbf{k}}^i < 0 \\ 0 \quad : \hat{\mathbf{n}} \cdot \hat{\mathbf{k}}^i \geq 0 \end{cases}, \qquad (3)$$

where $\hat{\mathbf{k}}^i$ is the unit propagation vector of the incident plane wave. It is noted that the first-order currents are non-zero only where the unit normal vector is facing towards the incident plane wave, regardless of any intervening geometry. In the classical PO method, shadowing by other portions of the surface must be taken into account as shown in Figure 1(a). In IPO, only the facing direction of each facet is checked relative to the direction of incidence. This obviously puts first-order currents inside the incident shadow region where they do not belong, as shown in Figure 3(a) on surface, S_2. However, this is only the initial set of currents for the IPO algorithm.

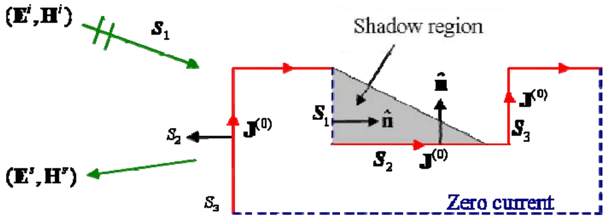

(a) Initial IPO currents.

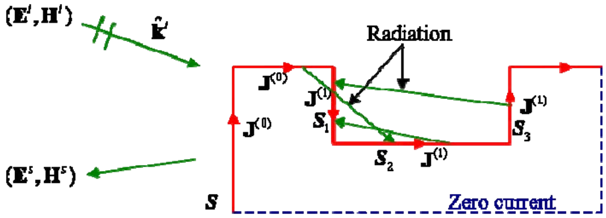

(b) IPO currents after the first iteration.

Fig. 3. IPO currents on a concave structure.

The IPO algorithm solves the modified PO equivalent of the MFIE of (1) as,

$$\mathbf{J}(\mathbf{r}) = \mathbf{J}^{(0)}(\mathbf{r}) + 2\hat{\mathbf{n}} \times \mathbf{H}_{IPO}(\mathbf{J}), \qquad (4)$$

where the IPO definition of the magnetic field radiation integral is given by,

$$\mathbf{H}_{IPO}(\mathbf{J}) = \mathrm{P}\int_{\hat{\mathbf{n}}\cdot\hat{\mathbf{R}}'<0} \mathbf{J}(\mathbf{r}') \times \hat{\mathbf{R}}' \frac{e^{-jkR'}}{4\pi R'}\left(jk + \frac{1}{R'}\right) dS'. \qquad (5)$$

It is noticed that this is the same as (2), but the integration is only over the portion of the surface where $\hat{\mathbf{n}} \cdot \hat{\mathbf{R}}' < 0$, which is the *IPO shadowing rule*. This rule is applied only to test points on the surface. By definition the equivalent currents radiate in free space regardless of which way they are facing. The IPO shadowing rule is one property that makes IPO much more efficient than the conventional MoM, because only a small fraction of the whole surface radiates to a given test point on the surface.

Classical Jacobi iteration may be used to solve (4) [18]. At the q^{th} iteration the currents are given by

$$\mathbf{J}^{(q)}(\mathbf{r}) = \mathbf{J}^{(0)}(\mathbf{r}) + 2\hat{\mathbf{n}} \times \mathbf{H}_{IPO}(\mathbf{J}^{(q-1)}) . \qquad (6)$$

Accordingly, the currents for the first iteration shown in Figure 3(b) are given by,

$$\mathbf{J}^{(1)}(\mathbf{r}) = \mathbf{J}^{(0)}(\mathbf{r}) + 2\hat{\mathbf{n}} \times \mathbf{H}_{IPO}(\mathbf{J}^{(0)}) . \qquad (7)$$

As the radiation arrows show, the first-order currents on the lit outer surface of the target radiate to the concave part on S_1, S_2 and S_3. This radiation tends to cancel the incident field on S_2, thus filling in the shadow region with a continuous field. The original currents on S_2 and S_3 also radiate into the concave region. However, these currents do not radiate to the outer surface because of the IPO shadowing rule.

As the iteration is continued, the currents in the concave region will eventually converge. The iteration may be halted after a prescribed number of interactions are included, or a convergence criterion is reached. A useful error convergence definition is,

$$\frac{\left\| \mathbf{J}^{(q)} - \mathbf{J}^{(q-1)} \right\|}{\left\| \mathbf{J}^{(0)} \right\|} < \varepsilon , \qquad (8)$$

assuming $\left\| \mathbf{J}^{(0)} \right\| > 0$. Alternatively, the convergence of the scattered field may be monitored.

Each iteration of the IPO algorithm essentially adds another multi-bounce term. Thus, IPO intrinsically includes an arbitrary number of interactions, and shadow regions are filled in without abrupt shadow boundaries. If the algorithm diverges for some cases, a relaxed Jacobi version of (7) may be used as,

$$\mathbf{J}^{(q)}(\mathbf{r}) = \frac{1}{2}\mathbf{J}^{(0)}(\mathbf{r}) + \frac{1}{2}\mathbf{J}^{(q-1)} + \hat{\mathbf{n}} \times \mathbf{H}_{IPO}(\mathbf{J}^{(q-1)}) . \qquad (9)$$

In fact, there are many forms of classical iterative algorithms that have been found to work well with IPO, such as Gauss-Seidel and successive over-relaxation [18]. A forward-backward version of IPO (FBIPO) was presented for inlet cavity scattering in [3]. That version was found to have the best convergence for geometries with a very high degree of multi-bounce. FBIPO is technically the same as the method of symmetric successive over-relaxation. Krylov subspace methods based on minimizing the residual error of the matrix equation have also been investigated [2]. However, these methods have not been successful with IPO because the IPO operator of (5) is not analytic due to the IPO shadowing rule. Also, the simple physical interpretation of IPO is lost on such methods.

III. IMPLEMENTATION

PO currents by nature do not have the strong singularities that may be present in MoM solutions, and hence, the radiation integral of (5) may be evaluated numerically by point sampling. This makes the IPO method easy to implement on faceted CAD geometries if the surface mesh is made on the order of the required numerical sampling density. Then, only one point per facet is needed. Because of the smoothness of the PO currents, it has been found that a sampling density of 9 to 16 points per square wavelength yields very good accuracy [1]. This is in contrast to MoM and FEM discretization which typically requires a minimum sampling density of 64 to 100 points per square wavelength.

With point sampling of the currents and point-wise numerical integration, it is easy to evaluate (6) as

$$\mathbf{J}^{(q)}(\mathbf{r}_m) = \mathbf{J}^{(0)}(\mathbf{r}_m) + \sum_{n=1}^{N} 2A_n \hat{n} \times \left[\mathbf{J}^{(q-1)}(\mathbf{r}_n) \times \hat{\mathbf{R}}_{mn} \right] \cdot \frac{e^{-jkR_{mn}}}{4\pi R_{mn}} \left(jk + \frac{1}{R_{mn}} \right) \Bigg|_{\substack{n \neq m \\ \hat{\mathbf{n}} \cdot \hat{\mathbf{R}}_{mn} < 0}} , \qquad (10)$$

where A_n is the area of the n^{th} facet, $\mathbf{r}_n$ is the vector to the center of the n^{th} facet and $\mathbf{R}_{mn} = \mathbf{r}_m - \mathbf{r}_n$. It is possible to rewrite (10) in matrix format in order to store a system matrix. However, since there may be a very large number of facets and the expression in the summation does not require numerical integration of a basis function, it has been found to be more practical to recompute the terms on the fly for each iteration. The extra cost of this operation is ameliorated by performing the iterative solution for multiple excitations simultaneously. Then, only the currents themselves need to be stored. Therefore, the memory requirement is O(N).

Fast Far-Field Approximation

The computational cost of the operation of (10) is still O(N^2), even though only a fraction of the facets contribute to any given test point. To reduce the cost to O($N^{3/2}$), the fast far-field approximation (FaFFA) [19] may be applied as described in [2]. Similar to the fast multi-pole method [20], the geometry is broken up into small groups of facets. Contributions from receiving groups that are in the far-field of the transmitting group are computed by using the far-field approximation which naturally factorizes the Green's function in the radiation kernel. The interactions between near-field groups are computed in the usual fashion. FaFFA has been found to reduce the computation time by an order of magnitude in practical applications.

Model Based Parameter Estimation

The efficiency of IPO for RCS pattern computations has been further improved by using it in conjunction with adaptive Model Based Parameter Estimation (MBPE) for fast angle or frequency sweeps [21]. MBPE has been used to accelerate the RCS computation when only an angle or frequency is swept. When MBPE is used, the coefficients of the surface currents are approximated by a ratio of M^{th} and N^{th} order polynomials as

$$c(\alpha) \approx \frac{\sum_{m=0}^{M} a_m \alpha^m}{1+\sum_{n=1}^{N} b_n \alpha^n}, \qquad (11)$$

where α is the angle or frequency that is swept, $c(\alpha)$ is a surface current coefficient, and a_m and b_n are unknowns to be determined. Since there are $L = M + N + 1$ unknowns, values of each surface current coefficient are evaluated at L sample points uniformly distributed within the range of α to solve for these unknowns. After the unknowns are determined, RCS values computed by using (11) and those obtained without MBPE are compared at midpoints between sample points to check the accuracy of the MBPE implementation. If the MBPE implementation is not sufficiently accurate in magnitude and phase at all the midpoints, the range of α is divided into two equal subintervals, and MBPE is applied in each subinterval again. This procedure of dividing each interval into two equal subintervals, applying MBPE in each subinterval and checking the accuracy at midpoints of all MBPE subintervals is adaptively repeated until the desired accuracy is achieved at all the midpoints. The adaptive MBPE algorithm is illustrated in Fig. 4.

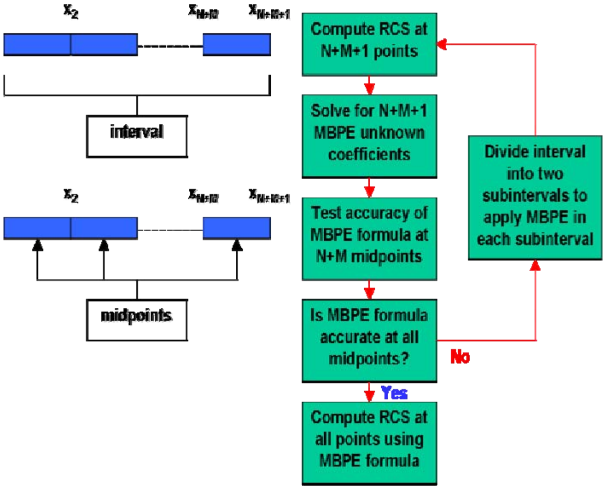

Fig. 4. Adaptive MBPE algorithm.

An RCS prediction code named rcsASET was developed based on IPO. The rcsASET code was parallelized with Message Passing Interface (MPI) and ported to SGI, IBM and Linux platforms at the Major Shared Resource Center (MSRC) of the U.S. Army Research Laboratory (ARL). The code was validated, and its efficiency and accuracy in RCS computation were demonstrated by computing the RCS of several benchmark targets for various frequencies and scattering angles, and comparing the results with those generated by using other software or measured data. In summary, the IPO method gets its efficiency from the following factors:

1. Memory requirement is O(*N*),
2. IPO shadowing rule greatly reduces the number of facet-to-facet interactions,
3. Numerical sampling density is only 9 to 16 points per square wavelength,
4. Number of iterations is related to the number of significant multi-bounce terms,
5. Fast far-field approximation accelerates summations,
6. Model based parameter estimation minimizes the number of RCS pattern points,
7. Parallelization helps reduce the computation time.

These properties allow the IPO method to routinely handle RCS problems involving electrically large and realistically complex structures.

IV. NUMERICAL RESULTS

The results of this section demonstrate the efficiency, accuracy and convergence of the IPO algorithm for several practical examples. Following that, the MBPE technique is applied to reduce the number of RCS data points necessary to generate a continuous pattern.

Trihedrals

The first case demonstrates convergence in terms of the number of iterations. Figure 5 shows the mono-static RCS vs. azimuth patterns of a 1 m square trihedral for an elevation angle of 45° at a frequency of 1 GHz comparing IPO with a method of moments (MoM) reference solution. The incident polarization is vertical. The levels are in very good agreement, even in angular regions where the concave side of the trihedral is partially shadowed, such as in the range 90° and 180°. The agreement in cross-polarization is also very good.

Figure 6 shows the RCS patterns for the same trihedral for different iterations. The solid curve is the converged IPO result which took 5 iterations. The dashed curve is for zero iterations, which is simply the first-order PO result. First-order PO only predicts the direct scattering and not the multi-bounce, so it agrees well with the converged solution only in angular regions where the multi-bounce is not significant. Note that first-order PO predicts a zero cross-polarization component, so it is not included in the cross-polarization plot. The dot-dash curves are for 1 iteration, which includes the second-order terms corresponding to double-reflection, double-diffraction, reflection-diffraction and diffraction-reflection (in addition to the first-order terms). The 1 iteration curves agree well with the converged solution where the dihedral reflection is dominant, such as around 0° and 90° azimuth. Also note the region between 90° and 180° where the concave side of the trihedral is partially shadowed. IPO with 1 iteration predicts this well, whereas the first-order PO solution does not. The dotted curves are for 2 iterations, which includes the third-order terms (in addition to the first and second-order terms). The triple-bounce off the trihedral is dominant in the angular 0° to 90°, which is predicted very well with 2 iterations of IPO. These results demonstrate how each iteration of IPO adds the next higher-order interaction terms.

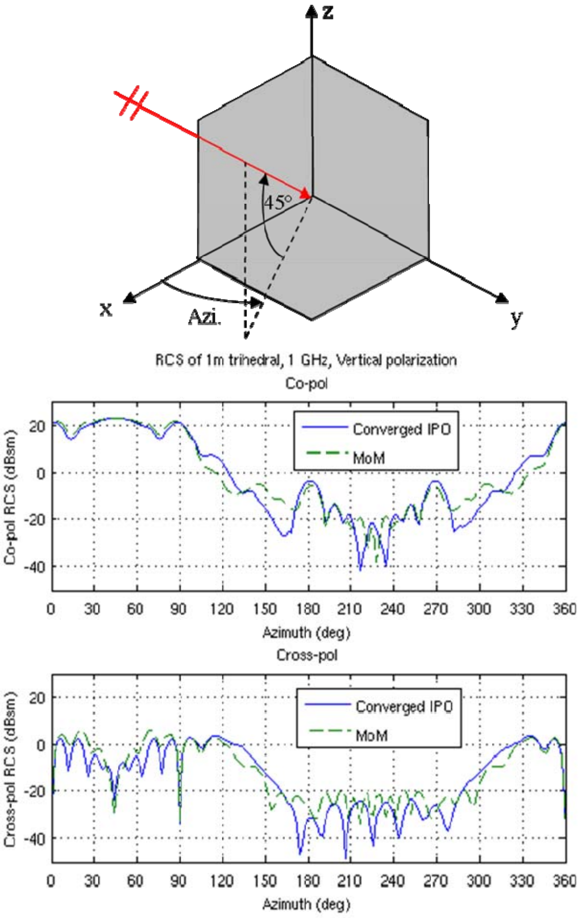

Fig. 5. Mono-static RCS patterns of a 1 m square PEC trihedral computed with IPO and MoM. Frequency is 1 GHz, elevation is 45° and the incident polarization is vertical.

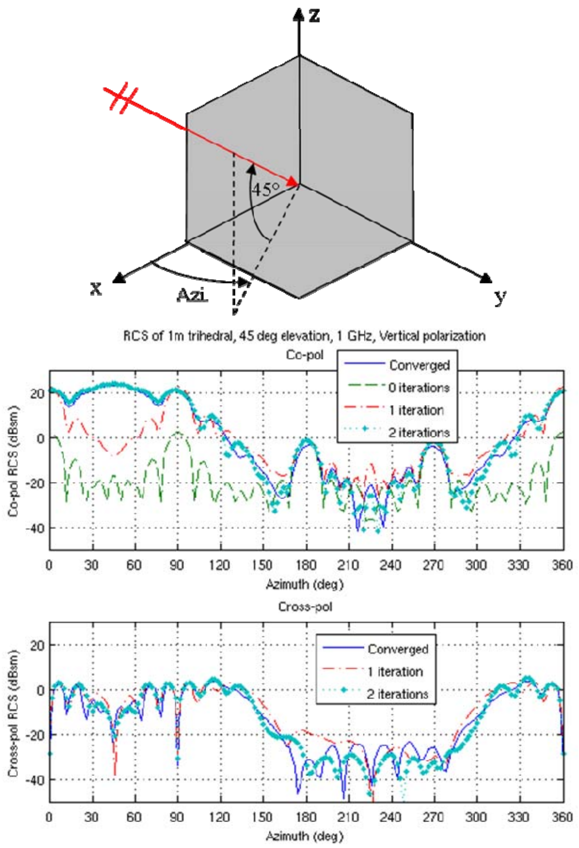

Fig. 6. Convergence of RCS patterns of a 1 m square PEC trihedral computed with IPO. Frequency is 1 GHz, 45° elevation, and the incident polarization is vertical. Cross-polarization for 0 iterations is not plotted because it is identically zero.

First, the mono-static RCS of a tilted trihedral, which is 142.24 x 60.96 x 20.32 cm in size as shown in Fig. 7, was computed by using IPO at 3 and 9 GHz for 0-90° azimuth, 10° elevation, and co-polarized fields. CAD models for this target consist of 1,169 and 10,078 triangular facets at 3 and 9 GHz, respectively, corresponding to about 10 facets per square wavelength. There is a good agreement between IPO results and the results obtained by using MLFMM available from electromagnetic simulation software, FEKO, as shown in Fig. 8 at 3 GHz. The mesh for the MLFMM results required 14,357 triangular facets corresponding to about 123 facets per square wavelength at 3 GHz, which is typical of purely numerical methods. The IPO results also compare well with measured data as shown in Fig. 9 at 9 GHz. It is noted that the measured data is averaged

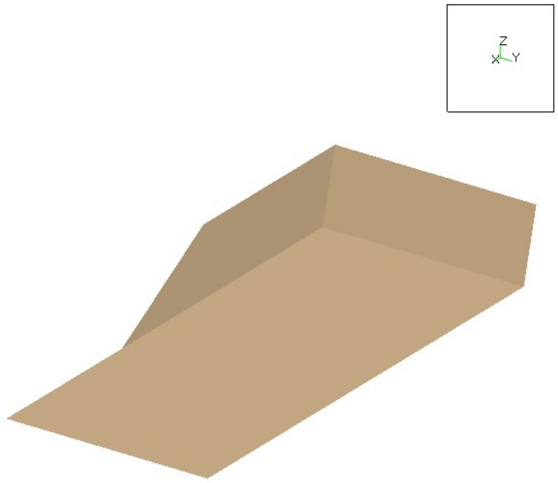

Fig. 7. CAD model for the tilted trihedral.

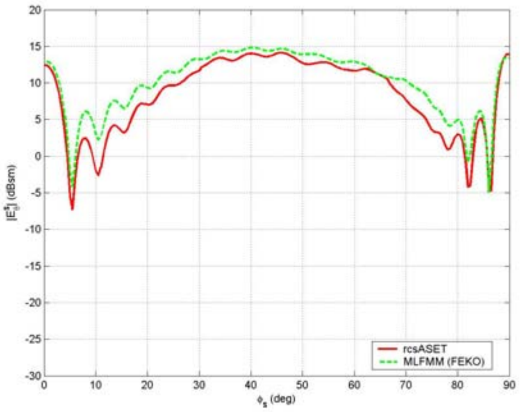

(a) Vertical polarization.

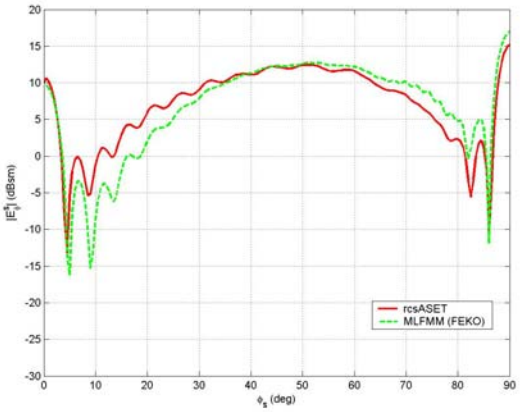

(b) Horizontal polarization.

Fig. 8. IPO results for co-polarized mono-static RCS of the tilted trihedral compared to the MLFMM results obtained by using FEKO for 0-90° azimuth and 10° elevation at 3 GHz.

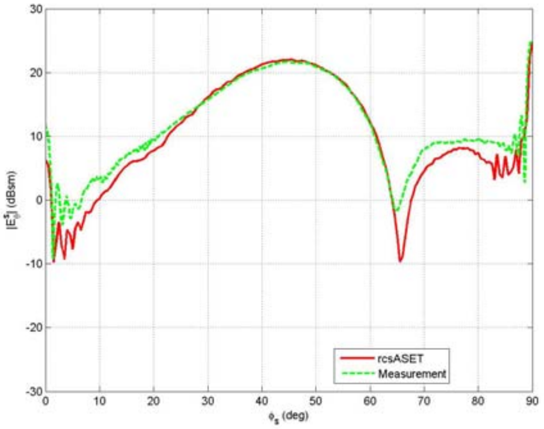

(a) Vertical polarization.

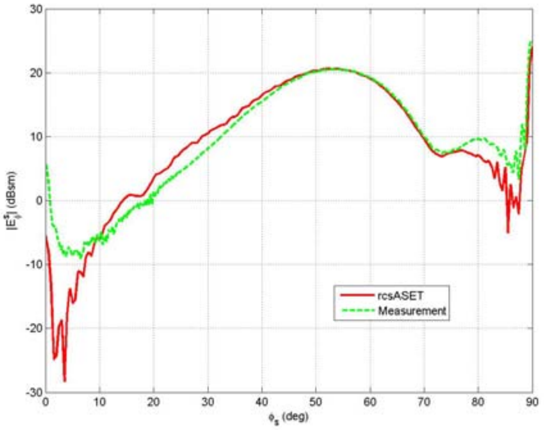

(b) Horizontal polarization.

Fig. 9. IPO results for co-polarized mono-static RCS of the tilted trihedral compared to measured data for 0-90° azimuth and 10° elevation at 9 GHz. Measured data is averaged over a 1 GHz bandwidth.

over a 1 GHz bandwidth [22]. Since IPO takes multi-bounce into consideration, it can capture the null in Fig. 9(a) which cannot be captured properly by using only PO. First-order PO and converged IPO current distributions at 94 GHz for 45° azimuth and 10° elevation are shown in Fig. 10. IPO currents exhibit a standing wave behavior due to multi-bounce as expected, whereas PO currents do not show such behavior.

A smooth corner trihedral shown in Fig. 11 was considered next. Unlike the tilted trihedral, plates forming the smooth corner trihedral are perpendicular to each other and have finite thicknesses. Mono-static RCS of this target, which is 62.00 x 62.00 x 31.40 cm in size, was computed

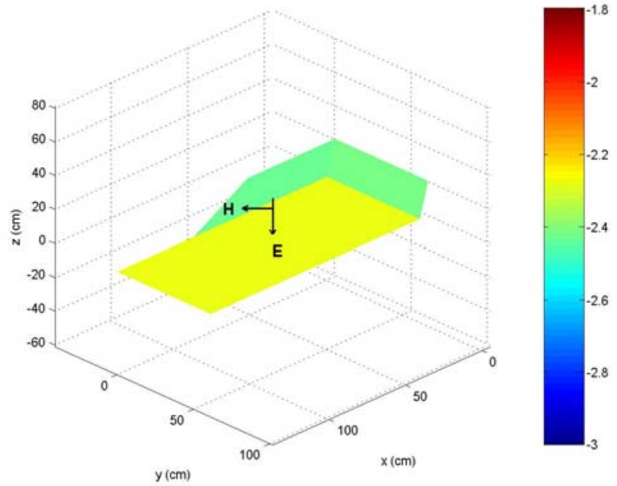

(a) First-order PO currents.

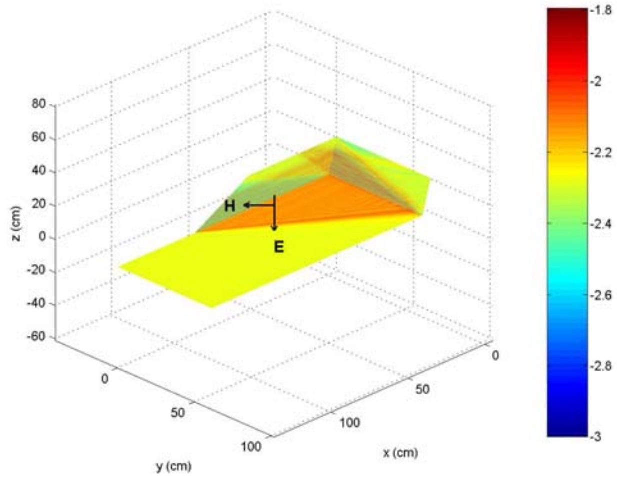

(b) Converged IPO currents.

Fig. 10. Surface current distributions over the tilted trihedral for 45° azimuth, 10° elevation and vertical polarization at 94 GHz.

by using IPO at 9 GHz for co-polarized fields. The CAD model for the target consists of 7,064 triangular facets at this frequency, corresponding to about 10 facets per square wavelength. IPO results compare well with measured data as shown in Figure 12 for 0-90° azimuth and 10° elevation. It is noted that the measured data was obtained in the near-field of the trihedral, which explains the shift in the peak near 90° [23]. Moreover, first-order PO and converged IPO current distributions at 94 GHz for 45° azimuth and 10° elevation are shown in Fig. 13, which respectively behave similar to the PO and IPO currents over the tilted trihedral shown in Fig. 9.

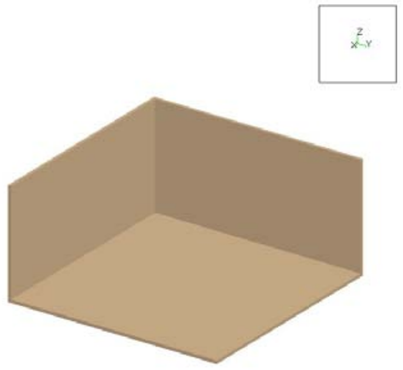

Fig. 11. CAD model for the smooth corner trihedral.

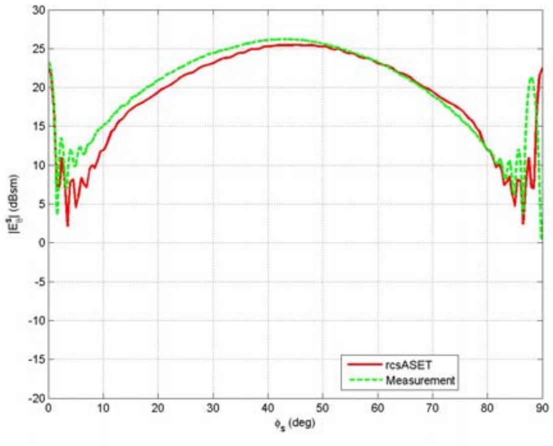

(a) Vertical polarization.

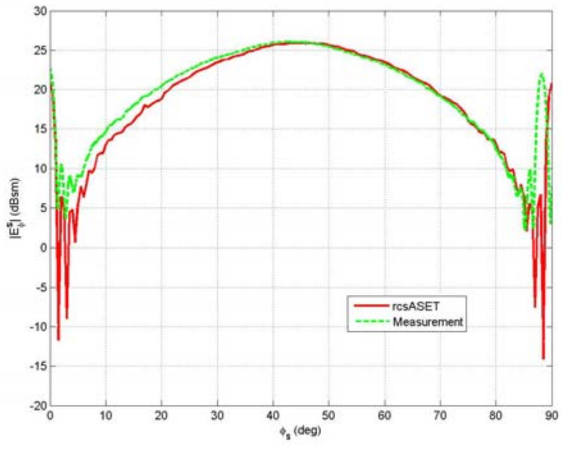

(b) Horizontal polarization.

Fig. 12. IPO results for co-polarized mono-static RCS of the smooth corner trihedral compared to measured data for 0-90° azimuth and 10° elevation at 9 GHz. Measured data was obtained in the near-field of the trihedral.

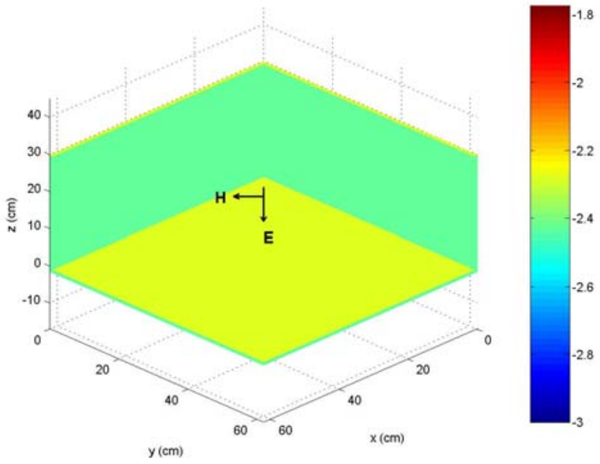

(a) First-order PO currents.

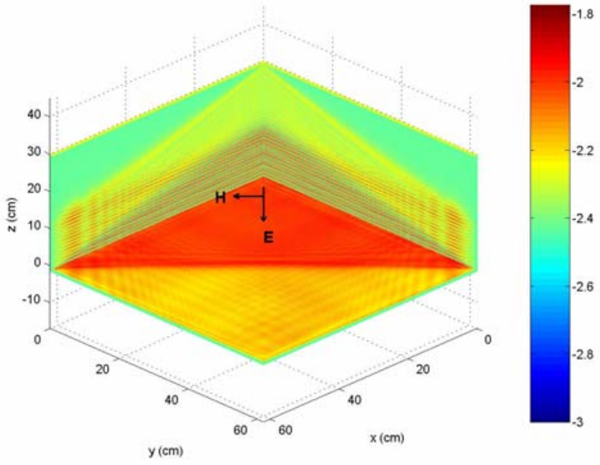

(b) Converged IPO currents.

Fig. 13. Surface current distributions over the smooth corner trihedral for 45° azimuth, 10°elevation and vertical polarization at 94 GHz.

SLICY

The mono-static RCS of another target shown in Fig. 14 was also computed. This target is historically known as DICY since it consists of canonical shapes such as dihedrals and cylinders. It was later used by Sandia National Laboratories where it was renamed SLICY. The mono-static RCS of this target, which is 244.49 x 275.05 x 167.96 cm in size, was computed by using IPO at 9 GHz for co-polarized fields. The CAD model for the target consists of 322,468 triangular facets at this frequency, corresponding to more than 12 facets per square wavelength. IPO results are shown in comparison with the results obtained by using electromagnetic simulation software, XPatch, in Fig. 15 for 0-360° azimuth while elevation is 10° and 30° for vertical and horizontal polarizations, respectively. It is noted that the XPatch results are averaged over a 1 GHz bandwidth. The IPO results were found to be close to the measured data (not shown) whereas Xpatch underestimates the RCS by 2-3 dB in the 90-270° azimuth range since it can not account for the third bounce properly. First-order PO and converged IPO current distributions at 9 GHz for 225° azimuth and 10° elevation are also shown in Fig. 16.

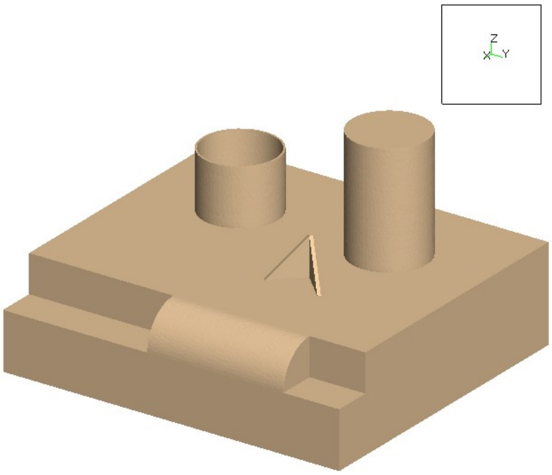

Fig. 14. CAD model for SLICY.

ZSU-23-4 Anti-Aircraft Tank

The mono-static RCS of an anti-aircraft tank, ZSU-23-4, shown in Fig. 17 was also studied. The mono-static RCS of this target, which is 598.5 x 308.7 x 364.3 cm in size, was computed by using IPO at 2 and 9 GHz for 0-360° azimuth, 30° elevation and co-polarized fields. The CAD model for IPO consists of 118,712 triangular facets at 2 GHz, corresponding to about 10 facets per square wavelength. The IPO results compare well with the results obtained by using electromagnetic simulation software, Maxwell Solver Physical Optics (MSPO), as shown in Fig. 18 at 2 GHz. The IPO results are also consistent with measured data as shown in Fig. 19 at 9 GHz. It should be noted that the IPO results are angle averaged whereas the measured data are frequency averaged over a 2 GHz bandwidth. Also, the measurements were performed with the target on an absorber-covered in-ground turntable [24], whereas the IPO results for this case are in free space. This explains the discrepancies in the details of the patterns, whereas the envelope levels are in good agreement. A coarse CAD model with 1,027,796 triangular facets, corresponding to less than 10 facets per square wavelength, has been used at 9 GHz to reduce computation time. It has been observed that good accuracy can be achieved with IPO if a minimum of 4-9 facets per square wavelength are used. First-order PO and converged IPO current distributions at 9 GHz for 0° azimuth and 15° elevation are also shown in Figure 20.

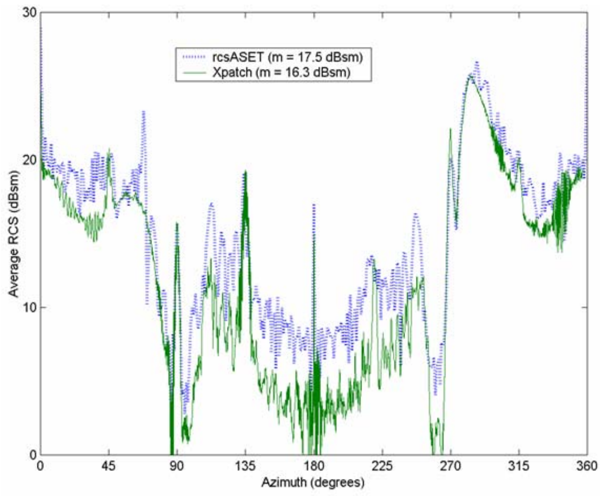

(a) Vertical polarization for 10° elevation.

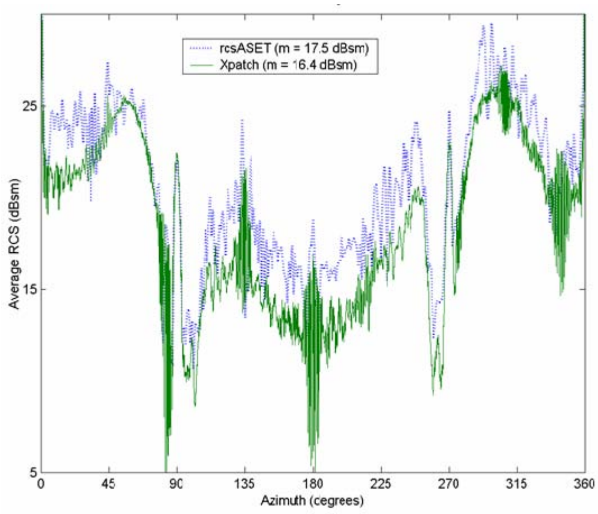

(b) Horizontal polarization for 30° elevation.

Fig. 15. IPO results for co-polarized mono-static RCS of SLICY compared to the results obtained by using XPatch for 0-360° azimuth at 9 GHz. Xpatch results are frequency averaged over a 1 GHz bandwidth.

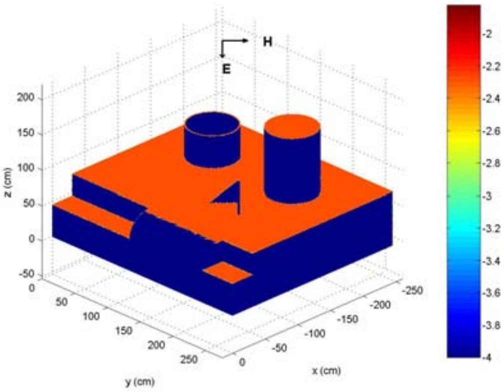

(a) First-order PO currents.

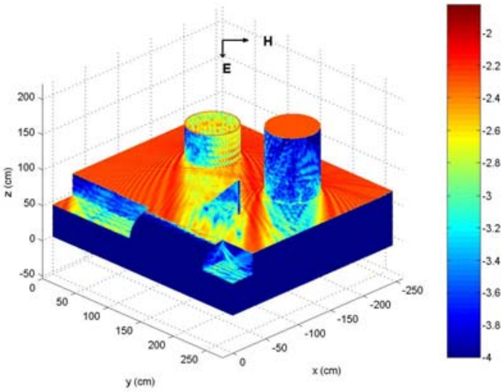

(b) Converged IPO currents.

Fig. 16. Surface current distributions over SLICY for 225° azimuth, 10° elevation and vertical polarization at 9 GHz.

Fig. 17. CAD model for ZSU-23-4.

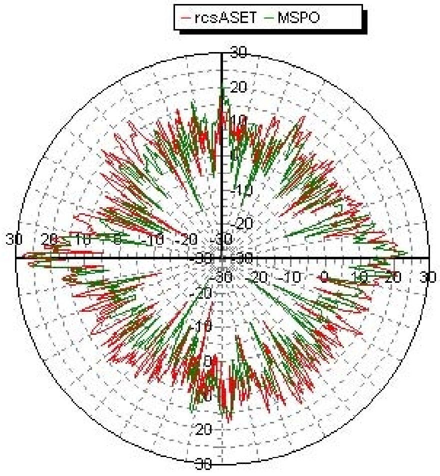

(a) Vertical polarization.

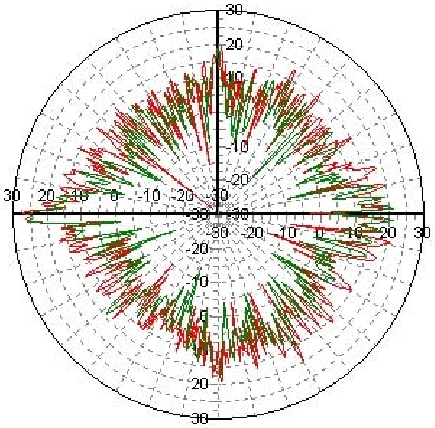

(b) Horizontal polarization.

Fig. 18. IPO results for co-polarized mono-static RCS of ZSU-23-4 compared to the results obtained by using MSPO for 0°-360° azimuth and 30° elevation at 2 GHz.

Generic Tank Model

A generic tank shown in Figure 21 was considered last. The mono-static RCS of this target, which is 609.60 x 325.12 x 218.44 cm in size, was computed by using IPO at 10 GHz for co-polarized fields. CAD model for the target consists of 521,932 triangular facets at this frequency, corresponding to about 10 facets per square wavelength. IPO results are shown in comparison with the results obtained by using XPatch and measured data in Fig. 22 for 0-360° azimuth and 10° elevation. Overall, the IPO results

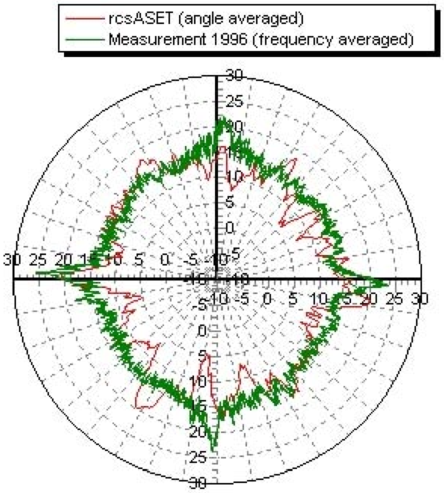

(a) Vertical polarization.

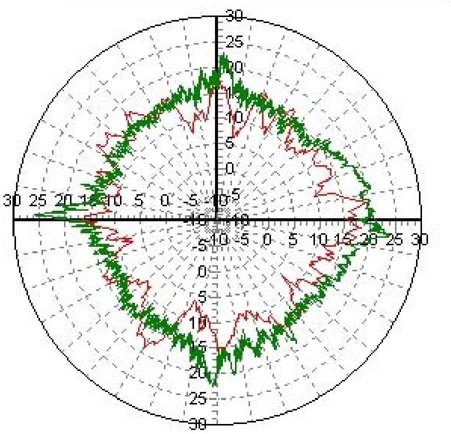

(b) Horizontal polarization.

Fig. 19. IPO results for co-polarized mono-static RCS of ZSU-23-4 compared to measured data for 0-360° azimuth and 30° elevation at 9 GHz. The IPO results are angle averaged whereas the measured data is frequency averaged over a 2 GHz bandwidth, and the measurements were performed with the target on an absorber-covered in-ground metal turntable whereas the IPO results are in free space.

are closer to the measured data than the results generated by using Xpatch. It should be noted that the IPO results are angle averaged whereas the others are frequency averaged over a 0.66 GHz bandwidth [25]. First-order PO and converged IPO current distributions at 10 GHz for 0° azimuth and 30° elevation are also shown in Fig. 23.

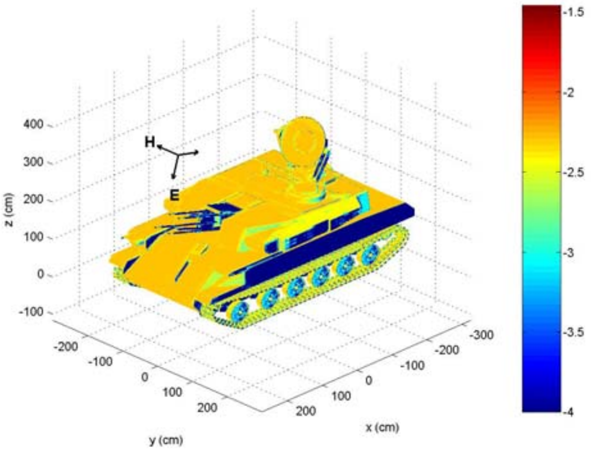

(a) First-order PO currents.

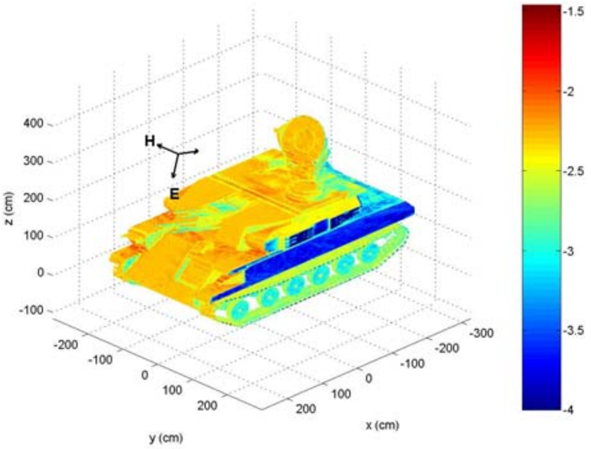

(b) Converged IPO currents.

Fig. 20. Surface current distributions over ZSU-23-4 for 0° azimuth, 15° elevation and vertical polarization at 9 GHz.

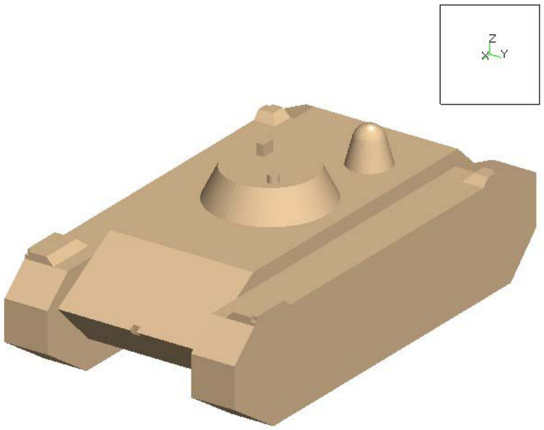

Fig. 21. CAD model for the generic tank.

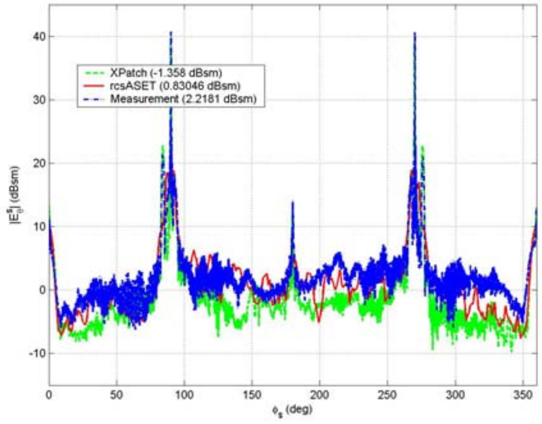

(a) Vertical polarization.

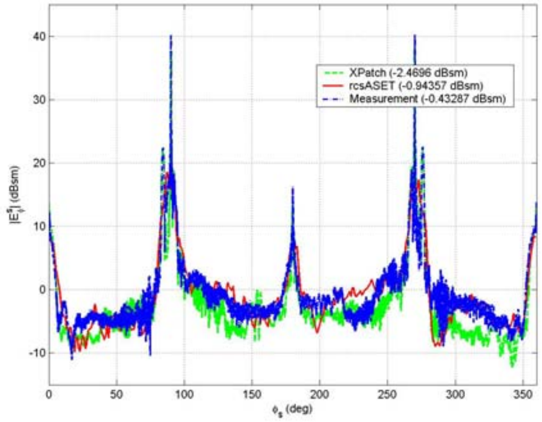

(b) Horizontal polarization.

Fig. 22. IPO results for co-polarized mono-static RCS of the generic tank compared to the results obtained by using XPatch and measured data for 0-360° azimuth and 10° elevation at 10 GHz. Xpatch and measured data are frequency averaged over a 0.66 GHz bandwidth.

Parallelization of the rcsASET code helped reduce the computation time significantly. The mono-static RCS is computed for vertical and horizontal polarizations at each scattering angle in the code. Because of the low memory requirement of IPO, parallelization of the code makes it possible to allocate the RCS computation for each polarization and small ranges of scattering angles to a different processor. The efficiency of the code is greatly improved by computing the IPO currents for multiple angular excitations simultaneously (typically 10 to 20) so that the terms in (10) do not have be recomputed for every angle. The mono-static RCS patterns of the tilted trihedral, smooth corner trihedral, SLICY, ZSU-23-4 and generic tank were computed at high frequencies by using the parallel version of the rcsASET code to demonstrate the reduction in computation time. Results were obtained in a few days with the parallel version of the code on multiple processors, which would otherwise take a few years to get the same results with its serial version on a single processor. The computation time with the parallel version of the code are shown in Table 1 for the benchmark targets considered.

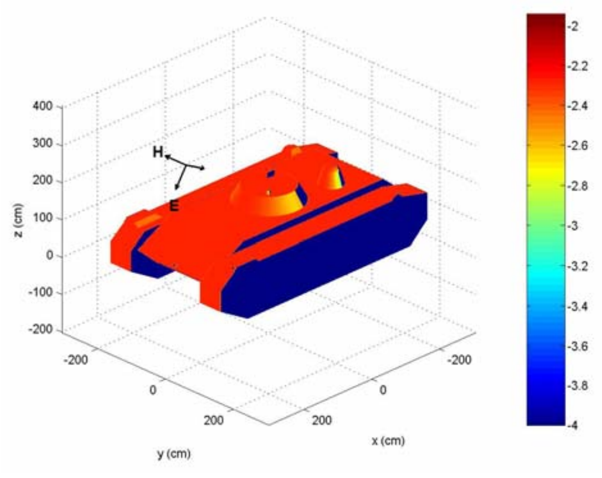

(a) First-order PO currents.

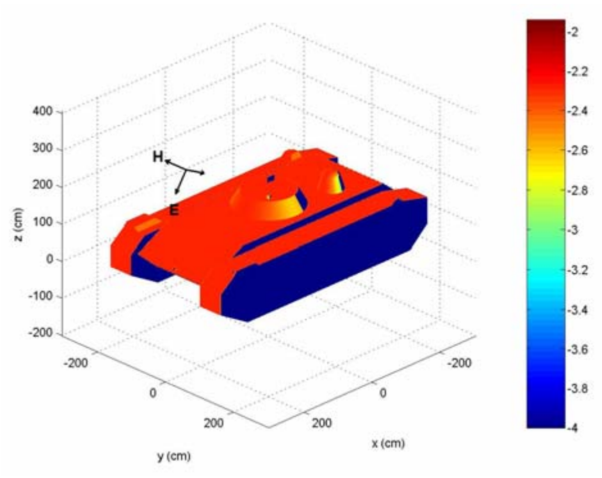

(b) Converged IPO currents.

Fig. 23. Surface current distributions over the generic tank for 0° azimuth, 30° elevation and vertical polarization at 10 GHz.

Table 1: Savings in computation time with the parallel version of the rcsASET code.

Target	Freq. (GHz)	Number of facets	Number of angles	Number of processors	Max. time per proc. (hours)
Tilted trihedral	94	1,092,548	362	91	84
Smooth corner trihedral	94	764,224	362	91	69
SLICY	34	3,960,290	360	180	116
ZSU-23-4	9	1,027,796	720	360	91
Generic tank	10	2,267,544	360	360	70

The rcsASET code for RCS pattern computations has been further improved by using it in conjunction with MBPE for fast angle or frequency sweeps. When MBPE is employed adaptively, the reduction in computation time changes with M and N. Different targets may also have different optimum values for M and N. Variations in computation time with the values of M and N are shown in Fig. 24 for frequency and azimuth sweeps in computing the RCS of the tilted trihedral and smooth corner trihedral, respectively. Approximately 19 and 14 times speed-up can be achieved respectively in the frequency and azimuth sweeps shown in Fig. 24 with optimum values of M and N.

Accuracy is not much compromised with MBPE, even though substantial speed-up is achieved with MBPE as was shown in Fig. 24. RCS results with and without MBPE, and MBPE points are shown in Figs. 25, 26 and 27 respectively for the tilted trihedral, smooth corner trihedral and SLICY where MBPE points are not always uniformly distributed due to adaptive implementation of MBPE. It is shown in Figs. 25-27 that MBPE can accurately capture the nulls in the RCS even when there are no MBPE points at these nulls. Thus, MBPE is much more than a regular interpolation method. Although optimum values of M and N giving the lowest computation time are not investigated for SLICY, the values of M and N that are used in MBPE yield 9 times speed-up for 1 MHz frequency increment as shown in Fig. 27.

V. CONCLUSIONS

The IPO method has been shown to be very efficient, robust and accurate for handling RCS problems involving electrically large and realistically complex structures. It is physically insightful for capturing multiple interactions up to

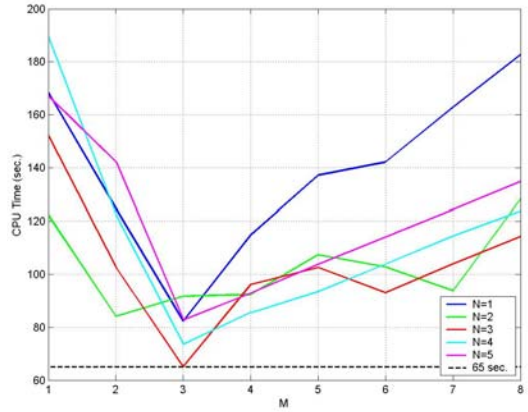

(a) Frequency sweep for tilted trihedral with 45° azimuth and 10° elevation at 2-3 GHz where the lowest time is obtained with M=3 and N=3 resulting in 19 times speed-up for 1 MHz frequency increment. Time for full sweep is 1,235 seconds.

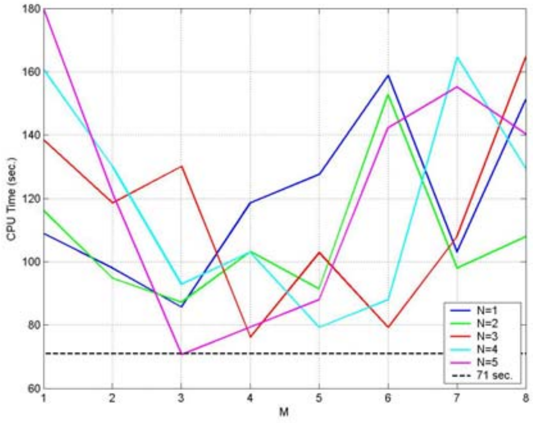

(b) Azimuth sweep for smooth corner trihedral with 0-90° azimuth and 10° elevation at 3 GHz where the lowest time is obtained with M=3 and N=5 resulting in 14 times speed-up for 0.1° azimuth increment. Time for full sweep is 994 seconds.

Fig. 24. Variation of mono-static RCS computation time with values of *M* and *N*.

a specified order via the number of iterations. It tends to be more efficient but less accurate than rigorous numerical methods, and more accurate but less efficient than ray tracing methods. As such, it bridges the gap between these two extremes with a viable solution for practical engineering problems. Typically, an order of magnitude reduction in the number of unknowns with respect to purely numerical methods is possible, while the memory requirement is O(N). Another order of magnitude reduction is possible by combining the MPBE method with IPO for generating swept frequency and angle patterns. The IPO solution has also been applied to the performance analysis of antennas installed on realistic platforms such as aircraft and ships [26].

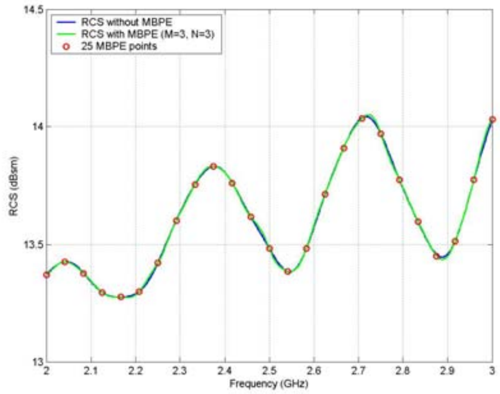

(a) Vertical polarization.

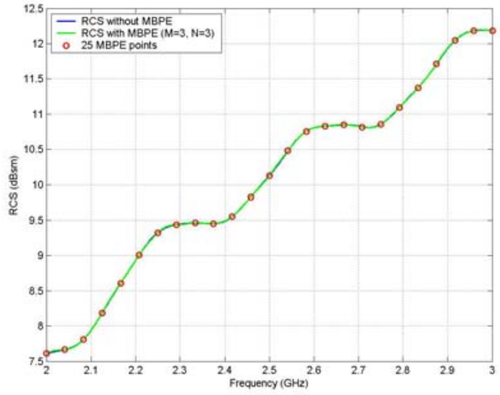

(b) Horizontal polarization.

Fig. 25. IPO frequency sweep results for co-polarized mono-static RCS of tilted trihedral with (M=3 and N=3 as optimum values) and without MBPE, and 25 MBPE points for 45° azimuth and 10° elevation at 2-3 GHz.

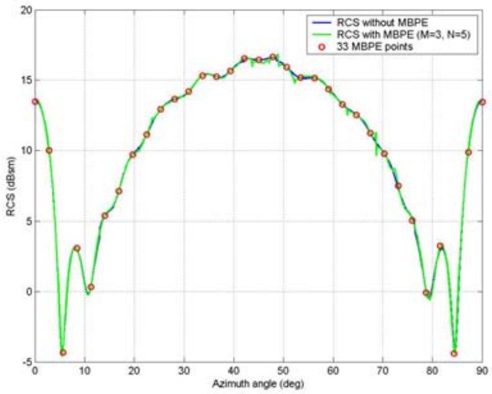

(a) Vertical polarization.

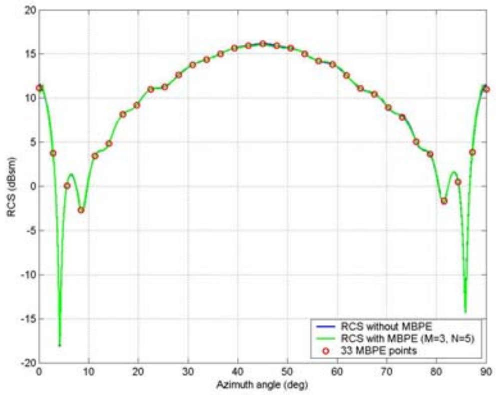

(b) Horizontal polarization.

Fig. 26. IPO azimuth sweep results for co-polarized mono-static RCS of smooth corner trihedral with (M=3 and N=5 as optimum values) and without MBPE, and 33 MBPE points for 0-90° azimuth and 10° elevation at 3 GHz.

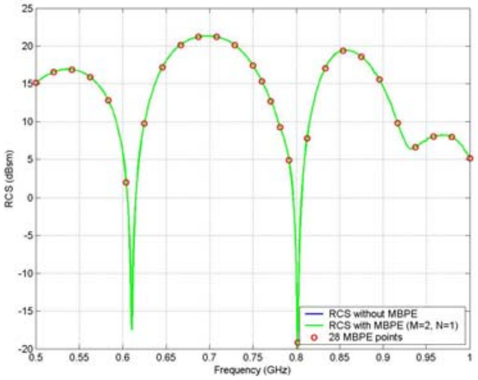

(a) Vertical polarization.

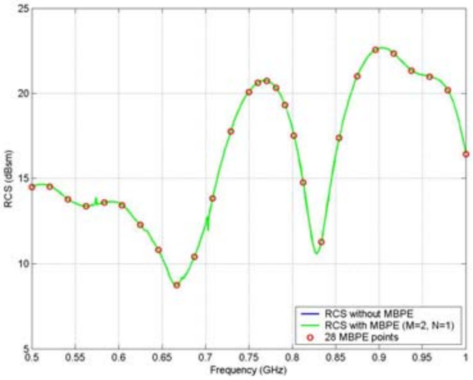

(b) Horizontal polarization.

Fig. 27. IPO frequency sweep results for co-polarized mono-static RCS of SLICY with (M=2, N=1) and without MBPE, and 28 MBPE points for 0° azimuth and 30° elevation at 0.5-1 GHz. Although the M and N values used may not be optimum, 9 times speed-up is achieved for 1 MHz frequency increment.

REFERENCES

[1] F. Obelleiro, J. L. Rodriguez and R. J. Burkholder, "An iterative physical optics approach for analyzing the electromagnetic scattering by large open-ended cavities," *IEEE Trans. Antennas Propagat.*, vol. 43, No. 4, pp. 356-361, April 1995.

[2] R. J. Burkholder, "A fast and rapidly convergent iterative physical optics algorithm for computing the RCS of open-ended cavities," *App. Comput. Electro. Soc. J.*, vol. 16, No. 1, pp. 53-60, March 2001.

[3] R. J. Burkholder and T. Lundin, "Forward-backward iterative physical optics algorithm for computing the RCS of open-ended cavities," *IEEE Trans. Antennas Propagat.*, vol. 53, No. 2, pp. 793-799, Feb. 2005.

[4] R. F. Harrington, *Field computation by moment methods*. New York: Macmillan, 1968.

[5] J. M. Jin, *The Finite Element Method in Electromagnetics*, New York: Wiley, 2002.

[6] S. Velamparambil, W. C. Chew and J. M. Song, "10 Million Unknowns: Is it that Big?" *IEEE Antennas Propagat. Mag.*, vol. 45, No. 2, pp. 43-58, April 2003.

[7] B. Stupfel, "A Fast-Domain Decomposition Method for the Solution of Electromagnetic Scattering by Large Objects," *IEEE Trans. Antennas Propagat.*, vol. 44, No. 10, pp. 1375-1385, Oct. 1996.

[8] Y. J. Li and J. M. Jin, "A Vector Dual-Primal Finite Element Tearing and Interconnecting Method for Solving 3-D Large-Scale Electromagnetic Problems," *IEEE Trans. Antennas Propagat.*, vol. 54, No. 10, pp. 3000-3009, Oct. 2006.

[9] H. Ling, R. C. Chou and S. W. Lee, "High-Frequency RCS of Open Cavities with Rectangular and Circular Cross Sections," *IEEE Trans. Antennas Propagat.*, vol. 35, No. 4, pp. 391-398, April 1987.

[10] G. Crabtree, "A Numerical Quadrature Technique for Physical Optics Scattering Analysis," *IEEE Trans. Magnetics*, vol. 27, No. 5, pp. 4291-4294, Sep. 1991.

[11] P. H. Pathak and R. J. Burkholder, "High frequency scattering," *Section 1.5.2 in Scattering: Scattering and Inverse Scattering in Pure and Applied Science*, pp. 245-276, Edited by E.R. Pike and P. Sabatier, Academic Press, Ltd., London, 2002.

[12] F. S. de Adana, S. Nieves, E. Garcia, I. Gonzalez, O. Gutierrez and M. F. Catedra, "Calculation of the RCS from the Double Reflection Between Planar Facets and Curved Surfaces," *IEEE Trans. Antennas Propagat.*, vol. 51, No. 9, pp. 2509-2512, Sep. 2003.

[13] J. Baldauf, S. W. Lee, L. Lin, S. K. Jeng, S. M. Scarborough and C. L. Yu, "High-Frequency Scattering from Trihedral Corner Reflectors and Other Benchmark Targets – SBR Versus Experiment," *IEEE Trans. Antennas Propagat.*, vol. 39, No. 9, pp. 1345-1351, Sep. 1991.

[14] XPATCH: A High-Frequency Electromagnetic-Scattering Prediction Code and Environment for Complex Three-Dimensional Objects," *IEEE Antennas Propagat. Mag.*, vol. 36, No. 1, pp. 65-69, Feb. 1994.

[15] P. H. Pathak, "Techniques for High Frequency Problems," in *Antenna Handbook, Theory, Application and Design*, edited by Y. T. Lo and S. W. Lee, Van Nostrand Reinhold Co. Inc., New York, 1988.

[16] S. H. Park, K. K. Park, J. H. Jung, H. T. Kim and K. T. Kim, "Construction of Training

Database Based on High Frequency RCS Prediction Methods for ATR," *J. of Electromagnetic Waves App.*, vol. 22, No. 5-6, pp. 693-703, 2008.

[17] F. Obelleiro, M. G. Araujo and J. L. Rodriguez, "Iterative Physical Optics Formulation for Analyzing Large Waveguildes with Lossy Walls," *Microwave Opt. Tech. Lett.*, vol. 28, No. 1, pp. 21-26, Jan. 5, 2001.

[18] G. H. Golub and C. F. Van Loan, *Matrix Computations*, Third Edition, The Johns Hopkins University Press, Baltimore, 1996.

[19] C. C. Lu and W. C. Chew, "Fast Far-Field Approximation for Calculating the RCS of Large Objects," *Microwave Opt. Tech. Lett.*, vol. 8, No. 5, pp. 238-241, 1995.

[20] R. Coifman, V. Rokhlin and S. Wandzura, "The Fast Multipole Method for the Wave Equation: A Pedestrian Prescription," *IEEE Antennas Propagat. Mag.*, vol. 35, No. 3, pp. 7-12, 1993.

[21] Y. E. Erdemli, J. Gong, C. J. Reddy and J. L. Volakis, "Fast RCS Pattern Fill Using AWE Technique," *IEEE Trans. Antennas Propagat.*, vol. 46, No. 11, pp. 1752-1753, Nov. 1998.

[22] W. O. Coburn, C. D. Le, C. S. Kenyon, W. A. Spurgeon, and S. L. Carter, "The RCS of a Canonical Corner Target Including Lossy Dielectric Materials," *Army Research Lab Report* ARL-TR-3112, LIMITED, 2003.

[23] W. A. Spurgeon, C. D. Le, W. O. Coburn, R. L. Bender, and S. R. Stratton, "Modeling and Measuring the Radar Cross Section of Two Trihedrons at X, Ka, and W Bands," *Army Research Lab Report* ARL-TR-3098, LIMITED, 2003.

[24] W. O. Coburn and C. D. Le, "An Investigation of the ZSU-23-4 Radar Cross Section at X-Band," *Army Research Lab Report* ARL-TR-3003, 2003.

[25] W. Spurgeon, W. Nixen, J. Sizemore and S. Carter, "Modeling and Validation of the Effects of a Ground Plane on the RCS of a Second Revised T5M3 Ground Vehicle Simulator," *Army Research Lab Report* ARL-TR-3391, January 2005.

[26] R. J. Burkholder, P. H. Pathak, K. Sertel, R. J. Marhefka, J. L. Volakis and R. W. Kindt, "A Hybrid Framework for Antenna/Platform Analysis," Invited paper, *Applied Computational Electromagnetics Society Journal, Special issue on array antennas*, vol. 21, No. 3, pp. 177-195, Nov. 2006.

Robert J. Burkholder received the B.S., M.S., and Ph.D. degrees in electrical engineering from The Ohio State University, Columbus, in 1984, 1985, and 1989, respectively. Since 1989, he has been with The Ohio State University ElectroScience Laboratory, Department of Electrical and Computer Engineering, where he is currently a Senior Research Scientist and Adjunct Professor. Dr. Burkholder's research specialties are high-frequency asymptotic techniques and their hybrid combination with numerical techniques for solving large-scale electromagnetic radiation, propagation, and scattering problems.

Çağatay Tokgöz received the B.S. degree from Bilkent University, Ankara, Turkey, in 1994, the M.S. degree from the Middle East Technical University, Ankara, Turkey, in 1997, both in electrical and electronics engineering, and the Ph.D. degree in electrical engineering from The Ohio State University, Columbus, OH, in 2002. He has been working for Applied EM, Incorporated, Hampton, VA, as a Senior Research Engineer since 2002. His research interests include closed-form Green's function techniques for stratified media, and asymptotic high-frequency techniques particularly Iterative Physical Optics (IPO) and Uniform Geometrical Theory of Diffraction (UTD) for solving antenna radiation, antenna coupling and radar signature prediction problems associated with electrically large complex structures.

C. J. Reddy received B.Tech. degree in Electronics and Communications Engineering from Regional Engineering College (now National Institute of Technology), Warangal, India in 1983. He received his M.Tech. degree in Microwave and Optical Communication Engineering and Ph.D. degree in Electrical Engineering, both from Indian Institute of Technology, Kharagpur, India, in 1986 and 1988 respectively. Currently, Dr. Reddy is the President and Chief Technical Officer of Applied EM Inc, a small company specializing in computational electromagnetics, antenna design and development. Dr. Reddy also serves as the President of EM Software & Systems (USA) Inc. At EMSS (USA), he is leading the marketing and support of commercial 3D electromagnetic software, FEKO in the US, Canada, Mexico and Central America. Dr. Reddy is a member of the Board of Directors of the Applied Computational Electromagetics Society.

William O. Coburn received his BS in Physics from Virginia Polytechnic Institute in 1984. He received an MSEE in Electro physics in 1991 and Doctor of Science in Electromagnetic Engineering from George Washington University (GWU) in 2005. His dissertation research was in traveling wave antenna design. He has 27 years experience as an electronics engineer at the Army Research Laboratory (formerly the Harry Diamond Laboratories) primarily in the area of CEM for EMP coupling/hardening, HPM and target signatures. He currently is in the RF Electronics Division of the Sensors and Electron Devices Directorate applying CEM tools for antenna design and analysis.

2009 INSTITUTIONAL MEMBERS

AUSTRALIAN DEFENCE LIBRARY
Northcott Drive
Canberra, A.C.T. 2600 Australia

BAE SYSTEMS
W423A Warton Aerodome
Preston, Lancashire
United Kingdom PR4 1AX

DARTMOUTH COLLEGE
6193 Murdough Center
Hanover, NH 03755-3560

DSTO-DSTORL EDINBURGH
Jets AU/33851-99, PO Box 562
Milsons Point, NSW
Australia 1565

DTIC-OCP/LIBRARY
8725 John J. Kingman Rd. Ste 0944
Ft. Belvoir, VA 22060-6218

ELLEDIEMME
Libri Dal Mondo
PO Box 69/Poste S. Silvestro
Rome, Italy 00187

ELSEVIER
Bibliographic Databases
PO Box 2227
Amsterdam, Netherlands 1000 CE

ENGINEERING INFORMATION, INC
PO Box 543
Amsterdam, Netherlands 1000 Am

ETSE TELECOMUNICACION
Biblioteca, Campus Lagoas
Vigo, 36200 Spain

FGAN-FHR
Neuenahrerstrasse 20
Wachtberg, Germany 53343

FLORIDA INTERNATIONAL UNIV
10555 W. Flagler Street
Miami, FL 33174

GEORGIA TECH LIBRARY
225 North Avenue, NW
Atlanta, GA 30332-0001

HANYANG UNIVERSITY
Paiknam Academic Info. Ctr Library
17 Haengdang-Dong
Seongdong-Ku
Seoul, South Korea 133-791

HRL LABS, RESEARCH LIBRARY
3011 Malibu Canyon
Malibu, CA 90265

IEE INSPEC/Acquisitions Section
Michael Faraday House
6 Hills Way
Stevenage, Herts UK SG1 2AY

IND CANTABRIA
PO Box 830470
Birmingham, AL 35283

INSTITUTE FOR SCIENTIFIC INFO.
Publication Processing Dept.
3501 Market St.
Philadelphia, PA 19104-3302

L-3 IS
1133 Wood Valley Drive
Woodway, TX 76712

LIBRARY – DRDC OTTAWA
3701 Carling Avenue
Ottawa, Ontario, Canada K1A OZ4

LIBRARY of CONGRESS
Reg. Of Copyrights
Attn: 40T Deposits
Washington DC, 20559

LINDA HALL LIBRARY
5109 Cherry Street
Kansas City, MO 64110-2498

LULEA UNIV. OF TECHNOLOGY
Porson
Lulea, Sweden 97187

MISSISSIPPI STATE UNIV LIBRARY
PO Box 9570
Mississippi State, MS 39762

MISSOURI S&T
400 W 14th Street
Rolla, MO 56409

MIT LINCOLN LABORATORY
Periodicals Library
244 Wood Street
Lexington, MA 02420

NATIONAL DEFENSE ACADEMY
1-10-20 Hashirimizu
Yokosuka, Kanagawa
239-8686 Japan

NAVAL POSTGRADUATE SCHOOL
Attn:J. Rozdal/411 Dyer Rd./ Rm 111
Monterey, CA 93943-5101

NDL KAGAKU
C/0 KWE-ACCESS
PO Box 300613 (JFK A/P)
Jamaica, NY 11430-0613

OHIO STATE UNIVERSITY
1320 Kinnear Road
Columbus, OH 43212

OVIEDO LIBRARY
PO BOX 830679
Birmingham, AL 35283

PENN STATE UNIVERSITY
126 Paterno Library
University Park, PA 16802-1808

DAVID J. PINION
1122 E PIKE STREET #1217
SEATTLE, WA 98122

SOUTHWEST RESEARCH
INSTITUTE
6220 Culebra Road
San Antonio, TX 78238

SWETS INFORMATION SERVICES
160 Ninth Avenue, Suite A
Runnemede, NJ 08078

TELSTRA
13/242 Exhibition Street
Melbourne, Victoria
3000 Australia

TIB & UNIV. BIB. HANNOVER
DE/5100/G1/0001
Welfengarten 1B
Hannover, Germany 30167

TU DARMSTADT
Schlossgartenstrasse 8
Darmstadt, Hessen
Germany D-64289

UNIV OF CENTRAL FLORIDA LIB.
4000 Central Florida Boulevard
Orlando, FL 32816-8005

UNIVERSITY OF KANSAS –
WATSON
1425 Jayhawk Blvd 210S
Lawrence, KS 66045-7594

UNIVERSITY OF MISSISSIPPI
JD Williams Library
University, MS 38677-1848

UNIVERSITY OF PALERMO
PO Box 69- Poste S. Silvestr
Rome, 00187, Italy

VIRTUAL EM INC.
2019 Georgetown Blvd.
Ann Arbor, MI 48105

ACES COPYRIGHT FORM

This form is intended for original, previously unpublished manuscripts submitted to ACES periodicals and conference publications. The signed form, appropriately completed, MUST ACCOMPANY any paper in order to be published by ACES. PLEASE READ REVERSE SIDE OF THIS FORM FOR FURTHER DETAILS.

TITLE OF PAPER:	RETURN FORM TO: Dr. Atef Z. Elsherbeni University of Mississippi Dept. of Electrical Engineering Anderson Hall Box 13 University, MS 38677 USA
AUTHORS(S)	
PUBLICATION TITLE/DATE:	

PART A - COPYRIGHT TRANSFER FORM

(NOTE: Company or other forms may not be substituted for this form. U.S. Government employees whose work is not subject to copyright may so certify by signing Part B below. Authors whose work is subject to Crown Copyright may sign Part C overleaf).

The undersigned, desiring to publish the above paper in a publication of ACES, hereby transfer their copyrights in the above paper to The Applied Computational Electromagnetics Society (ACES). The undersigned hereby represents and warrants that the paper is original and that he/she is the author of the paper or otherwise has the power and authority to make and execute this assignment.

Returned Rights: In return for these rights, ACES hereby grants to the above authors, and the employers for whom the work was performed, royalty-free permission to:

1. Retain all proprietary rights other than copyright, such as patent rights.
2. Reuse all or portions of the above paper in other works.
3. Reproduce, or have reproduced, the above paper for the author's personal use or for internal company use provided that (a) the source and ACES copyright are indicated, (b) the copies are not used in a way that implies ACES endorsement of a product or service of an employer, and (c) the copies per se are not offered for sale.
4. Make limited distribution of all or portions of the above paper prior to publication.
5. In the case of work performed under U.S. Government contract, ACES grants the U.S. Government royalty-free permission to reproduce all or portions of the above paper, and to authorize others to do so, for U.S. Government purposes only.

ACES Obligations: In exercising its rights under copyright, ACES will make all reasonable efforts to act in the interests of the authors and employers as well as in its own interest. In particular, ACES REQUIRES that:

1. The consent of the first-named author be sought as a condition in granting re-publication permission to others.
2. The consent of the undersigned employer be obtained as a condition in granting permission to others to reuse all or portions of the paper for promotion or marketing purposes.

In the event the above paper is not accepted and published by ACES or is withdrawn by the author(s) before acceptance by ACES, this agreement becomes null and void.

AUTHORIZED SIGNATURE	TITLE (IF NOT AUTHOR)
EMPLOYER FOR WHOM WORK WAS PERFORMED	DATE FORM SIGNED

Part B - U.S. GOVERNMENT EMPLOYEE CERTIFICATION

(NOTE: if your work was performed under Government contract but you are not a Government employee, sign transfer form above and see item 5 under Returned Rights).

This certifies that all authors of the above paper are employees of the U.S. Government and performed this work as part of their employment and that the paper is therefor not subject to U.S. copyright protection.

AUTHORIZED SIGNATURE	TITLE (IF NOT AUTHOR)
NAME OF GOVERNMENT ORGANIZATION	DATE FORM SIGNED

PART C - CROWN COPYRIGHT

(NOTE: ACES recognizes and will honor Crown Copyright as it does U.S. Copyright. It is understood that, in asserting Crown Copyright, ACES in no way diminishes its rights as publisher. Sign only if *ALL* authors are subject to Crown Copyright).

This certifies that all authors of the above Paper are subject to Crown Copyright. (Appropriate documentation and instructions regarding form of Crown Copyright notice may be attached).

AUTHORIZED SIGNATURE	TITLE OF SIGNEE
NAME OF GOVERNMENT BRANCH	DATE FORM SIGNED

Information to Authors

ACES POLICY

ACES distributes its technical publications throughout the world, and it may be necessary to translate and abstract its publications, and articles contained therein, for inclusion in various compendiums and similar publications, etc. When an article is submitted for publication by ACES, acceptance of the article implies that ACES has the rights to do all of the things it normally does with such an article.

In connection with its publishing activities, it is the policy of ACES to own the copyrights in its technical publications, and to the contributions contained therein, in order to protect the interests of ACES, its authors and their employers, and at the same time to facilitate the appropriate re-use of this material by others.

The new United States copyright law requires that the transfer of copyrights in each contribution from the author to ACES be confirmed in writing. It is therefore necessary that you execute either Part A-Copyright Transfer Form or Part B-U.S. Government Employee Certification or Part C-Crown Copyright on this sheet and return it to the Managing Editor (or person who supplied this sheet) as promptly as possible.

CLEARANCE OF PAPERS

ACES must of necessity assume that materials presented at its meetings or submitted to its publications is properly available for general dissemination to the audiences these activities are organized to serve. It is the responsibility of the authors, not ACES, to determine whether disclosure of their material requires the prior consent of other parties and if so, to obtain it. Furthermore, ACES must assume that, if an author uses within his/her article previously published and/or copyrighted material that permission has been obtained for such use and that any required credit lines, copyright notices, etc. are duly noted.

AUTHOR/COMPANY RIGHTS

If you are employed and you prepared your paper as a part of your job, the rights to your paper initially rest with your employer. In that case, when you sign the copyright form, we assume you are authorized to do so by your employer and that your employer has consented to all of the terms and conditions of this form. If not, it should be signed by someone so authorized.

NOTE RE RETURNED RIGHTS: Just as ACES now requires a signed copyright transfer form in order to do “business as usual”, it is the intent of this form to return rights to the author and employer so that they too may do “business as usual”. If further clarification is required, please contact: The Managing Editor, R. W. Adler, Naval Postgraduate School, Code EC/AB, Monterey, CA, 93943, USA (408)656-2352.

Please note that, although authors are permitted to re-use all or portions of their ACES copyrighted material in other works, this does not include granting third party requests for reprinting, republishing, or other types of re-use.

JOINT AUTHORSHIP

For jointly authored papers, only one signature is required, but we assume all authors have been advised and have consented to the terms of this form.

U.S. GOVERNMENT EMPLOYEES

Authors who are U.S. Government employees are not required to sign the Copyright Transfer Form (Part A), but any co-authors outside the Government are.

Part B of the form is to be used instead of Part A only if all authors are U.S. Government employees and prepared the paper as part of their job.

NOTE RE GOVERNMENT CONTRACT WORK: Authors whose work was performed under a U.S. Government contract but who are not Government employees are required so sign Part A-Copyright Transfer Form. However, item 5 of the form returns reproduction rights to the U. S. Government when required, even though ACES copyright policy is in effect with respect to the reuse of material by the general public.

January 2002

APPLIED COMPUTATIONAL ELECTROMAGNETICS SOCIETY JOURNAL
http://aces.ee.olemiss.edu

INFORMATION FOR AUTHORS

PUBLICATION CRITERIA

Each paper is required to manifest some relation to applied computational electromagnetics. **Papers may address general issues in applied computational electromagnetics, or they may focus on specific applications, techniques, codes, or computational issues.** While the following list is not exhaustive, each paper will generally relate to at least one of these areas:

1. **Code validation.** This is done using internal checks or experimental, analytical or other computational data. Measured data of potential utility to code validation efforts will also be considered for publication.

2. **Code performance analysis.** This usually involves identification of numerical accuracy or other limitations, solution convergence, numerical and physical modeling error, and parameter tradeoffs. However, it is also permissible to address issues such as ease-of-use, set-up time, run time, special outputs, or other special features.

3. **Computational studies of basic physics.** This involves using a code, algorithm, or computational technique to simulate reality in such a way that better, or new physical insight or understanding, is achieved.

4. **New computational techniques** or new applications for existing computational techniques or codes.

5. **"Tricks of the trade"** in selecting and applying codes and techniques.

6. **New codes, algorithms, code enhancement, and code fixes.** This category is self-explanatory, but includes significant changes to existing codes, such as applicability extensions, algorithm optimization, problem correction, limitation removal, or other performance improvement. **Note: Code (or algorithm) capability descriptions are not acceptable, unless they contain sufficient technical material to justify consideration.**

7. **Code input/output issues.** This normally involves innovations in input (such as input geometry standardization, automatic mesh generation, or computer-aided design) or in output (whether it be tabular, graphical, statistical, Fourier-transformed, or otherwise signal-processed). Material dealing with input/output database management, output interpretation, or other input/output issues will also be considered for publication.

8. **Computer hardware issues.** This is the category for analysis of hardware capabilities and limitations of various types of electromagnetics computational requirements. Vector and parallel computational techniques and implementation are of particular interest.

Applications of interest include, but are not limited to, antennas (and their electromagnetic environments), networks, static fields, radar cross section, inverse scattering, shielding, radiation hazards, biological effects, biomedical applications, electromagnetic pulse (EMP), electromagnetic interference (EMI), electromagnetic compatibility (EMC), power transmission, charge transport, dielectric, magnetic and nonlinear materials, microwave components, MEMS, RFID, and MMIC technologies, remote sensing and geometrical and physical optics, radar and communications systems, sensors, fiber optics, plasmas, particle accelerators, generators and motors, electromagnetic wave propagation, non-destructive evaluation, eddy currents, and inverse scattering.

Techniques of interest include but not limited to frequency-domain and time-domain techniques, integral equation and differential equation techniques, diffraction theories, physical and geometrical optics, method of moments, finite differences and finite element techniques, transmission line method, modal expansions, perturbation methods, and hybrid methods.

Where possible and appropriate, authors are required to provide statements of quantitative accuracy for measured and/or computed data. This issue is discussed in "Accuracy & Publication: Requiring, quantitative accuracy statements to accompany data," by E. K. Miller, *ACES Newsletter,* Vol. 9, No. 3, pp. 23-29, 1994, ISBN 1056-9170.

SUBMITTAL PROCEDURE

All submissions should be uploaded to ACES server through ACES web site (http://aces.ee.olemiss.edu) by using the upload button, journal section. Only pdf files are accepted for submission. The file size should not be larger than 5MB, otherwise permission from the Editor-in-Chief should be obtained first. Automated acknowledgment of the electronic submission, after the upload process is successfully completed, will be sent to the corresponding author only. It is the responsibility of the corresponding author to keep the remaining authors, if applicable, informed. Email submission is not accepted and will not be processed.

PAPER FORMAT (INITIAL SUBMISSION)

The preferred format for initial submission manuscripts is 12 point Times Roman font, single line spacing and single column format, with 1 inch for top, bottom, left, and right margins. Manuscripts should be prepared for standard 8.5x11 inch paper.

EDITORIAL REVIEW

In order to ensure an appropriate level of quality control, papers are peer reviewed. They are reviewed both for technical correctness and for adherence to the listed guidelines regarding information content and format.

PAPER FORMAT (FINAL SUBMISSION)

Only camera-ready electronic files are accepted for publication. The term **"camera-ready" means that the material is neat, legible, reproducible, and in accordance with the final version format listed below.**

The following requirements are in effect for the final version of an ACES Journal paper:

1. The paper title should not be placed on a separate page. The title, author(s), abstract, and (space permitting) beginning of the paper itself should all be on the first page. The title, author(s), and author affiliations should be centered (center-justified) on the first page. The title should be of font size 16 and bolded, the author names should be of font size 12 and bolded, and the author affiliation should be of font size 12 (regular font, neither italic nor bolded).

2. An abstract is required. The abstract should be a brief summary of the work described in the paper. It should state the computer codes, computational techniques, and applications discussed in the paper (as applicable) and should otherwise be usable by technical abstracting and indexing services. The word "Abstract" has to be placed at the left margin of the paper, and should be bolded and italic. It also should be followed by a hyphen (—) with the main text of the abstract starting on the same line.

3. All section titles have to be centered and all the title letters should be written in caps. The section titles need to be numbered using roman numbering (I. II. ….)

4. Either British English or American English spellings may be used, provided that each word is spelled consistently throughout the paper.

5. Internal consistency of references format should be maintained. As a guideline for authors, we recommend that references be given using numerical numbering in the body of the paper (with numerical listing of all references at the end of the paper). The first letter of the authors' first name should be listed followed by a period, which in turn, followed by the authors' complete last name. Use a coma (,) to separate between the authors' names. Titles of papers or articles should be in quotation marks (" "), followed by the title of journal, which should be in italic font. The journal volume (vol.), issue number (no.), page numbering (pp.), month and year of publication should come after the journal title in the sequence listed here.

6. Internal consistency shall also be maintained for other elements of style, such as equation numbering. As a guideline for authors who have no other preference, we suggest that equation numbers be placed in parentheses at the right column margin.

7. The intent and meaning of all text must be clear. For authors who are not masters of the English language, the ACES Editorial Staff will provide assistance with grammar (subject to clarity of intent and meaning). However, this may delay the scheduled publication date.

8. Unused space should be minimized. Sections and subsections should not normally begin on a new page.

ACES reserves the right to edit any uploaded material, however, this is not generally done. It is the author(s) responsibility to provide acceptable camera-ready pdf files. Incompatible or incomplete pdf files will not be processed for publication, and authors will be requested to re-upload a revised acceptable version.

COPYRIGHTS AND RELEASES

Each primary author must sign a copyright form and obtain a release from his/her organization vesting the copyright with ACES. Copyright forms are available at ACES, web site (http://aces.ee.olemiss.edu). To shorten the review process time, the executed copyright form should be forwarded to the Editor-in-Chief immediately after the completion of the upload (electronic submission) process. Both the author and his/her organization are allowed to use the copyrighted material freely for their own private purposes.

Permission is granted to quote short passages and reproduce figures and tables from and ACES Journal issue provided the source is cited. Copies of ACES Journal articles may be made in accordance with usage permitted by Sections 107 or 108 of the U.S. Copyright Law. This consent does not extend to other kinds of copying, such as for general distribution, for advertising or promotional purposes, for creating new collective works, or for resale. The reproduction of multiple copies and the use of articles or extracts for commercial purposes require the consent of the author and specific permission from ACES. Institutional members are allowed to copy any ACES Journal issue for their internal distribution only.

PUBLICATION CHARGES

All authors are allowed for 8 printed pages per paper without charge. Mandatory page charges of $75 a page apply to all pages in excess of 8 printed pages. Authors are entitled to one, free of charge, copy of the journal issue in which their paper was published. Additional reprints are available for a nominal fee by submitting a request to the managing editor or ACES Secretary.

Authors are subject to fill out a one page over-page charge form and submit it online along with the copyright form before publication of their manuscript.

ACES Journal is abstracted in INSPEC, in Engineering Index, DTIC, Science Citation Index Expanded, the Research Alert, and to Current Contents/Engineering, Computing & Technology.